Physik - Department

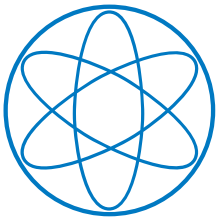

Advanced Event Reconstruction in LENA and Precision Attenuation-Length Measurements in Liquid Scintillators

Dissertation
von

DOMINIKUS ANTON HELLGARTNER

Technische Universität München

Technische Universität München
Physik-Department
Lehrstuhl für Experimentalphysik und Astroteilchenphysik

Advanced Event Reconstruction in LENA and Precision Attenuation-Length Measurements in Liquid Scintillators

Dominikus Anton Hellgartner

Vollständiger Abdruck der von der Fakultät für Physik der Technischen Universität München zur Erlangung des akademischen Grades eines

Doktors der Naturwissenschaften (Dr. rer. nat.)

genehmigten Dissertation.

Vorsitzender:	Univ.-Prof. Dr. Alejandro Ibarra
Prüfer der Dissertation:	
	1. Univ.-Prof. Dr. Lothar Oberauer
	2. Priv.-Doz. Dr. Andreas Ulrich

Die Dissertation wurde am 07.05.2015 bei der Technischen Universität München eingereicht und durch die Fakultät für Physik am 24.06.2015 angenommen.

Abstract

The planned 20 kt JUNO (**J**iangmen **U**nderground **N**eutrino **O**bservatory) and the proposed 50 kt LENA (**L**ow **E**nergy **N**eutrino **A**stronomy) detector are two next generation liquid scintillator neutrino experiments.

To ensure a successful operation of these detectors, sophisticated techniques to extract the properties of an event from the observed light signal are required. Thus, a reconstruction algorithm for MeV events (e.g., caused by geo-neutrinos or astrophysical neutrinos) in LENA was developed which is based on a full likelihood fit to the photon signal. Testing the performance of the reconstruction on 0.2 MeV to 3 MeV events simulated with a Geant4-based Monte Carlo simulation, the position resolution was found to be better than 25 cm and the start-time resolution was found to be below 0.6 ns. Furthermore, a relative energy resolution of $\Delta T_s/T_s^{\mathrm{true}} \approx 6\,\%/\sqrt{T_s^{\mathrm{true}}/\mathrm{MeV}}$, where T_s^{true} is the true kinetic energy of the electron, could be achieved which is compatible with the theoretical limit given by photon statistics.

Applying this reconstruction method to events with a dark-noise rate of up to 50 kHz per photomultiplier tube (PMT), which is the maximum dark noise expected for JUNO, showed that the harmful effect of the dark noise on the reconstruction accuracy (up to a factor 5 degradation in resolution) only influences events with sub-MeV visible energies. Additionally, it was shown that using detector electronics which register more than the first-photon arrival time of each PMT is a prerequisite for a high stability of the position reconstruction. Moreover, a dedicated study showed that the energy reconstruction is not affected by the transit-time spread of the PMTs.

Subsequently, the reconstruction was extended to cover events with single lepton tracks of ∼100 MeV, which is a prerequisite for reconstructing the full interactions of ∼GeV (atmospheric or beam) neutrinos. Testing the algorithm with 0.2 GeV to 1 GeV muon events yielded a start-point resolution of 10 cm, a start-time resolution better than 0.15 ns and an angular resolution better than 5 deg for single muons. Electron events were also successfully reconstructed, albeit at a degraded resolution: The resolution of the start point and the start time was found to be up to 5 times the corresponding resolution for muon events and the angular resolution was found to deteriorate by about 50 %.

The likelihood approach was found not to be applicable to full neutrino interactions of ∼GeV neutrinos due to the high variability of the events. Thus, a set of tools was devised to better characterize these events: First, a method was developed which separates primary from secondary events. Furthermore, the energy response of LENA to high-energy neutrinos was determined. Subsequently, an algorithm was devised to visualize the event. Based on this visualization, the vertex of simulated 1 GeV to 10 GeV neutrino interactions could be determined with an excellent resolution which is below 10 cm. Using this information as input, the number and the direction of all particle tracks with significant length could be determined, providing a handle to discriminate between neutral current (NC) and electron-neutrino charged current (CC) interactions. As ν_e appearance is the most important signal channel for conventional long baseline neutrino beams, an enhanced discrimination between NC and ν_e-CC events allows to improve the performance of LENA as a far detector of a neutrino beam.

Due to the vast size of the next generation of liquid scintillator detectors, the attenuation

length of the scintillator needs to be $> 10\,\mathrm{m}$ (LENA) and $> 24\,\mathrm{m}$ (JUNO), respectively, to ensure a sufficient photo-electron yield. Thus, an experiment was devised for a precise measurement of the scintillator's attenuation length. It allowed to measure the light attenuation in a scintillator-filled horizontal tube with an adjustable length between 1 m and 5 m. The length can be changed in steps of 1 m. The light was provided by a pulsed LED and it was detected by PMTs. Using this experiment, the attenuation length of the measured Linear Alkylbenzene (LAB) sample at a wavelength of 430 nm was determined to be $(8.89 \pm 0.05(\mathrm{stat})^{+0.59}_{-0.53}(\mathrm{syst}))\,\mathrm{m}$. Additionally, the effective index of refraction of the LAB was determined to be $1.59 \pm 0.05(\mathrm{stat}) \pm 0.10(\mathrm{syst})$.
The achieved accuracy of the measured attenuation length was still too low to test whether the attenuation length of the JUNO scintillator meets its requirements. Thus a second, improved experiment to measure the attenuation length was developed sacrificing the possibility to measure the effective index of refraction. Using a halogen light bulb with a narrow-band wavelength filter as light source and a temperature-stabilized CCD-camera as detector allowed to reduce temporal variations to below 10^{-3}. The attenuation length of the measured LAB sample at a wavelength of 430 nm was determined to be $(9.60 \pm 0.04(\mathrm{stat}) \pm 0.11(\mathrm{syst}))\,\mathrm{m}$. This corresponds to an absorption length of $(15.6 \pm 0.8(\mathrm{stat}) \pm 0.9(\mathrm{syst}))\,\mathrm{m}$. The expected accuracy for an attenuation length of 24 m is 6.5 %, which is sufficient for the measurements required for JUNO.
Finally, an upgrade of the experiment was designed: It aims at reducing the error down to 1.2 % for an attenuation length of 24 m by using a vertical tube.

Zusammenfassung

JUNO und LENA sind zwei zukünftige Neutrinodetektoren der nächsten Generation mit einer Masse von 20 bzw. 50 kt.
Um die physikalischen Eigenschaften der beobachteten Ereignisse untersuchen zu können, müssen diese aus dem Lichtsignal, das von den Photomultipliern (PMTs) aufgenommen wurde, rekonstruiert werden. Im Rahmen dieser Arbeit wurde ein Algorithmus entwickelt, der MeV-Ereignisse (verursacht z.B. durch Wechselwirkungen von Geoneutrinos oder von solaren Neutrinos) in LENA mit Hilfe eines Maximum-Likelihood-Fits aus dem Photonensignal rekonstruiert. Die Leistungsfähigkeit des Algorithmus wurde anhand von simulierten Ereignissen im Energiebereich zwischen 0.2 MeV und 3 MeV bestimmt. Die Position eines Ereignisses konnte dabei auf weniger als 25 cm genau bestimmt werden bei einer Zeitauflösung von unter 0.6 ns. Die relative Energieauflösung lässt sich beschreiben durch $\Delta T_s/T_s^{\mathrm{true}} \approx 6\,\%/\sqrt{T_s^{\mathrm{true}}/\mathrm{MeV}}$ (T_s^{true} ist die wahre kinetische Energie der Elektronen), was mit der durch die Photonenstatistik vorgegebenen Grenze vereinbar ist.
Außerdem wurde gezeigt, dass der Fit auf Ereignisse mit einer Dunkelzählrate von bis zu 50 kHz pro PMT anwendbar ist, auch wenn sich die erreichbaren Auflösungen um bis zum 5-fachen verschlechtern. Dies betrifft jedoch nur Ereignisse mit einer sichtbaren Energie unter einem MeV. Es konnte gezeigt werden, dass für die Stabilität der Rekonstruktion eine Detektorelektronik, welche nicht nur das erste Photon zeitlich auflösen kann, vorteilhaft ist. Zusätzlich konnte gezeigt werden, das die Form der Verteilung des Signallaufzeitunterschieds in PMTs sich nicht auf die erzielbare Energieauflösung auswirkt.
Im Weiteren wurde das Verfahren erweitert und ist somit auch auf isolierte Leptonen im Energiebereich einiger 100 MeV anwendbar. Für Myonen mit einer kinetischen Energie zwischen 0.2 GeV und 1 GeV konnte der Startpunkt mit einer Unsicherheit von unter 10 cm bestimmt werden. Die Unsicherheit der Startzeit war besser als 0.15 ns und die Richtung des Myons konnte mit einem Fehler von unter 5 Grad bestimmt werden. 0.5 GeV-Elektronen konnten ebenfalls erfolgreich rekonstruiert werden, allerdings mit einer deutlich schlechteren Auflösung: Die Genauigkeit der rekonstruierten Startpunkte und Startzeiten verschlechtert sich um bis zu einem Faktor 5, die erreichbare Winkelauflösung um bis zu 50 %.
Durch die hohe Vielfalt von GeV Neutrino-Wechselwirkungen (z.B. durch atmosphärische Neutrinos oder Beschleunigerneutrinos) war es nicht möglich, den Likelihood-Fit auch auf diese Ereignisse anzuwenden. Dennoch wurde versucht, so viele Eigenschaften dieser Ereignisse wie möglich zu bestimmen: Zuerst wurde eine Methode entwickelt, die primäre von sekundären Ereignissen trennt. Darauf basierend konnte die energetische Detektorantwort auf GeV-Neutrino-Wechselwirkungen bestimmt werden. Im Weiteren wurde ein Algorithmus entwickelt, mit dem sich ein Ereignis visualisieren lässt. Darauf basierend konnte der Wechselwirkungspunkt des Neutrinos mit einer Auflösung von besser als 10 cm bestimmt werden. Unter Nutzung dieser Information wurde eine Methode entwickelt, welche die Richtung aller Teilchenspuren mit einer signifikanten Länge bestimmen kann. Dies kann dafür verwendet werden, zwischen ν_e-CC- und NC-Wechselwirkungen zu unterscheiden. Da das Erscheinen von ν_e der wichtigste Signalkanal für einen konventionellen Neutrinostrahl ist, führt eine verbesserte Unterscheidung zwischen ν_e-CC und NC Ereignissen zu einer erhöhten Leistungsfähigkeit von LENA als ferner Detektor eines Neutrinostrahls.

Durch die großen Ausmaße von JUNO und LENA benötigen beide Detektoren Szintillatoren mit einer Abschwächlänge von mehr als 10 m (LENA) bzw. mehr als 24 m (JUNO). Um diese Größe präzise zu vermessen, wurde ein Experiment entwickelt, das auf einem horizontalen Rohr mit einer einstellbaren Länge zwischen 1 m und 5 m basiert. Die Rohrlänge konnte dabei in 1 m Schritten geändert werden. Das von PMTs detektierte Licht wurde von einer gepulsten LED erzeugt. Mit diesem Experiment konnte die Abschwächlänge einer Linear Alkylbenzene (LAB) Probe zu $(8.89 \pm 0.05(\text{stat})^{+0.59}_{-0.53}(\text{syst}))$ m bestimmt werden. Zusätzlich ergab sich der effektive Brechungsindex von LAB zu $1.59 \pm 0.05(\text{stat}) \pm 0.10(\text{syst})$. Die systematischen Fehler für die Abschwächlänge der ersten Generation des Experimentes waren zu hoch, um zu testen ob der Szintillator für JUNO den Anforderungen genügt. Deshalb wurde eine weitere Generation des Experiments entwickelt. Mit diesem neuen Experiment ist die Messung des effektiven Brechungsindexes allerdings nicht mehr möglich. Durch Verwendung einer Lichtquelle bestehend aus einer Halogenlampe und einem Bandpassfilter sowie einer temperaturstabilisierten CCD-Kamera als Detektor, konnten die relativen zeitlichen Schwankungen auf unter ein Promille gesenkt werden. Mit diesem System konnte die Abschwächlänge einer LAB-Probe bei 430 nm zu $(9.60 \pm 0.04(\text{stat}) \pm 0.11(\text{syst}))$ m bestimmt werden. Dies entspricht einer Absorptionslänge von $(15.6 \pm 0.8(\text{stat}) \pm 0.9(\text{syst}))$ m. Die erwartete Auflösung von 6.5 % bei 24 m Abschwächlänge ist ausreichend für die von JUNO benötigten Messungen.
Um die Genauigkeit weiter zu erhöhen wurde ein Upgrade des Experiments entwickelt: Durch die Nutzung eines vertikalen Rohres soll eine Messgenauigkeit von 1.2 % bei 24 m Abschwächlänge erreicht werden.

Contents

Chapter 1

Introduction

Experimental neutrino physics started with the detection of (anti-)neutrinos emitted from a nuclear power plant in 1956 [1, 2] using a liquid scintillator (LSc) detector. Today, more than 60 years later, detectors based on LSc technology like Borexino [3] and KamLAND [4] are still the only real-time detectors available which can detect neutrinos below the $\sim$5 MeV [5] threshold of current water-Cerenkov detectors. Despite their success, the current generation of LSc detectors is limited by their small target mass of less than 1 kt which severely limits the available statistics as well as the available shielding. Thus, there are currently two proposed next-generation neutrino detectors: The 20 kt **J**iangmen **U**nderground **N**eutrino **O**bservatory (JUNO) [6] which focuses on a precision measurement of reactor anti-neutrino oscillations and the 50 kt **L**ow **E**nergy **N**eutrino **A**stronomy (LENA) [7] detector which is designed as a multi-purpose neutrino observatory for natural neutrino sources.
Charged particles traveling through the LSc excite the scintillator molecules. The relaxation of these excitations produces photons which are detected in the photomultiplier tubes (PMTs) surrounding the LSc tank. To ensure the success of the next generation of LSc-detectors, it is crucial to develop algorithms which determine the properties of an event from the observed time and charge signal of these PMTs. This task is complicated by the huge size of the next-generation detectors as absorption and especially scattering in the scintillator are much more relevant compared to the current detector generation and thus have to be taken into account properly.
While the large size is a challenge for the reconstruction of events, it allows LSc detectors to extend their scope and to deal with events with GeV energies which are generally not contained in the current detector generation. Neutrinos at these energies are either atmospheric neutrinos or accelerator neutrinos which might be able to shed light on the currently unknown mass hierarchy. Again, the success of this endeavor critically depends on the capability to reconstruct GeV neutrino interactions which often feature many particles in their reaction exit channels. Although the observed light in LSc detectors features no inherent directionality like in water-Cerenkov detectors, it is principally possible to reconstruct these events using the time information of the detected photons, given the track-length of the particles is at least of the order of $\sim$1 m.
The huge size of the next-generation neutrino detectors also implies a technical challenge for the development of a scintillator: It has to feature a sufficient transparency to allow photons from the center of the detector volume to reach the PMTs at the detector boundary. Such a development requires a possibility to precisely determine the transparency of

the scintillator in a laboratory scale experiment.

In the remainder of this chapter, neutrino oscillations, our current knowledge of neutrino properties, and possibilities to extend this knowledge will be briefly introduced. Subsequently, chapter 2 will provide a short introduction into neutrino interactions as well as into the basic principles of current real-time neutrino detectors. As the main focus of this thesis is on the LENA detector, it will be described in chapter 3. The algorithms developed to reconstruct ∼MeV neutrino interactions will be presented in chapter 4 along with the obtained performance. In chapter 5, these methods will be extended to cover single lepton tracks with lepton energies in the 100 MeV range. While a full reconstruction of ∼GeV energy neutrino events could not be accomplished with the technique described in chapter 5, chapter 6 introduces algorithms which have been developed to extract global information from these events. Additionally, the performance of these algorithms is discussed in the context of determining the mass hierarchy using a 2300 km baseline neutrino beam.
The second part of this thesis deals with the measurement of the transparency of the scintillator: Chapter 7 describes the set-up, the performance and the results of a measurement to determine the LSc's transparency. Based on these results, an improved set-up is devised which is presented in chapter 8. There additionally the result of the measurement and its impact on the next generation of LSc detectors are discussed.

1.1 Neutrinos in the Standard Model

The Standard Model (SM) of particle physics is the unified theory of three of the four fundamental interactions, namely the electromagnetic interaction, the weak interaction and the strong interaction. In this framework, the theory of the electromagnetic and the weak interaction is based on the spontaneously broken local gauge symmetry $SU(2) \times U(1)$ [8]. While the left handed fermion fields transform as doublets under $SU(2)$ the right handed fields are singlets [9]:

$$\begin{pmatrix} \nu_e \\ e^- \end{pmatrix}_L, \begin{pmatrix} \nu_\mu \\ \mu^- \end{pmatrix}_L, \begin{pmatrix} \nu_\tau \\ \tau^- \end{pmatrix}_L, e_R,\ \mu_R,\ \tau_R. \tag{1.1}$$

Here, the indices L and R denote left handed and right handed fields, respectively. The neutrinos only interact via the weak interaction, i.e. they are neither affected by the electromagnetic nor the strong force. Note, that there are, by assumption, no right handed neutrinos in the SM. Hence, it is not possible to generate neutrino masses via the standard Higgs-mechanism leading to massless neutrinos in the SM[8].

1.2 Neutrino oscillations in vacuum

Contrary to the lepton family number conservation predicted by the SM, several experiments have collected compelling evidence for transitions between different neutrino flavors: Being first observed in atmospheric neutrino experiments [10], they have also been detected in reactor neutrino experiments at different baselines [4, 11], solar neutrino experiments [12] and experiments with long baseline neutrino beams [13].

To describe the experimental results, a mixing among all three[1] currently known neutrino flavors is required [15]. This means that the weak flavor eigenstates $|\nu_\alpha\rangle,\ \alpha \in \{e, \mu, \tau\}$ can be described as a superposition of mass eigenstates $|\nu_i\rangle,\ i \in \{1, \ldots, 3\}$ with definite masses m_i [16]:

$$|\nu_\alpha\rangle = \sum_{i=1}^{3} U_{\alpha i} |\nu_i\rangle. \tag{1.2}$$

Here, $U_{\alpha i}$ is the unitary neutrino mixing matrix which is called the Pontecorvo-Maki-Nakagawa-Sakata (PMNS) Matrix [9]. It is commonly parametrized[2] using three angles of rotation ϑ_{ij} and one CP-violating phase δ [18]:

$$U = \begin{pmatrix} 1 & 0 & 0 \\ 0 & c_{23} & s_{23} \\ 0 & -s_{23} & c_{23} \end{pmatrix} \begin{pmatrix} c_{13} & 0 & s_{13}e^{-i\delta} \\ 0 & 1 & 0 \\ -s_{13}e^{-i\delta} & 0 & c_{13} \end{pmatrix} \begin{pmatrix} c_{12} & s_{12} & 0 \\ -s_{12} & c_{12} & 0 \\ 0 & 0 & 1 \end{pmatrix}, \tag{1.3}$$

where the abbreviations $c_{ij} = \cos(\vartheta_{ij})$ and $s_{ij} = \sin(\vartheta_{ij})$ are used.

The following derivation for neutrino oscillations is based on the assumption that the neutrino mass eigenstates can be treated as plain waves. Furthermore the exact nature of the neutrino production and the neutrino detection reactions are not taken into account. For a more rigorous theoretical treatment, see [19].
As neutrino mass eigenstates are eigenstates of the free Hamiltonian, their time evolution is given by[3] [18]:

$$|\nu_i(t)\rangle = \exp(-iE_i t)|\nu_i(0)\rangle, \tag{1.4}$$

where E_i is the energy of the neutrino mass eigenstate $|\nu_i(t)\rangle$. Hence, the time dependent probability $P_{\nu_\alpha \to \nu_\beta}(t)$ to detect a neutrino, which was produced in the flavor state $|\nu_\alpha\rangle$, in the flavor state $|\nu_\beta\rangle$ is given by [19]:

$$P_{\nu_\alpha \to \nu_\beta}(t) = |\langle \nu_\beta | \nu_\alpha(t) \rangle|^2 = \left| \sum_{i=1}^{3} U^*_{\beta i} \exp(-iE_i t) U_{\alpha i} \right|^2. \tag{1.5}$$

For antineutrinos, U has to be replaced by U^* in equation (1.5)[20].
Using relativistic kinematics, the energy of the flavor eigenstate E_i can be calculated to be:

$$E_i = \sqrt{p_i^2 + m_i^2} \approx p_i + \frac{m_i^2}{2p_i} \approx E + \frac{m_i^2}{2E}, \tag{1.6}$$

where the ultra-relativistic approximation ($E_i \gg m_i$) was used [19]. The ultra relativistic condition was fulfilled for all detected neutrinos up to now. It also implies, that for neutrinos

$$L \approx t \tag{1.7}$$

[1] There are some experimental results, that point in the direction of additional sterile neutrinos. However, even with the addition of sterile neutrinos, an explanation of all currently observed data is difficult [14].

[2] If neutrinos are of Majorana-type, two additional phases show up. As they do not affect flavor oscillation, they are not discussed here [17].

[3] $\hbar = c = 1$

holds, where L is the distance the neutrino traveled from its point of creation at $t = 0$. Hence, equation (1.5) becomes [17]:

$$P_{\nu_\alpha \to \nu_\beta}(L) = \left| \sum_{i=1}^{3} U^*_{\beta i} \exp\left(-\frac{i m_i^2}{2E} L \right) U_{\alpha i} \right|^2 . \tag{1.8}$$

Using that U is a unitary matrix, this can be further evaluated to [17, 20]:

$$\begin{aligned} P_{\overset{(-)}{\nu_\alpha} \to \overset{(-)}{\nu_\beta}} &= \delta_{\alpha\beta} \\ &- 4 \sum_{i>j} \Re(U^*_{\alpha i} U_{\beta i} U_{\alpha j} U^*_{\beta j}) \sin^2 \left[1.27 \frac{\Delta m^2_{ij}}{\mathrm{eV}^2} \frac{L/\mathrm{km}}{E/\mathrm{GeV}} \right] \\ &\overset{+}{(-)} \; 2 \sum_{i>j} \Im(U^*_{\alpha i} U_{\beta i} U_{\alpha j} U^*_{\beta j}) \sin \left[2.54 \frac{\Delta m^2_{ij}}{\mathrm{eV}^2} \frac{L/\mathrm{km}}{E/\mathrm{GeV}} \right], \end{aligned} \tag{1.9}$$

where $\Delta m^2_{ij} = m^2_i - m^2_j$. The numeric prefactors appear when taking the SI-values of $\hbar$ and c into account. This equation shows, that the probability to detect a neutrino, emitted in a pure flavor state $|\nu_\alpha\rangle$ in a flavor state $|\nu_\beta\rangle$ is generally non-vanishing and oscillating in L/E. Hence, this phenomenon is called neutrino oscillations.
The oscillation amplitude is determined by the matrix elements, i.e. by the mixing angles and the CP-violating phase δ. The oscillation frequency on the other hand is proportional to Δm^2_{ij}. Hence, the observation of neutrino oscillations requires $|\Delta m_{ij}| > 0$ for at least one pair (i, j). Consequently, at least one neutrino mass eigenstate has to have a non vanishing mass. Furthermore, as neutrino oscillations depend only on mass squared differences, no information about the absolute neutrino mass scale can be gained from neutrino oscillations.
Finally, the oscillation probability $P_{\nu_\alpha \to \nu_\beta}$ differs from the oscillation probability for antineutrinos $P_{\bar{\nu}_\alpha \to \bar{\nu}_\beta}$ only if $\Im(U^*_{\alpha i} U_{\beta i} U_{\alpha j} U^*_{\beta j})$ is non vanishing. As a CP-transformation transforms $\nu_\alpha \to \nu_\beta$ to $\bar{\nu}_\alpha \to \bar{\nu}_\beta$, this implies CP violation [20].
Hence, CP is only violated in the neutrino sector, if $\delta \neq 0$ and $\delta \neq \pi$. Note, that for disappearance experiments ($\alpha = \beta$)

$$\Im(U^*_{\alpha i} U_{\beta i} U_{\alpha j} U^*_{\beta j}) = \Im(|U_{\alpha i}|^2 |U_{\alpha j}|^2) = 0 \tag{1.10}$$

holds. Therefore, to observe leptonic CP-violation and to measure δ an apperance experiment ($\alpha \neq \beta$) is required.

1.3 Current knowledge of oscillation parameters

The current knowledge of the oscillation parameters is summarized in table 1.1. Despite the huge amount of data collected, there is still some information missing:

- While the amplitude of the oscillation driven by ϑ_{23} is known to be close to maximum, the octant of the ϑ_{23} angle is still not known.

Parameter	Value
$\sin^2(2\vartheta_{12})$	$0.857^{+0.023}_{-0.025}$
$\Delta m^2_{21}[10^{-5}\,\mathrm{eV}^2]$	$7.50^{+0.19}_{-0.20}$
$\sin^2(2\vartheta_{23})$	> 0.95 (90% CL)
$\lvert\Delta m^2_{23}\rvert[10^{-3}\,\mathrm{eV}^2]$	$2.32^{+0.12}_{-0.08}$
$\sin^2(2\vartheta_{13})$	0.095 ± 0.010

Table 1.1: Current values for the known oscillation parameters [21]. As long as not noted otherwise, the presented errors are at the 1σ level. Currently, there are no significant experimental results on the phase δ.

- Up to now, only the absolute value of Δm^2_{23} is known. Therefore two different orderings of the mass eigenstates are possible. They are typically called normal hierarchy (NH) $\Delta m^2_{23} > 0$ and inverted hierarchy (IH) $\Delta m^2_{23} < 0$ [22]. Note that the sign of Δm^2_{12} is known due the observation of the MSW effect in the sun [23].
- The value of the phase δ is completely unknown. While some global fits show preferred regions, they are all well below the 3σ level [15].

There are currently numerous proposals to determine the mass hierarchy (MH) using atmospheric neutrinos [24, 25], reactor neutrinos [26] or using long baseline beam based experiments [27]. The measurement of δ is more difficult and will require a beam based experiment, probably with a next generation beam facility. For an in depth review of the physics potential of beam based experiments and novel experiments for the mass hierarchy, see [22].

1.4 Neutrino oscillations in matter

When traveling through matter, the interactions of the neutrinos with the surrounding material lead to an additional, effective potential for the neutrinos. As neutral current (NC) interactions do not differ between the different neutrino flavors, this additional potential leads to a global potential offset which does not affect neutrino oscillations (see equation (1.5)).
Charged current (CC) interactions on the other hand, single out the electron neutrino as there are no muons and tauons in normal matter. Hence, coherent forward ν_e-electron scattering leads to an additional potential for ν_e of [20]

$$V = \sqrt{2} G_F N_e, \tag{1.11}$$

where N_e is the electron number density and G_F is the Fermi constant. For anti-electron neutrinos, V has to be replaced by $-V$. As this potential acts only on the $|\nu_e\rangle$ flavor eigenstate, the mass eigenstates are no longer independent of each other. Hence, a re-diagonalization has to be done, leading to effective mixing angles and mass differences.
Here, it is instructive to look at the simplified two flavor case, where neutrino oscillations can be described by only one mixing angle ϑ and one mass squared difference Δm^2. In

matter, the corresponding effective mixing angle ϑ_M and mass squared difference Δm^2_M are [20]:

$$\Delta m^2_M = \Delta m^2 \sqrt{\sin^2(2\vartheta) + (\cos(2\vartheta) - A)^2} \tag{1.12}$$

$$\sin^2(2\vartheta_M) = \frac{\sin^2(2\vartheta)}{\sin^2(2\vartheta) + (\cos(2\vartheta) - A)^2} \tag{1.13}$$

$$\text{with } A = \frac{2\sqrt{2} G_F N_e E}{\Delta m^2}. \tag{1.14}$$

Note that the matter effects scale with A, i.e., they are dependent on the product of neutrino energy and electron density. Furthermore, $A \propto 1/\Delta m^2$. Hence, the effect of matter on neutrino oscillations depends on the sign of Δm^2. Therefore a large influence of matter effects on neutrino oscillations is desirable in an experiment trying to determine the mass hierarchy. Note that, to first order, the influence of the CP-violating phase δ is independent of the size of the matter effects [28].

From the proposals to measure mass hierarchy mentioned in 1.3, the determination of the mass hierarchy using long baseline neutrino beams is relevant for this thesis. As neutrino beams can reach neutrino energies of several GeV, matter effects are significant despite the relatively low electron density in the earth.
In a neutrino beam, the vast majority of the produced neutrinos (typically more than 99% [13]) are muon (anti-)neutrinos[4]. To determine the mass hierarchy, the most important channel is the electron neutrino appearance channel [27]. The corresponding oscillation probability $P_{\nu_\mu \to \nu_e}$ is shown in figure 1.1 as a function of the neutrino energy for three different baselines L of 259 km, 2300 km and 8770 km for both mass hierarchies. The shown distances correspond to the existing T2K beam [13], the proposed beam from Cern to the Pyhäsalmi Mine in Finland (CN2PY) [27] and a hypothetical beam from Cern to the Super Kamiokande detector (see section 2.2).
As expected due to the L/E dependency of the neutrino oscillation probability (compare equation (1.9)), the oscillation maximum, which is highest in energy, shifts to higher energies with increasing baseline. Hence, the influence of matter effects rises with increasing baseline. As discussed above, this also increases the sensitivity of the oscillation probability to the mass hierarchy. This is visualized by comparing the red (NH) and blue (IH) shaded bands of the graphs in figure 1.1, which show the possible ranges of $P_{\nu_\mu \to \nu_e}$. The width of the bands is determined by the variation of the oscillation probability due to the unknown CP-violating phase δ.
For the relatively short, existing T2K beam (top plot in figure 1.1), the shaded bands show a strong overlap. Hence, determining the mass hierarchy using the T2K beam is challenging and only possible for a small fraction of all possible δ values. For the CN2PY beam (central plot in figure 1.1) in contrast, the oscillation probabilities are clearly separated for neutrino energies above 2.5 GeV. This principally allows to determine the mass hierarchy for all possible values of δ without knowing the value of δ. The separation between the two hierarchies is even further increased for the longest possible beam shown in figure 1.1.

[4] There are proposals for next-generation neutrino beam facilities like β-beams [29] or neutrino factories [30] where other neutrino flavors are produced. Hence, for these facilities, oscillation channels other than $\nu_\mu \to \nu_e$ are the most important channel.

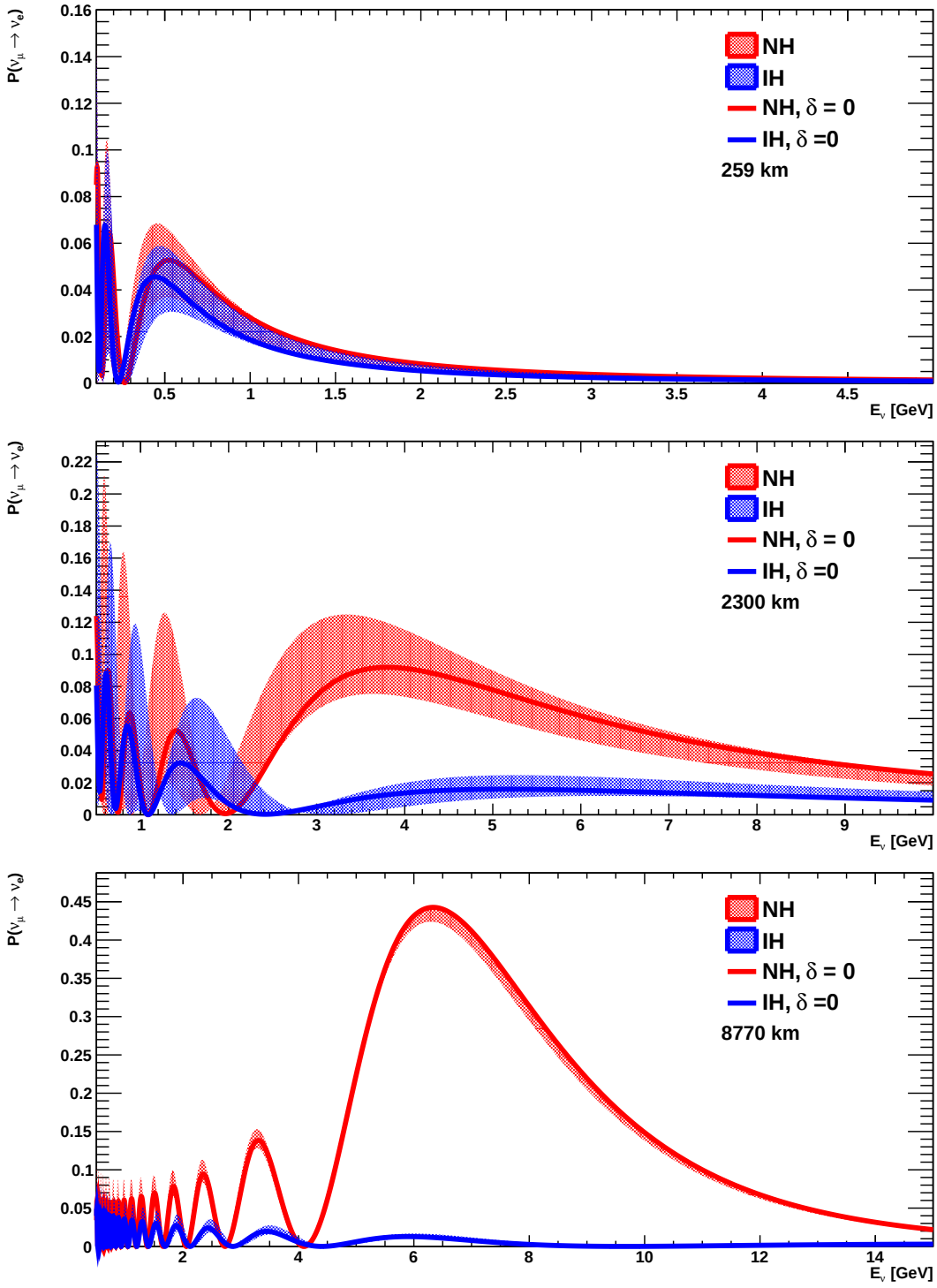

Figure 1.1: The $\nu_\mu \to \nu_e$ oscillation probability as a function of the neutrino energy for the inverted (IH) and normal (NH) mass hierarchy, respectively. The corresponding baselines are denoted in the graphs. The 259 km baseline (top) corresponds to the baseline of the T2K experiment [13], the 2300 km baseline (center) to the beam from Cern to Pyhäsalmi [27] and the 8770 km baseline (bottom) to a hypothetical beam from Cern to the Super Kamiokande detector. The solid graphs show the oscillation probability for $\delta = 0$ while the shaded areas indicate the variability of the oscillation probability due to varying δ. Note the different energy scales of the graphs. The graphs were generated with the GLoBES [31, 32] library using the Preliminary reference Earth model [33, 34] to model the density distribution in the earth's crust.

Note that while for the longer baselines, the maximum difference in oscillation probability between normal and inverted hierarchy is of order 10%, the difference in oscillation probability between two extreme values of δ is typically about 4%. Hence, a determination of the value of δ will be more challenging than the determination of the mass hierarchy using a long baseline beam.

Chapter 2

Neutrino detection

As neutrinos do not carry electric charge, they cannot be detected directly. The only way to determine the kinetic quantities of neutrinos in an experiment is to detect the products of neutrino interactions. From the measured properties of the secondary particles, the neutrino properties can be determined.
The different types of neutrino interactions occurring at the energies relevant in this thesis are discussed in section 2.1. Subsequently, sections 2.2 and 2.3 introduce two currently used detector-concepts aiming at measuring the secondary particles created in neutrino interactions: The water Cerenkov detector and the liquid scintillator detector.

2.1 Neutrino interactions

As already noted in section 1.1, neutrinos interact only via the weak interaction. At neutrino energies in the MeV range, only interactions with the complete nuclei of the target material as well as with the electrons of the atomic shell are possible, as the transferred momenta are too small to resolve the substructure of the nuclei. This case is treated in section 2.1.1. Section 2.1.2 successively deals with the situation for neutrinos in the GeV range. At this energy, the transferred momenta are typically high enough to resolve the individual nucleons in a nucleus or even the quarks contained in the nucleons.

2.1.1 Neutrinos with energies in the MeV-region

The most important reaction currently used to detect neutrinos with MeV energies, is the elastic scattering off electrons:

$$\overset{(-)}{\nu}_x + e^- \rightarrow \overset{(-)}{\nu}_x + e^-. \tag{2.1}$$

While for $\overset{(-)}{\nu}_\mu$ and $\overset{(-)}{\nu}_\tau$ this reaction occurs only via the NC channel, an additional CC channel is present for $\overset{(-)}{\nu}_e$. Thus, the cross section for $\overset{(-)}{\nu}_e$ is enhanced.
Generally, the cross sections for elastic scattering off electrons scale linearly with energy and are in the range [35]

$$0.95 \cdot 10^{-44}\,\mathrm{cm}^2 < \frac{\sigma_{\overset{(-)}{\nu}_x}}{E_\nu/\mathrm{MeV}} < 0.13 \cdot 10^{-44}\,\mathrm{cm}^2, \tag{2.2}$$

with the cross section being maximal for ν_e and minimal for $\bar{\nu}_{\mu,\tau}$.
As the neutrino in the exit channel is not detected, its energy is unknown. Hence, it is impossible to determine the energy of the incident neutrino on an event by event basis from the kinetic energy of the electron alone[1].

In materials containing free protons, such as liquid scintillators, there is an additional interaction channel for $\bar{\nu}_e$, the inverse beta decay (IBD) [36]:

$$p + \bar{\nu}_e \rightarrow n + e^+. \tag{2.3}$$

The energy threshold of this nuclear reaction is 1.8 MeV. A rough approximation of the cross section yields [36]

$$\sigma \approx 9.52 \cdot 10^{-44}\,\mathrm{cm}^2 \frac{p_e E_e}{\mathrm{MeV}^2}, \tag{2.4}$$

where p_e and E_e are the momentum and the energy of the emitted positron, respectively. Thus, typically the inverse beta decay cross section is at least one order of magnitude higher than the cross section of the elastic scattering. As the emitted positron is much lighter than the emitted neutron, the neutron recoil can typically be neglected. Hence, in contrast to the elastic scattering, the energy of the incident neutrino can be determined on an event by event basis from the energy of the produced positron using [36]:

$$E_e \approx E_\nu - \Delta, \tag{2.5}$$

where $\Delta = m_n - m_p = 1.293\,\mathrm{MeV}$ is the difference between the neutron and the proton rest energy.
Note that the produced neutron typically thermalizes in the detection medium and is successively captured on a proton[2], releasing the deuterium binding energy of 2.2 MeV. This provides a signal which can be used to suppress backgrounds via a delayed coincidence in time.

Additionally, there are some CC reactions of $\overset{(-)}{\nu}_e$ on carbon, which are possible in a liquid scintillator detector. For a summary of these reactions, see [35].

In all of the mentioned detection reactions, the products are in the MeV range. The range of electrons with these energies is typically below 1 cm [38] and the range of heavier products is even smaller. Hence, from the point of view of reconstructing these events, the energy deposition in the detection medium can be considered to be point-like.

2.1.2 Neutrinos with energies in the GeV-region

The energy range covered in this thesis for high energy neutrino interactions is set by the CN2PY neutrino beam (compare figure 1.1 central plot, [27]), producing neutrino energies in the range from ∼1 GeV to ∼10 GeV. In this energy region, multiple interaction types are possible [39]:

[1] If the direction of the incident neutrino is known, an event by event energy reconstruction would be principally possible by measuring the direction of the recoil electron.

[2] A neutron capture on other elements of the detection medium like carbon is also possible. Some experiments even dope the detection medium with a material like gadolinium which has a high thermal neutron capture cross section and releases more energy on neutron capture (see e.g. [37]).

- **Quasielastic scattering (QEL):**
  For energies below ∼1 GeV, neutrinos predominantly scatter elastically off a single nucleon in the target nucleus, which is typically called quasielastic scattering (QEL). Hence, the relevant CC reactions are

$$\nu_l + n \rightarrow l^- + p \quad \text{and} \tag{2.6}$$
$$\bar{\nu}_l + p \rightarrow l^+ + n \tag{2.7}$$

  where $l \in \{e, \mu, \tau\}$. If the target nucleon is not free but initially part of a nucleus, nuclear effects have to be taken into account: Due to the confinement of the nucleons to the nucleus, the target proton is no longer at rest. The mean momentum of a nucleon in ^{12}C is 227 MeV/c [40]. This leads to a physical limit of the achievable resolution for the neutrino energy if it is reconstructed only from the direction and energy of the lepton. Furthermore, as the secondary particles are produced inside the nucleus, they can interact with the other nucleons of the nucleus while leaving the nucleus. Thus, additional particles can be emitted from the nucleus. This leads to final states which are more complex than the final states in equations (2.6) and (2.7).
  Nevertheless, the signatures induced by CC QEL interactions are the preferable signatures from the point of view of reconstructing theses events. Due to the large mass of the nucleons, their range is relatively short[3] even at kinetic energies of a few 100 MeV. Hence, theses events typically can be approximated as a point-like energy deposition at the vertex and an additional lepton track.
  Apart from that, QEL interactions of NC type[4] are also possible:

$$\overset{(-)}{\nu_l} + N \rightarrow \overset{(-)}{\nu_l} + N \quad \text{with } N \in \{n, p\}. \tag{2.8}$$

  The energy carried away by the neutrino in the exit channel leaves the detector. Hence, the energy deposited in the detector is much lower, typically around 42% of the energy of the incoming neutrino[5], than the neutrino energy. Hence, a reconstruction of the neutrino energy is very challenging in this case, as a kinematic reconstruction of the neutrino energy would require a reconstruction of the direction, energy and type of all particles. Note that this is only possible if the direction of the incident neutrino is known, i.e. if the neutrinos are from a source with known position like in the case of a neutrino beam.

- **Resonant pion production (RES):**
  At the given energies, neutrinos can also interact inelastically with nucleons. In this case, intermediate excited states N^* can be produced, most prominently the $\Delta(1232)$ resonance. These states successively decay back to a stable[6] nucleon and additional particles. Typically, this results in the production of a single additional

[3] The range of a 100 MeV proton in scintillator is about 10 cm [38].

[4] In [39], NC QEL events are denoted as NC elastic scattering.

[5] This number is derived from about 92 000 NC QEL neutrino interactions on the LENA scintillator (see section 3.1.2), featuring a flat distribution of incident neutrino energies for all types of neutrino interactions [41]. The interactions were simulated using the GENIE neutrino Monte Carlo event generator [42].

[6] In this context, the neutron is considered a stable nucleon.

pion. The corresponding CC interaction reads

$$\overset{(-)}{\nu_l} + N \to l^{\pm} + \quad N^* \tag{2.9}$$

$$N^* \quad \to N' + \pi \quad \text{with } \pi \in \{\pi^{\pm}, \pi^0\}. \tag{2.10}$$

Note, that N and N' are not necessarily the same nuclei.
The process can also occur via NC interaction. In this case, equation (2.9) has to be replaced with

$$\overset{(-)}{\nu_l} + N \to \overset{(-)}{\nu_l} + N^*. \tag{2.11}$$

Compared to the QEL events, the event signature is now considerably more difficult, as the pion can have sufficient energy to have a non-negligible range. Hence, compared to QEL events, there is an additional track. Additionally, as pions are not stable their decay products have to be taken into account. This is especially important for π^0s, which typically decay in flight ($\tau_{\pi^0} = 8.52 \cdot 10^{-17}\,\text{s}$ [21]).
Note, that while the decay in a single pion is most common, the excited nucleon can also decay into multiple pions and/or create heavier mesons.

- **Coherent pion production (COH)**
  Instead of interacting with a single nucleon, the neutrinos can also interact with the whole nucleus A at once:

$$\overset{(-)}{\nu_l} + A \longrightarrow l^{\pm} + A + \pi^{\mp}\ (\text{CC}), \quad \text{and} \quad \overset{(-)}{\nu_l} + A \longrightarrow \overset{(-)}{\nu_l} + A + \pi^0\ (\text{NC}). \tag{2.12}$$

  For the neutrino to interact with the whole nucleus, COH events typically feature a comparatively low momentum transfer just above the threshold for pion production. This fact, combined with the large mass of the nucleus leads to the emission of the pion along the direction of the incoming neutrino.

- **Deep inelastic scattering (DIS):**
  At higher transferred momenta, the neutrinos interact with the individual quarks q of the nucleon. Hence, such a reaction has a lepton and a quark in the final state:

$$\overset{(-)}{\nu_l} + q \quad \to \quad l^{\pm} + q' \quad (\text{CC}) \tag{2.13}$$

$$\overset{(-)}{\nu_l} + q \quad \to \quad \overset{(-)}{\nu_l} + q \quad (\text{NC}). \tag{2.14}$$

  In the case of a CC reaction, the lepton is the charged partner of the neutrino, in the case of a NC reaction, the lepton is a neutrino. As the quark in the exit channel and the spectator quarks cannot exist outside of a hadron, hadronisation takes place. Hence, multiple hadrons are present in the exit channel. Typically most of them are pions. At sufficient energies, these produced hadronic particles manifest themselves as a hadronic shower in the detector. Due to the high particle multiplicity that can be created in such a shower, this event type is very difficult to reconstruct in a detector.

Figure 2.1 shows the neutrino cross section per neutrino energy and per nucleon as a function of the neutrino energy for a ^{12}C target. Additionally, the different subprocesses are shown. The energy range up to 10 GeV can be divided into three ranges: For neutrino energies around 1 GeV, QEL interactions dominate. In the region around 2 GeV, most

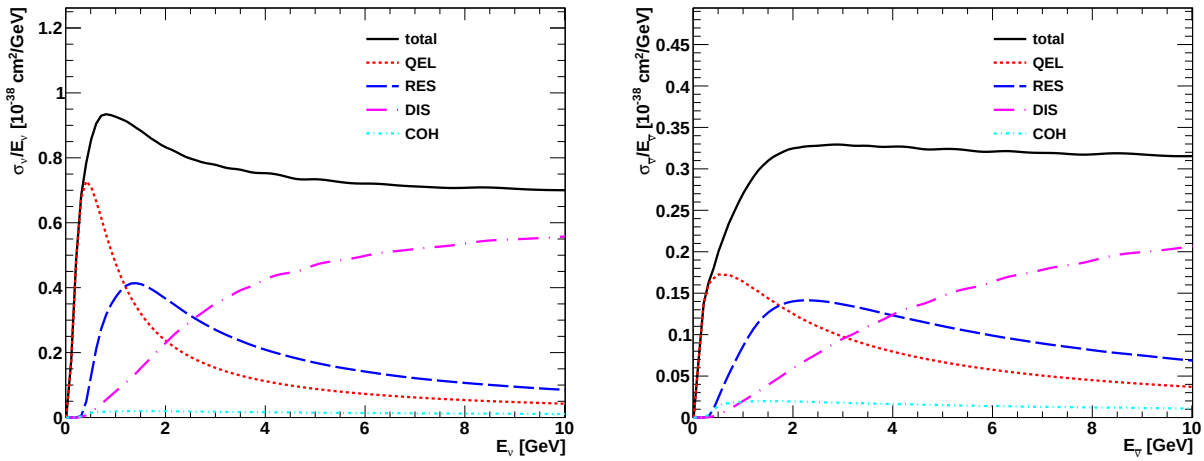

Figure 2.1: CC neutrino cross section per neutrino energy and per nucleon as a function of the neutrino energy [42]. The depicted cross sections are for interactions of ν_e (left) and $\bar{\nu}_e$ (right) with ^{12}C. The different curves indicate the different possible interaction types.

of the interaction are of RES type. Finally, for neutrino energies above 4 GeV, DIS interactions dominate. Due to the transition between QEL and DIS interactions, this energy range is called the transition region. The cross section for the COH process is much smaller than the total cross section over the whole energy range.

2.2 Water Cerenkov detectors

After covering the neutrino interactions in the last section, this section presents a detector concept where the secondary particles are detected by their Cerenkov emission in water.

A particle traveling through a dielectric medium at a speed higher than the speed of light in the medium emits Cerenkov light [43]. Hence, the minimum energy E_{thr} necessary to produce Cerenkov light is given by

$$E_{\text{thr}}(\lambda) = \frac{E_0}{\sqrt{1 - \frac{1}{n^2(\lambda)}}}, \tag{2.15}$$

where E_0 is the rest energy of the particle, λ is the wavelength of the emitted photon and $n(\lambda)$ is the medium's index of refraction at the required wavelength. In water at 20 °C, the index of refraction is $n(400\,\text{nm}) = 1.34356$ [44], hence the threshold energy for electrons is $E_{\text{thr}} = 765\,\text{keV}$.
Due to the coherent emission, an electromagnetic shock wave is created which resembles the Mach-cone of a supersonic jet. The cone opening angle θ depends on the velocity of the particle that transverses through the water [45]:

$$\cos(\theta) = \frac{1}{\beta n(\lambda)}. \tag{2.16}$$

The well determined shape of the Cerenkov cone can be used to reconstruct the direction of the particle. While it is principally possible to determine also the velocity and therefore

the energy of the particle from the shape of the Cerenkov cone, the particle's energy is typically determined from the number of emitted photons. The position of the vertex can finally be determined from the time when the photons are detected.
The photon emission spectrum $\frac{dN_\gamma}{d\lambda} \propto \frac{1}{\lambda^2}$, hence most photons will be emitted at short wavelengths. A particle traveling through water at the speed of light, produces about 215 photons per cm in the wavelength region between 400 and 700 nm [45]. Note that typically no Cerenkov photons are emitted at X-ray energies, as the index of refraction at these wavelengths is typically close to 1.
As water is cheap and features a high attenuation length of up to 100 m [46], it is perfectly suited as a detection medium for a large volume neutrino detector. Typically the produced photons are detected by an array of PMTs. The up to now largest example for such a detector is the Super-Kamiokande [46] experiment. It consists of a cylindrical stainless steel tank with a height of 42 m, a diameter of 39 m and has a fiducial volume of about 32 kt. The produced Cerenkov light was originally detected by 11446PMTs[7] with a diameter of 50 cm each. Thus, about 40% of the cylinder wall is photosensitive.

2.3 Liquid scintillator detectors

When a secondary, charged particle, created in a neutrino interaction, transverses a scintillator, a part of the deposited energy (typically a few percent) is converted into scintillation light. The emitted light can successively be detected by PMTs observing the scintillation volume. The observed signal allows to deduce the energy and the vertex of the secondary particle.
First, the basic principles of liquid scintillators are introduced in section 2.3.1. The following section 2.3.2 presents the currently running LSc based neutrino experiment Borexino. Finally section 2.3.3 presents a proposed next-generation LSc detector: JUNO. The LENA detector, which is the detector this thesis focuses on, is presented in more detail in chapter 3.

2.3.1 Basic scintillation processes

Organic LScs typically are aromatic systems. Hence, their lowest excited states are defined by the delocalized π-electrons. The ground state is commonly denoted with S_0. There are two types of excited states: Singlet states S_i and triplet states T_i. Apart from the electronic excitation, there are also vibrational and rotational excitations of the molecule, which lead to a sub structure of the electronic levels. An overview of a typical level scheme is given in figure 2.2.
A charged particle traveling through a scintillator interacts electromagnetically with the molecules close to the track. A part of its energy loss goes into excitation of electronic states in the scintillator molecules (straight black arrows in figure 2.2) and ionization (straight green arrows in figure 2.2) of the scintillator molecules. Direct excitation via electronic interactions typically populates higher singlet states S_i, with $i \geq 2$ [48]. These

[7] On November 12$^{\text{th}}$, 2001 a PMT implosion and the successive shock wave destroyed about 60% of the PMTs. Hence, the experiment was forced to run with a reduced PMT number until the losses were replaced [46].

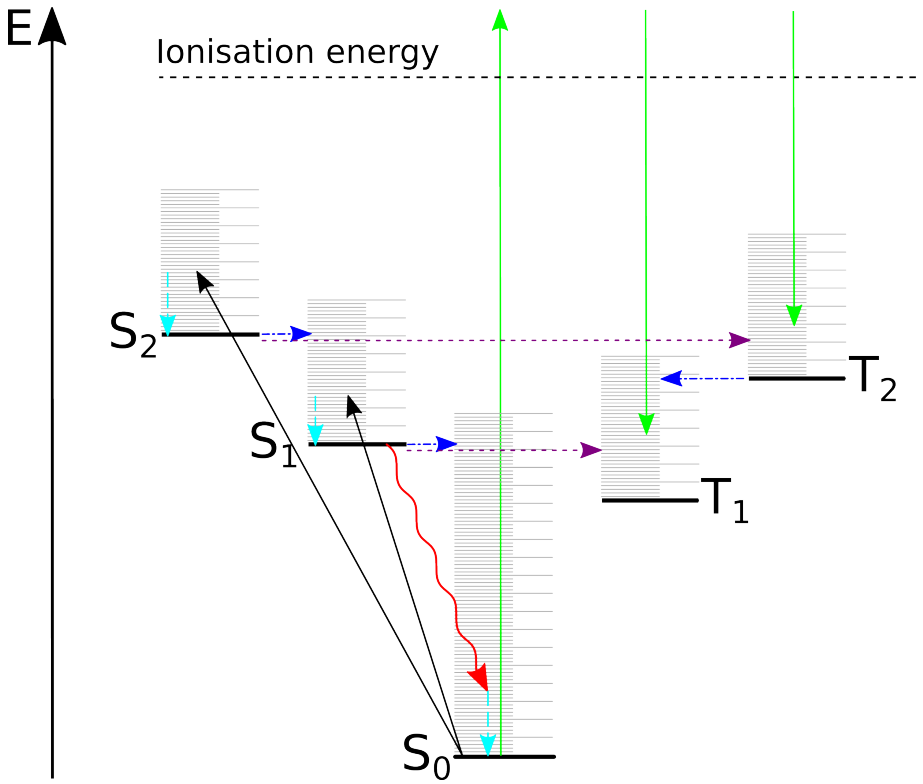

Figure 2.2: Jablonski diagram schematically showing the possible excited states in an organic LSc (not to scale). Sketch adapted from [47]. Singlet and triplet states are marked by horizontal black lines and are labeled with S_i and T_i respectively. The long and short horizontal gray lines indicate the corresponding vibrational and rotational[8] sub-states. The different arrows indicate the possible processes which can occur: The straight black arrows indicate direct excitations and the green straight arrows ionization and recombination. Furthermore the light-blue colored short-dashed arrows indicate radiationless vibrational cascades, the dark blue long-short dashed arrows internal conversion the violet long dashed arrows intersystem crossings. Finally, the red curly arrow indicates the transition where radiation is emitted.

excited singlet stated decay radiationlessly through internal conversion into the lowest excited singlet state S_1 (light blue short-dashed and dark blue long-short dashed arrows in figure 2.2). This processes take place on a time scale of order ps to ns. The observed scintillation light is predominantly emitted in the $S_1 \rightarrow S_0$ decay (red curly arrow in figure 2.2). Note that this decay is typically not directly into the ground state, but into one of the vibrational levels associated to the ground state. Hence it is not mono-energetic. The decay of the vibrational sub-state of S_0 into the ground state again proceeds radiationlessly. The time behavior of the process is governed by the time constant of the radiative transition, which is typically in the range of some ns for organic LScs. Hence, the decay of the excited singlet states gives rise to a prompt emission of photons which is commonly called fluorescence. [47].
The triplet states T_i on the other hand are mainly populated via ion recombination (straight green arrows in figure 2.2), which leads to triplet states in 75% of all recombina-

[8]Note that, despite the fact that they are shown equidistant in the schematic, the rotational sub-states are not equidistant but feature $E \propto l(l+1)$, where l is the quantum number of the angular momentum.

tions. Additionally a direct population is possible by inelastic collisions of the molecules with very slow electrons [49]. As in the case of the singlet decay, the excited states typically rapidly decay into the lowest exited triplet state T_1. The transition of this state into the ground state is forbidden. Hence, the associated time constant is very large, typically $> 10^{-5}$ s [47]. As there are faster processes which deplete this state, the direct transitions to the ground state rarely happen. In areas with small excitation density, the most probable process is the inter-system crossing $T_1 \rightarrow S_0$ into high vibrational states of the ground state. In regions with higher ionization density, also interactions between two triplet states have to be taken into account. One possibility is the reaction

$$2T_1 \rightarrow S_1 + S_0. \tag{2.17}$$

The produced S_1 state successively decays into S_0 emitting radiation. This leads to a second, slower component of the scintillation light which is commonly called phosphorescence [49]. The time constant of the slow component is typically governed by the time structure of the reaction (2.17). Note that this reaction does not necessarily follow an exponential decay.

In a LSc, the excitation energy can be transferred between two adjacent molecules. This energy transfer can proceed either via formation of intermediate excimers or via direct transfer. The timescale at which one of this processes takes place, is typically a few orders of magnitude smaller than the decay time constant of the S_1 state, i.e. these energy transfer processes do not influence the emission time behavior of the LSc. This also means that the excitation energy can be transferred between multiple scintillator molecules before it decays away [47].

Often, the organic molecules forming the bulk of the scintillator, the so called solvent, are only bad scintillators by themselves. The encountered problems include [48]:

- A long time constant of the radiative decay of the S_1 state of order $\sim$30 ns. This also implies that the branching ratio for concurrence processes is relatively large, resulting in a low probability for photon emission.
- Their emission wavelength distribution is often mainly in the UV regime, where common PMTs feature only a reduced sensitivity due to the reduced transparency of standard PMT glass in the wavelength region below $\sim$350 nm [35].
- Due to the high concentration of the solvent, the probability of re-absorption of the emitted photon is relatively large, rendering the scintillator basically opaque to its emitted photons.

To counter these problems, an additional solute is added to the scintillator at concentrations of a few g/l. This solute is commonly called the primary fluor. Its properties are chosen to counteract the disadvantages of the solvent, i.e., it features a short decay time and emits in a longer wavelength region compared to the solvent. Due to its low concentration the self absorption is greatly reduced.
The energy transfer between the solvent and the solute molecules takes place non radiatively at a time scale of order 10 ps. It occurs via resonant dipole-dipole interactions between the solute and the solvent molecules, so called Förster interactions. Their strength

and their range is related to the overlap between the emission spectrum of the solvent and the absorption spectrum of the solute. The characteristic range of these interactions is called the Förster radius which is of order 20-60 Å, indicating that the range of these interactions is several molecules [47]. As already expected from the higher emission wavelength, the S_1 state of the solute has a lower energy than the corresponding state in the solvent. Hence, a transfer of the energy back to the solvent is highly improbable and the energy is effectively trapped at the solute molecules. This also implies that, given the solute concentration is sufficient that no "energy hopping" between solvent molecules is required, the observed time constant of the fluorescence is not the decay constant of the solvent but of the solute S_1 state.
To improve the transparency of the scintillator to its scintillation light, often a secondary fluor is added to the scintillator mixture at concentrations about 100 times lower than the concentration of the first solute. The energy of the relevant S_1 state is even smaller than in the corresponding primary fluor resulting in an even longer emission wavelength. The energy transfer between the primary and the secondary solute occurs primarily non-radiatively [47], though some radiative transfer might be present at very low concentrations [50].

The number of photons emitted by a LSc is generally not directly proportional to the overall deposited energy but depends on the stopping power dE/dx of the primary particle. This phenomenon is typically called quenching. Birk's formula [50]

$$\frac{dN}{dx} = \frac{S\frac{dE}{dx}}{1 + k_b\frac{dE}{dx}} \tag{2.18}$$

provides an empirical description of this effect, where dN/dx is the number of produced photons per unit path-length, S is the light yield and k_b is Birk's constant. The latter has to be determined empirically for each scintillator mixture and each primary particle. Note that for minimum ionizing particles often $k_b dE/dx \ll 1$. Hence, the number of produced photons still scales linearly with the energy for these event types.

2.3.2 Borexino

One example for a LSc experiment is the Borexino experiment. It is located in the Laboratori Nazionali del Gran Sasso (LNGS) underground laboratory [3]. The basic setup is schematically depicted in figure 2.3. The neutrino target, which is located in the center of the detector, consists of ∼300 t of LSc. It is enclosed by a nylon vessel of 4.25 m radius. Two layers of buffer liquid with outer radii of 5.50 m and 6.85 m are surrounding the target. While the target and the inner buffer are surrounded by thin, transparent nylon barriers, the outer buffer is contained by a stainless steel sphere (SSS). The latter also serves as a mounting structure for the 2212 8'-PMTs observing the neutrino target. 1800 of the Borexino PMTs[9] are equipped with optical light concentrators (LCs). This increases the effective photon collection area of the individual PMTs. The downside of the LCs is that photons with an incident angle of above 32.5 deg are no longer accepted [3]. Due to the geometry of Borexino, all photons from the central scintillator volume are

[9] The remaining PMTs do not feature light concentrators. They are required for the reconstruction of high energy events which do not cross the fiducial volume. Thus, they do need a larger field of view.

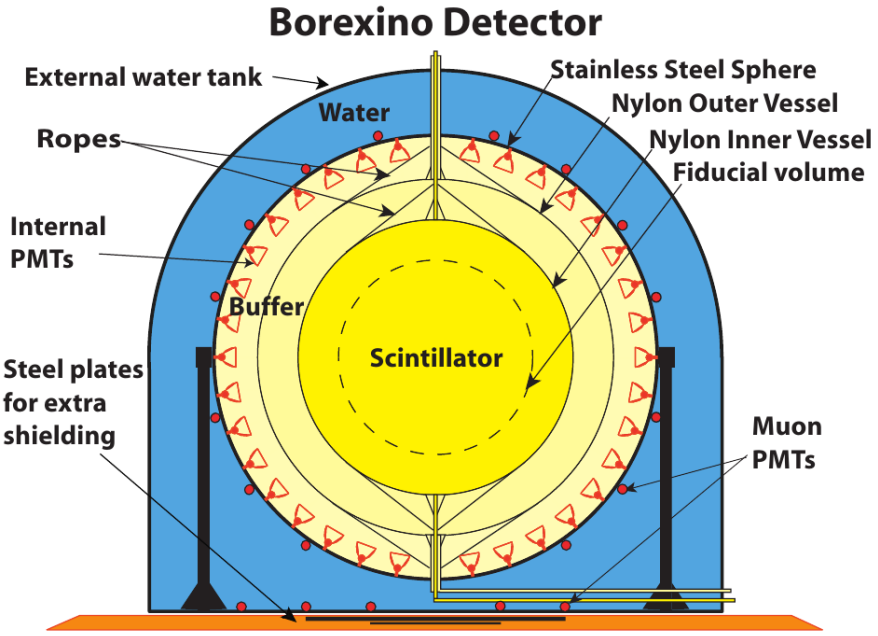

Figure 2.3: Schematic drawing of the Borexino detector [3]. The active scintillator is contained in the innermost nylon vessel. The volumes between the two nylon vessels and between the outer nylon vessel and the stainless steel sphere act as buffer volumes. The PMTs observing the active volume are mounted on the stainless steel sphere. The whole detector is surrounded by an instrumented external water tank.

accepted by the LCs.
Everything insides the SSS is called the inner detector. It is surrounded by the outer detector, a water tank filled with 2 100 t of ultra-pure water which is instrumented by 208 8'-PMTs. The outer detector serves a dual purpose: First, the water acts as a shield for fast neutrons produced by cosmic muons in the surrounding rock. Due to the instrumentation, it can additionally be use as an active, Cerenkov-based veto for cosmic muons crossing the detector.

Borexino's main physics goal is the detection of solar neutrinos. As the expected rates are in the order of a few counts per day and 100 kt, the control of backgrounds is crucial. This is achieved using the 3800 meters of water equivalent [51] shielding provided by the LNGS laboratory. Additionally, the scintillator was cleaned to a very high radiopurity: In Borexino, a level of $(1.6 \pm 0.1) \cdot 10^{-17}$ g/g uranium[10] and $(6.8 \pm 1.5) \cdot 10^{-18}$ g/g thorium was achieved [52].
Up to now, Borexino was able to precisely determine the flux of the ^{7}Be-neutrinos [53], to measure the ^{8}B rate down to 3 MeV [54], to give a measurement of the pep-neutrino flux, to provide the currently strongest constraint on the CNO-flux [23] and to directly measure the pp-neutrino flux [55].

[10]The unit "g/g" denotes g of a radioactive nucleus per g of LSc.

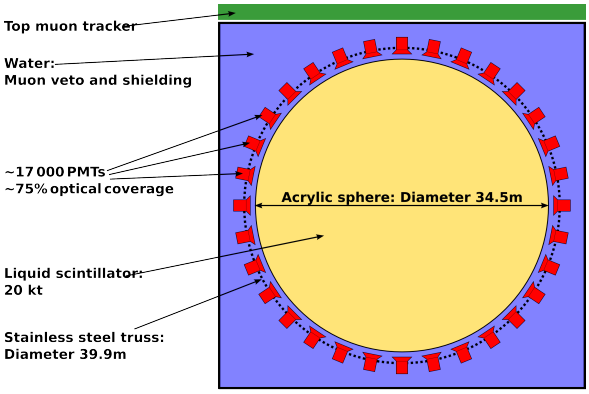

Figure 2.4: Schematic set-up of the JUNO detector (currently favored option). The center of the detector consists of a 34.5 m diameter acrylic sphere filled with 20 kt of LSc. It is immersed in a water tank serving as a protection against radioactivity and as an active muon veto. The light is detected by ∼17 000 PMTs with a total optical coverage of ∼75 %. They are mounted in a stainless steel scaffolding which also provides the required stability for the acrylic sphere. To increase the muon reconstruction capabilities, an additional muon veto with tracking capability will be mounted on the top of the detector.

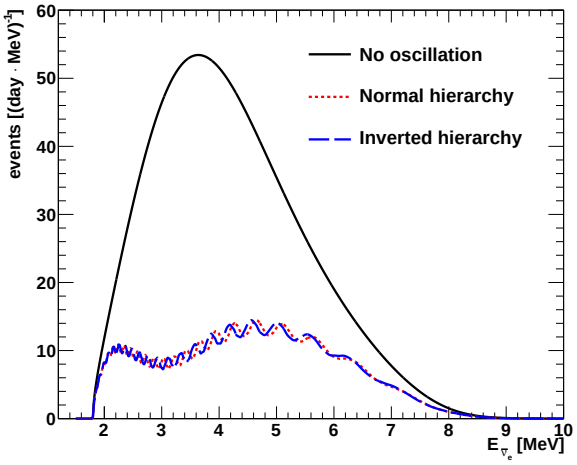

Figure 2.5: The expected $\bar{\nu}_e$ event spectrum in JUNO for both normal and inverted hierarchy [56]. Additionally, the expected event spectrum without oscillations is shown.

2.3.3 JUNO

One proposal to determine the neutrino mass hierarchy mentioned in section 1.3 is a precision measurement of the reactor anti-neutrino survival probability at a distance of ≈53 km from the reactor core [26]. **J**iangmen **U**nderground **N**eutrino **O**bservatory (JUNO) [6] is a planned LSc detector located in southern China designed for this purpose. The currently preferred set-up is sketched in figure 2.4. As a $\bar{\nu}_e$ target, 20 kt of LSc are contained in a ∼34.5 m diameter acrylic sphere. To protect the target from external radiation, the target is immersed in a cylindrical water tank which also serves as a muon veto. The ∼17 000 PMTs observing the fiducial volume are also immersed in the water. They are mounted in a stainless steel strut, which also serves as a mechanical support for the acrylic sphere. Figure 2.5 shows the expected $\bar{\nu}_e$ spectrum for both hierarchies. For a discrimination between the hierarchies, the small differences in the oscillations driven by Δm^2_{13} and Δm^2_{23} have to be resolved, requiring an unprecedented energy resolution of 3 % at 1 MeV deposited energy [26] corresponding to a photo-electron yield of at least 12 000 p.e./MeV. Thus, a very high number of PMTs will be used to obtain the maximum possible optical coverage of ∼75 %. Additionally, an exceptionally clean LSc with an attenuation length (see chapter 7) of $\Lambda_{\text{att}} \gtrsim 24$ m is required. In chapters 7 and 8, methods to precisely measure the required attenuation lengths are presented.

Chapter 3

LENA

Low **E**nergy **N**eutrino **A**stronomy (LENA) [7] is a proposed 50 kt liquid scintillator neutrino observatory. With its huge target mass, it will be the next generation sucessor to currently running detectors like Borexino (see section 2.3.2).
The huge size of LENA causes a different geometrical set-up (see section 3.1.1) compared to the current generation of LSc detectors. The differences in geometrical shape are driven by the optical limitations of the used scintillator (see section 3.1.2), by the challenge to instrument the surface of the detector (see section 3.1.3) at a reasonable cost and by the restrictions imposed by the feasibility of the caverne construction.

LENA's huge size combined with its 200 keV threshold and its background discrimination capabilities leads to a very wide physics program: The increased statistics compared to todays LSc detectors allows for precision measurements of already detected neutrino fluxes, like geoneutrinos (section 3.2.1) or solar neutrinos (section 3.2.2). Also a galactic supernova could be observed at high statistics (section 3.2.3). Apart from the precise measurement of known sources, the huge target mass allows to search for faint neutrino fluxes, like the diffuse supernova neutrino background (DSNB) (section 3.2.4), which has not been detected yet. This includes also other rare processes like the proton decay (section 3.2.5).
Due to the vast extensions of the detector, even high energy events at the GeV scale have a good chance to be fully contained in LENA. This offers the opportunity to use LENA for high energy neutrino physics, i.e. to scrutinize atmospheric neutrinos (section 3.2.6) or act as as a far detector for a long baseline neutrino beam (section 3.2.7).

The feasibility of building such a detector underground as well as the physics potential of such a detector was studied in the framework of the European founded LAGUNA-LABNO design study. This study lasted till 31st August 2014 and showed that the construction of LENA is technically feasible.

3.1 Detector set-up

3.1.1 Overall set-up

The overall set-up of the LENA detector is sketched in figure 3.1. In contrast to Borexino, LENA will feature a cylindrical shape [57]. The tank containing the LSc will be 100 m

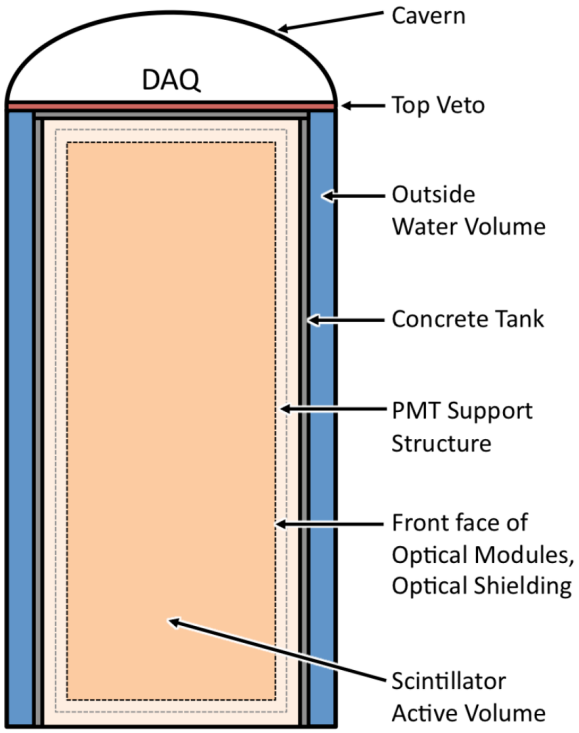

Figure 3.1: Schematic set-up of the LENA detector [57]. The center of the detector is made up by 50 kt of LAB based LSc. It is instrumented with ∼30 000 12'-PMTs equipped with light concentrators (LCs). Together with a pressure encapsulation, they make up the optical modules which also contain a small buffer volume in front of the PMT inside the LC. Their apertures are arranged around the active volume. The active volume is optically separated from the area between the active volume and the concrete tank containing the LSc. It is surrounded by an instrumented water tank serving as a passive shielding against fast neutrons and as active veto for inclined muons. An additional muon veto, consisting e.g. of plastic scintillator strips, will be placed on top of the detector.

high and will have a radius of 16 m. At a distance of about 1 m to the wall of the tank, a scaffolding containing the optical modules will be constructed. An optical module (OM) consists of a PMT with an attached optical LC. To stand the hydrostatic pressure at the bottom of the tank the OM will be encapsulated in a pressure tight housing. The interior of the housing will be filled with a non scintillating buffer liquid, shielding the active region from the radioactivity of the PMT glass.
The apertures of the OMs will be at a distance of 2 m from the wall. Hence they define an active volume with a radius of 14 m and a height of 96 m, that will contain about 50 kt of LSc. Due to the radioactivity of the tank and of the PMTs, the expected rate in the region between the OM apertures and the tank wall is much higher than in the target volume. To ensure that these background events do not interfere with the events inside the active volume, the active volume will be optically decoupled using opaque foils mounted between the apertures of the OMs.
The area between the outside of the tank and the cavern wall will be filled with water and will also be instrumented. It has a dual purpose: First it serves as a passive shielding against radioactivity from the surrounding rock and more importantly against fast neutrons created by cosmogenic muons in the rock. Additionally, it is used as a Cerenkov based muon veto for inclined muons. To tag muons coming straight from above, an additional muon veto will be placed on top of the tank. For the top veto, multiple options are currently discussed, ranging from plastic scintillator panels to resistive plate chambers. The veto will have to provide some tracking capability in any case, to determine the direction of the detected muons.
The preferred location for the LENA detector is the Pyhäsalmi mine in Finland. It provides a suitable position for the construction of LENA at a depth of 1400 m, which corresponds to a shielding of about 4000 meters of water equivalent.

3.1.2 Scintillator

The solvent for the LENA scintillator will be Linear Alkylbenzene (LAB) [58]. The primary wavelength shifter 2,5-Diphenyloxazole (PPO) [59] will be added, at a concentration of currently 3 g/l. Its concentration is the minimum concentration at which all energy is transfered from the solvent to the solute (see section 2.3.1). It therefore provides the optimum trade-off between a high light yield and a low light attenuation at the same time. To further improve the attenuation length, a secondary wavelength shifter will be added at a concentration of 20 mg/l. The chosen substance is 1,4-Bis(2-methylstyryl)benzen (Bis-MSB) [60].

The properties of the LENA scintillator have been investigated in dedicated experiments:

- As explained in section 2.3.1, the time behavior of the fast component of the LSc is dominated by the properties of the wavelength shifter. The slow component however has a more complicated time structure as two triplet states have to interact with each other for a deexcitation. Nevertheless, the overall pulse shape of a LSc can be approximated by a superposition of N exponential decays:

$$P_{\mathrm{LSc}}(t) = \sum_{i=1}^{N} \frac{n_i}{\tau_i} \exp\left(-\frac{t}{\tau_i}\right), \tag{3.1}$$

Component	τ_i [ns]	n_i [%]
1	$6.9 \pm 0.1(\text{stat}) \pm 0.2(\text{syst})$	$59.1 \pm 0.6(\text{stat})^{+4.3}_{-2.7}(\text{syst})$
2	$26.4 \pm 0.8(\text{stat})^{+2.0}_{-2.2}(\text{syst})$	$22.2 \pm 0.4(\text{stat})^{+7.0}_{-1.9}(\text{syst})$
3	$141.0 \pm 4.3(\text{stat})^{+3.6}_{-14.6}(\text{syst})$	$18.3 \pm 0.7(\text{stat})^{+2.1}_{-2.5}(\text{syst})$

Table 3.1: The decay time components of the LENA scintillator [61] for electron excitation according to equation (3.1).

where n_i and τ_i are the strength and the decay times of the respective components. The values measured in [61] for the LENA scintillator excited by electrons/gammas are shown in table 3.1. Note that these values are generally dependent on the type of the exciting particle.

- The absolute light yield, i.e., the number of produced photons per deposited energy is typically assumed to be $\sim$10 000 MeV^{-1}. While this value has not been directly measured for the LENA scintillator, a value of $(9.6 \pm 1.0) \cdot 10^3\,\text{MeV}^{-1}$ [62] has been determined for the scintillator of the Double Chooz muon veto which is basically a diluted LENA scintillator. Additionally, for a mixture of LAB with 2 g/l PPO and 20 mg/l Bis-MSB, the light yield was determined to be $(99.7 \pm 0.2(\text{stat}) \pm 3.0(\text{syst}))\%$ [63] of the light yield of the Borexino scintillator which is $(11.5 \pm 1.1) \cdot 10^3\,\text{MeV}^{-1}$ [64]. As an increase in PPO concentration increases the light yield, this indicates that $10^4\,\text{MeV}^{-1}$ might actually a bit conservative.

- The measured emission spectrum of the LENA scintillator is shown in figure 3.2. Note that the shown emission spectrum is taken after the scintillation light transversed about 0.5 cm of liquid scintillator. As the attenuation length around 400 nm is of the order of a few cm [65], the emission spectrum is underestimated for wavelengths $\lesssim 400$ nm.

- The scattering length, i.e the mean free path between two scatterings, has been measured to be (25.0 ± 2.5) m [66]. The scattering in LAB occurs via two different processes: Anisotropic Rayleigh scattering with a scattering length of (40 ± 5) m and absorption-reemission processes causing isotropic scattering with an associated scattering length of (67 ± 6) m. Note that the absorption-reemission process also has an associated time constant.

- The attenuation length of LAB has been reported to be between 10 and 20 m [57]. A more exact measurement of this quantity is presented in chapters 7 and 8.

Currently, efforts are ongoing to improve the (optical) properties of the scintillator by cleaning the scintillator using filters which contain Al_2O_3.

3.1.3 Instrumentation

To detect the photons emitted by the LSc, a proper instrumentation of the tank is required. As already mentioned in section 3.1.1, the current idea is to use OMs containing a PMT and a LC.

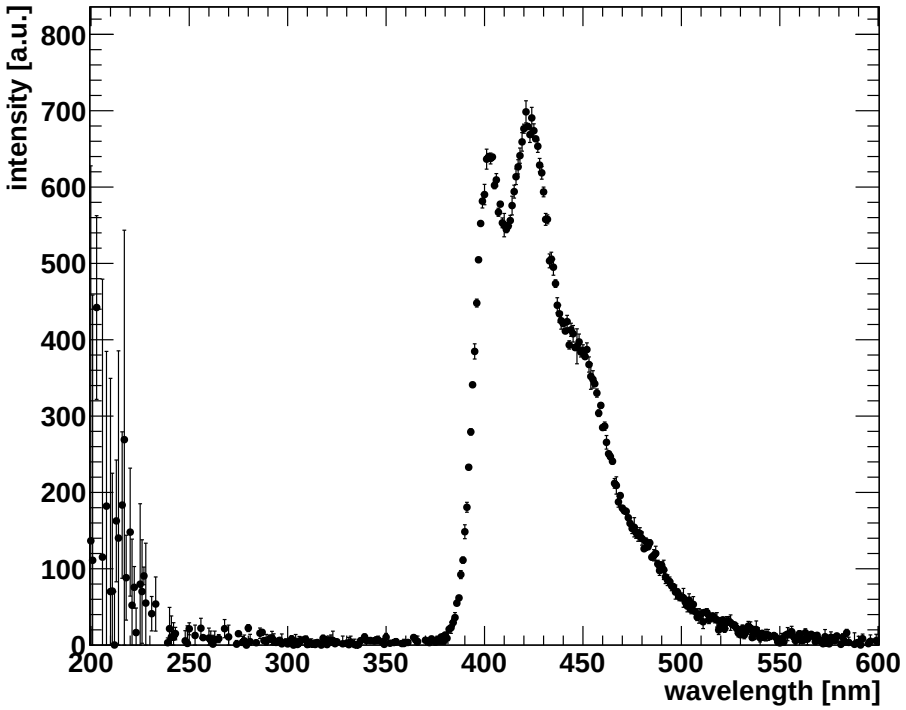

Figure 3.2: The emission spectrum of the LENA scintillator. The scintillator was excited by monochromatic light with a wavelength of 190 nm. Note that the scintillation light has to travel through about 0.5 cm of liquid scintillator to be detected. Data taken from [65].

The number and the size of the required OMs is determined by the required energy resolution and the targeted threshold of the detector[1], which translates in an average number of photons to be detected (p.e.) per MeV electron equivalent energy deposited in the detector. Currently, the baseline design is to have at least 200 p.e./MeV. Taking the optical properties of the LSc into account, this means that 6% of all photons hitting the detector wall have to be detected [7]. As PMTs have a typical quantum-efficiency of 20%, this implies an effective optical coverage of 30%. Using OMs with 12" PMTs, the total number of required OMs is about 30 000 [7]. Note that the area covered by the OM aperture is bigger than 30% of the detector wall, as the field of view of a LC does not cover the whole detector. For an in depth study of different optical modules and LCs, see [68].
For the read out of the detectors, there are currently two options [7]:
As the recorded information is contained in the output signals of the PMTs, the optimum solution would be to have a readout system based on fast ADCs[2] (FADCs) with a sampling frequency of at least 1 Gs/s and a resolution of at least 8 bits. This allows to conserve nearly all the information contained in the output signals. While this system would allow to extract the maximum amount of information from each event and therefore provides the optimum physics performance, it is also very expensive and requires huge amounts of

[1] Using the planned instrumentation, the detector threshold will be determined by the ^{14}C background (endpoint around 156 MeV [67]). The achievable energy threshold nevertheless is determined by the average number of photoelectrons detected as the resolution around the ^{14}C endpoint determines the smearing of the ^{14}C β-spectrum and thus the achievable threshold.

[2] **A**nalog to **D**igital **C**onverter

data to be handled.
An alternative, cheaper solution with worse performance is based on the PMm^2 approach [69], where a matrix of currently 16 PMTs is handled by one read out unit which provides the time of the first photon detected and the integrated charge for each PMT in the detector.

3.2 Physics program

3.2.1 Geo-neutrinos

The earth generates about 40 TW of heat [35]. A part of this heat generation is attributed to the natural radioactivity in the earth, i.e., to the decay of radioisotopes from the ^{238}U and ^{232}Th decay chains as well as from the decays of ^{40}K [7]. In the β^--decays of the decay chains and in the decay of ^{40}K, antineutrinos are generated which can be detected. These antineutrinos are pretty low in energy; the highest end point is at about 3.3 MeV [35].
The detection reaction for these antineutrinos is the IBD (see equation (2.3)). Due to its threshold of 1.8 MeV, the antineutrinos from the ^{40}K-decay cannot be detected.
Up to now, geo-neutrinos have been observed by two experiments: KamLAND [70] and Borexino [71]. Both experiments suffer from low statistics, having detected 116^{+28}_{-27} and 25^{+19}_{-18} geo-neutrino candidates, respectively. LENA on the other hand, with its fiducial volume of 50 kt would detect about 10^3 geo-neutrino events per year.
Antineutrinos produced by nuclear reactors cause an indistinguishable background for geo-neutrino detection. As Pyhäsalmi is far away from the central European reactors, this background is relatively small with about 240 events per year in the relevant energy region [72]. Currently multiple reactors are in construction or are approved in Finland. If all of these reactors are built, the number of expected background events will nearly double, which is still nearly a factor four below the background rate in a central European underground laboratory like Frejus [7]. Furthermore, the reactor antineutrino spectrum extends up to 10 MeV, hence the reactor neutrino rate can be determined in situ with a high precision. As the reactor neutrino spectrum is well known [73], it can be statistically subtracted.
Additionally, there is a background due to cosmogenically produced β-n-emitters which can mimic the delayed coincidence. By vetoing a cylinder around each muon track for two seconds, it can be reduced to a negligible rate of about one event per year while introducing only 0.1% of dead time [7]. Finally, fast neutrons produced by cosmic muons in the rock surrounding LENA can mimic an IBD signal. As most of the the induced events are at higher energies, the produced rate in the geo-neutrino energy region is only about 10 events per year [7].
Finally, another background is due to the ^{210}Po contamination of the LSc. The α-particles produced in ^{210}Po decays can produce neutrons inside the scintillator via ^{13}C(α,n)^{16}O reactions. Assuming Borexino radiopurity conditions, this background will contribute about 10 events per year [7]. Hence, LENA will provide a high precision geo-neutrino measurement with high statistics and low backgrounds. The overall geo-neutrino rate can be determined at an accuracy of 4% after one year of measurement time. After a measurement time of 10 years, the error on the overall rate will be down to 1%. Additionally, the ratio of geo-neutrinos coming from the ^{238}U and ^{232}Th decay chains can be determined

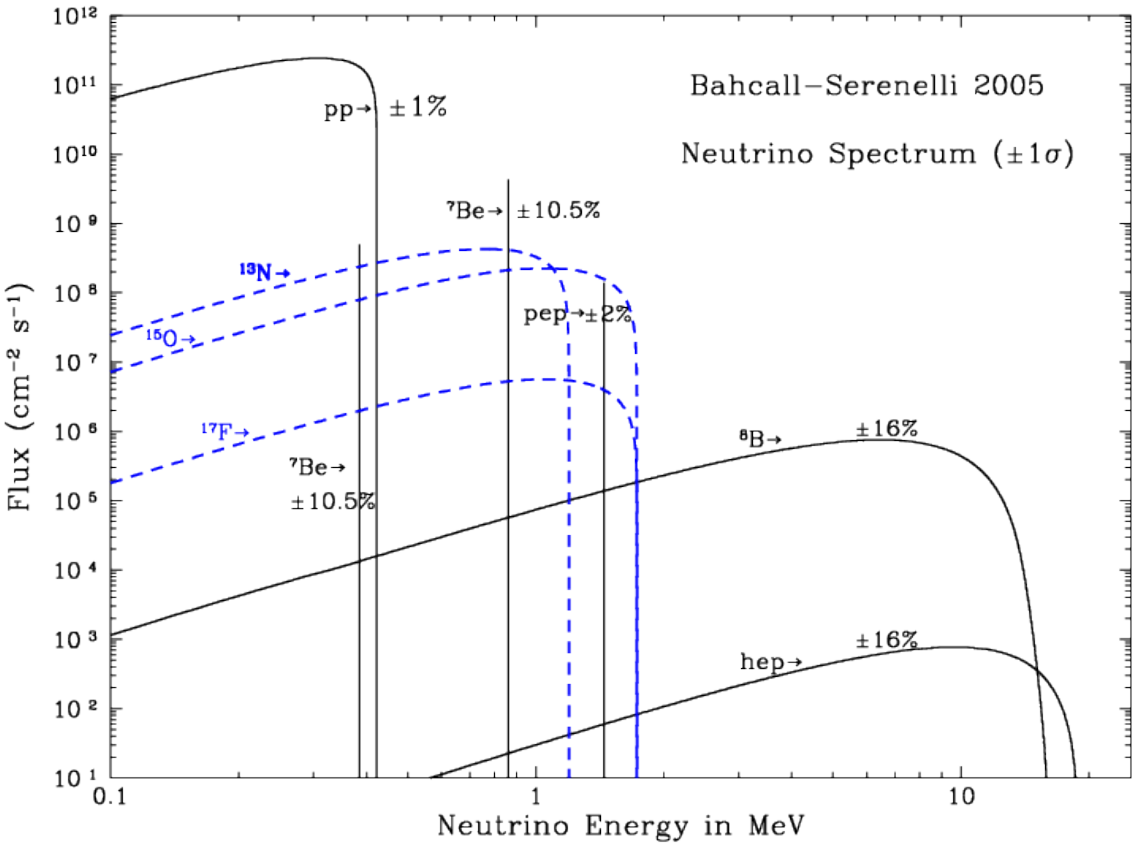

Figure 3.3: The solar neutrino spectrum as calculated from the standard solar model [75]. Neutrino fluxes from pp-Chain reactions are plotted as black solid lines while the fluxes expected from the CNO cycle are shown as dashed blue lines.

at 5 % to 6 % accuracy after 10 years, dependent on the exact position and power of the upcoming Finnish nuclear power plants [7]. Both values will provide an important input for geochemical models of the earth. However, due to the missing directionality of LAB-based LSc detectors [72] an additional detector would be necessary to disentangle the contributions of the earth's crust and mantle to the geo-neutrino flux.

3.2.2 Solar neutrinos

In the sun, energy is produced by fusing hydrogen to helium. The overall reaction reads [74]

$$4p \longrightarrow {}^4\mathrm{He} + 2e^+ + 2\nu_e + 26.73\,\mathrm{MeV}. \tag{3.2}$$

The fusion process takes place in several steps, either via the so called pp-chain or via the CNO-cycle [74]. Most energy is produced via the pp-chain, while the CNO-cycle, contributes only to a small fraction (about 2%), which is however not precisely known up to now. The resulting neutrino spectrum can be calculated in the well established framework of the standard solar model [75] and is shown in figure 3.3. In LENA, the

Nuclear reaction	Expected event rate [d^{-1}]
pp	$2.3 \cdot 10^3$
^{7}Be	$1.1 \cdot 10^4$
pep	$8.5 \cdot 10^2$
CNO	$8.8 \cdot 10^2$
^{8}B	$1.3 \cdot 10^2$
hep	0.4

Table 3.2: The expected neutrino interaction rates in LENA for 36 kt fiducial volume and 200 keV energy threshold [41].

detection reaction with the highest rate for solar neutrinos is the elastic neutrino electron scattering (compare equation (2.1)). The expected rates are shown in table 3.2.
While a few thousand pp-neutrinos will be detected per day, it will be very difficult to extract the pp-neutrino signal from the ^{14}C background. ^{14}C decays via β^--decay with a half-life of about 5 700 a and a Q-value of 156 keV [67]. The expected induced background rate above 200 keV is $\sim$1 kHz [41] and therefore many orders of magnitude above the pp-signal. Due to the limited energy resolution in this energy range, the ^{14}C events are smeared out over the whole visible pp-neutrino range making a detection of pp-neutrinos very challenging.
Similar to Borexino, the ^{7}Be-neutrinos are clearly detectable in LENA. As LENA features very high statistics in this channel (confer table 3.2), this channel is well suited to study modulations in the solar neutrino flux. For periodic modulations with periods from 10 min to 10 a, a sub-percent accuracy will be achieved after 10 a of measurement time [76]. This capability allows searching for day-night variations in the neutrino flux or for correlations of the flux to the solar cycle. Additionally, a modulation could be present due to helioseismic waves in the sun. LENA should be able to detect these so-called g-mode oscillations which are not accessible by other means as they do not propagate to the surface of the sun.
Even though CNO-neutrinos feature a high enough rate to be detected in LENA, their detection is challenging as the signal has to be extracted from the cosmogenic ^{11}C and the intrinsic ^{210}Bi backgrounds. Compared to Borexino, which could only place an upper limit on the CNO flux [23], LENA has a few advantages [41]: Due to the larger shielding of the laboratory in Pyhäsalmi compared to the LNGS, the ^{11}C rate is smaller in LENA. Furthermore, due to LENA's large size, a precise determination of the ^{210}Bi rate will be possible by counting the decays of the daughter nucleus ^{210}Po. This allows for a statistical subtraction of the ^{210}Bi spectrum. Note that this only works if ^{210}Bi and ^{210}Po are in radioactive equilibrium. Finally, the good statistics ease the separation between the CNO and the background components via a spectral fit. Despite these advantages, a detection of the CNO-flux remains challenging.
In the sun, the matter effects on neutrino oscillations lead to a resonant flavor conversion, the so called MSW effect [77]. This effect induces a transition between vacuum and matter dominated oscillations in the energy range between $\sim$2 MeV and $\sim$5 MeV. This transition region is very sensitive to new physics, therefore a precise measurement of the electron neutrino survival probability $P_{\nu_e \to \nu_e}(E_\nu)$ in this energy region is necessary. As ^{8}B-neutrinos feature a continuous energy spectrum ranging up to 15 MeV [35] they are

a good probe for $P_{\nu_e \to \nu_e}(E_\nu)$. Due to it's large size, LENA allows for a very stringent fiducial volume cut, efficiently removing nearly all external radioactivity which limits the ^{8}B detection threshold in Borexino to 3 MeV [54]. Hence an energy threshold of 2 MeV visible energy can be achieved [41]. In [41] it was shown, that this allows to refute a model with constant $P_{\nu_e \to \nu_e}$ at the 5-σ level after 4 a of measurement time.

3.2.3 Supernova neutrinos

The life of a single star with an initial mass of more than 8 solar masses ends in a gravitational core collapse supernova (SN) [78]. 99% of the released gravitational energy of $\sim 10^{53}$ erg $= 10^{49}$ J is radiated away in neutrinos of all flavors with a mean energy in the order of 10 MeV. The neutrino signal typically lasts up to $\sim$10 s post bounce [79]. Even though SNe emit a huge number of neutrinos, only SNe in our galaxy can be observed with detectors of the size of LENA. As the expected SN rate in our galaxy is about 1-2 SNe per century [78], a SN during the lifetime of LENA (about 30 a) is not guaranteed.
Up to now, SN1987A was the only SN which lead to an observed neutrino signal. In total 24 events[3] were observed in various detectors [80]. In contrast to the very limited statistics acquired during SN1987A, a core collapse supernova in the milky way during the life-time of LENA would allow for a high statistics measurement of SN-neutrinos with a total of about 16 000 events [81] for a SN at a distance of 10 kp, according to the GVKM[4] model [82].
Nearly 10 000 of these events are expected in the IBD channel (see equation (2.3)). As the IBD channel allows for event by event neutrino energy reconstruction and can be discriminated from other channels due to the delayed coincidence, this channel alone will provide a high statistics time and energy resolved picture of the evolution of the $\bar{\nu}_e$ luminosity.
Additionally, there are two CC channels on ^{12}C [81]:

$$\bar{\nu}_e + {}^{12}\mathrm{C} \;\rightarrow\; e^+ + {}^{12}\mathrm{B}; \quad {}^{12}\mathrm{B} \rightarrow {}^{12}\mathrm{C} + e^- + \bar{\nu}_e \quad (E_{\mathrm{thr}} = 14.4\,\mathrm{MeV}) \tag{3.3}$$

$$\nu_e + {}^{12}\mathrm{C} \;\rightarrow\; e^- + {}^{12}\mathrm{N}; \quad {}^{12}\mathrm{B} \rightarrow {}^{12}\mathrm{C} + e^+ + \nu_e \quad (E_{\mathrm{thr}} = 17.3\,\mathrm{MeV}). \tag{3.4}$$

The re-decay of the produced nuclei can be used to tag the CC reactions. However, the re-decays of both channels feature a too similar signature to discriminate these channels on an event by event base. Nevertheless, it is possible to statistically separate the channels by fitting the energy and time spectrum of the re-decays. This yields the total ν_e flux above the threshold.
Apart from that, there is also a NC channel which leads to an excited state in ^{12}C [7]:

$${}^{12}\mathrm{C} + \nu_x \rightarrow {}^{12}\mathrm{C}^* + \nu_x; \quad {}^{12}\mathrm{C}^* \rightarrow {}^{12}\mathrm{C} + \gamma(15.1\,\mathrm{MeV}). \tag{3.5}$$

As the de-excitation of ^{12}C* is monoenergetic, this gamma line can be used to determine the total neutrino flux above the 15.1 MeV threshold of reaction (3.5). Finally, there is the elastic scattering of neutrinos on electrons (confer equation (2.1)) and on protons. As discussed in section 2.1.1, these interactions do not provide event by event neutrino energy information. Nevertheless, the expected recoil spectra from a given supernova model can

[3] Additionally, the LSD detector detected a cluster of 5 events. As the arrival time of these events is in significant conflict with the other detected events [80], they are not attributed to SN1987A here.
[4] GVKM: Gava-Kneller-Volpe-McLaughlin

be tested against the observed distributions. While the number of proton scatterings is expected to be approximately one order of magnitude higher than the number of electron recoils [81], the proton recoils are shifted to lower energies due to the quenching in the LSc. Thus, the usable number of proton recoils strongly depends on the proton quenching in the LSc and on the achieved threshold, which is determined by the ^{14}C background. Note that the elastic scattering of neutrinos on protons, in contrast to neutron electron scattering, is a pure NC channel and therefore yields the overall spectrum.
The combined, time resolved information from the different channels allow for a stringent test of current SN models.

Apart from that, it might be possible to extract information about the neutrino properties from the observed SN neutrino signal. The problem is, that the current SN models are not that robust, especially in later stages of the SN evolution. Hence, it is difficult to find a signal characteristic which is stable enough against model variations, to allow for a determination of neutrino properties. Currently, the ability of LENA to extract the neutrino mass hierarchy from the risetime of the $\bar{\nu}_e$ signal is studied [83]. Just from a statistical point of view, a discrimination capability of about 2σ is expected.

As the observation of a SN would be of great importance and as SN in our galaxy are rare, an early warning would help to have all available detectors online during a SN. Due to its huge size and low energy threshold, LENA can provide such an early warning by detecting the neutrinos from the final burning stage of a star. This is possible for SNe up to a distance of several kpc [61].

3.2.4 Diffuse supernova neutrino background

As the interaction cross section of neutrinos is very low, most neutrinos from former SNe still have not interacted after their emission from the SN. These neutrinos form the isotropic diffuse supernova background neutrino (DSNB) flux [66]. As SNe emit all flavors of (anti)neutrinos, the DSNB is also a mixture of all neutrino flavors. Note that the energy spectrum of the DSNB neutrinos is shifted to lower energies compared to neutrinos from a SN due to the redshift since their emission.
A detection of the DSNB therefore provides a mean to access the average SN neutrino spectrum. Furthermore, it allows to measure the redshift dependent SN rate [41]. Up to now, the DSNB has not been detected. The current best limit for the $\bar{\nu}_e$ DSNB-flux $\Phi_{\bar{\nu}_e}$ was provided by Super Kamiokande: $\Phi_{\bar{\nu}_e} < 3.1\,\mathrm{cm}^{-2}\mathrm{s}^{-1}$ for $E_{\bar{\nu}_e} > 17.3\,\mathrm{MeV}$ [84] using the IBD as detection reaction.
Compared to Super Kamiokande, LENA has two major advantages. First its fiducial mass is about two times higher as the fiducial mass of Super Kamiokande. Second, in contrast to Water Cerenkov detectors, LENA is able to detect the 2.2 MeV gammas from the neutron capture on Hydrogen. Thus, the delayed coincidence technique can be used to significantly suppress the backgrounds to the DSNB measurement. The capabilites of LENA to detect the DSNB were studied in [41]. It was found that after all cuts, the expected DSNB rate, dependent on the used model[5], would be between 18 and 35 events per 10 a for $9.5\,\mathrm{MeV} < E_{\bar{\nu}_e} < 25\,\mathrm{MeV}$. In the same time and energy interval, 28 background

[5] In [41], thermal distributions for the resulting SN antineutrino sprectrum with mean neutrino energies between 12 MeV and 21 MeV were assumed.

events are expected after cuts. Assuming that the expected background rate is known at 5% accuracy, a detection of the DSNB would be possible after 10 a of measurement with more than 3σ. If no DSNB signal is found, the Super Kamiokande limit would be improved by a factor of 8. This would also imply that all current DSNB models would be excluded at more than 90% C.L..

3.2.5 Proton decay

In the Standard Model, the proton is stable due to baryon number conservation. However, baryon number conservation is not linked to a fundamental gauge symmetry but was introduced "ad hoc" as proton decay was not observed. Thus, theories beyond the Standard Model typically include a proton decay [85].
Generally, grand unified theories (GUTs), e.g. models based on the SU(5) group, predict the decay channel

$$p \rightarrow l^+ + \pi^0 \tag{3.6}$$

to be dominant [85, 86]. Currently, the best limits for this decay branch are imposed by Super Kamiokande: $\tau(p \rightarrow e^+ + \pi^0) > 8.2 \cdot 10^{33}$ a and $\tau(p \rightarrow \mu^+ + \pi^0) > 6.6 \cdot 10^{33}$ a at 90% C.L. [86], already ruling out minimal $SU(5)$ based models. The lepton in the exit channel generates a visible Cerenkov-ring in the Super Kamiokande detector, while the two gammas created in the π^0 decay create one additional ring each. This so called three ring event is very hard to replicate, with the only known backgrounds coming from atmospheric neutrino interactions. The selection can be made even more stringent by reconstruction the momenta of the different particles and requiring the momenta to cancel and the invariant mass to coincide with the proton mass. As, in addition to the excellent background rejection, Super Kamiokande already achieved a huge exposure, LENA will not be competitive in these channels.
However, the situation changes for supersymmetric (SUSY) model. Often, these theories favor the decay into a Kaon and a neutrino [85]:

$$p \rightarrow \bar{\nu} + K^+. \tag{3.7}$$

With $\tau(p \rightarrow \bar{\nu} + K^+) > 2.3 \cdot 10^{33}$ a at 90% C.L. [87], the best limit on the channel is again from Super Kamiokande. Contrary to the π^0 channel, this limit can be significantly improved by LENA, as the K^+ in the exit channel is below the Cerenkov threshold. Thus, the signature for the Kaon channel in Super Kamiokande relies on the detection of the decay products of the Kaon which is very hard to separate from resonant atmospheric neutrino interactions which can also produce Kaons and a recoil nucleus below the Cerenkov threshold that goes unnoticed. In a LSc detector, the produced Kaon is directly visible. Furthermore, the K^+ decays with $\tau \approx 12$ ns [21] resulting in an additional signal in the LSc. This leads to a characteristic double peak structure (see figure 3.4 for an example) which efficiently allows to discriminate the signal against the atmospheric neutrino background. Using this method, a sensitivity of $\tau(p \rightarrow \bar{\nu} + K^+) > 4 \cdot 10^{34}$ a at 90% C.L. can be achieved after 10 a of measurement time [88]. As the predicted decay time of many models is below 10^{35} a [85], this would allow to considerably reduce the available parameter space.

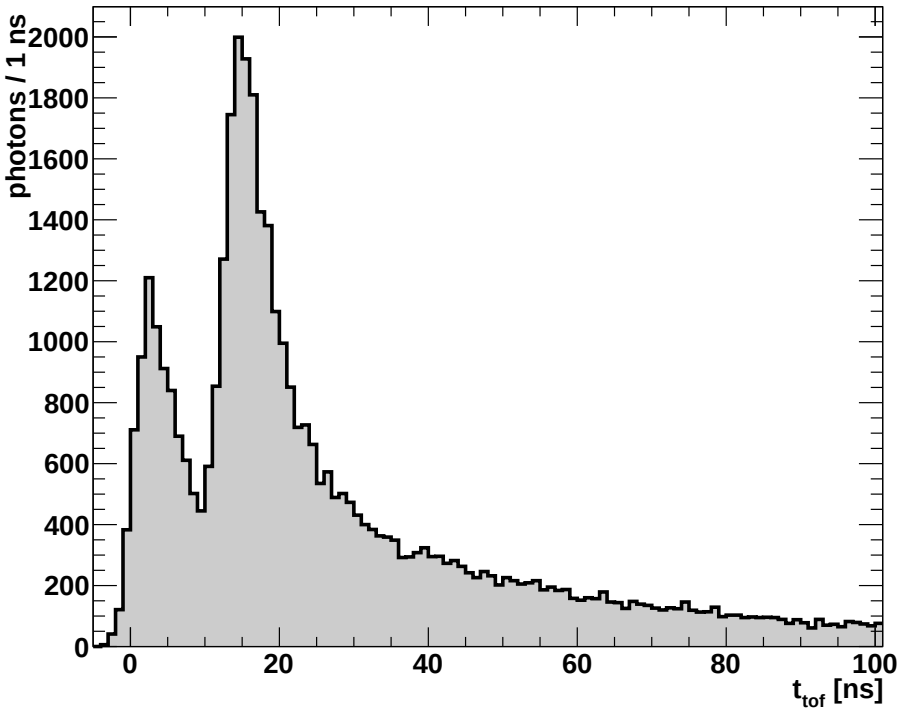

Figure 3.4: Simulated, time of flight corrected, photoelectron arrival time spectrum of a $p \to \bar{\nu} + K^+$ decay. The first peak is due to the energy deposited by the K^+, while the second peak is caused by its decay products.

3.2.6 Atmospheric neutrinos

Atmospheric neutrinos are created by the interactions of cosmic rays in the upper atmosphere [89]. Their energy spectrum starts at a few MeV [41] of energy. At energies above $\sim$1 GeV, the atmospheric muon flux Φ follows a power law $\Phi \propto E^{-\gamma}$ where $2.7 < \gamma < 3.2$ [90]. Furthermore, depending on the zenith angle of the incident neutrinos, the distance between the neutrino production and the detector varies from a few km up to approximately twice the earth's radius. Thus, using atmospheric neutrinos a wide range of L/E values is accessible. Note, that the direction of the incoming neutrino has to be reconstructed from the observed event to determine L, which can be done by reconstruction the direction of the primary lepton that is correlated to the direction of the incoming neutrino. Using this technique, neutrino oscillations have already been successfully studied [91].
Moreover, atmospheric neutrinos feature a very long baseline when traveling through the earth. As discussed in section 1.4, this is beneficial to determine the correct mass hierarchy. Therefore, currently there are various proposals to determine the mass hierarchy using CC interactions of atmospheric $\overset{(-)}{\nu}_\mu$ in the range from a few GeV up to about 20 GeV [92, 93, 94][6]. Note, that despite the huge baseline, measuring the mass hierarchy using atmospheric neutrinos is challenging due to the systematic errors of the flux calcu-

[6]These detectors can rely only on CC-$\overset{(-)}{\nu}_\mu$ interactions as they cannot determine the direction of electromagnetic showers created by CC-$\overset{(-)}{\nu}_e$ events. LENA principally could also use the latter events.

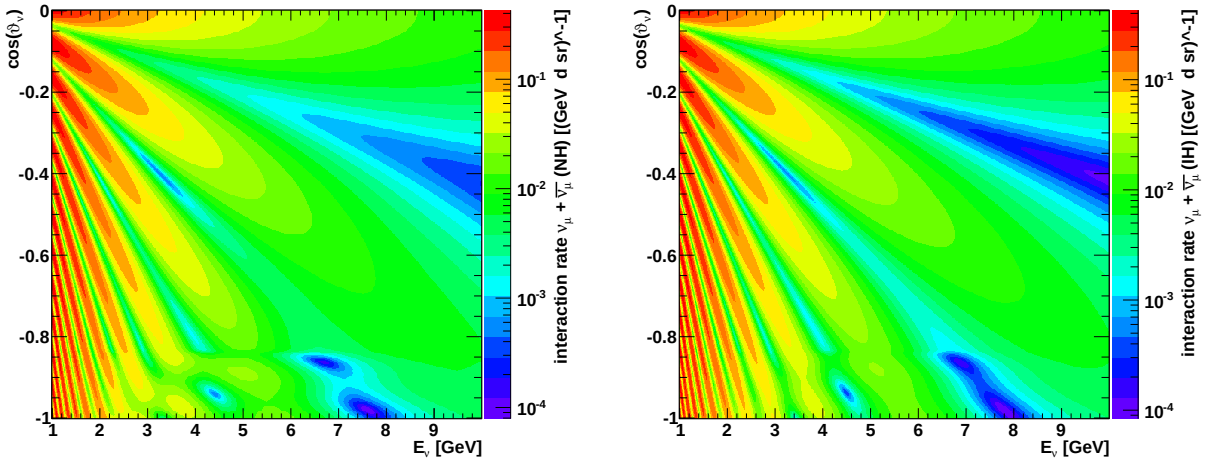

Figure 3.5: The expected doubly differential CC atmospheric muon-neutrino interaction rate in LENA as a function of the cosine of the zenith angle and the neutrino energy assuming the normal hierarchy (left) and the inverted hierarchy (right), respectively.

lations and the fact, that the initial neutrino flavor is not known. Furthermore, neutrinos as well as antineutrinos are used. As it is technically difficult to magnetize a detector of the required size, a distinction between the flavors is only possible on a statistical level. Thus it is not possible to measure only one oscillation channel but only a sum of multiple oscillation channels.

As the LENA detector is too small to contain $\overset{(-)}{\nu}_\mu$-CC events with deposited energies above ∼10 GeV, only the lower energetic part of the $\overset{(-)}{\nu}_\mu$ parameter space is accessible. A calculation of the atmospheric neutrino rate with and without detector effects can be found in appendix A, here only the results are shown. Figure 3.5 shows the expected doubly differential CC rates for $\overset{(-)}{\nu}_\mu$ in LENA as a function of the neutrino direction and the neutrino energy. This translates to an integral rate of approximately one event above 4 GeV neutrino energy per day assuming a fiducial volume of 50 kt. While this distributions show some usable structure, these structures are washed out by the energy and position resolution. Assuming a neutrino energy resolution of 9 % (see section 6.3) and assuming that the event reconstruction is able to determine the direction of the primary lepton without error, figure 3.5 becomes figure 3.6. The difference between normal and inverted hierarchy is shown in figure 3.7 with and without detector resolution. As the detector resolution smears out the relevant structures at lower energies, only small differences above ∼ 5 GeV remain after taking into account the detector resolution.

Due to the low statistics in this high energy region, a determination of the mass hierarchy using LENA and atmospheric neutrinos will be very challenging. The only viable possibility would be to improve the event reconstruction to be able to reconstruct the energy and the direction of the hadronic cascade as well the energy and the direction of the produced lepton. This would allow for a full kinematic reconstruction of the neutrino interactions and thus to determine the neutrino direction with a higher accuracy. Thus, the smaller structures at lower energies where also the rate is higher would become accessible. Attempts for such a reconstruction are presented in chapter 6.

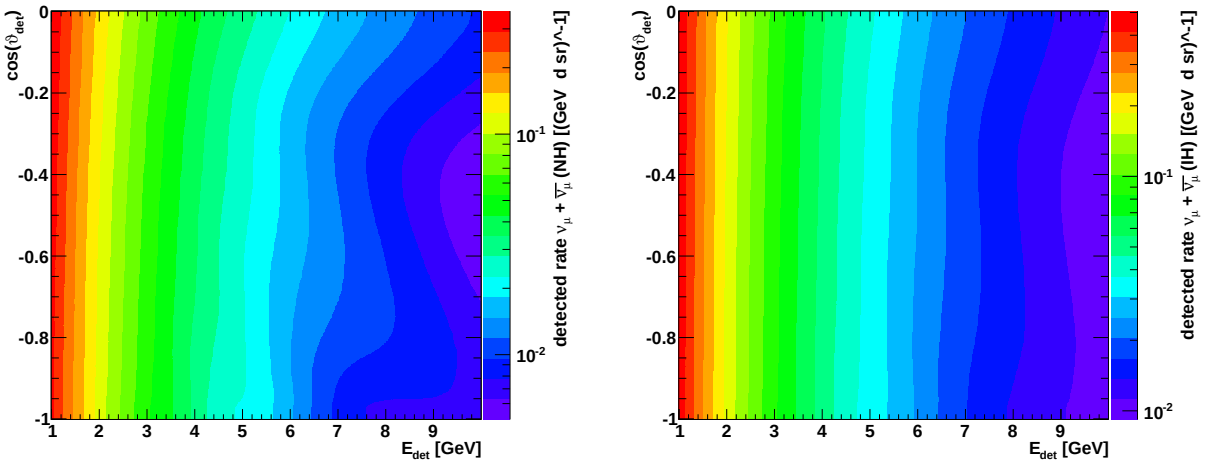

Figure 3.6: The expected reconstructed doubly differential CC atmospheric muon-neutrino interaction rate in LENA as a function of the cosine of the zenith angle and the neutrino energy assuming the normal hierarchy (left) and the inverted hierarchy (right), respectively. The energy resolution was assumed to be 9 % and the resolution in the position reconstruction was modeled by the deviation between the neutrino direction and the direction of the primary lepton.

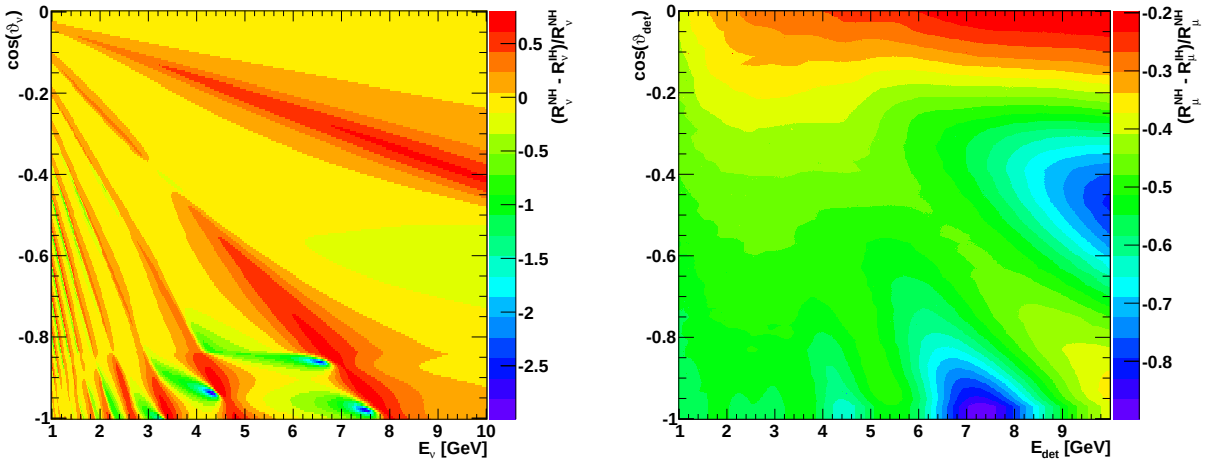

Figure 3.7: Relative difference between the NH and IH expected doubly differential CC atmospheric muon-neutrino interaction rates in LENA as a function of the cosine of the zenith angle and the neutrino with (right) and without (left) detector resolution. The energy resolution was assumed to be 9 % and the resolution in the position reconstruction was modeled by the deviation between the neutrino direction and the direction of the primary lepton.

3.2.7 Long baseline neutrino oscillations

As already discussed in section 1.4, long baseline neutrino beams are a promising opportunity to determine the MH using the $\overset{(-)}{\nu}_\mu \rightarrow \overset{(-)}{\nu}_e$ channel. Moreover, they provide the possibility of an appearance experiment and are therefore sensitive to δ. To utilize the matter effects to determine the MH, a neutrino beam with neutrino energies in the GeV range is required, corresponding to a baseline of a few 1000 km (compare figure 1.1). As a 2 GeV muon has a range of approximately 10 m, all current LSc detectors are too small to fully contain the produced particles, which is required for a good energy resolution[7]. As the distance between CERN and Pyhäsalmi is about 2 300 km, a neutrino beam from CERN to Pyhäsalmi would be a very suitable candidate. This proposed beam, which is called the CN2PY beam, was considered as preferred option in the LAGUNA-LBNO design study. Here, a conventional neutrino beam was assumed. In such a beam, the SPS of the CERN accelerator chain is used to accelerate protons to[8] 400 GeV at a beam power of 750 kW [96]. This corresponds to about $1.0\text{-}1.5{\cdot}10^{20}$ protons on target (POT). These protons are directed on a light target to produce secondary pions. The pions are successively focused into a decay tunnel using a magnetic horn. While they travel trough the decay tunnel, the pions decay mainly through the [21]

$$\pi^\pm \rightarrow \overset{(-)}{\nu}_\mu + \mu^\pm \tag{3.8}$$

channel. At the end of the tunnel, there is an absorber which stops the produced muons. Dependent on the current direction through the magnetic horn, either only π^+ or π^- are focused into the decay tunnel. Therefore it is possible to select the neutrino polarity though the direction of the horn current. The resulting beam spectra are shown in figure 3.8 for both possible horn settings. As expected from the decay (3.8), the spectrum is dominated by $\overset{(-)}{\nu}_\mu$. Additionally, there are admixtures from wrong sign neutrinos and $\overset{(-)}{\nu}_e$ which are produced by rare decays of pions and kaons, by in flight decays of the produced muons as well as by pions of the wrong charge state which are accidentally focused [97]. The CN2PY beam planned to run for 10 a with 5 a running in neutrino mode and 5 a running in antineutrino mode.

To be able to extract the MH or δ from the observed interactions of neutrino beam events, a far detector basically has to fulfill three requirements. They are discussed assuming a beam in neutrino mode:

- The size of the detector has to be sufficient to collect reasonable statistics within the run time of the neutrino beam. Using a large detector like LENA additionally has the advantage, that the probability that an event is contained is higher. Figure 3.9 shows the probability of an event to be contained as a function of the true neutrino energy. While the efficiency to contain ν_μ-CC events significantly drops with rising energy, the efficiency for ν_e-CC events, resulting from the $\nu_\mu \rightarrow \nu_e$ oscillations, is above 75% for the whole energy range. Thus, the size of LENA is sufficient to act as a far detector for the CN2PY beam.

[7] This requirement does not hold if the detector would be magnetized, which is however very difficult due to the size of the detector.

[8] While the SPS is capable of delivering 450 GeV protons, reaching this energy requires to cross a tune resonance which would result in a significant loss of beam power [95].

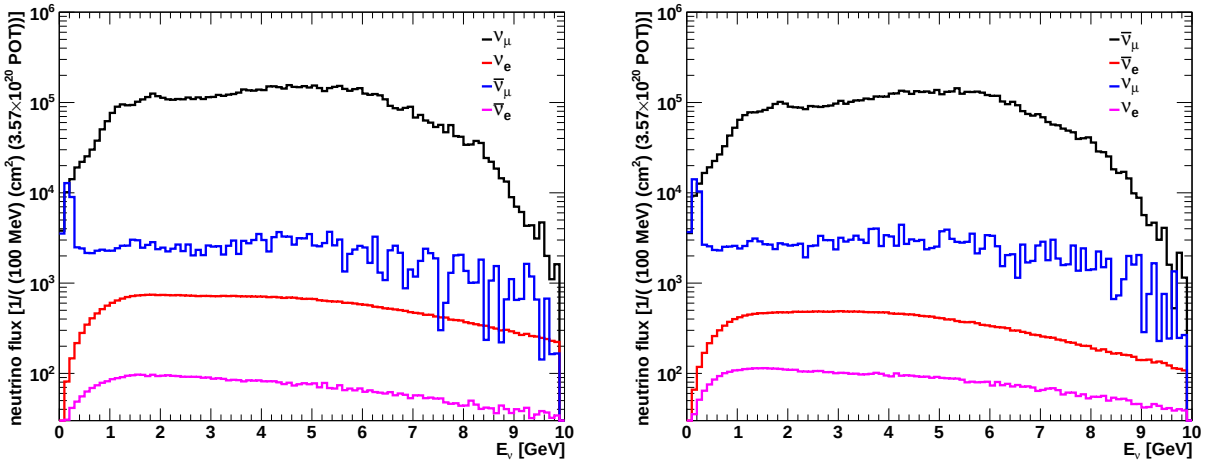

Figure 3.8: Expected neutrino spectrum from the CN2PY beam at 2 300 km distance for neutrino mode (left) and antineutrino mode (right). The different colors show the contributions from the different neutrino flavors. Data taken from [98].

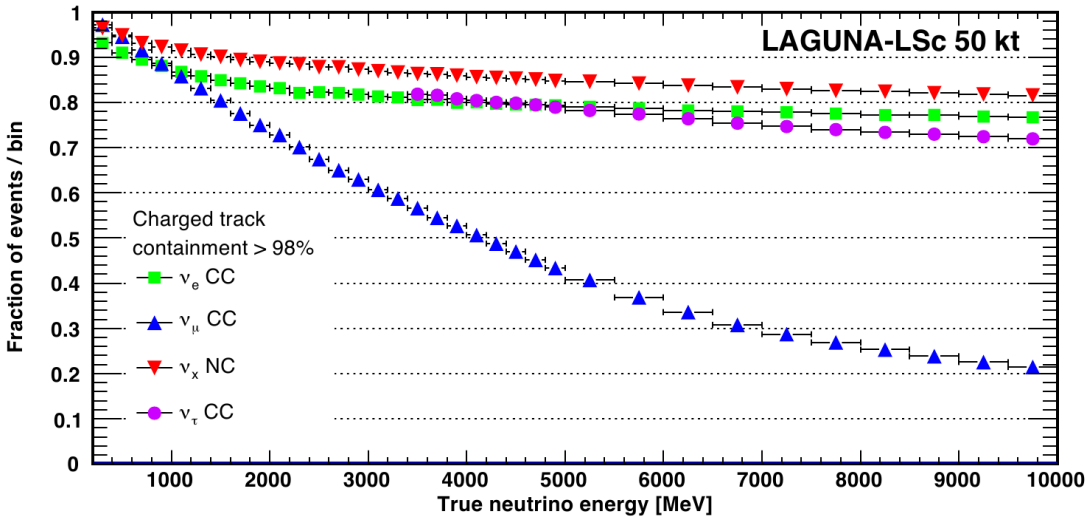

Figure 3.9: Probability that an event with given neutrino flavor is contained in LENA as a function of the neutrino energy [96]. An event is counted as contained if more than 98% of its total track length is contained in the fiducial volume.

- The energy resolution of the detector has to be sufficient to map the oscillation spectrum and thus determine the oscillation parameters. For contained events, LENA basically acts as a big, totally active calorimeter, allowing for a very good energy resolution. The reconstruction of the neutrino energy along with the achieved resolution is presented in section 6.3.

- In order to study the $\nu_\mu \rightarrow \nu_e$ oscillation channel, the signal, i.e. interactions from the oscillated ν_e, has to be discriminated from interactions of the other neutrino types. This leads to two kinds of background:
  The first kind of background is due to the impurities of the beam. As the beam is not a pure ν_μ beam (see figure 3.8), ν_e are already present in the beam. Thus also unoscillated ν_e from the beam are tagged as signal events. Additionally, the beam

also has a $\bar{\nu}_e$ contamination. As LENA is not magnetized, neutrino and antineutrino interactions generally cannot be discriminated at an event by event basis[9]. Thus also $\bar{\nu}_e$ events contribute to the background. Furthermore, $\bar{\nu}_e$ can also be produced by $\bar{\nu}_\mu \rightarrow \bar{\nu}_e$ oscillations from the $\bar{\nu}_\mu$ contamination of the beam. These backgrounds induced by the beam typically cannot be discriminated from signal events. As the contamination of the beam typically is very low (see figure 3.8), these background are of the order of a few percent of the signal events [96].
The second type of background is due to misidentification of other event types as ν_e-CC events. First of all, ν_μ-CC events can be misidentified as ν_e-CC events. Due to the large extension of the muon tracks at GeV energies, the pulse shape of electron and muon events is different [99] which allows for an efficient discrimination of ν_μ-CC events. More critical are NC events caused by neutrinos of all flavors. NC QEL events typically lead to the emission of a nucleon (see section 2.1.2). As these events feature a low momentum transfer and the nucleon is strongly quenched, these events are typically reconstructed at energies below the relevant region. NC DIS events are more difficult, especially as they can have electromagnetic sub showers due to produced π^0s. Currently, NC events are discriminated in LENA using a multi variate analysis (MVA) based on a boosted decision tree (BDT) [100]. The input parameters for the BDT are determined from the overall pulse shape. Using this method, the NC background can be reduced by 89% at the expense of reducing the signal efficiency to 27% [101]. Finally, due to neutrino oscillations, the beam also contains ν_τ at the detector site. The τ-leptons produced in CC interactions can decay nearly instantly into $e^\pm$ (17.8% branching ratio), thus faking ν_e-CC events. As the decay time of the τ-lepton is very short ($\approx 3 \cdot 10^{-13}$ s [21]), these events are nearly indistinguishable from real ν_e-CC events. Additionally, they can decay into $\mu^\pm$ and into hadrons. Thus, ν_τ-CC events can also mimic ν_μ-CC and NC events which can in turn be misidentified as ν_e events.

While LENA is big enough to gain reasonable statistics and features a good energy resolution, its physics performance is currently limited by the relatively inefficient discrimination of NC-background events. While this is still good enough to determine the mass hierarchy at 5σ significance independent of the value of δ (see section 6.6 for details), there is basically no sensitivity to the CP-violating phase δ.
To improve the performance of LENA as a far detector for a neutrino beam, the discrimination of NC events has to be improved. This means that further input parameters for the BDT are required. To obtain such additional parameters, the pulse shape of the individual PMTs instead of the overall pulse shape has to be taken into account. Attempts to construct such a set of more sophisticated parameters are presented in section 6.5.

[9]Discriminating neutrino and antineutrino events might be possible on a statistical level by counting the number of produced neutrons.

Chapter 4

Reconstruction of low energy events

When (anti-)neutrinos with MeV energies interact inside a liquid scintillator, typically electrons or positrons with energies in the MeV range are created in the exit channel (see section 2.1.1). Thus, the range of the secondary particles is generally smaller than 1 cm which is below the spatial resolution achieved in LENA. Hence, these events can be treated as point-like events. This is typically also true for all background events resulting from β-decaying isotopes.
For each of these events, the position $\boldsymbol{r}_s$, the time t_s and the initial kinetic energy T_s have to be determined from the signal recorded at the PMTs. A precise knowledge of each of these parameters is a crucial basis for each kind of physics analysis.
As LENA has not been built yet, the performance of the reconstruction can only be studied using sophisticated Monte Carlo (MC) simulations. The basic set-up of the simulation, used in this thesis, is presented in section 4.1. The data obtained from the simulation is successively preprocessed. This is detailed in section 4.2. The determination of the physical parameters is based on a logarithmic likelihood fit, which is presented in section 4.4. As this fit is based on a numerical minimization, it requires an approximate set of parameters as input which is used as a starting point (see section 4.3). While the start values already give a rough indication of the event parameters, the performance achieved using the full fit, which is presented in section 4.5, improves the resolution of the event parameters by about an order of magnitude.

4.1 Simulation set-up

The LENA detector is simulated using a Monte Carlo (MC) simulation which is based on the Geant4 toolkit [102, 103]. The used simulation was mainly written by R. Möllenberg and is presented in depth in [41]. Here, only the parts relevant for this thesis are briefly outlined.
The geometrical setup consists of a series of nested cylinders which form the fiducial volume, the buffer, the tank and the water-Cerenkov veto. The dimensions correspond to the planned dimensions of LENA (see section 3.1.1).
The cylindrical structure also defines the used coordinate system: Its origin is set to the center of LENA. The symmetry axis of the cylinder defines the z-axis while the x- and y-axis are oriented in a plane perpendicular to the z-axis. The distance from the symmetry axis is given by the radius $\rho = \sqrt{x^2 + y^2}$.
The implemented target consists of pure LAB (see section 3.1.2), the small contributions

Component	τ_i [ns]	n_i [%]
1	4.6	71
2	18	22
3	156	7

Table 4.1: The decay time components of the LENA scintillator for electron excitation used in the LENA simulation according to equation (3.1). Note that these parameters do not correspond to the parameters given in table 3.1 as the simulations were performed before this data was available. They were taken from [88].

of the wavelength shifters are neglected. Using three exponential decay components, the decay-time distribution of the scintillator is implemented following equation (3.1). Table 4.1 shows the decay time parameters used in the simulation. The optical model of the scintillator includes absorption ($\Lambda_{\text{abs}} = 20\,\text{m}$), Rayleigh-scattering ($\Lambda_{\text{ray}} = 40\,\text{m}$) and isotropic scattering ($\Lambda_{\text{iso}} = 60\,\text{m}$). As isotropic scattering basically consists of an absorption-reemission process, the scattered photon is delayed according to an exponential distribution with 1.2 ns decay time constant. The quenching of the scintillator was simulated according to Birk's formula (see equation (2.18) with $k_B = 0.15\,\text{mm/MeV}$). To save computation time, wavelength dependent effects are neglected. All optical properties correspond to the optical properties at a wavelength of 430 nm, which is the wavelength with the maximum contribution to the observed signal when all wavelength dependent effects are taken into account.

The photons are detected by 30542 12" PMTs with attached LCs. As no OMs for 12" PMTs were available when the simulations were made, it is assumed that the optical properties of the Borexino LCs [104] can be transferred from the 8" Borexino PMTs to the 12" PMTs. To save computation time, the LCs were not simulated as geometrical shapes. Instead, the PMTs are approximated as light sensitive, flat disks with an area corresponding to the aperture of the LCs. The effects of the LCs are implemented by applying an angle dependent detection efficiency (see figure 4.1) to the PMTs. It was determined using a full geometrical model of the Borexino LC and an 8" PMT [41]. Additionally, the quantum efficiency of the PMTs, which was assumed to be 20%, was set to 100% while reducing the light yield of the scintillator from $10\,000\,\text{MeV}^{-1}$ to $2\,000\,\text{MeV}^{-1}$. Hence, the photoelectron yield remains unchanged but the number of photons to simulate is reduced by a factor of 5 leading to a significant reduction in computation time. All photons detected by a PMT are recorded. No PMT effects were included at this point. They will be added during the post processing of the data (see section 4.2). This separation of physics simulation and simulation of PMT effects allows to study the effects of different PMT characteristics without having to run the time consuming simulation for each configuration.
This study is limited to the central part of the fiducial volume, i.e. $|z| < 25\,\text{m}$. In this region of the detector, the influence of the lid and of the bottom on the photon distribution of an event can be neglected [41]. This facilitates the tabulation of precomputed values (see section 4.4.2 and section 4.4.3) and thus increases the computational performance of the reconstruction. Note that this choice of the fiducial volume leads to a conservative statement for the performance of the algorithm: In the regions with $|z| > 25\,\text{m}$ the PMTs

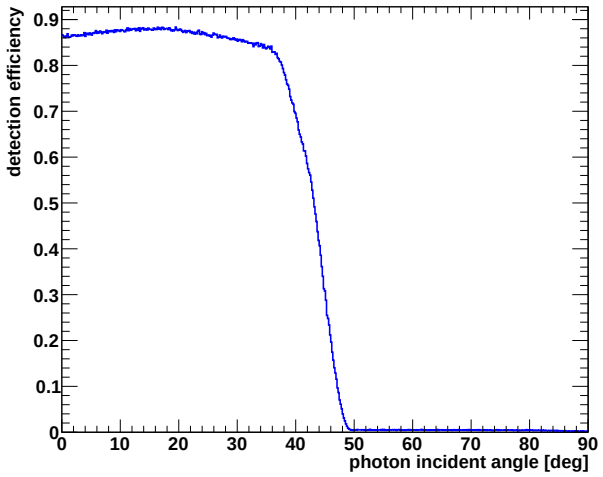

Figure 4.1: The detection efficiency of the optical module as a function of the angle between the incident photon and the surface normal of the aperture. Data taken from [41]. Note that the detection efficiency is greater than 0 even for incident angles above the critical angle as the photons might be scattered towards the PMT while transversing the LC. On the other side, the efficiency is below 1 even for vertical photons as the reflectivity of the LSc is smaller than 1 (86%).

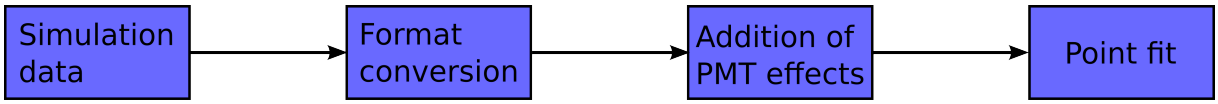

Figure 4.2: The data flow for the reconstruction of low-energy events. The data from the simulation is first converted to a format more suitable for fitting. Successively PMT effects are added. Finally, the resulting event is fitted assuming a point-like energy deposition.

on the end-caps provide additional information thus increasing the precision of the reconstruction. Additionally note that the $|z| < 25\,\mathrm{m}$ region was chosen for technical reasons only, the developed method is applicable to the full detector.
In this configuration the obtained average photoelectron yield is $N_{pe} = 265\,\mathrm{p.e./MeV}$ corresponding to a theoretical limit[1] of the energy resolution of

$$\left(\frac{\Delta T_s}{T_s^{\mathrm{true}}}\right)_{\mathrm{opt}}(T_s^{\mathrm{true}}) = \frac{1}{\sqrt{N_{pe} \cdot T_s^{\mathrm{true}}}} = \frac{6.1\%}{\sqrt{T_s^{\mathrm{true}}/\mathrm{MeV}}}. \tag{4.1}$$

where T_s is the initial kinetic energy of the electron. The index "true" indicates the true value of a variable as opposed to the value returned by the reconstruction.

4.2 Data processing

The data flow used in this analysis is shown in figure 4.2. In a first step, the data is reorganized into a format more suitable for fitting. In this step, the single detected

[1] This limit could theoretically be broken by determining the length of the electron track, which, however, is not possible in LENA at MeV-energies.

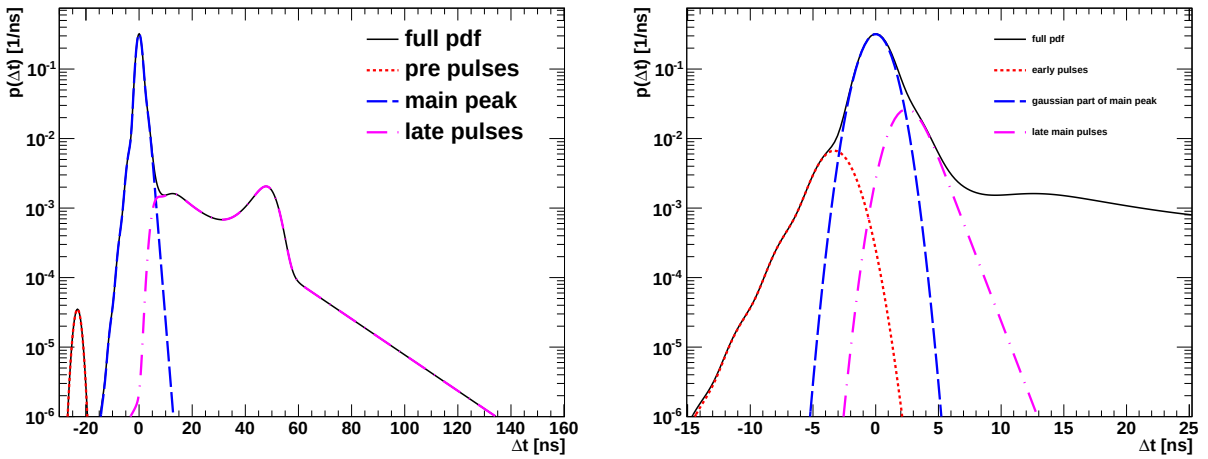

Figure 4.3: The mean transit time PDF of the Borexino PMTs. Data taken from [105]. The left plot shows the overall PDF while the right plot shows a detailed view of the main peak. The PDF consists of three main parts, a dominating peak, a small amount of early pre-pulses and a tail of late pulses. The main peak can again be subdivided into a Gaussian part, early and late pulses. Note that $\Delta t = 0$ is chosen to match the maximum of the PDF, it does not correspond to the arrival time of the photon.

photons resulting from the simulation are associated with the corresponding OMs.
In the successive step, two effects intrinsic to PMTs are added: First, the transit time of the electron avalanche through the PMT is not constant but follows a probability density function (PDF), the so called transit-time spread (TTS). For the Borexino PMT, this PDF was extensively investigated in [105]. The result is shown in figure 4.3. It can be subdivided into three main parts, a dominating main peak, a very small amount of pre-pulses and a tail of late pulses. A discussion of possible underlying physical effects can be found in [105]. Currently, there is ongoing work to suppress the unwanted effects, which cause a deviation of the TTS from a Gaussian shape. There are also stringent limits on the TTS characteristics of the PMTs that are in question for LENA [7]. As the TTS of the PMTs that will be used in LENA is currently not known, a simple assumption is made concerning the PMT TTS: It is taken to be of Gaussian shape with a standard deviation of $\sigma_{\mathrm{TTS}} = 1\,\mathrm{ns}$. All photons from the simulation were smeared according to this TTS PDF. This assumption will be used in the remainder of this thesis except where explicitly noted. The effects of the deviation from this assumption are discussed in section 4.5.3.
Additionally, PMTs also produce so-called dark counts, i.e. they produce a photon signal even though no photon was detected at the photocathode. This leads to a so-called dark noise (DN). These event occur randomly in time. Thus they where added randomly in the event time window, i.e. between the first and the last detected photon of a given event. Typically, the dark noise of a 12" PMT is in the kHz range [105]. This value is, however, strongly dependent on the ambient temperature, the applied voltage and the time the PMT has already been in the dark. For this section, the basic assumption is a dark rate of 1 kHz dark noise per PMT.
The smeared photons and the dark counts together form the set of "hits" which is used for further analysis.
The last step in the data flow consists of the actual fitting of the event, which is described in the following sections.

4.3 Primary estimates for the fit parameters

Before the event can be finally fitted, rough estimates are determined for the fit parameters $\boldsymbol{X} = \{\boldsymbol{r}_s, t_s, T_s\}$, i.e. for the position, the time and the initial kinetic energy of the event. These rough estimates later on serve as start parameters for the numerical minimization algorithms used in the final fits.

Estimate for the position of the event:
First of all the charge barycenter[2] $\boldsymbol{r}_{\mathrm{bc}}$ of the event is determined:

$$\boldsymbol{r}_{\mathrm{bc}} = \frac{\sum_{i=0}^{N_{\mathrm{PMT}}} q_i w_i \boldsymbol{r}_i}{\sum_{i=0}^{N_{\mathrm{PMT}}} q_i w_i}. \tag{4.2}$$

Here, q_i and $\boldsymbol{r}_i$ are the total number of hits detected on the i$^{\mathrm{th}}$ OM (i.e. the charge of the corresponding PMT) and the position of the i$^{\mathrm{th}}$ OM, respectively. w_i is a weighting factor introduced by [41] and slightly modified in a way that no MC-truth information is required for its computation:

$$w_i = \begin{cases} \sum_{j=0}^{q_i} \exp\left(-\frac{t_j + 50\,\mathrm{ns} - t_{\mathrm{min}}}{50\,\mathrm{ns}}\right) & \text{if } q_{\mathrm{tot}} < 6000 \\ 1 & \text{else,} \end{cases} \tag{4.3}$$

where t_j is the time of the j^{th} hit on the i$^{\mathrm{th}}$ PMT, q_{tot} is the total number of hits registered in an event and t_{min} is the time of the first hit in the event. The resulting value for $\boldsymbol{r}_{\mathrm{bc}}$ serves as a first estimate of the event position.
The estimated position resulting from the barycenter can successively be improved using a simplified fit to the charge of the individual PMTs which is based on a negative logarithmic likelihood (NLL) fit[3]. The NLL $\mathcal{L}$ is defined as

$$\mathcal{L}(\boldsymbol{r}_s) = -\ln[L(\boldsymbol{r}_s|\boldsymbol{q})] = -\ln[P(\boldsymbol{q}|\boldsymbol{r}_s)], \tag{4.4}$$

where $\boldsymbol{q} = \{q_i\}$ and $P(\boldsymbol{q}|\boldsymbol{r}_s)$ is the probability density function (PDF)[4] to obtain the experimental result $\boldsymbol{q}$ given the parameters $\boldsymbol{r}_s$. L is commonly called the likelihood function. It can be shown [106] that the event position $\boldsymbol{r}_s$ maximizing $L(\boldsymbol{r}_s|\boldsymbol{q})$ and therefore minimizing $\mathcal{L}(\boldsymbol{r}_s)$, is a good estimator for the true values of $\boldsymbol{r}_s$.
Thus, to determine a good estimate for $\boldsymbol{r}_s$, $P(\boldsymbol{q}|\boldsymbol{r}_s)$ has to be determined. It is given by a product of Poisson distributions of all PMTs:

$$P(\boldsymbol{q}|\boldsymbol{r}_s) = \prod_{i=0}^{N_{\mathrm{PMT}}} \frac{\mu_i(\boldsymbol{r}_s)^{q_i}}{q_i!} \exp[-\mu_i(\boldsymbol{r}_s)] \tag{4.5}$$

[2] Note that the charge barycenter is not equivalent to the barycenter of the event's deposited energy.
[3] For details of likelihood fits see section 4.4 and [106].
[4] In this case $P(\boldsymbol{q}|\boldsymbol{r}_s)$ actually is not a PDF but a probability as q_i are integer values. During the remainder of the thesis, no distinction shall be made between PDFs and actual probabilities as the differences in normalization are not relevant here.

where μ_i is the expected charge on the i$^{\text{th}}$ PMT. For details of the structure of the PDF see sections 4.4.1 and 4.4.2. At this point, only a fast, approximate calculation of $\mu_i(\boldsymbol{r}_s)$ is performed which neglects scattering in the scintillator and DN. Hence,

$$\mu_i(\boldsymbol{r}_s) \approx N_\gamma \underbrace{\frac{A_{\text{PMT}}}{4\pi|\boldsymbol{r}_s - \boldsymbol{r}_{\text{i}}|^2} \cdot \frac{\hat{\boldsymbol{n}}_i \cdot (\boldsymbol{r}_s - \boldsymbol{r}_{\text{i}})}{|\boldsymbol{r}_s - \boldsymbol{r}_{\text{i}}|}}_{\text{solid angle}} \underbrace{\exp\left(-\frac{|\boldsymbol{r}_s - \boldsymbol{r}_{\text{i}}|}{\Lambda_{\text{abs}}}\right)}_{\text{absorption}} \underbrace{P_{\text{LC}}\left(\frac{\hat{\boldsymbol{n}}_i \cdot (\boldsymbol{r}_s - \boldsymbol{r}_{\text{i}})}{|\boldsymbol{r}_s - \boldsymbol{r}_{\text{i}}|}\right)}_{\text{effect of LC, see figure 4.1}}, \quad (4.6)$$

where $\boldsymbol{r}_i$ is the position of the i$^{\text{th}}$ PMT, $\hat{\boldsymbol{n}}_i$ is the normal vector of the i$^{\text{th}}$ PMT which is pointing away from the center of the detector, $P_{\text{LC}}(\cos(\alpha))$ is the detection efficiency of the LCs (see figure 4.1) and N_γ is the number of photons initially emitted at the vertex. However, N_γ is not known at the time the fit is performed, but experience shows that the number only needs to be in the right order of magnitude to get a good estimate for $\boldsymbol{r}_s$. Thus, it is estimated using

$$N_\gamma = 10 q_{\text{tot}}. \quad (4.7)$$

While this yields already good results for the z component of $\boldsymbol{r}_s$, the radius ρ_s shows a systematic error due to the neglection of the scattering[5]. Thus, ρ_s is corrected using the polynomial correction function:

$$\rho_{\text{corr}} = 30\,\text{cm} + 0.907 \cdot \rho_s, \quad (4.8)$$

where the parameters have been determined from the simulation. The final value for $\boldsymbol{r}_s$ is therefore given by

$$\boldsymbol{r}_s = \begin{pmatrix} x_s \\ y_s \\ z_s \end{pmatrix} \rightarrow \begin{pmatrix} x_s \cdot \rho_{\text{corr}}/\rho \\ y_s \cdot \rho_{\text{corr}}/\rho \\ z_s \end{pmatrix}. \quad (4.9)$$

Estimate for the kinetic energy of the event:
The kinetic energy of the event, can be estimated from the position $\boldsymbol{r}_s$ of the event and the total charge q_{tot} deposited in the event [41]:

$$T_s = T_s(\boldsymbol{r}_s, q_{\text{tot}}). \quad (4.10)$$

As only the region with $|z| < 25\,\text{m}$ is considered, T_s only depends on ρ_s and q_{tot}. Neglecting quenching effects, the energy of an event can be estimated using

$$T_s = k_{\text{cal}}(\rho_s) q_{\text{tot}}, \quad (4.11)$$

where k_{cal} is a calibration factor which has to be extracted from calibration. Here, a set of 200 000 events with $0.2\,\text{MeV} < T_s < 3\,\text{MeV}$, which were randomly distributed across the fiducial volume, was used to estimate k_{cal} as a function of ρ_s. The result of this calibration is shown in figure 4.4. As k_{cal} is the inverse of the mean photo-electron yield, figure 4.4 shows that the photo-electron yield is approximately constant for $\rho_s \lesssim 7\,\text{m}$. The slight rise of the light yield from the center to $\rho_s \approx 7\,\text{m}$ is due to the influence of light attenuation and scattering. For $\rho_s \gtrsim 7\,\text{m}$, the light yield drops significantly as the event vanishes from the field of view of more and more OMs due to the influence of the LCs.

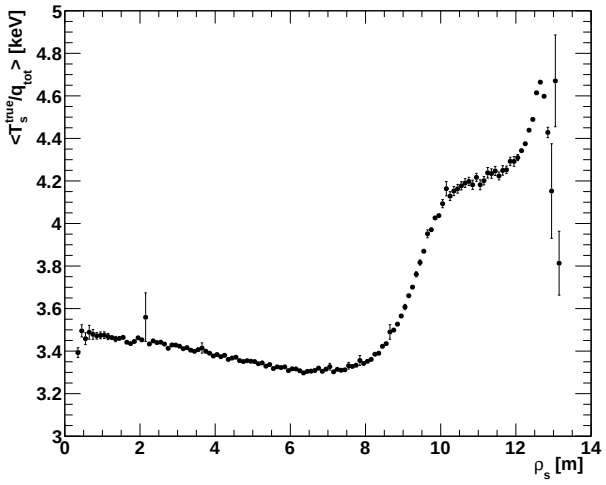

Figure 4.4: The true kinetic energy of the simulated electrons divided by the obtained mean number of photoelectrons as a function of the estimated radius ρ_s. The result shown is obtained from 200 000 events with $0.2\,\mathrm{MeV} < T_s^\mathrm{true} < 3\,\mathrm{MeV}$, which are randomly distributed across the fiducial volume. Note that the shown quantity $\langle T_s^\mathrm{true}/q_\mathrm{tot}\rangle$ corresponds to the inverse photoelectron yield.

Estimate of the start time of the event:
Finally, the time of the event has to be estimated. To obtain this value from the hit times on the PMTs, the time of flight (TOF) of the photons and also the scintillator pulse shape have to be taken into account. A TOF correction can be done, as an estimate of the vertex position is available. Thus, for any given PMT at the position $\boldsymbol{r}_i$ which has a hit at time t_j the TOF corrected time is

$$t_j^\mathrm{TOF} = t_j - \frac{n}{c_0}|\boldsymbol{r}_s - \boldsymbol{r}_i|, \tag{4.12}$$

where n is the refractive index of the scintillator ($n = 1.484$ for LAB) and c_0 is the speed of light in vacuum.
From the TOF corrected hit times, the start time of the event can be roughly estimated using an heuristic approach: In a first step, the TOF corrected first hits on each PMT are histogrammed using 2 ns wide bins. Afterwards, the bin b_max containing the maximum of the histogram is determined. Finally, the rough estimate for the start time t_s is the mean of all TOF corrected first hits with $t^\mathrm{TOF} < t_\mathrm{max}^\mathrm{TOF}$, where $t_\mathrm{max}^\mathrm{TOF}$ is the center of b_max. Considering only TOF corrected first hits with $t^\mathrm{TOF} < t_\mathrm{max}^\mathrm{TOF}$ ensures that most of the hits contributing to the mean are fast photons from the fast decay component of the scintillator and therefore the error due to the decay time of the scintillator is suppressed.

Performance of the estimates:
To quantify the performance of the parameter estimation algorithms, a sample of 200 000

[5] No dependency of z is observed due to the choice of using only events with $|z| < 25\,\mathrm{m}$. Thus, the effect of the scattering is upwards and downwards symmetric.

events between 0.2 MeV and 3 MeV was simulated and successively progressed. As the performance of the algorithms primarily depends on the visible energy of the event[6], three distinct 200 keV wide data sets were used: $0.2\,\mathrm{MeV} < T_s < 0.4\,\mathrm{MeV}$, $0.9\,\mathrm{MeV} < T_s < 1.1\,\mathrm{MeV}$ and $2.8\,\mathrm{MeV} < T_s < 3\,\mathrm{MeV}$.
Figure 4.5 shows the distribution of the distances between true and estimated event position for each of the three data sets. Assuming that the deviations from the true event position follow a Gaussian distribution with width σ for each of the three coordinate axes, the distance distribution should follow

$$P(d|\sigma) = \mathcal{N}(\sigma) \cdot d^2 \exp\left(-\frac{d^2}{2\sigma^2}\right). \tag{4.13}$$

Here, $\mathcal{N}(\sigma)$ is a normalization factor and $d = |\boldsymbol{r}_s^{\mathrm{true}} - \boldsymbol{r}_s|$ is the distance between the true and the reconstructed event position. The corresponding fits are also shown in figure 4.5 along with the fit results for σ. Obviously, the obtained distributions do not follow the assumed distribution but feature significant tails to higher distances. Nevertheless, the obtained σ can be used as a measure for the resolution: At the detector threshold the obtained resolution is above 2 m, at 1 MeV it is still above 1 m and even at 3 MeV it is still around 0.75 m. The observed improvement of the resolutions with rising energy is due to the increase in photo-electron statistics.
The distribution of the deviations of the reconstructed kinetic energy from the true kinetic energy is shown in figure 4.7 along with Gaussian fits to the obtained data. The obtained resolutions are all significantly above the theoretical limit (see equation (4.1)). Additionally the distributions were found to be significantly non-Gaussian.
Finally, figure 4.6 shows the distribution of the deviations of the estimated start times from the true start times. The obtained distributions show a significant asymmetry and feature tails towards too low reconstructed start times. These tails are more pronounced for low-energy events. They are due to the finite resolutions of the position estimation, as an error in the position reconstruction leads to some of the TOF corrected hit times being too small.
While the obtained resolutions are not sufficient for physics analysis of the events, they are good enough to serve as a start parameter for the required final fit, which is presented in section 4.4.

4.4 Likelihood fit

One method to estimate a set of physical parameters $\boldsymbol{X}$ from data collected in an experiment $\boldsymbol{D}$ is a so-called likelihood fit [106]. In this approach, the estimated values $\hat{\boldsymbol{X}}$ are determined by maximizing the likelihood function $L(\boldsymbol{X})$ with respect to $\boldsymbol{X}$. The likelihood function is defined as [106]:

$$L(\boldsymbol{X}|\boldsymbol{D}) = P(\boldsymbol{D}|\boldsymbol{X}), \tag{4.14}$$

where $P(\boldsymbol{D}|\boldsymbol{X})$ is the PDF to obtain the data $\boldsymbol{D}$ given the set of parameters $\boldsymbol{X}$. Note, that $L(\boldsymbol{X}|\boldsymbol{D})$ is not a PDF, as the reversal of the argument and the parameter of the

[6] The performance also depends on the radius where the event occurs. As only a qualitative picture is required here, this dependency is neglected.

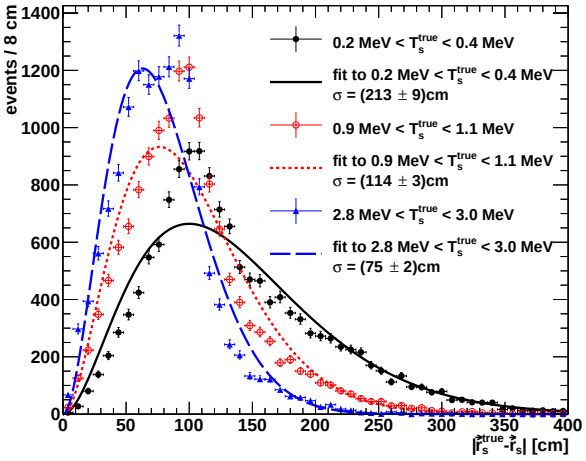

Figure 4.5: The distributions of the distances between the estimated position of the event $\boldsymbol{r}_s$ from the true event position $\boldsymbol{r}_s^{\text{true}}$ for three different energy bands (see legend). For each band, 14 000 events were simulated randomly distributed across the fiducial volume. Each obtained distribution was fitted assuming the deviations follow a Gaussian distribution with width σ along each coordinate (see equation (4.13)). The widths σ obtained from the fits are indicated in the legend.

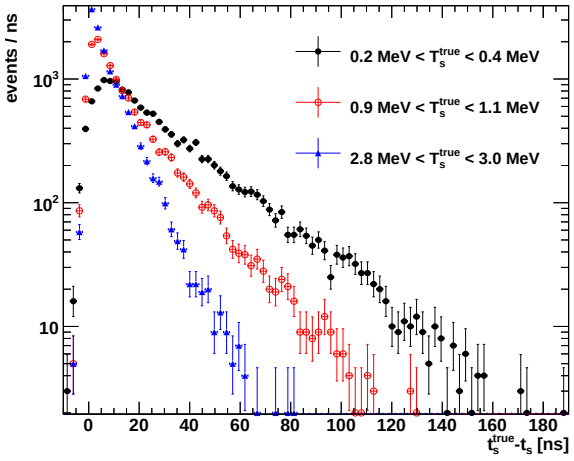

Figure 4.6: The distributions of the deviations of the estimated start time of the event t_s from the true start time of the event t_s^{true} for three different energy bands (see legend). For each band, 14 000 events were simulated randomly distributed across the fiducial volume.

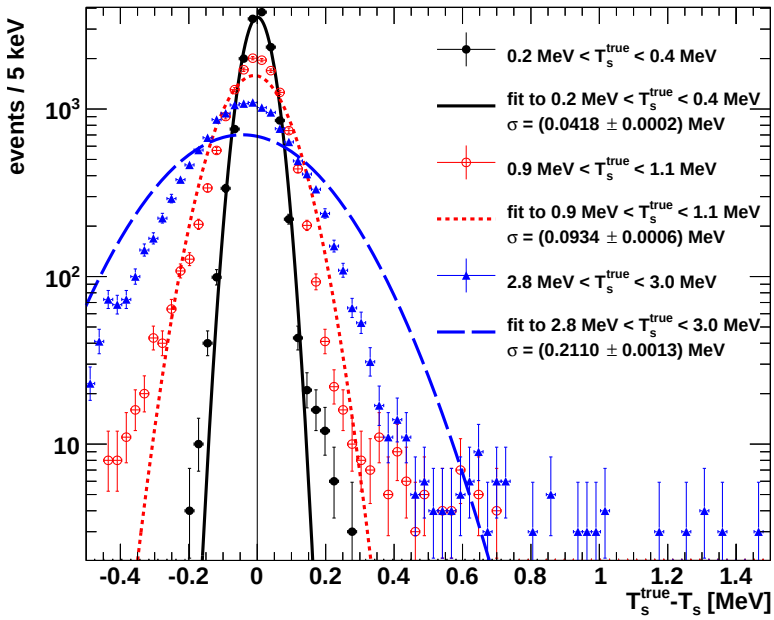

Figure 4.7: The distribution of the deviation of the estimated kinetic energy T_s from the true kinetic energy T_s^{true} of the simulated electrons for three different energy bands (see legend). For each band, 14 000 events were simulated randomly distributed across the fiducial volume. Each obtained distribution was fitted with a Gaussian. The resulting resolutions are indicated in the legend.

PDF requires using a prior and subsequent renormalization. Mathematically speaking, $\hat{\boldsymbol{X}}$ can be determined by finding the maximum of $L(\boldsymbol{X}|\boldsymbol{D})$, i.e. by solving:

$$\frac{\partial L}{\partial x_i} = 0 \quad \forall i, \tag{4.15}$$

where x_i is a component of $\boldsymbol{X}$. In the case presented here, these equations cannot be solved analytically. Thus, the maximum has to be found numerically. For greater numerical stability, typically $\hat{\boldsymbol{X}}$ is not determined by maximizing $L(\boldsymbol{X}|\boldsymbol{D})$ but by minimizing the negative logarithmic likelihood (NLL) function

$$\mathcal{L}(\boldsymbol{X}|\boldsymbol{D}) = -\ln\left[L(\boldsymbol{X}|\boldsymbol{D})\right] = -\ln\left[P(\boldsymbol{D}|\boldsymbol{X})\right]. \tag{4.16}$$

In this work, the minimization is done using the `MIGRAD` [107] algorithm which is implemented in the ROOT [108] data analysis framework.

The parameters of interest $\boldsymbol{X}$ in the reconstruction of a point like event in LENA have already been introduced in section 4.3. In the fit, however, not the kinetic energy of the electron is taken as free parameter but the number of photons at the vertex N_γ. This can subsequently be translated into a kinetic energy given the light emitting particle is known. Thus,

$$\boldsymbol{X} = \{\boldsymbol{r}_s, t_s, N_\gamma\}. \tag{4.17}$$

The data available from the LENA detector to reconstruct an event, depends on the assumptions for the used electronics. The reconstruction presented in this chapter is designed to allow for the two most extreme conditions:

- **Conservative electronics**: In a very conservative approach, an electronics scheme like in Borexino is used, which would allow to measure only the deposited charge q_i, i.e. the number of detected hits, on an OM. For OMs which feature at least one hit, also the time t_i^0 of the first hit is available.
- **Optimistic electronics**: In a more modern scheme, a flash ADC would be used to record the OM waveforms. Thus, some information about later hits can be gained. In the most optimistic scenario, timing information $\boldsymbol{t}_i$ on every detected hit would be available. As long as the visible energy is in the MeV range, this scenario is not unrealistic as the mean number hits per OM is low and thus the time differences between two detected hits are generally large which makes them easy to separate.

In any case, the informations to be used for the fit are the charge and the hit times of the OMs:

$$\boldsymbol{D} = \{\boldsymbol{q}, \boldsymbol{t}\}. \tag{4.18}$$

Thus, in order to do the fit, the PDF $P(\boldsymbol{q}, \boldsymbol{t}|\boldsymbol{X})$ has to be calculated, which is described in the following sections.

4.4.1 Basic structure of the probability density function

The PDF $P(\boldsymbol{q}, \boldsymbol{t}|\boldsymbol{X})$ is of very high dimension, but can be split into a product of PDFs of smaller dimension. First, this is done for the case of the optimistic electronics setup.

PDF for optimistic electronics:

Assuming, that all OMs in LENA are independent, the global PDF can be broken down into a product of individual PDFs for the individual OMs:

$$P(\boldsymbol{q}, \boldsymbol{t}|\boldsymbol{X}) = \prod_{i=1}^{N_{\mathrm{OM}}} P_i(q_i, \boldsymbol{t}_i|\boldsymbol{X}), \tag{4.19}$$

where $P_i(q_i, \boldsymbol{t}_i|\boldsymbol{X})$ denotes the PDF that the i$^{\mathrm{th}}$ OM registered q_i hits and hit times[7] $\boldsymbol{t}_i$. This assumption should generally hold very well as the different OMs are correlated only via electronic crosstalk which should be negligible in LENA. Additionally assuming that all OMs are equal, instead of one PDF per OM as used in equation (4.19), one general PDF can be used which additionally depends on the position $\boldsymbol{r}_i$ and the direction of the respective OM. The direction of the OM is characterized by its unit normal vector $\hat{\boldsymbol{n}}_i$ ($|\hat{\boldsymbol{n}}_i| = 1$). It is required to point away from the detector center to resolve the ambiguity in the direction of $\hat{\boldsymbol{n}}_i$. Thus,

$$P(\boldsymbol{q}, \boldsymbol{t}|\boldsymbol{X}) = \prod_{i=1}^{N_{\mathrm{OM}}} P(q_i, \boldsymbol{t}_i|\boldsymbol{X}, \boldsymbol{r}_i, \hat{\boldsymbol{n}}_i). \tag{4.20}$$

Note that the second assumption will generally not be fulfilled exactly in reality as each PMT typically has slightly different properties. Such, when applying this decomposition to a real world detector, it might become necessary to add additional parameters characterizing the PMT to the PDF, such as the quantum efficiency. Additionally, note that as all OMs are mounted on the cylinder walls, $\hat{\boldsymbol{n}}_i$ is unambiguously determined by the position of the OM, i.e. $\hat{\boldsymbol{n}}_i(\boldsymbol{r}_i)$. Thus, in the following, $\hat{\boldsymbol{n}}_i$ will not be mentioned explicitly as parameter of a function which already depends on $\boldsymbol{r}_i$.
As OMs with no registered hits do not depend on the hit time, their PDF simply becomes the probability for no hits, i.e. $P_q(q_i = 0|\boldsymbol{X}, \boldsymbol{r}_i)$. For all other OMs, follows

$$P(q_i \neq 0, \boldsymbol{t}_i|\boldsymbol{X}, \boldsymbol{r}_i) = P_q(q_i|\boldsymbol{X}, \boldsymbol{r}_i) \prod_{j=1}^{q_i} P_t(t_{i,j}|\boldsymbol{X}, \boldsymbol{r}_i), \tag{4.21}$$

where $P_q(q_i|\boldsymbol{X}, \boldsymbol{r}_i, \hat{\boldsymbol{n}}_i)$ is the probability to detect exactly q_i hits on the i$^{\mathrm{th}}$ OM and $P_t(t_{i,j}|\boldsymbol{X}, \boldsymbol{r}_i)$ is the PDF to get a hit on the i$^{\mathrm{th}}$ OM at time $t_{i,j}$ given the respective parameters. Thus, for the optimistic electronics, the final expression for the decomposed PDF is:

$$P(\boldsymbol{q}, \boldsymbol{t}|\boldsymbol{X}) = \prod_{i}^{q_i=0} P_q(q_i = 0|\boldsymbol{X}, \boldsymbol{r}_i) \prod_{i}^{q_i \neq 0} \left[P_q(q_i|\boldsymbol{X}, \boldsymbol{r}_i) \prod_{j=1}^{q_i} P_t(t_{i,j}|\boldsymbol{X}, \boldsymbol{r}_i) \right], \tag{4.22}$$

where the products run over all OMs without and with detected hits, respectively.

[7] The information about the number of detected hits is of course also available via the dimension of the vector $\boldsymbol{t}_i$. For clarity reasons it is nevertheless advantageous to separate q_i from this information.

PDF for conservative electronics:

For the conservative electronics set-up, a similar reasoning can be done. The only difference is that the PDF of the arrival time of the first hit on an OM depends on the collected charge on the OM. Nevertheless, a similar decomposition as in equation (4.21) can be done using the definition of conditional probability [109]. Thus

$$P(q_i \neq 0, \boldsymbol{t}_i | \boldsymbol{X}, \boldsymbol{r}_i) = P_q(q_i | \boldsymbol{X}, \boldsymbol{r}_i) \cdot P_t^0(t_i^0 | \boldsymbol{X}, \boldsymbol{r}_i, q_i). \tag{4.23}$$

This finally yields

$$P(\boldsymbol{q}, \boldsymbol{t} | \boldsymbol{X}) = \prod_i^{q_i=0} P_q(q_i = 0 | \boldsymbol{X}, \boldsymbol{r}_i) \prod_i^{q_i \neq 0} \left[P_q(q_i | \boldsymbol{X}, \boldsymbol{r}_i) \cdot P_t^0(t_i^0 | \boldsymbol{X}, \boldsymbol{r}_i, q_i) \right]. \tag{4.24}$$

Thus, the whole PDF can be calculated from three different sub-PDFs. P_q will be calculated in section 4.4.2, P_t will be developed in section 4.4.3 and P_t^0 will be deduced in section 4.4.4.

4.4.2 The charge probability density function

The PDF for an OM at position[8] $\boldsymbol{r}$ to feature q hits is given by the Poisson distribution:

$$P(q | \boldsymbol{X}, \boldsymbol{r}) = \frac{\mu^q}{q!} \exp(-\mu), \tag{4.25}$$

where $\mu = \mu(\boldsymbol{X}, \boldsymbol{r})$ is the expected charge on the OM. It can be split into three parts

$$\mu = \mu_{\text{direct}} + \mu_{\text{scat}} + \mu_{DN}, \tag{4.26}$$

where μ_{direct} is the expected number of hits due to photons which have not been scattered between their vertex and the detection, μ_{scat} is the expected number of hits due to photons which have scattered at least once and μ_{DN} is the expected number of hits due to dark noise on the OM. In the following, the three contributions to the total charge μ_{direct}, μ_{scat} and μ_{DN} will be calculated.

The expected charge due to direct hits μ_{direct}:

μ_{direct} can be analytically calculated:

$$\mu_{\text{direct}} = N_\gamma \frac{\Omega_{LC}(\boldsymbol{X}, \boldsymbol{r})}{4\pi} \exp\left[-\frac{|\boldsymbol{r}_s - \boldsymbol{r}|}{\Lambda_{\text{att}}} \right], \tag{4.27}$$

where Λ_{att} is the attenuation length (see chapter 7) and $\Omega_{\text{LC}}(\boldsymbol{X}, \boldsymbol{r})$ is the solid angle of the OM including the effects of the light concentrator. It is given by:

$$\Omega_{LC}(\boldsymbol{X}, \boldsymbol{r}) = \int_{\text{OM entrance surface}} \frac{d\boldsymbol{A} \cdot (\boldsymbol{r}_s - \boldsymbol{r}_\Omega)}{|\boldsymbol{r}_s - \boldsymbol{r}|^2} P_{\text{LC}} \left[\frac{\boldsymbol{A} \cdot (\boldsymbol{r}_s - \boldsymbol{r}_\Omega)}{|\boldsymbol{A}||\boldsymbol{r}_s - \boldsymbol{r}_\Omega|} \right], \tag{4.28}$$

[8] As this section and the following sections deal with the PDF for one OM only, the indices for the OM number are dropped for simplicity.

where $\boldsymbol{r}_\Omega$ is the position on the OM entrance surface where the integration is currently processing and $P_{\mathrm{LC}}(\cos(\alpha))$ is the detection efficiency of the LCs (see figure 4.1). Note that $d\boldsymbol{A}$ is defined to always point away from the detector center. As this integration is computationally too demanding to calculate Ω on the fly during fitting, it is tabulated beforehand and read from the table during fitting. Due to the rotational symmetry of the OM, Ω actually only depends on the distance $d = |\boldsymbol{r}_s - \boldsymbol{r}|$ between the OM and the event as well as on the angle α between $\hat{\boldsymbol{n}}$ and $\boldsymbol{r}_s - \boldsymbol{r}$. This reduces the table to two dimensions. Values between the data points saved in the table are estimated from the neighboring points by a two dimensional linear interpolation. If d is much larger than the diameter of the OM, equation (4.28) can be approximated by

$$\Omega_{LC}(\boldsymbol{X}, \boldsymbol{r}) \approx \frac{A_{\mathrm{OM}}}{d^2} \frac{\hat{\boldsymbol{n}} \cdot (\boldsymbol{r}_s - \boldsymbol{r})}{d} P_{\mathrm{LC}} \left(\frac{\hat{\boldsymbol{n}} \cdot (\boldsymbol{r}_s - \boldsymbol{r})}{d} \right), \tag{4.29}$$

where A_{OM} is the active area of the OM. Figure 4.8 shows the relative deviation between the true and the approximated solid angle as a function of d for various angles α. The approximate calculation shows significant errors for $d \lesssim 1\,\mathrm{m}$. Note that for α being close to the critical angle of the light concentrator (blue-dashed curve in figure 4.8), the approximate solution converges to the correct solution much more slowly. This is due to the fact that, seen from the event vertex, a part of the OM is below the critical and a part of the OM is above the critical angle. This drastically changes the effective area of the OM. As the point fit has to work reliably for the whole detector to do a proper fiducial volume cut, this is not acceptable. Thus, the approximate solution is not used[9].

The expected charge due to scattered hits μ_{scat}:

The expected amount of scattered light μ_{scat} cannot be calculated analytically. For reasons of numerical stability, it is advantageous not to determine μ_{scat} directly but to extract the main dependencies and deal with them analytically, i.e

$$\begin{aligned} \mu_{\mathrm{scat}} &= R(\boldsymbol{r}_s, \boldsymbol{r}) \mu_{\mathrm{direct}}^{\text{no LC}} \\ &= N_\gamma \frac{\Omega(\boldsymbol{X}, \boldsymbol{r})}{4\pi} \exp\left[-\frac{|\boldsymbol{r}_s - \boldsymbol{r}|}{\Lambda_{att}} \right] R(\boldsymbol{r}_s, \boldsymbol{r}), \end{aligned} \tag{4.30}$$

where $\mu_{\mathrm{direct}}^{\text{no LC}}$ is the expected direct charge on an OM *without* LC which has the same diameter as the LC aperture, $\Omega(\boldsymbol{X}, \boldsymbol{r})$ is the solid angle of the OM *without* the effects of the LCs and $R(\boldsymbol{r}_s, \boldsymbol{r})$ is a factor which accounts for the effect of scattering. Thus, R is defined as

$$R = \frac{\text{Expected number of scattered photons detected including LC effects}}{\text{Expected number of direct photons detected without LC effects}}. \tag{4.31}$$

Note that the expected number of photons expected on an OM without LC is used as reference instead of μ_{direct} as the latter tends to zero for photons with incident angles above

[9] In previous works [99], the detector featured an additional buffer volume which ensured that the events did not come too close to the OM. Furthermore, no LCs were taken into account in these studies which reduces the deviation between the correct and the approximate distribution. Thus, the approximate calculation was close enough to the correct one to be used.

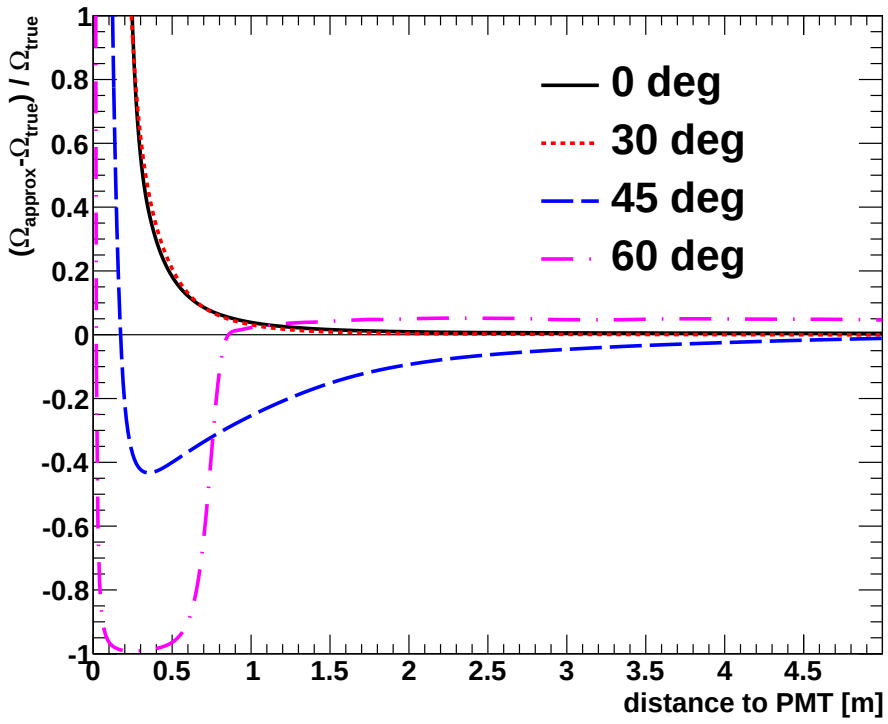

Figure 4.8: The relative deviation between the approximate solid-angle calculation (see equation (4.29)) and the exact calculation (see equation (4.28)) as a function of the distance between the OM and the event for various angles between the normal vector of the OM and the connection between the center of the OM and the event (color online).

the critical angle of the LC. Furthermore, $\mu_{\text{direct}}^{\text{no LC}}$ is simpler and faster to calculate. An analytical calculation of R is not possible as the integrals involved in (multiple) scattering cannot be solved. A numerical evaluation is also not possible due to the high dimension of the integrals. Thus, R has to be estimated using the LENA MC simulation and the results have to be tabulated. To reduce the number of required events in the simulation and to reduce the table size, the dimensionality of R has to be decreased. This can be done exploiting the symmetries of the detector:
Natively, $R(\boldsymbol{r}_s, \boldsymbol{r})$ is of dimension six. As only events which are not influenced by the lid and the bottom of the detector ($|z| < 25\,\text{m}$) are used, the OMs on the lid and bottom can be neglected and the cylinder can be extended to infinity. Thus, by using the rotational symmetry of the detector and the translational symmetry in z arising due to the neglection of the end caps, a coordinate system s'[10] can be found with $\boldsymbol{r} \to \boldsymbol{r}' = (\rho_{\text{OM}}, 0, 0)$, where ρ_{OM} is the mounting radius of the OM[11]. Due to the exploited symmetries, R is invariant under the transformation: $R'(\boldsymbol{r}'_s, \boldsymbol{r}') = R(\boldsymbol{r}'_s, \boldsymbol{r}')$. As $\boldsymbol{r}'$ is fully defined, this means that only three of the six original dimensions of R are remaining: $R(\boldsymbol{r}_s, \boldsymbol{r}) = R(\boldsymbol{r}'_s)$. This parameter space to be covered by the simulation and the table mentioned above can be further reduced by using the mirror symmetry of the detector with respect to the x-z-plane and the x-y-plane. Thus, $R(\boldsymbol{r}'_s) = R(x'_s, |y'_s|, |z'_s|)$. This reduced parameter space is used to determine R using a MC simulation and to tabulate the results. Note that if the

[10] The origin of s' has the coordinates $(0, 0, z_s)$ in the LENA system.
[11] As the lid and the bottom are negligible, ρ_{OM} is a constant

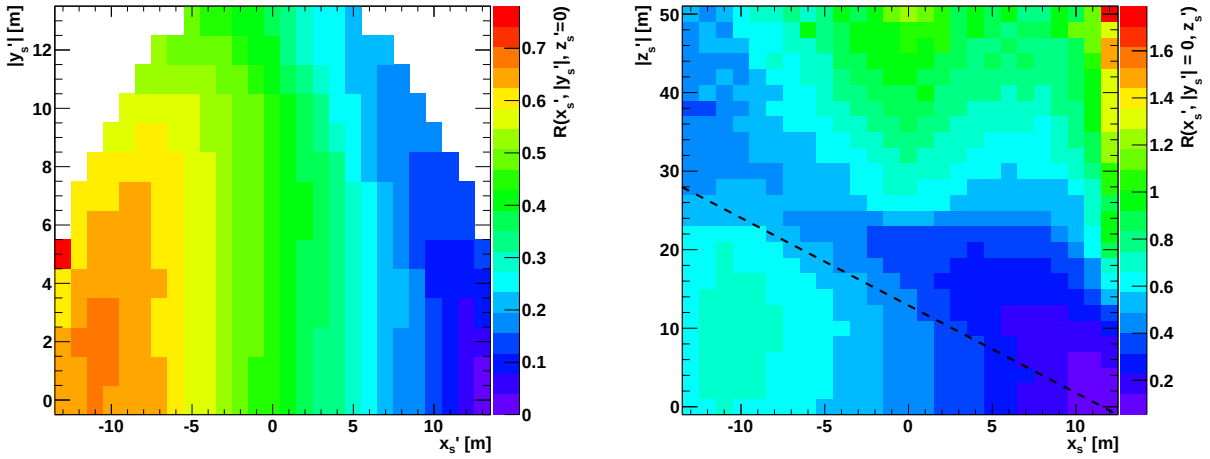

Figure 4.9: The ratio between the expected number of scattered photons detected in an OM and the expected number of direct photons detected in an OM with the same aperture but no LC as a function of x'_s and $|y'_s|$ for $|z'_s| = 0$ (left) and as a function of x'_s and $|z'_s|$ for $|y'_s| = 0$ (right). The coordinates with the primes indicate a coordinate system where the relevant OM is at the position $(\rho_{\mathrm{OM}}, 0, 0)$, where $\rho_{\mathrm{OM}} = 14\,\mathrm{m}$ is the mounting radius of the OM. The dashed line in the right plot indicates the opening angle of the LC acceptance.

full detector is used for the simulation, i.e. the end caps can no longer be neglected, the dimensionality reduction using systematics can still be done but the required dimension of the tables increases to four (see appendix B).
Figure 4.9 shows R for two slices through the detector: For the slice with $|z'_s| = 0$ (left) and for the slice with $|y'_s| = 0$ (right). As expected, the slice with $|z'_s| = 0$ shows that R increases with rising distance between the relevant OM (at $(\rho_{\mathrm{OM}}, 0, 0)$) as the probability for a photon to be scattered rises. The slice through the x'_s-$|z'_s|$-plane shows a more complicated behavior: For events in the field of view of the LC, R still rises with the distance from the OM. For events at the boundary of the LCs' field of view, scattered light is actually suppressed since small angle forward scattering, as favored by Rayleigh scattering, is no longer possible due to the suppression of the LC around its critical angle. Thus, scatterings with larger scattering angles are required for a photon to be detected on the OM. This means that the light path through the scintillator is much longer than for direct light which leads to a suppression due to absorption of the light. Finally, for events far outside the field of view of the LC, R rises again, as the solid angle for a direct detection gets very small while scattered light can use an indirect way and thus can exploit a higher solid angle.
Note that in figure 4.9, $0 < R \lesssim 1.7$. This shows that the amount of scattered light is in the same order of magnitude than the direct light over the whole detector. Hence, it cannot be neglected. Furthermore, this illustrates why instead of directly tabulating μ_{scat} the decision was made to tabulate R and deal with the primary dependencies analytically: R is varying much more slowly compared to μ_{scat}. This reduces the errors introduced due to the finite statistics of the MC, the binning of the table and the required interpolation.

The expected charge due to dark noise μ_{DN}:
The expected number of hits on the OM due to DN can be calculated to be

$$\mu_{DN} = f_{DN} \Delta t_{\mathrm{event}}\,, \tag{4.32}$$

where f_{DN} is the dark noise frequency of the PMT and Δt_{event} is the duration of the event. Note, that in a real detector, f_{DN} would typically vary from PMT to PMT and thus has to be measured in-situ using scalers and the resulting values have to be considered via a table for each PMT individually.

4.4.3 The timing probability density function

A photon which is emitted at the event time t_s from the event vertex $\boldsymbol{r}_s$ and which directly hits the OM at its center without being scattered would arrive at the OM at the time

$$t_{\text{exp}} = t_s + \frac{n}{c}|\boldsymbol{r}_s - \boldsymbol{r}|. \tag{4.33}$$

However, the real arrival time is influenced by various physical effects which have to be taken into account:

1. The decay-time distribution of the scintillator $P_{\text{LSc}}(t)$ (confer equation (3.1))
2. The transit-time spread (TTS) of the PMT $P_{\text{TTS}}(t)$ (confer section 4.2)
3. The finite size of the OMs
4. The scattering in the scintillator
5. The dark noise of the PMT

Considering these effects, the hit-time distribution is spread out around this expected value, thus

$$P_t(t|\boldsymbol{X}, \boldsymbol{r}) = \tilde{P}_t(\Delta t_h|\boldsymbol{r}_s, \boldsymbol{r}) \quad \text{with} \quad \Delta t_h = t - t_{\text{exp}}. \tag{4.34}$$

Note that $\tilde{P}_t$ does not depend on N_γ as it is the PDF for an arbitrary photon which is thus not influenced by other photons. In the remainder of this section, $\tilde{P}_t$ will be constructed step by step including the effects listed above in their given order.
Taking only the first two points into account, i.e. the transit time spread and the LSc decay time, the PDF is given by a convolution of both effects:

$$P_{12}(\Delta t_h) = P_{\text{LSc}}(t) \otimes P_{\text{TTS}}(t) = \int_{-\infty}^{\infty} P_{\text{LSc}}(\tau) \cdot P_{\text{TTS}}(\Delta t_h - \tau) d\tau \tag{4.35}$$

Note that P_{12} is independent of $\boldsymbol{r}_s$ and $\boldsymbol{r}$. In figure 4.10, P_{12} is shown as a function of Δt_h for the two different TTS distributions discussed in section 4.2. Note that the convolution with the scintillator decay significantly reduces the impact of the TTS on the final pulse shape.

Given, that the connection vector $\boldsymbol{d}$ between $\boldsymbol{r}_s$ and $\boldsymbol{r}$ is generally not parallel to the normal vector of the OM, the **finite size of the OM** (item 3 of the enumeration above) leads to a smearing of $\tilde{P}_t(\Delta t_h|\boldsymbol{r}_s, \boldsymbol{r}, \hat{\boldsymbol{n}})$ due to the induced difference in the path the photon travels dependent on the point where it hits the OM. The maximum effect is achieved when the incident photon arrives nearly parallel to the LC surface. In this case the maximum difference in expected arrival time $\Delta t^{\text{max}}_{\text{finite}}$ is

$$\Delta t^{\text{max}}_{\text{finite}} = \frac{n}{c} d_{\text{OM}} \sim 1\,\text{ns}, \tag{4.36}$$

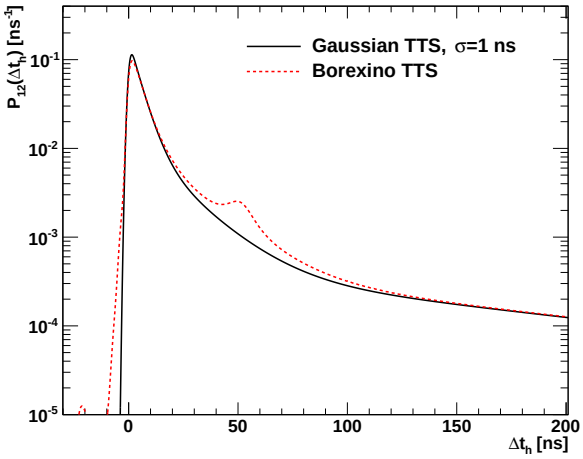

Figure 4.10: The time PDF as a function of the TOF-corrected hit time for different TTS distributions. The black curve shows the PDF resulting from the assumption of a Gaussian shaped TTS with $\sigma = 1\,\text{ns}$, where σ is the standard deviation of the Gaussian TTS, while the red, dotted curve shows the PDF resulting from the Borexino TTS (taken from [105]).

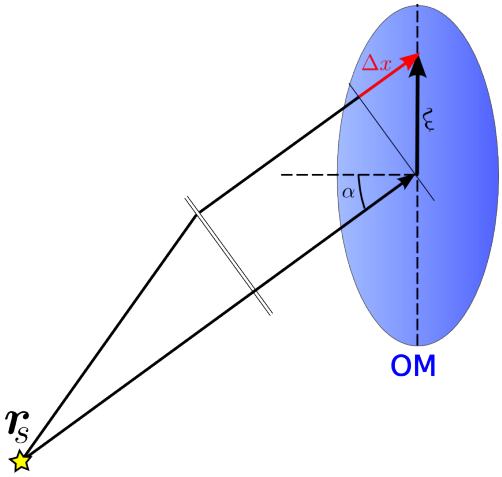

Figure 4.11: An illustration of the effect of the arrival-time smearing due to the finite size of the OM for a photon arriving in the plane perpendicular to the OM and including $\boldsymbol{r}_s$ and the center of the OM: If the connection vector between $\boldsymbol{r}_s$ and the center of the OM is not orthogonal to the OM surface, the expected arrival time of a photon depends on the position at which the photon hits the OM. Also illustrated is the far-field approximation done to calculate the influence of this effect.

where d_{OM} is the diameter of the OM aperture. Thus, $\Delta t^{\text{max}}_{\text{finite}}$ is of the same order of magnitude as the OM TTS. However, as LCs suppress light from high angles, the effect is typically much smaller. It can be treated using the far-field approximation, which is sketched in figure 4.11. It assumes that distance between the OM and $\boldsymbol{r}_s$ is sufficiently high that the momentum direction of all arriving photons can be considered to be parallel independent of their arrival position on the OM's surface. In the special case shown in figure 4.11, the detected photon is in the plane I given by $\boldsymbol{d} = \boldsymbol{r} - \boldsymbol{r}_s$ and $\hat{\boldsymbol{n}}$ and which includes the center of the OM. In this case

$$\Delta t^{I}_{\text{finite}}(\xi) = \frac{n}{c}\Delta x(\xi) = \frac{n}{c}\xi\sin(\alpha) = \frac{n}{c}\xi\sqrt{1 - \left(\frac{\hat{\boldsymbol{n}}\cdot(\boldsymbol{r}_s - \boldsymbol{r})}{|\boldsymbol{r}_s - \boldsymbol{r}|}\right)^2}, \tag{4.37}$$

where α is the angle between $\boldsymbol{d}$ and $\hat{\boldsymbol{n}}$ and ξ is the distance of the point of photon arrival and the center of the OM (see figure 4.11). To calculate the effect for a general photon arrival point $\boldsymbol{r}'$ on the OM surface, the arrival point has to be projected into the plane I. Thus,

$$\Delta t_{\text{finite}}(\boldsymbol{r}') = \Delta t^{I}_{\text{finite}}\cos(\varphi_{\text{OM}}) = \frac{n}{c}\xi\cos(\varphi_{\text{OM}})\sqrt{1 - \left(\frac{\hat{\boldsymbol{n}}\cdot(\boldsymbol{r}_s - \boldsymbol{r})}{|\boldsymbol{r}_s - \boldsymbol{r}|}\right)^2}. \tag{4.38}$$

Here a coordinate system on the OM surface is used, where the vertex is given by the OM center and the x-axis is in the plane I. The coordinates $(\xi, \varphi_{\text{OM}})$ describe a point on the active area of the OM using polar coordinates. A mathematically stricter derivation

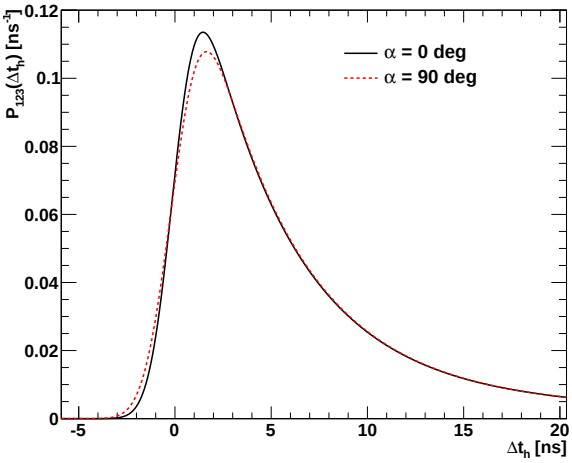

Figure 4.12: The time PDF as a function of the TOF-corrected hit time for different incident angles and a Gaussian TTS. The black curve corresponds to a photon-arrival direction perpendicular to the photocathode while the red, dotted curve corresponds to an arrival direction parallel to the photocathode.

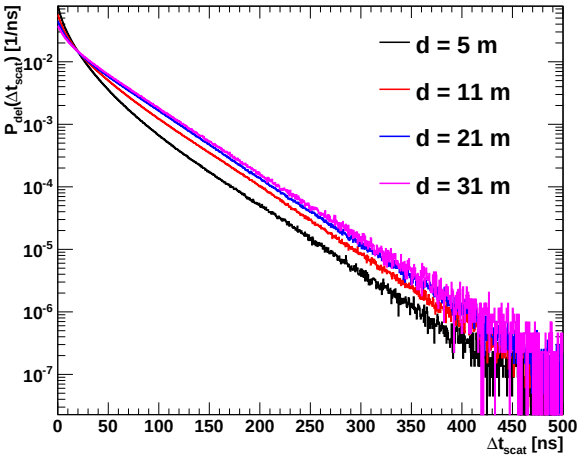

Figure 4.13: The PDF to obtain a time loss Δt_{scat} due to scattering as a function of Δt_{scat} for various distances d between the OM and the vertex.

of equation (4.38) can be found in [99].
To include this effect into the PDF, P_{12} has to be averaged over the active surface ∂OM of the OM:

$$P_{123}(\Delta t_h|\alpha) = \frac{1}{A_{\text{OM}}} \int_{\partial \text{OM}} dA \; P_{12}\left(\Delta t_h + \Delta t_{\text{finite}}(\boldsymbol{r'})\right). \tag{4.39}$$

Note that $P_{123}(\Delta t_h|\alpha)$ can be described by the parameter α alone due to the rotational symmetry of the OM and due to the used far-field approximation. Figure 4.12 shows the resulting PDFs for the extreme cases of $\alpha = 0$ and $\alpha = 90$ degrees as a function of Δt_h. As expected, the difference is small and mainly visible on the rising flank and the peak of the PDF.

In a next step, the **scattering in the scintillator** has to be taken into account (item 4 of the enumeration above). A scattered photon arriving at an OM has a longer TOF than a direct photon. Additionally, if the scattered photon undergoes an absorption-reemission process, an additional delay due to the time time required to re-emit the photon appears. This smears the PDF towards longer times. As not all photons are scattered, the total PDF is a weighted superposition of the direct photon PDF $P_{123}(\Delta t_h|\alpha)$ and the PDF of the scattered photons $P_{\text{scat}}(\Delta t_h|\boldsymbol{r}_s, \boldsymbol{r})$:

$$P_{1234}(\Delta t_h|\boldsymbol{r}_s, \boldsymbol{r}) = \frac{1}{\mu_{\text{direct}} + \mu_{\text{scat}}} \left[\mu_{\text{direct}} P_{123}(\Delta t_h|\alpha) + \mu_{\text{scat}} P_{\text{scat}}(\Delta t_h|\boldsymbol{r}_s, \boldsymbol{r})\right]. \tag{4.40}$$

Using equations (4.27), (4.30) and the approximation for the solid angle (4.29) this evaluates to

$$P_{1234}(\Delta t_h|\boldsymbol{r}_s, \boldsymbol{r}) \approxeq \frac{P_{\text{LC}}\left(\frac{\hat{\boldsymbol{n}}\cdot(\boldsymbol{r}_s - \boldsymbol{r})}{d}\right) P_{123}(\Delta t_h|\alpha) + R(\boldsymbol{r}_s, \boldsymbol{r}) P_{\text{scat}}(\Delta t_h|\boldsymbol{r}_s, \boldsymbol{r})}{P_{\text{LC}}\left(\frac{\hat{\boldsymbol{n}}\cdot(\boldsymbol{r}_s - \boldsymbol{r})}{d}\right) + R(\boldsymbol{r}_s, \boldsymbol{r})}. \tag{4.41}$$

$P_{\text{scat}}(\Delta t_h|\boldsymbol{r}_s,\boldsymbol{r})$ is given by the convolution of $P_{123}(\Delta t_h|\alpha)$ with the PDF for the time loss Δt_{scat} of the photon due to scattering $P_{\text{del}}(\Delta t_{\text{scat}}|\boldsymbol{r},\boldsymbol{r}_s)$:

$$\begin{aligned} P_{\text{scat}}(\Delta t_h|\boldsymbol{r}_s,\boldsymbol{r}) &= P_{123}(\Delta t'_h|\alpha) \otimes P_{\text{del}}(\Delta t_{\text{scat}}|\boldsymbol{r},\boldsymbol{r}_s) \\ &= \int_{-\infty}^{\infty} d\tau\ P_{123}(\tau|\alpha) P_{\text{del}}(\tau - \Delta t_h|\boldsymbol{r},\boldsymbol{r}_s). \end{aligned} \tag{4.42}$$

$P_{\text{del}}(\Delta t_{\text{scat}}|\boldsymbol{r},\boldsymbol{r}_s)$ finally cannot be calculated analytically anymore but has to be determined by the simulation. To reduce the required simulation data, the approximation that P_{scat} only depends on the distance d between $\boldsymbol{r}_s$ and $\boldsymbol{r}$ is used:

$$P_{\text{del}}(\Delta t_{\text{scat}}|\boldsymbol{r},\boldsymbol{r}_s) \approx P_{\text{del}}(\Delta t_{\text{scat}}|d). \tag{4.43}$$

Note, that this approximation is done as the neither the memory nor the computation time to produce a full table of $P_{\text{del}}(\Delta t_{\text{scat}}|\boldsymbol{r},\boldsymbol{r}_s)$ is available. While it is generally a reasonable assumption for photons from the field of view of the OM, it is generally not valid for photons traveling close to a detector wall.
Examples for the obtained $P_{\text{del}}(\Delta t_{\text{scat}}|d)$ for various distances are shown in figure 4.13. Note that the distributions get shifted to higher Δt_{scat} with increasing d as for high d even a small angular deviation from the straight track has a large influence. Additionally, note that for $\Delta t_{\text{scat}} \gtrsim 200\,\text{ns}$ the PDFs can be well described by an exponential function. This feature is used to extrapolate the PDF obtained from simulations to larger[12] Δt_{scat}: The result of a fit with an exponential decay to the obtained distributions in the range $200\,\text{ns} < \Delta t_{\text{scat}} < 1200\,\text{ns}$ is used instead of the obtained distribution for $\Delta t_{\text{scat}} > 200\,\text{ns}$. As the calculations required to obtain P_{1234} are very time consuming, it is precomputed and stored in a table for later readout using the same reduced parameter space already discussed in section 4.4.2 for the tabulation of $R(\boldsymbol{r_s},\boldsymbol{r})$.

Finally the **DN of the PMTs** has to be taken into account. As the PDF for hits due to DN is flat, the final PDF reads:

$$\tilde{P}_t(\Delta t_h|\boldsymbol{r_s},\boldsymbol{r}) = \frac{1}{\mu}\left[(\mu_{\text{direct}} + \mu_{\text{scat}})\, P_{1234}(\Delta t_h|\boldsymbol{r}_s,\boldsymbol{r}) + \mu_{\text{DN}} \frac{1}{\Delta t_{\text{event}}}\right]. \tag{4.44}$$

To crosscheck the obtained PDF, 30 000 electrons with a kinetic energy of 1 MeV were simulated in the center of the detector with $t_s = 0$. The obtained data was successively processed (compare section 4.2) with an assumed DN rate of 0. Figure 4.14 shows the resulting hit-time distribution on the PMT ring with $z = 10\,\text{m}$ compared to the calculated PDF. The calculated PDF was scaled to match the height of the hit-time distribution but no further free parameters were allowed. As can be seen, the PDF matches the distribution from the simulation well and thus can be used to fit the events.

4.4.4 The timing probability density function for first hits

The timing PDF for first hits, $P_t^0(t^0|\boldsymbol{X},\boldsymbol{r},q)$, can be constructed from the PDF for an arbitrary hit $P_t(t|\boldsymbol{X},\boldsymbol{r})$ which was derived in the last section. The PDF for a first hit at

[12] While photons arriving more than 200 ns after the direct light generally carry only very little information about the event, it is necessary to properly take them into account to keep the PDF normalized.

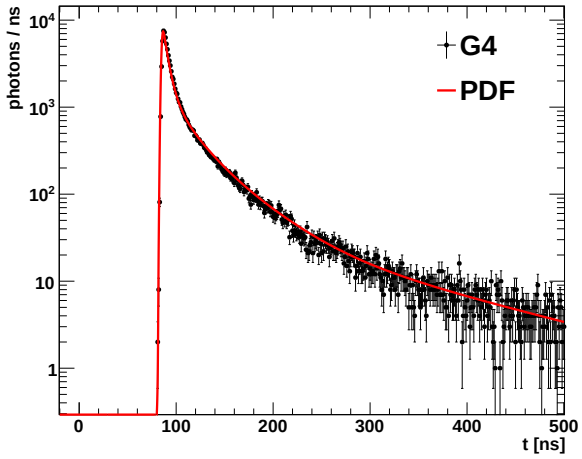

Figure 4.14: Comparison between the PDF without DN for a point like event in the center of the detector as a function of the time (red line) with the result of a MC simulation (black dots). The simulated data was obtained from 30 000 1 MeV electrons as seen from the PMT ring with $z = 10\,\mathrm{m}$. Note that the PDF was scaled to match the distribution but there are no free fit parameters.

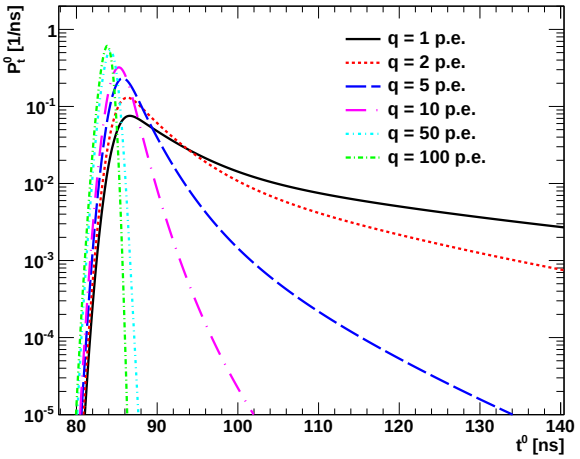

Figure 4.15: The PDF P_t^0 for the first hit time on an OM as a function of the time of the first hit t^0 for various charges q collected on the OM. The shown calculations assume the vertex to be in the center of the detector. No DN was considered in the calculation of the PDFs.

the time t^0 is proportional to the PDF for an arbitrary hit at t^0 times the probability that none of the other $q-1$ hits occurred before t^0:

$$P_t^0(t^0|\boldsymbol{X},\boldsymbol{r},q) = P_t(t^0|\boldsymbol{X},\boldsymbol{r})\left[1-\int_{-\infty}^{t^0} d\tau\; P_t(\tau|\boldsymbol{X},\boldsymbol{r})\right]^{(q-1)}\cdot q. \tag{4.45}$$

The combinatorial factor q is due to the fact, that each of the hits at the OM could possibly be the first hit.
Again, the integral in equation (4.45) cannot be calculated analytically and the numerical calculation is too time consuming to do it on the fly. Thus, not only P_{1234} but also $\int_{-\infty}^{t} d\tau P_{1234}$ is precomputed and tabulated to speed up the reconstruction procedure.

Figure 4.15 shows the resulting P_t^0 as a function of the time of the first hit t^0 for different total charges collected on the PMT. With increasing q, P_t^0 gets narrower, as the probability that the first photon is a late photon decreases with the number of available photons. Note that for high q values, the shape of the PDF is nearly independent of q again: The obtained shapes for 50 and for 100 p.e. are very similar. While such high values for q are not relevant for the low-energy regime, this observation will become important for the reconstruction of ∼GeV neutrino interactions (see chapter 6).

4.4.5 Fitting close to the outer edge of the detector

Figure 4.16 shows the total charge q_{tot} as a function of x and z with $y = 0$ as determined from the MC simulation for a part of the region close to the edge of the active volume.

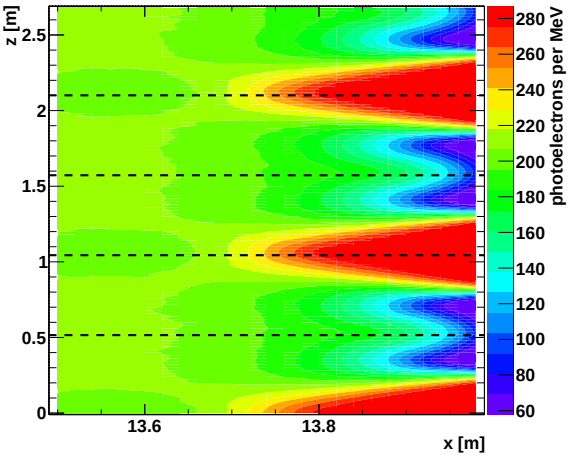

Figure 4.16: The expected total charge for 1 MeV electrons as a function of x and z for $y = 0$ for the region close to the detector wall. The black dashed lines show the positions of the LCs. Their effect is clearly visible. The data was obtained by simulating 1 MeV electrons on a grid with 2 cm spacing and recording the total collected charge. For each point 1000 electron events have been simulated.

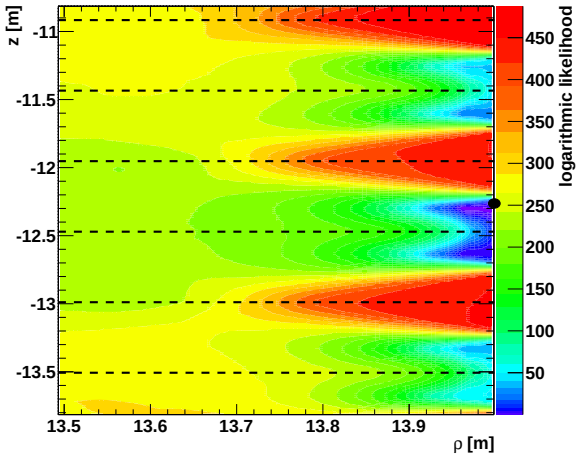

Figure 4.17: The NLL as a function of ρ and z for a simulated event featuring an electron with $T_s = 1.8$ MeV kinetic energy at the position $(10.1, 9.7, -12.3)$ m corresponding to a radius of nearly 14 m. The shown plane includes the true position of the simulated event (shown by a black dot). t_s and N_γ were kept at their true values. Apart from the true minimum at $z = -12.3$ m multiple additional local minima due to the discrete positions of the LCs (shown by the black dashed lines) are visible. Note that the minimum corresponding to the true position is the deepest.

This area of the detector was found to be relatively inhomogeneous, not only in light yield but also in the scattering properties. Due to the regular arrangements of the PMTs, a regular pattern caused by the effects of the LCs can be observed. A part of this regular pattern[13] is also transferred to the NLL function which thus can acquire additional, local minima for events close to the boundary of the fiducial volume. This is shown in figure 4.17 for a sample event with a true radius of nearly 14 m. As the start parameters are not precise enough to discriminate the event position between different rows of PMTs, this can lead to the numerical minimization ending in a local, wrong minimum.
It turned out that all fits which resulted in a reconstructed radius of $\rho > 12.5$ m where possibly prone to this problem. Thus their resulting parameters are tagged as preliminary $\boldsymbol{X}_{\text{prelim}}$. Successively, three additional fits were started, one featuring $\boldsymbol{X}_{\text{prelim}}$ as start parameters and the other two using the same start parameters but with $z_s = z_{s,\text{prelim}} \pm \Delta z_{\text{ring}}$ where Δz_{ring} is the z distance between two adjacent PMT rings. The final result was determined by the fit resulting in the smallest NLL value[14].

[13] Two successive rows of OMs show a different behaviour as the OMs on the walls are arranged on an hexagonal gid. Thus all even as well as all odd OMs rows show the same behaviour.
[14] Fits which did not converge were not taken into account.

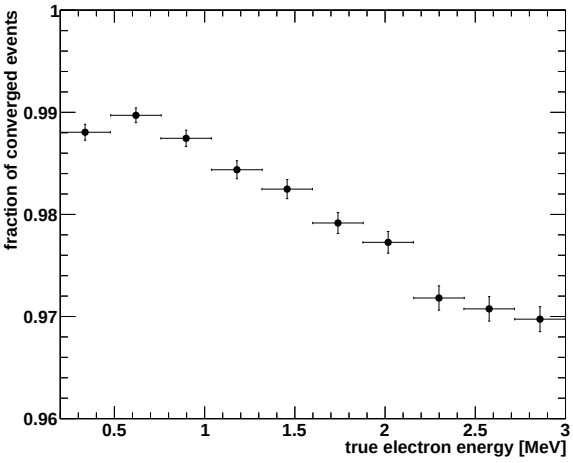

Figure 4.18: The fraction of converged events as a function of the true kinetic energy of the electron. While the vertical error bars show the statistical variations the horizontal error bars show the width of the used bins.

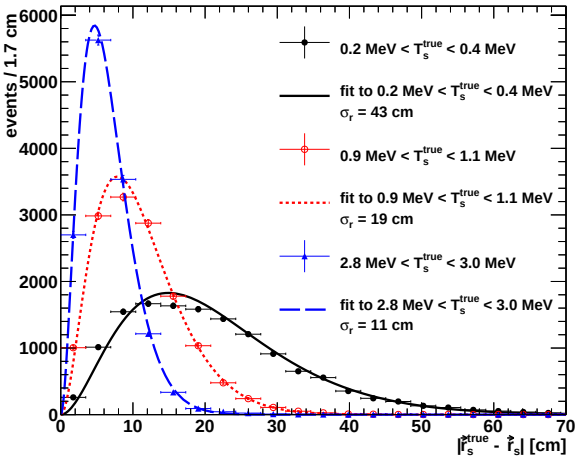

Figure 4.19: The distribution of the distance between true and reconstructed vertex for three different energy bins. The lines indicate a fit $\propto |\boldsymbol{r}_s^{\text{true}} - \boldsymbol{r}_s|^2 \exp(-|\boldsymbol{r}_s^{\text{true}} - \boldsymbol{r}_s|^2/(2\sigma_r^2))$. The resulting resolutions are shown in the legend. Note that no errors are quoted as the statistical errors are negligible compared to the error due to the assumption of one common resolution for all coordinates.

4.5 Performance

Applying the reconstruction algorithm to simulated events, the performance can be determined by comparing the obtained parameters with the MC truth information.

For the results shown in the following sections, electron events were simulated randomly distributed in the fiducial volume using the simulation presented in section 4.1. Their initial energies were randomly distributed from the projected detector threshold of 200 keV up to 3 MeV. By default, the "optimistic electronics" (confer section 4.4) were used assuming a Gaussian TTS with $\sigma_{tts} = 1$ ns and a DN of 1 kHz per OM (see section 4.2). Deviations from this specifications will explicitly be mentioned in the relevant sections.

In the following section, the performance for electron events will be discussed using the default electronics parameters. In the succeeding sections 4.5.2 and 4.5.3 the influence of the DN level and the shape of the TTS will be discussed.

4.5.1 Electrons

The following results are based on a data set of 200 000 simulated events. Figure 4.18 shows the fraction of the events where the fit actually converged. This is the case between 97% and 99% of all times. The fraction of converged events was found to decrease slightly with rising energy which is probably caused by the increased probability for Bremsstrahlung emission at higher energies, which can turn a point-like event into an extended event.

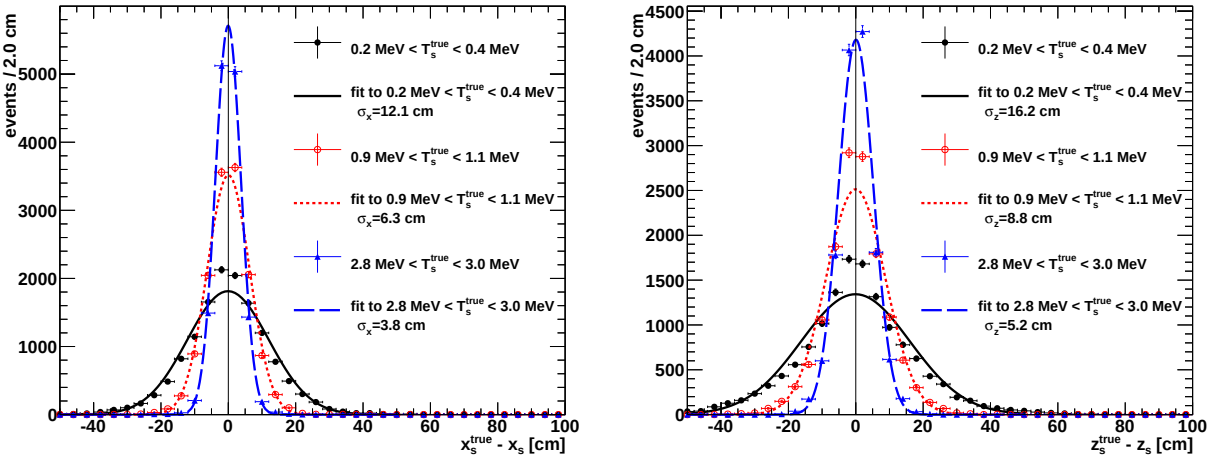

Figure 4.20: The distribution of the deviations in x (left) and the deviations in z (right) between the true vertex and the reconstructed vertex for different energy slices. The lines show the results of Gaussian fits to the obtained distributions. The resulting widths σ_x and σ_z are indicated in the legend. Note that no errors are quoted as the resulting statistical errors are negligible compared to the variations of the resolutions with the radius of the event.

To characterize the overall **position resolution**, figure 4.19 shows the distribution of the distance between the true and the reconstructed vertex $\Delta\boldsymbol{r} = \boldsymbol{r}_s^{\text{true}} - \boldsymbol{r}_s$ for three different energy bins: A bin right at the projected detector threshold $T_l = [0.2\,\text{MeV}, 0.4\,\text{MeV}]$, a mid ranged bin around 1 MeV, $T_m = [0.9\,\text{MeV}, 1.1\,\text{MeV}]$ and a bin at the upper range of the simulated energy range, $T_h = [2.8\,\text{MeV}, 3.0\,\text{MeV}]$. The obtained distributions were fitted with the distribution expected in case the resolution would be of Gaussian shape in all three directions and would feature a common resolution σ_r in all three directions which is independent on the position in the detector:

$$P(|\Delta\boldsymbol{r}|) \propto |\Delta\boldsymbol{r}|^2 \exp\left(-\frac{|\Delta\boldsymbol{r}|^2}{2\sigma_r^2}\right). \tag{4.46}$$

Even though the latter assumption is generally not fulfilled, except for the peak region the fits match the data nicely. This shows that the deviations of the fit results from the MC truth do not feature any significant non-Gaussian tails, which is a prerequisite for suppressing external radiation using a fiducial volume cut (see e.g. [41]). Additionally, as expected due to the increased photo-electron statistics, it is obvious that the position resolution works better at higher energies. Comparing the resolutions obtained in the fits with the resolutions obtained using the first estimates for the event position (section 4.3), the improvement due to the more sophisticated fit compared to the simple first estimates is found to be about one order of magnitude.

Figure 4.20 shows the distribution of the x-deviations (left) and the z-deviations (right) of the reconstructed from the true vertex for the three energy bins introduced above. The obtained distributions have been fitted with Gaussians which fit the resulting distributions well in the tails but show deviations in the peak regions, as the obtained resolution is dependent on the ρ-position of the event in the detector. Note, that in the following the y-coordinate will not be dealt with separately as it is equivalent to the x-axis due to the cylindrical symmetry of the detector. This equivalence was also found to be reflected

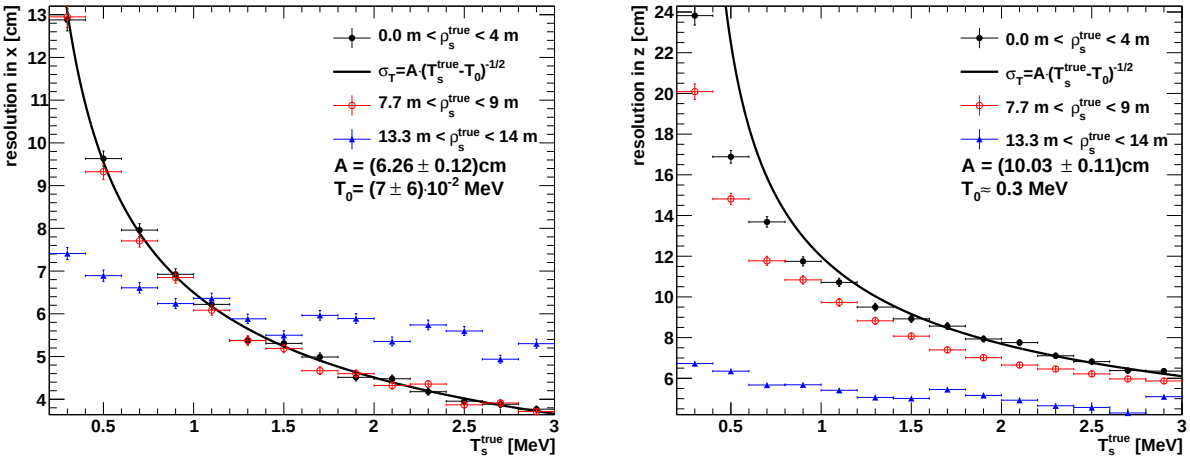

Figure 4.21: The resolution in x (left) and in z (right) as a function of the true kinetic energy T_s^{true} of the electron for different radial bins. A fit $\sigma_{x,z} = A/\sqrt{T_s^{\text{true}} - T_0}$ to the radial bin $\rho < 4\,\text{m}$ is shown as a black line, where $\sigma_{x,z}$ denotes the x- and z-resolution, respectively. The resulting parameters A and T_0 are indicated in the plot. No error margin is given for the T_0-value resulting from the fit to the resolution in z as the error returned from the fit is unrealistically small ($\sim 10^{-6}\,\text{MeV}$) due to the deviation of the data from the fit. The shown errors in resolution are of statistical nature only while the errors in energy indicate the size of the used energy bins. Note that the size of the radial bins was adapted to yield the same statistics in each bin.

in the data.
Comparing the resolutions obtained in x and z, the resolutions in x outperform the resolutions in z, as the cylindrical geometry of the detector allows for a better determination of the x-position: Timing information can be used most effectively, if a deviation in a coordinate moves the event directly in the direction of a PMT as this results in the largest TOF effect. Thus, moving an event in the x-y-plane, a deviation from the true event position always induces a maximal effect in two PMTs and lots of PMTs are positioned close to optimal. For a deviation in z in contrast, only the lid/bottom PMTs (which are not used anyway) are placed in the optimum position. As these optimal PMTs are much farther away than in the x-y case, the timing information is washed out due to scattering of light in the scintillator and small statistics.
To investigate the dependency of the position resolution on the kinetic energy of the event, the events have been binned in equidistant energy bins. For three different radial bins ($\rho_l = [0\,\text{m}, 4.0\,\text{m}]$, $\rho_m = [7.7\,\text{m}, 9.0\,\text{m}]$, $\rho_h = [13.3\,\text{m}, 14.0\,\text{m}]$), the resulting resolutions in x and z are shown in figure 4.21 as a function of the true kinetic energy. Note that each of the radial bins was adjusted to have the same number of expected events. All obtained resolutions improve with energy as expected due to the increase in statistics. The behavior in the two inner radial bins (ρ_l and ρ_m) differs from that in the bin ρ_h close to the detector edge. In the bulk of the detector, the position resolution scales approximately with $1/\sqrt{T_s^{\text{true}}}$ while a much flatter behavior is observed at the detector boundary. The evolution of the resolution with rising radius is mainly determined by four different effects:

- **Photo-electron statistics:** The resolution improves with rising photo-electron statistics. Thus, from figure 4.4, beginning at the center a slight improvement would be expected with rising ρ_s up to about $\rho_s \approx 7\,\text{m}$. For higher radii, a decline

of the resolution would be expected. Assuming the resolution to be proportional to $1/\sqrt{N_{pe}}$, the magnitude of the decline should be about 10%.

- **Decreased scattering:** For events at higher radii, there are a couple of very close OMs. Thus the influence of the scattering on the timing PDF is reduced which results in a sharper PDF and thus in an increased resolution. On the other hand, the OMs on the opposite site of the detector are farther away, thus the PDF gets washed out by the increasing influence of scattering which leads to a reduction of the resolution. The former effect dominates as the close OMs feature a higher number of photoelectrons and are therefore statistically more relevant. Hence, in total, an improvement of the resolution is expected with rising radii due to the decreased scattering.

- **LCs' field of view:** For events with $\rho_s \gtrsim 7\,\mathrm{m}$ the extension of the LC field of view significantly decreases with higher radii. Thus, the event will be in the direct field of view of only a small set of OMs which feature a significantly increased charge compared to the OMs on which only scattered light can be detected. Hence, for events at high radii the position of the event is already strongly determined by the distribution of the charge on the different OMs which boosts the resolution. Note that this effect is stronger in z-direction than in x-direction due to the cylindrical geometry of LENA.

- **Detector inhomogeneities:** For events at very high radii, the detector is very inhomogeneous (compare figure 4.16). Even though a few problems arising with this inhomogeneity are dealt with (see section 4.4.5), this nevertheless causes a deterioration of the archived resolution, especially for the highest radii as the spacing of the used PDF-tables is bigger than the typical scale at which the detector parameters change. According to [41], this effect is expected to be significant only for $\rho_s \gtrsim 13.5\,\mathrm{m}$.

The results in figure 4.21 indicate that the resolution in the bulk of the detector is dominated by statistics while the resolution at the detector boundary is dominated by the systematic effects due to the very fine grained inhomogeneities close to the edge of the detector.
To investigate the radial behavior in more detail, figure 4.22 shows the radial dependency of the x- and the z-resolution. The z-resolution was found to improve towards higher radii and only deteriorates in the bin with the highest ρ, where the detector inhomogeneities dominate. This shows that for the z-resolution (excluding ρ_h), the effects of decreased scattering and LCs' field of view are more relevant than the photo-electron statistics. For the x-resolution, where the effect of the LCs' field of view is less significant, the improvement in resolution with rising ρ_s is smaller. There is even a region around $\rho_s \approx 11\,\mathrm{m}$ where a small deterioration can be observed of the resolution due to the reduced photo-electron statistics .

Finally, the systematic errors of the position resolution are investigated by comparing the means of the distributions of the reconstructed positions with the true positions. No significant deviations were found in this study.

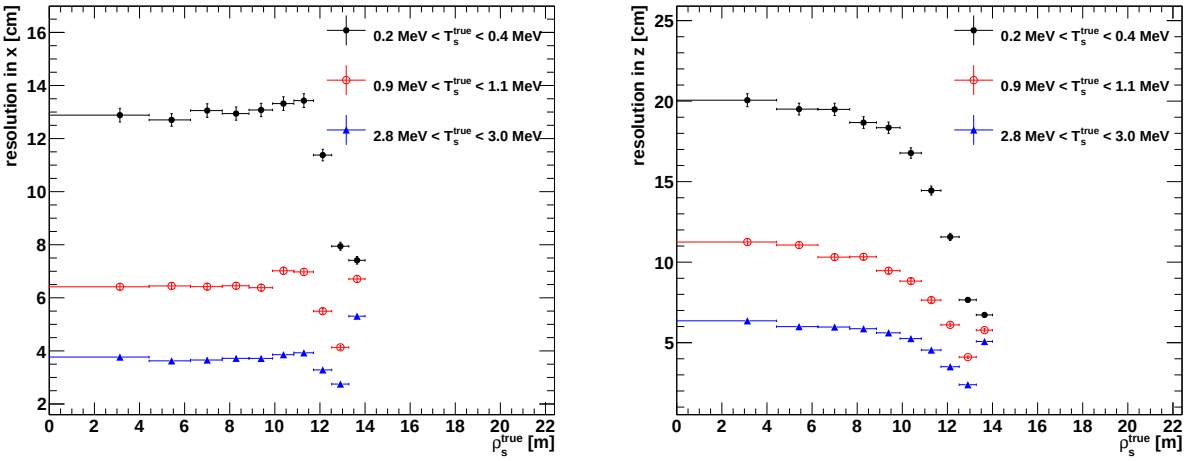

Figure 4.22: The resolution in x (left) and in z (right) as a function of the true vertex radius of the electron for different energy bins. The shown errors in resolution are of statistical nature only while the shown errors of the radius indicate the corresponding radial bin. Note that the size of the radial bins was adapted to yield the same statistics in each bin and that the points where set to the mean radius of the events in the bin.

The obtained spatial resolutions can be compared to the results of Borexino: In [110], a resolution of about 12 cm in x and y and of about 14 cm in z is reported at ^{214}Bi-^{214}Po energies. ^{214}Bi features a β-decay with an end-point energy of about 3.3 MeV [111]. Despite the smaller size of Borexino and the higher photoelectron yield compared to LENA, the obtained resolutions are superior to the values quoted in Borexino for a large part of the energy range covered by the ^{214}Bi decay. Note, however, that the ^{214}Bi decay can be accompanied by γ emission which artificially worsens the observed resolution of the algorithm due to the finite interaction length of the γ in the LSc. Thus, a direct comparison is difficult but it can be stated that the obtained performance is similar or better than the performance obtained in Borexino.

The distribution of the deviations of the **reconstructed start time** t_s from the true start time t_s^{true} is shown in figure 4.23 for the energy bins already used to characterize the position resolution. The obtained distributions can be well fitted by Gaussian functions which results in resolutions of $0.2\,\text{ns} \lesssim \sigma \lesssim 0.5\,\text{ns}$. Note, that in contrast to the position resolution, this time a systematic offset of about 0.1 ns is observed in the distributions. This offset was traced back to the numerics of the convolution between the PMT TTS and the LSc emission time distribution. As it was found to be constant with energy, it was not corrected as in a real experiment the global time scale cannot be determined to 0.1 ns precision anyhow.
Figure 4.24 shows the energy dependency of the start time resolution. Similar as for the position resolution, the radial bins in the bulk of the detector were found to follow a $1/\sqrt{T_s^{\text{true}}}$ dependency while the radial bin at the detector boundary was found to feature a flatter shape. Complementary, the start time resolution is shown as a function of true radius of the vertex in figure 4.25 for the three standard energy bins. A change in the start time resolution as a function of the radius of about 10% was observed for $\rho < 13.5\,\text{m}$ with the worst resolution at $\rho_s \approx 11\,\text{m}$. This shows that for $\rho_s \lesssim 11\,\text{m}$ the timing resolution is mainly determined by the photo-electron statistics while for higher radii the decrease

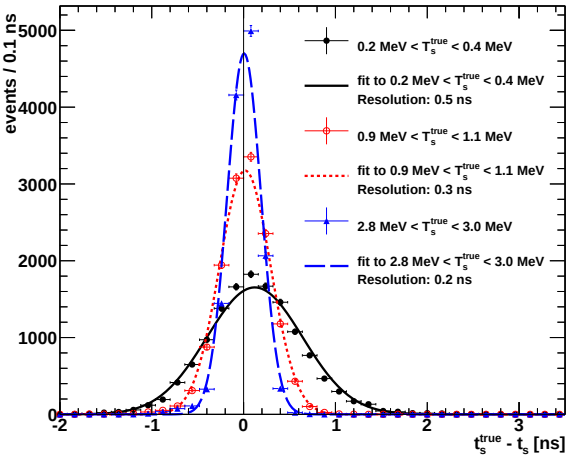

Figure 4.23: Distribution of the deviations between the true time of the event t_s^{true} and the reconstructed time of the event t_s for various energy bins. The lines indicate Gaussian fits to the data with the resulting resolutions being shown in the legend.

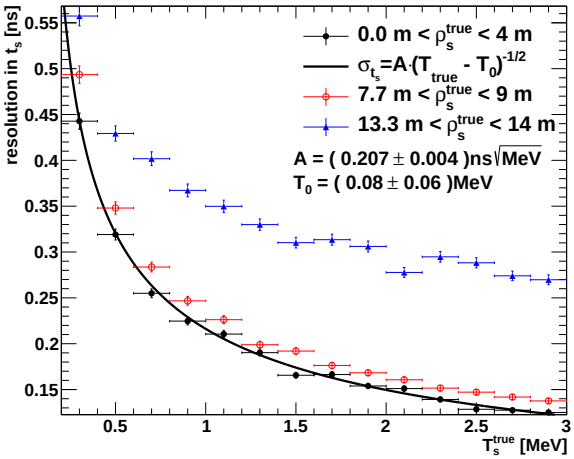

Figure 4.24: The resolution in t_s as a function of the true kinetic energy of the electron for different radial bins. A fit $\sigma_t = A/\sqrt{T_s^{\text{true}} - T_0}$ to the radial bin $\rho < 4\,\text{m}$ is shown as a black line, where σ_t is the start time resolution. The resulting parameters A and T_0 are indicated in the plot. The shown errors in resolution are of statistical nature only while the errors in energy indicate the size of the used energy bins. Note that the size of the radial bins was adapted to yield the same statistics in each bin.

in scattering starts to become important. As the charge PDF is independent of the hit times on the OMs, the timing resolution is not influenced by the LCs' field of view to first order. At very high radii, the detector inhomogeneities again dominate and deteriorate the resolution.

To determine the **initial kinetic energy of the electron** from the number of photons N_γ emitted from the vertex, which is estimated by the fit, a calibration is necessary. Thus, for all available events featuring a converged fit and with $\rho_s^{\text{true}} < 13\,\text{m}$, N_γ was plotted as a function of T_s^{true}. By fitting the resulting distribution with a linear function, T_s can be determined from N_γ.
The distributions of the deviations of the true initial kinetic energy of the electron from the reconstructed initial kinetic electron energy are shown in figure 4.26 for the usual energy bins. Common to the findings for the position resolution and the start time resolution above, the tails were found to be well described by a Gaussian while the peaks show some deviations due to the dependency of the energy resolution on the event radius.
Figure 4.27 shows the relative energy resolution as a function of the true initial kinetic energy of the electron for multiple radial bins. As already discussed in section 4.1 (compare equation (4.1)), in an optimal case where the energy resolution is dominated by statistics only, a $1/\sqrt{T_s^{true}}$ dependency of the relative energy resolution is expected with an energy resolution of 6.1% at $T_s^{true} = 1\,\text{MeV}$. To test this hypothesis, the found resolutions for

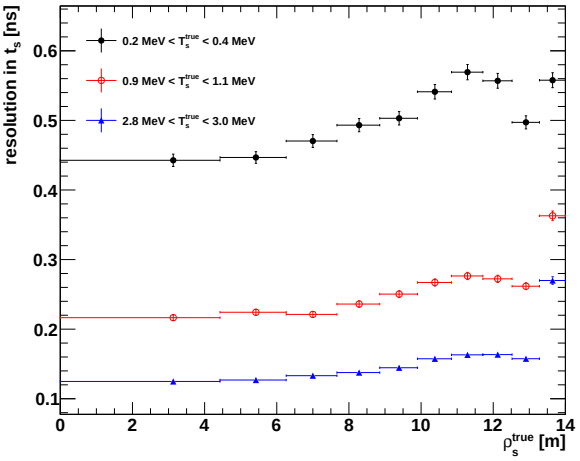

Figure 4.25: The resolution in t_s as a function of the true vertex radius of the electron for different energy bins. The shown errors in resolution are of statistical nature only while the shown errors of the radius indicate the corresponding radial bin. Note that the size of the radial bins was adapted to yield the same statistics in each bin and that the points where set to the mean radius of the events in the bin.

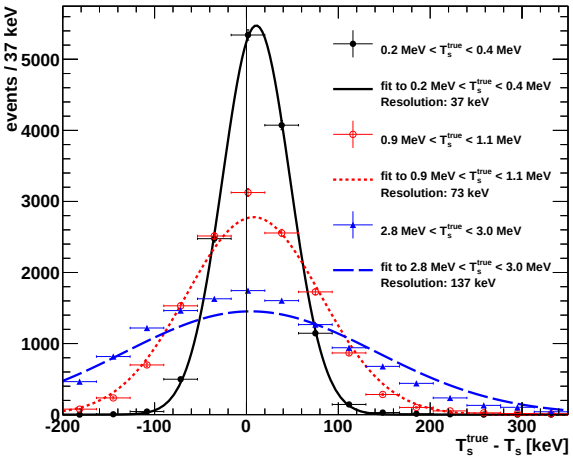

Figure 4.26: Distribution of the deviations between the true initial kinetic energy of the electron T_s^{true} and the reconstructed initial kinetic energy T_s of the electron for various energy bins. The lines indicate Gaussian fits to the data with the resulting resolutions being indicated in the legend.

$\rho_s^{\text{true}} < 4\,\text{m}$ were fitted with

$$\frac{\Delta T_s}{T_s^{\text{true}}} = \frac{A}{\sqrt{T_s^{\text{true}} - T_0}}, \tag{4.47}$$

with A and T_0 being fit parameters. As the resulting $T_0 = (1 \pm 6) \cdot 10^{-2}\,\text{MeV}$ is compatible with zero, no significant deviation from the statistics-only hypothesis is observed. Furthermore, the resulting $A = (6.0 \pm 0.1)\,\%\sqrt{\text{MeV}}$ is compatible with the optimum resolution possible due to photon statistics. This shows that the performance of the energy resolution for events in the center of the detector has reached its theoretical optimum. For events close to the detector boundary, however, this is no longer the case. A closer look at the radial dependency of the energy resolution (see figure 4.28) reveals a bad performance of the outermost radial bin, common to the findings for the other parameters above. A closer investigation shows, that the energy of the event can only be reliably reconstructed for $\rho_s^{\text{true}} \lesssim 13.5\,\text{m}$, consistent with the results obtained in [41]. Except for the outermost radial bin, the energy resolution is dominated by the photoelectron-yield: The resolution slightly improves with rising radius for $\rho \lesssim 7\,\text{m}$ and successively degrades with rising radius for higher radii.

4.5.2 Influence of the dark-noise level

As the exact type and size of PMTs which will be used in the LENA OMs is not finally decided, also the DN is not yet defined. Especially very large PMTs [46] or novel light detector concepts feature significantly higher dark noises than the 1 kHz per device which was assumed up to this point. Thus, the influence of the DN on the performance of the electron reconstruction has been tested by varying the DN rate from $f_{\text{DN}} = 0\,\text{kHz}$

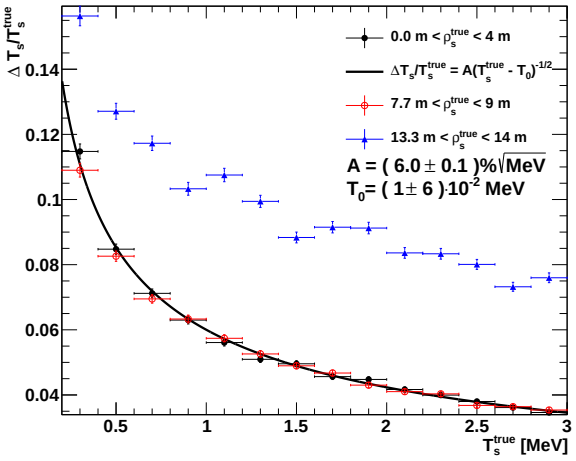

Figure 4.27: The relative energy resolution $\Delta T_s/T_s^{\text{true}}$ as a function of the true kinetic energy of the electron for different radial bins. A fit $\Delta T_s/T_s^{true} = A/\sqrt{T_s^{\text{true}} - T_0}$ to the radial bin $\rho < 4\,\text{m}$ is shown as a black line. The resulting parameters A and T_0 are indicated in the plot. The shown errors in resolution are of statistical nature only while the errors in energy indicate the size of the used energy bins. Note that the size of the radial bins was adapted to yield the same statistics in each bin.

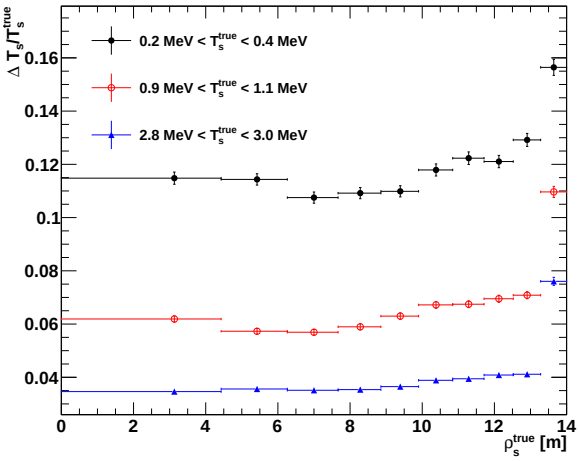

Figure 4.28: The relative energy resolution $\Delta T_s/T_s^{true}$ as a function of the true vertex radius of the electron for different energy bins. The shown errors in resolution are of statistical nature only while the shown errors of the radius indicate the corresponding radial bin. Note that the size of the radial bins was adapted to yield the same statistics in each bin and that the points where set to the mean radius of the events in the bin.

to $f_{\text{DN}} = 50\,\text{kHz}$ per OM. Note that the upper boundary of the DN region is a very conservative choice.
As with higher DN the occupancy of a single OM increases, the differences between the optimistic electronics and the conservative electronics (confer section 4.4) are expected to become more significant. Thus, the performances of both electronic approaches are compared in this section.
To reduce the parameter space, only events in the center of the detector with $\rho < 6\,\text{m}$ are taken into account in the analysis. As hardly any radial dependency of the resolutions in this region of the detector was observed, the radial dependency of the obtained resolutions is dropped. Furthermore, only the three energy bins already used in the previous sections are used to show energy dependencies.

Figure 4.29 shows the fraction of events which are successfully reconstructed as a function of the DN rate per device for both electronics approaches and for all three energy bins. For the optimistic electronics, the fraction of converged events is found to be significantly worse for events with zero DN than for low dark noise rates, with the effect being most prominent at higher electron energies. This counter-intuitive behavior is due to the numerical precision of the reconstruction algorithm: Without the constant DN term in $\tilde{P}_t(\Delta t_h|\boldsymbol{r_s}, \boldsymbol{r})$ (see equation (4.44)) can become zero for $\Delta t_h \gg \tau_3$ within the numerical accuracy. Thus, $\mathcal{L} = \ln P$ can no longer be calculated leading to an abortion

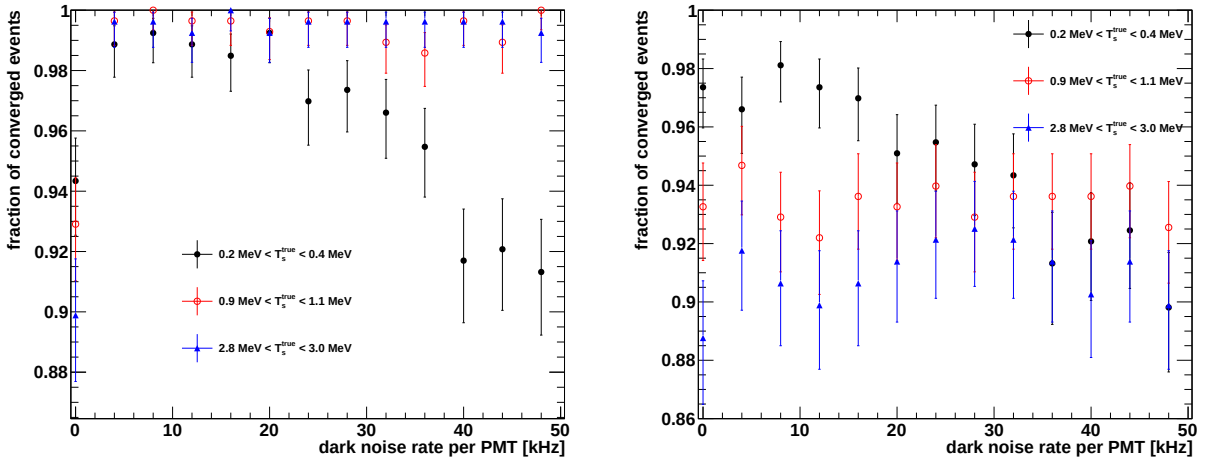

Figure 4.29: The fraction of converged events as a function of the dark noise rate per PMT for the optimistic electronics (left) and the conservative electronics (right). The obtained results are shown for three different energy bins and correspond to the performance in the center of the detector ($\rho_s^{\text{true}} < 6\,\text{m}$). The shown error bars are statistical only.

of the fit[15]. The probability that a photon is detected at very late times rises with the number of emitted photons and thus with the visible energy of the event. Therefore, the higher energy bins are more affected by this problem than the low energy bins. For the conservative electronics set-up, this effect is not observed within statistical precision. It is suppressed as such very late photons are often on an OM which has more than one hit just by statistics. As in the conservative set-up only the time of the first hit on an OM is taken into account, these events do not cause any harm here.
An influence of the DN on the fraction of converged events can only be seen for the energy bin with the lowest energy. Note, that for the case of the conservative electronics the probability of a fit to converge actually decreases with rising energy for DN below ≈30 kHz, as for higher electron energies the occupancy of an OM rises. Thus, fewer events in the tails of the time PDF, which were found to stabilize the fit, are available. Nevertheless, the fraction of converged events is still above 88%.

The obtained resolutions in x_s and t_s as well as the relative energy resolution $\Delta T_s/T_s^{\text{true}}$ are shown in figure 4.30 as a function of the dark noise rate per OM for the three common energy bins for the optimistic as well as for the conservative electronics set-up. All resolutions show a similar behavior with rising DN: Only for the low-energetic energy bin, a dependency of the obtained resolutions on the DN is observed while for energies above $\sim 1\,\text{MeV}$ the effect of the dark noise on the obtained resolutions is negligible. If only the charge of the OMs would be used, the energy resolution is expected to scale with the DN rate as

$$\frac{\Delta T_s}{T_s^{\text{true}}} = \frac{\Delta N_{\text{tot}}}{N_{\text{p.e.}}} = \frac{\sqrt{N_{\text{p.e}} + N_{\text{DN}}}}{N_{\text{p.e}}} = \sqrt{\frac{1}{N_{\text{p.e}}} + \frac{N_{\text{DN}}}{N_{\text{p.e}}^2}}, \tag{4.48}$$

[15] In the used code, this error is handled in the following way: If $P < 10^{-15}$ the PDF is replaced by an approximate PDF which is numerically much more stable. This results in a step in $\mathcal{L}$ which often causes the `MIGRAD` algorithm to fail. Using the more stable `SIMPLEX` algorithm however leads to biased results.

where $N_{\mathrm{p.e}}$ is the total charge created by photons, N_{DN} the charge created by dark counts and $N_{\mathrm{tot}} = N_{\mathrm{p.e}} + N_{\mathrm{DN}}$. This dependency was not observed in the obtained resolutions, showing the additional power of the combined fit in time and charge which also allows to use the pulse shape to determine $N_{\mathrm{p.e.}}$ and thus to mitigate the influence of the DN on the energy resolution.

Furthermore, no significant improvement in resolution was found for the optimistic electronics set-up compared to the conservative electronics set-up. There is one important difference though: In case of the conservative electronics the variation between the different obtained resolutions was much bigger than suggested by the error bars. As an example for this difference between the optimistic and the conservative electronics, a comparison of the distributions of the deviations between the true and the reconstructed x-position for both electronic set-ups is shown in figure 4.31 for $\sim$1 MeV electrons and a DN of 4 kHz. While the distribution obtained by the optimistic electronics can be well described by a Gaussian distribution, the conservative electronics show a group of three outliers at $|x_s^{\mathrm{true}} - x_s| \sim 10\,\mathrm{m}$. To further investigate the probability of the occurrence of outliers, the obtained x_s-deviation distributions have been fitted with a Gaussian distribution and all events with $|x_s^{\mathrm{true}} - x_s| > 5\sigma_{x_s}$ have been tagged as outliers. To increase statistics, all events with an energy $T_s^{\mathrm{true}} > 0.9\,\mathrm{MeV}$ and a radius $\rho_s^{\mathrm{true}} < 6\,\mathrm{m}$ have been taken into account.
Figure 4.32 shows the resulting probabilities for outliers as a function of the dark noise rate for both electronic assumptions. It can be seen, that the optimistic electronics show less outliers over the whole DN range and (within statistics) do not produce any outliers below a DN rate of 20 kHz. Note that the probability for an outlier seems to drop with rising DN rate in case of the conservative electronics (significance about 2.6σ), indicating that a higher DN rate might be beneficial as it produces a more homogeneous distribution of the dark counts.
The appearance of events with a deviation between the true and the reconstructed value which is much bigger than predicted by the distribution of the majority of the events poses a serious problem in case external γ-background has to be suppressed by a fiducial volume cut. As the γ-background rate exponentially drops with decreasing radius [41], even a small probability of events being reconstructed far off their actual position can spoil the background suppression. Thus, the LENA experiment would really benefit from an electronics set-up close to the optimum set-up.

4.5.3 Influence of the transit-time spread

Up to this point, the assumption of a Gaussian TTS with a standard deviation of 1 ns is used. To investigate the influence of the more complex TTS of the a real PMT, a study is done using the Borexino TTS (compare figure 4.3). To also investigate the case if the TTS is not known beforehand, additionally a data sample was prepared using the Borexino TTS but reconstructed assuming the standard Gaussian TTS. Note, that this assumption is very conservative as the general shape of the TTS will be measured before the experiment, however the different PMTs will feature some variation in TTS over the whole sample of PMTs which can be approximated using the worst-case assumption of not knowing the distribution at all.

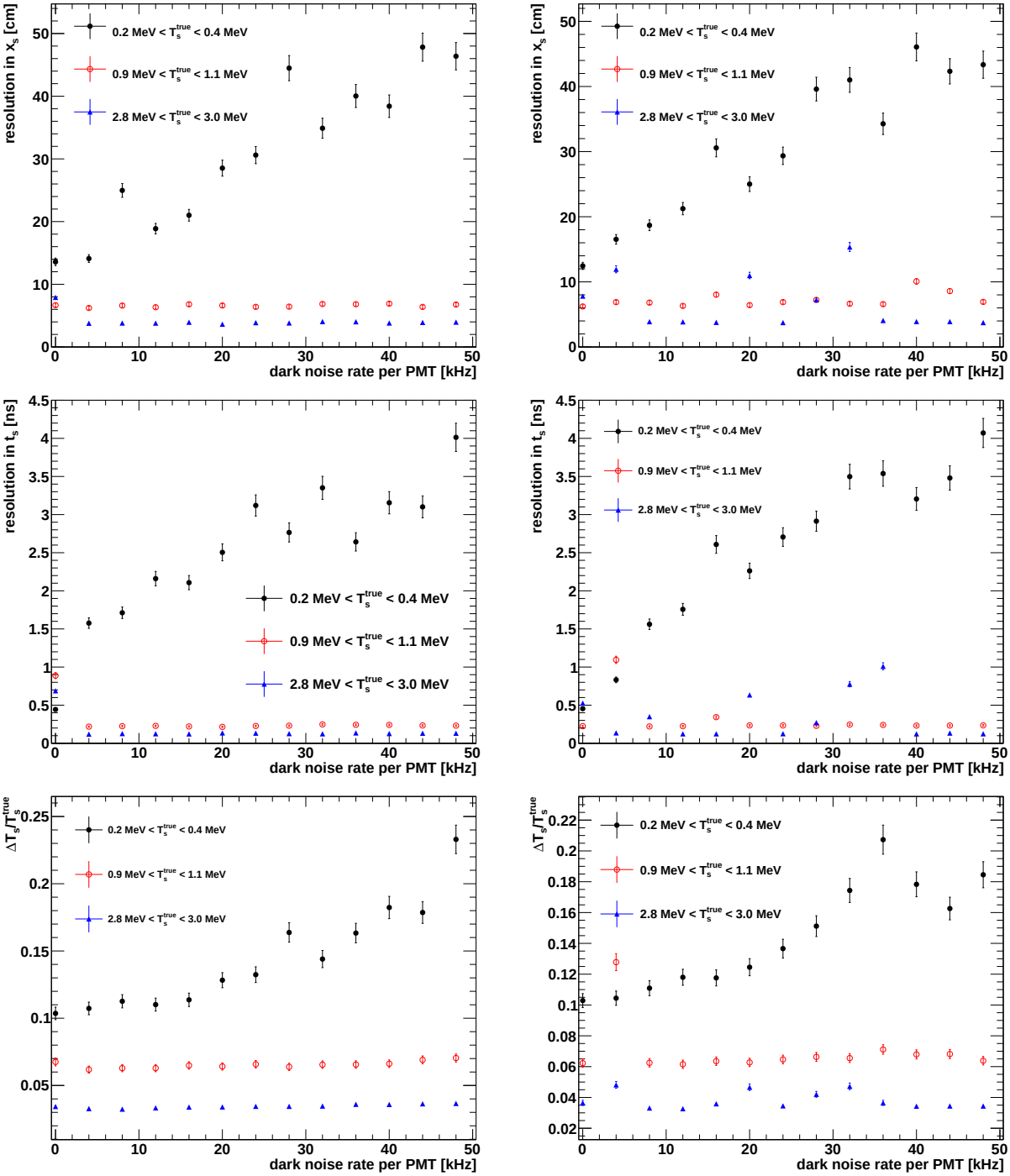

Figure 4.30: The resolution in x_s (top), the resolution in start time t_s (center) and the relative energy resolution $\Delta T_s/T_s^{\text{true}}$ (bottom) as a function of the dark noise rate per PMT for the optimistic electronics (left) and the conservative electronics (right). The obtained resolutions are shown for three different energy bins and correspond to the performance in the center of the detector ($\rho_s^{\text{true}} < 6\,\text{m}$). The shown error bars are statistical only.

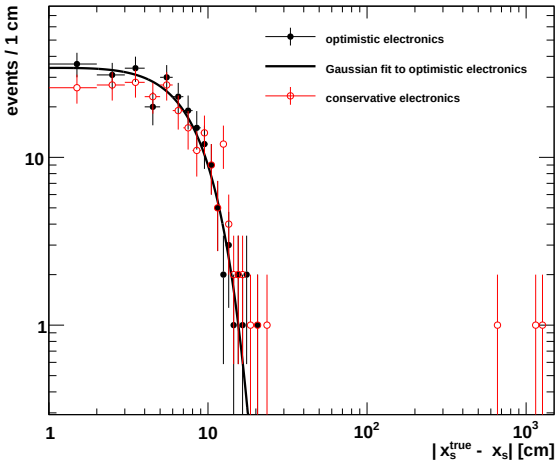

Figure 4.31: The distributions of the absolute deviations between the true and the reconstructed value of x_s for the optimistic electronics set-up and the conservative electronics set-up. The shown distributions feature events with $0.9\,\mathrm{MeV} < T_s^{\mathrm{true}} < 1.1\,\mathrm{MeV}$, $\rho_s^{\mathrm{true}} < 6\,\mathrm{m}$ and a DN of 4 kHz per OM. The solid line indicates a Gaussian fit to the optimistic electronics distribution.

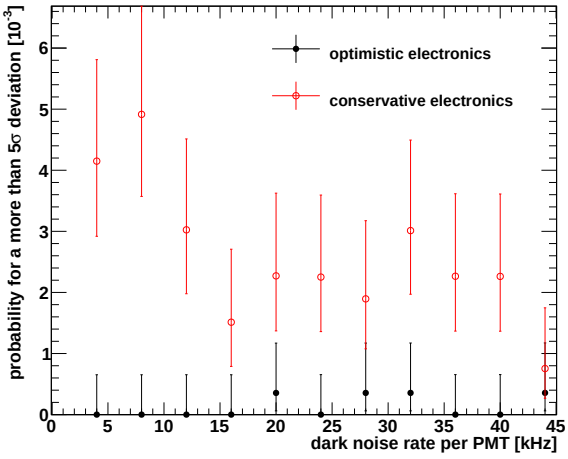

Figure 4.32: The probability for an event to feature a deviation between the true and the reconstructed x_s-position which is more than 5σ away from zero as a function of the dark noise per OM. The width of the distribution was determined by fitting a Gaussian in the range $|x_s^{\mathrm{true}} - x_s| < 30\,\mathrm{cm}$. The shown probabilities are for events with $T_s^{\mathrm{true}} > 0.9\,\mathrm{MeV}$ and $\rho_s^{\mathrm{true}} < 6\,\mathrm{m}$.

To reduce the dimensionality of the problem, again only events in the center of the detector $\rho_s^{\mathrm{true}} < 6\,\mathrm{m}$ are taken into account, the DN is fixed to 1 kHz per OM and only the optimistic electronics are used. No difference in the fraction of converged events was found (within statistics) between the three different assumptions. The obtained resolutions in x_s, z_s, t_s and T_s are shown in figure 4.33. It was found that the TTS shape has a small influence on the obtained position and start time resolutions: As expected, the best performance is achieved using the standard assumptions, followed by the sample where the Borexino TTS was used for both data generation and reconstruction while the sample where the data was produced using the Borexino TTS but the reconstruction was done using a Gaussian TTS performs worst. With the differences being ∼10%, they were found to be smaller than expected. Note that the energy resolution, which is mainly driven by the charge obtained on the OMs is not affected at all, as the loss in position reconstruction has no significant impact on the photoelectron yield in the center of the detector where the photo-electron yield is relatively flat.

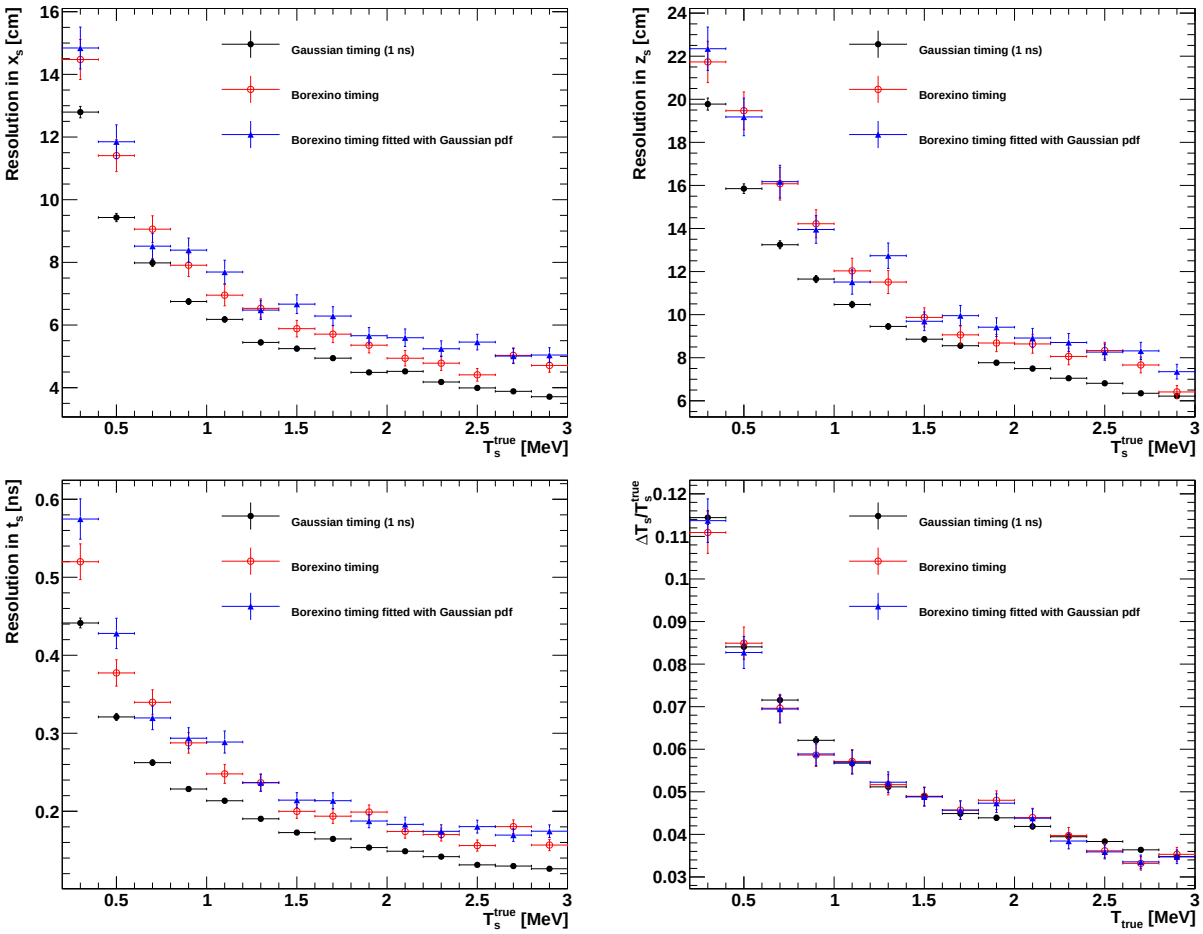

Figure 4.33: The resolution in x_s (top left), the resolution in z_s (top right), the resolution in start time t_s (bottom left) and the relative energy resolution $\Delta T_s/T_s^{\text{true}}$ (bottom right) as a function of true initial electron energy T_s^{true} for the center of the detector ($\rho_s^{\text{true}} < 6\,\text{m}$). The obtained resolutions are shown for the standard assumption for the TTS, for the Borexino TTS (see figure 4.3) and for the data generated according to the Borexino TTS but the fit assuming a Gaussian TTS. The shown error bars are statistical only.

Chapter 5

Reconstruction of single lepton tracks

In chapter 4, the typical deposited energy was in the 1 MeV range, thus the events have a point-like structure. Contrary, this chapter deals with reconstructing events featuring initial kinetic energies of more than ∼100 MeV which can no longer be considered as point-like. This kind of events is created by ∼GeV neutrino interactions. While these interactions typically produce quite complex event topologies with multiple different particles in the exit channel (compare section 2.1.2), this section deals with a simple prototype case: One isolated lepton track in the LSc.

Even though the LSc radiates isotropically, it is possible to determine the direction of an extended event using the time of the observed hits on the OMs. The underlying concept along with the fit parameters and the required assumptions are presented in section 5.1. Guided by this concept, an array of simple methods is presented in section 5.2 which already allows a rough determination of the properties of this event type. Similar to chapter 4, the precision of the results can be significantly improved by performing a full fit of the event to the data (see section 5.3). Finally, section 5.4 presents the archived performance of this method.

5.1 Concept

In contrast to Cerenkov light, the photon emission in LSc detectors is isotropic. Nevertheless, a reconstruction of the direction of a charged particle transversing the LSc is possible using the timing information of the photon arrival times, which was first realized in [112, 113]. The basic principle is sketched in figure 5.1 for a charged particle traveling through the scintillator at the speed of light: From each point of the particle's track, photons are emitted. The first-photon surface, i.e. the surface containing all instantly emitted direct photons, is spherical for each single point on the track (blue dashed circles in figure 5.1). By taking the envelope of all first-photon surfaces, the overall first-photon surface (solid red cone in figure 5.1) can be constructed. It features a distinctively asymmetric shape which can be used to reconstruct the track direction. Note, that in contrast to the Cerenkov case, no interference takes place as the photons are emitted non-coherently.

A general "track" of a particle is given by the function $\boldsymbol{r}(t)$, i.e. by the trajectory of the particle. From this trajectory, the parameters of the particle at the vertex can be

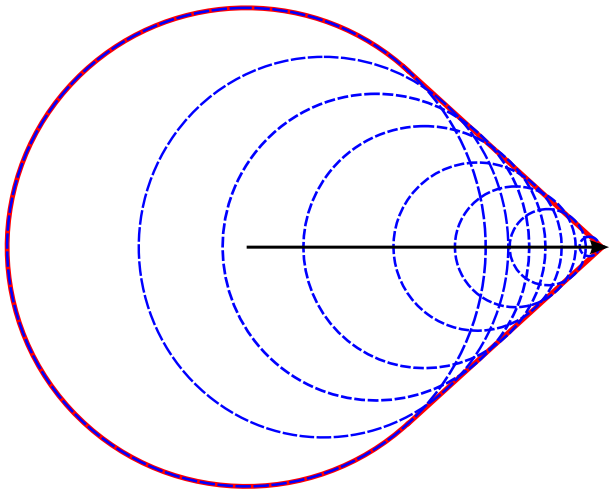

Figure 5.1: Schematic representation of the first-photon surfaces (dashed blue) created by a particle (solid black arrow) traveling through the LSc at the speed of light. The solid red cone represents the resulting, overall first-photon surfaces.

inferred. As a trajectory consists of an infinite number of points, it does not constitute an appropriate model for a fit. As already pointed out above, the physical parameters of interest are the properties of the particle at its vertex, i.e. the vertex position $\boldsymbol{r}_s$, the time the particle was created t_s, the initial kinetic energy of the particle T_s and the initial momentum direction defined in spherical coordinates by ϑ_s and φ_s. As the passage of a charged particle through a scintillator is a statistical process, $\boldsymbol{r}(t)$ is not fully defined by the particle's vertex properties. The strategy adopted in this work, is to neglect all statistical fluctuations of the passage of a charged particle through matter and to replace the corresponding fluctuations by their mean values. Thus the model is one particle straightly propagating through the LSc and emitting photons as expected due to its mean light yield. This means:

- All light produced by the particle is assumed to originate from a straight line. It is defined by the momentum direction and by the requirement to contain the vertex of the track. While this approximation is quite well fulfilled for heavy charged particles, it is a considerable simplification for $e^{\pm}$ which produce an electromagnetic shower that has a significant lateral extension.

- The mean light yield as a function of the position on the track is fully determined by the kinetic energy of the particle at its vertex. Again, this is a quite good approximation for heavy charged particles while the simplification for $e^{\pm}$ is much more significant.

- No statistical variations in the light output as a function of the position on the track, e.g. due to bremsstrahlung, are taken into account.

- The time the particle takes to travel from the vertex to a given point on the track is unique. While this seems trivial, it is a considerable simplification for showers where the time to reach a given distance from the vertex varies over the lateral extension of the shower.

As in this model the particle is fully defined by its vertex properties, the set of fit parameters for the track fit is

$$\boldsymbol{X}_t = \{\boldsymbol{r}_s, t_s, T_s, \vartheta_s, \varphi_s\}\,. \tag{5.1}$$

In section 4.4, two extreme cases for the LENA electronics were discussed, the conservative and the optimistic electronics. For the latter case it was stated, that a timing information for every hit is not unrealistic as the occupancy of the OMs is low. This no longer holds for deposited energies of more than a few hundred MeV as dealt with in this chapter. In this case, the occupancy on some OMs is so high, that a time information for every photon is no longer available and only the overall photon pulse shape can be recorded. While this can be used to extract some additional information compared to a conservative electronics set-up, including this information in the fits would require a simulation for the whole LENA electronics chain which is currently not available. Hence, with the exception of section 6.2, the conservative electronics will be used for the remainder of this thesis. Thus, the information available from the detector consists of the charge q_i of all OMs and the first hit time t_i^0 from all OMs with $q_i \neq 0$.

5.2 Primary estimates

Similar to chapter 4, the numerical minimization used to determine the fit parameters requires rough start values for the parameters. The determination of these parameters is described briefly in the following. For a more detailed description, see [99].

Before investigating the properties of an event, possible secondary events like muon decays or capture processes of neutrons created by the high-energetic particle are removed from the primary event by means of a dedicated clustering procedure which is described in detail in section 6.2.

Estimate for initial kinetic energy:
Successively, the barycenter of the event $\boldsymbol{r}_{bc}$ is determined using the same procedures as described in section 4.3. Using this barycenter and assuming the event to be point-like at $\boldsymbol{r}_{bc}$, an estimate for the initial kinetic energy is obtained by the same procedure already described in section 4.3.

Estimate for the direction of the track:
As a first step to estimate the direction of the track, a decision needs to be taken whether the track is more horizontal or more vertical. Figure 5.2 shows a typical horizontal event: a 1 GeV muon traveling from the center of the detector along the positive x-axis. As can be seen, the observed TOF corrected hit times show a significant dipolar asymmetry with the minimum being at the position where the extension of the track against the momentum direction of the particle intersects the detector wall while the maximum on the exact opposite side of the detector. For symmetry reasons, no dipolar behavior appears for vertical tracks[1]. Thus, the degree of the dipole anisotropy in the x-y plane can be used to discriminate between horizontal and vertical events.

[1] A dipolar behavior might show up on the lid/bottom of the detector. Due to the large height of LENA, it is strongly washed out due to scattering and low statistics. Apart from that, the lid and the bottom of the detector are neglected in this study

To exploit this feature, the φ position of the $N_{\mathrm{OM}}^{\mathrm{dir}} = 300$ OMs with the smallest first hit times are histogrammed. The parameter used to discriminate between horizontal and vertical events is the logarithm of the probability that the obtained distribution is flat [99]:

$$\ln[P_{\mathrm{flat}}(\boldsymbol{n})] = \ln\left[\prod_{i=1}^{N_{\mathrm{bins}}} \underbrace{\frac{\mu_f^{n_i}}{n_i!}\exp\left(-\mu_f\right)}_{\substack{\text{Poisson probability}\\ \text{for a flat distribution}}}\right] = -N_{\mathrm{bins}}\mu_f + \sum_{i=1}^{N_{\mathrm{bins}}}\left[n_i \ln(\mu_f) - \ln(n_i!)\right], \quad (5.2)$$

where $\boldsymbol{n} = \{n_i\}$ are the contents of the histogram's bins, N_{bins} is the overall number of bins and $\mu_f = N_{\mathrm{OM}}^{\mathrm{dir}}/N_{\mathrm{bins}} = \text{const.}$ is the expected number of OMs in each bin of the histogram. For 500 MeV muons with $\rho_s < 5\,\mathrm{m}$, figure 5.3 shows the mean $\ln[P_{\mathrm{flat}}(\boldsymbol{n})]$ as a function of $\cos(\vartheta)$. The dependency of this parameter on the inclination ϑ of the track is clearly visible. The used cut to distinguish vertical and horizontal events is given by [99]

$$\{\ln[P_{\mathrm{flat}}(\boldsymbol{n})]\}_{thr} = -0.0635\,\mathrm{MeV}^{-1}T_s - 237.5. \quad (5.3)$$

All events with $\ln[P_{\mathrm{flat}}(\boldsymbol{n}) < \{\ln[P_{\mathrm{flat}}(\boldsymbol{n})]\}_{thr}|$ are considered to be vertical. A very strict cut is used in a way that only the most vertical events are tagged as vertical (typically a few percent for isotropically distributed events), as the estimation of the track direction is more reliably using the method for horizontal events for all but a few events which are nearly totally vertical.

For all events which are tagged horizontal, again the observation of the dipolar asymmetry of the TOF corrected hit times from figure 5.2 is used: By determining the position $\boldsymbol{r}_{\mathrm{min}}$ of the minimum TOF-corrected hit time on the detector wall, the direction can be defined by connecting this point and the barycenter $\boldsymbol{r}_{bc}$. $\boldsymbol{r}_{\mathrm{min}}$ is determined separately in φ- and in z-direction: φ_{min} is determined by fitting a Gaussian to the φ distribution of the 500 OMs with the smallest first TOF-corrected hit times. Their distribution in z-direction is, apart from the track direction, also influenced by the attenuation of the light in the scintillator and the solid angle of the OMs, as the distances for the photons to travel from the track to the wall vary, dependent on ϑ_s. To counter the influence of these effects on the z-distribution of the 500 OMs with the smallest TOF-corrected hit times, the z-distribution is weighted with an empirical weighting factor for each OM [99]

$$w_i = \frac{\exp\left(-\frac{|\boldsymbol{r}_i - \boldsymbol{r}_{bc}|}{\Lambda_{\mathrm{scat}}}\right)}{1 - \exp(-\mu_i)}, \quad (5.4)$$

where r_i is the position of the respective OM and μ_i is the approximate number of expected photons as calculated by equation (4.6). By fitting the weighted distribution with a Gaussian, z_{min} is determined. Thus, the direction $\hat{\boldsymbol{d}}$ of the track can be estimated from

$$\hat{\boldsymbol{d}} = \frac{\boldsymbol{r}_{bc} - \boldsymbol{r}_{\mathrm{min}}}{|\boldsymbol{r}_{bc} - \boldsymbol{r}_{\mathrm{min}}|}. \quad (5.5)$$

For vertical events, this does not work anymore, as $\boldsymbol{r}_{\mathrm{min}}$ would be on the top/lid of the detector which is too far away to yield any useful information for events in the center of the detector. Thus, the start point of the track is estimated using the idea introduced

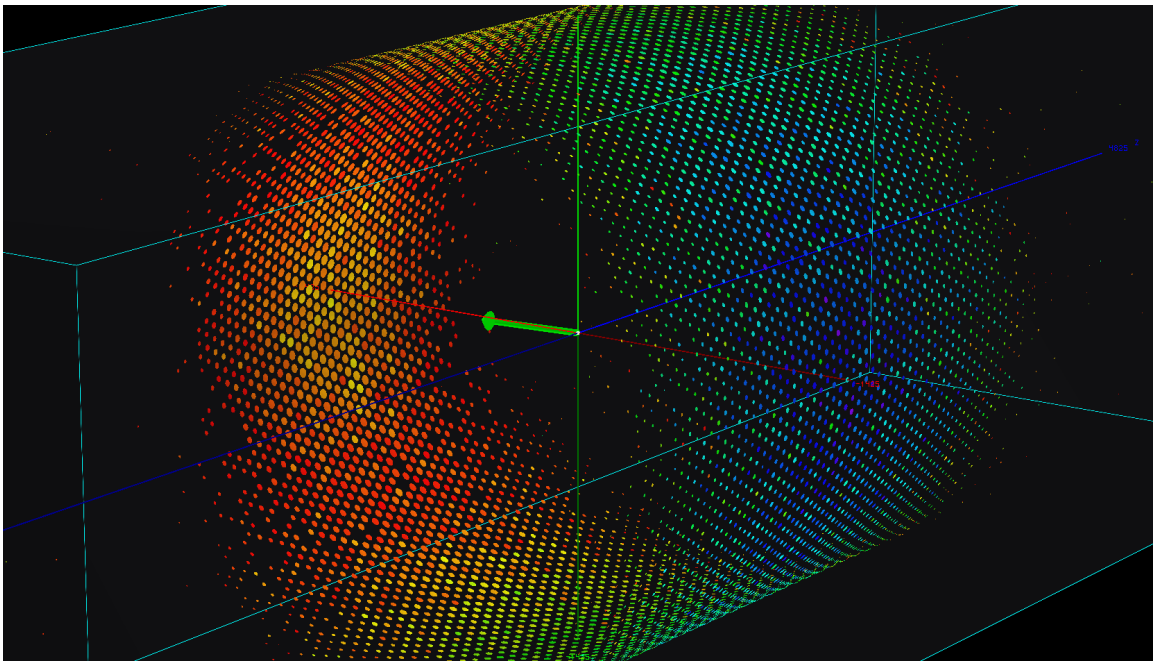

Figure 5.2: LENA event display showing a single muon with initial kinetic energy $T_s = 1\,\mathrm{GeV}$ and start time $t_s = 0\,\mathrm{ns}$ traveling from the center of the detector along the positive x-axis. While the green arrow shows the true muon track, the colored circles show the detector response: The areas of the circles show the charge of the OMs $q_i \in [0, 139]$ photo electrons while the color of the circles shows the TOF corrected (with respect to the barycenter) first hit times t_i^0 of the respective OMs from blue corresponding to $-15\,\mathrm{ns}$ to red corresponding to $10\,\mathrm{ns}$. All OMs with first hit times outside this time range or without hits are not shown.

in figure 5.1. Assuming the particle to travel parallel to a wall, obviously the point on the wall where the first hit occurs is the point closest to the start point $\boldsymbol{r}_s$. Hence, z_s is estimated from the z-position of the OM with the first overall hit. To also reconstruct ρ_s and φ_s, the first hit times in the OM-ring featuring the overall first hit times are fitted with the expectations coming only from the TOF and a point like source [99]:

$$t^0(\varphi_i) = t_s + \frac{n}{c_0}\sqrt{\rho_{\mathrm{OM}}^2 + \rho_s^2 - 2\rho_{\mathrm{OM}}\rho_s\cos(\varphi_i - \varphi_s)}, \tag{5.6}$$

where φ_i is the φ coordinate of the respective OM, ρ_{OM} is the mounting radius of the OMs and $\rho_s = \sqrt{x_s^2 + y_s^2}$ is the radius of the start point. Given this estimate for the start point, the direction can be determined analogously to equation (5.5).
Figure 5.4 shows the distribution of the angular deviations $\delta\alpha$ between the estimated and the true track for a sample of 450 muons with arbitrary directions, $T_s = 500\,\mathrm{MeV}$ and vertices with $\rho_s < 5\,\mathrm{m}$. It is fitted with

$$P(\Delta\alpha|\sigma_\alpha) \propto \sin(\Delta\alpha)\exp\left(-\frac{\Delta\alpha^2}{2\sigma_\alpha^2}\right), \tag{5.7}$$

where σ_α is the obtained resolution assuming a Gaussian distribution. The fit describes the distribution of the events well enough to provide a measure for the resolution of the estimate which was found to be about 17 deg for muons. This is enough to seed the final fits.

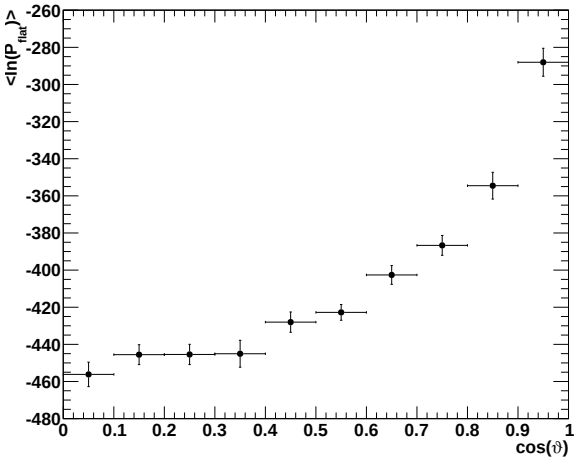

Figure 5.3: The mean $\ln[P_{\text{flat}}(\boldsymbol{n})]$ (compare equation (5.2)) as a function of the cosine of the track's inclination ϑ for a sample of 450 muons with arbitrary directions, $T_s = 500\,\text{MeV}$ and vertices with $\rho_s < 5\,\text{m}$.

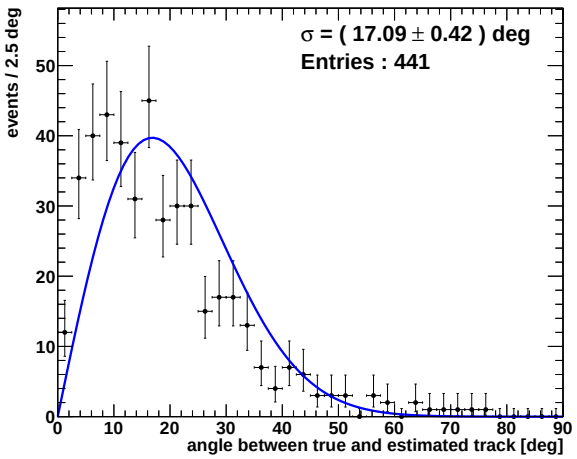

Figure 5.4: The distribution of the angular deviation between the estimated and the true muon track for 500 MeV muons with arbitrary directions and vertices with $\rho_s < 5\,\text{m}$. The obtained distribution is fitted using equation (5.7).

Estimate for the start point of the track:
The start point $\boldsymbol{r}_s$ of the track is estimated using

$$\boldsymbol{r}_s = \boldsymbol{r}_{bc} - \hat{\boldsymbol{d}} \cdot l_{bc}(T_s), \tag{5.8}$$

where $l_{bc}(T_s)$ is the mean distance of the barycenter from the start point of a muon track, which is calculated using a table for muon energy-loss in matter [114].

Estimate for the start time:
The start time t_s of the event is calculated using the same algorithm already presented in section 4.3.

5.3 Likelihood fit

To fit the tracks in the LSc, the same strategy as in section 4.4 is adopted. In this case, the parameters of interest are

$$\boldsymbol{X}_t = \{\boldsymbol{r}_s, t_s, T_s, \vartheta_s, \varphi_s\} \tag{5.9}$$

(see section 5.1) and the data available for the event is dictated by the conservative electronics (see section 4.4)

$$\boldsymbol{D} = \left\{\boldsymbol{q}, \boldsymbol{t^0}\right\}. \tag{5.10}$$

The considerations from section 4.4.1 remain fully valid, thus the charge PDF $P(q|\boldsymbol{X}_t, \boldsymbol{r})$ and the timing PDF $P_t^0(t^0|\boldsymbol{X}_t, \boldsymbol{r}, q)$ for one OM at the position $\boldsymbol{r}$ have to be derived. This is done in section 5.3.1 for the charge PDF and in section 5.3.2 for the timing PDF.

5.3.1 The charge probability density function

The charge probability density function for an OM at the position $\boldsymbol{r}$ to feature q hits is given by the Poisson distribution

$$P(q|\boldsymbol{X}_t, \boldsymbol{r}) = \frac{\mu_t^q}{q!} \exp(-\mu), \tag{5.11}$$

where $\mu_t = \mu_t(\boldsymbol{X}_t, \boldsymbol{r})$ is the expected charge on the OM due to the whole track. It can be calculated by integrating over the expected charge from all track points

$$\mu_t(\boldsymbol{X}_t, \boldsymbol{r}) = \mu_{\mathrm{DN}} + \int_{-\infty}^{\infty} \left(\frac{d\mu_t}{ds}\right) ds \tag{5.12}$$

$$= \mu_{\mathrm{DN}} + \underbrace{\int_{-\infty}^{\infty} \left\{ \mu_{\mathrm{direct}} \left[\boldsymbol{s}, \left\langle \frac{dL}{dx} \right\rangle (s)\right] + \mu_{\mathrm{scat}} \left[\boldsymbol{s}, \left\langle \frac{dL}{dx} \right\rangle (s)\right] \right\} ds}_{=:\mu_{\mathrm{ph}}}, \tag{5.13}$$

where $\boldsymbol{s} = \boldsymbol{r}_s + s \cdot \hat{\boldsymbol{d}}$ is a point on the track, μ_{DN}, μ_{direct} and μ_{scat} are the components of the expected charge from a single point on the track (see section 4.4.2). Furthermore, $\left\langle \frac{dL}{dx} \right\rangle (s)$ is the mean expected number of produced photons per unit track length at the distance s from the vertex. Note that $\left\langle \frac{dL}{dx} \right\rangle$ additionally depends on the particle type and on T_s. As $\left\langle \frac{dL}{dx} \right\rangle$ has a compact support[2], the integration in s has to be evaluated only on this support. To determine $\left\langle \frac{dL}{dx} \right\rangle$, a large number of electrons or muons with a given energy is simulated. The observed numbers of produced photons are successively averaged and tabulated as a function of s. For energies in between the simulated energies, $\left\langle \frac{dL}{dx} \right\rangle$ is calculated from the adjacent simulated energies by linear interpolation. Figure 5.5 shows $\left\langle \frac{dL}{dx} \right\rangle$ as a function of the distance s between the vertex and the point on the track for multiple energies for muons (left) and electrons (right). The obtained $\left\langle \frac{dL}{dx} \right\rangle$ characteristics are quite different: While muons are minimum ionizing during most of their path and feature a peak in light yield at the end of the track (Bragg Peak), the electrons are showering which leads to high light output at the start of the track and a long tail towards large distances due to the finite range of bremsstrahlung photons. Note that the high light yield peak at the end of the muon track does not contribute too strongly to the track fitting as the particle is traveling with a speed lower than the speed of light in the LSc at this point of the track. Thus, many of these photons from this peak will not be first photons.

5.3.2 The timing probability density function

To calculate the PDF $P_t^0(t^0|\boldsymbol{X}_t, \boldsymbol{r}, q)$ for the probability to observe the first photon on an OM at the time t^0, first the PDF $P_t(t|\boldsymbol{X}_t, \boldsymbol{r})$ to obtain any photon at the time t is calculated. $P_t^0(t^0|\boldsymbol{X}_t, \boldsymbol{r}, q)$ is successively calculated using equation (4.45).

$P_t(t|\boldsymbol{X}_t, \boldsymbol{r})$ can be calculated from a weighted average over the PDFs from all track

[2] Therefore there exist distances to the vertex $s_{\min}$ and $s_{\max}$, with $\left\langle \frac{dL}{dx} \right\rangle (s) = 0$ for $s \notin [s_{\min}, s_{\max}]$. Note that for electron showers $s_{\min} < 0$ is possible due to backscattering of shower particles. For showering particles $s_{\max}$ does generally not coincide with the endpoint of the primary particle.

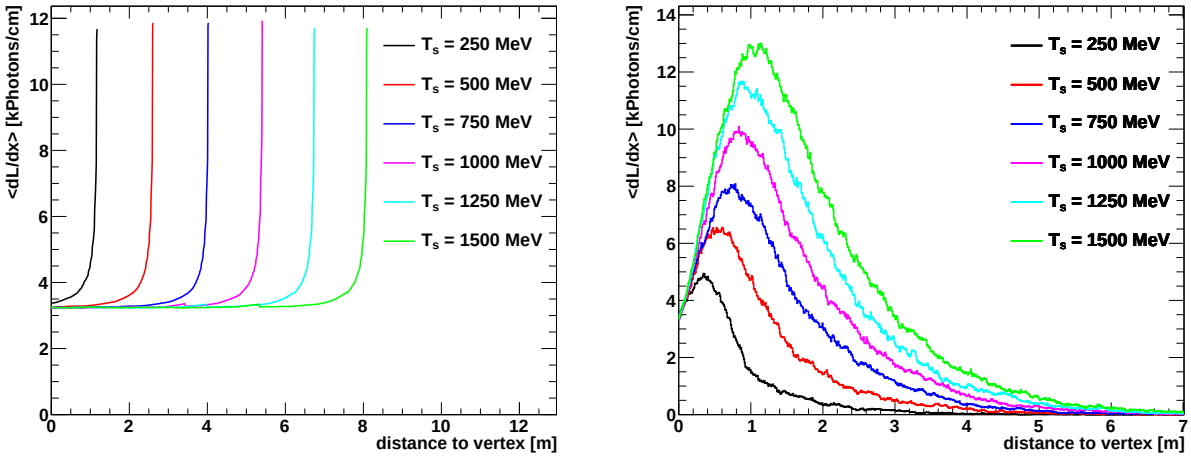

Figure 5.5: The mean expected number of produced photons per unit track length $\left\langle \frac{dL}{dx} \right\rangle$ as a function of the distance between the vertex and the position of the particle for muons (left) and electrons (right) for various initial kinetic energies T_s. The observed difference is due to the different energy loss mechanisms of the particles: While muons are minimum ionizing during most of their track, electrons loose most of their energy due to bremsstrahlung and thus tend to produce showers.

points, with the weighting factor being the charge μ_{ph} due to detected photons expected from a given point (see equation (5.13)):

$$P_t(t|\boldsymbol{X}_t, \boldsymbol{r}) = \frac{1}{\mu_t} \left\{ \mu_{\text{ph}} \int_{-\infty}^{\infty} ds \left(\frac{d\mu_t}{ds} \right) P_{1234} \left[t - \left(t_s + t_p(s) + \frac{n}{c_0} |\boldsymbol{s} - \boldsymbol{r}| \right) \middle| \boldsymbol{s}, \boldsymbol{r} \right] + \frac{\mu_{\text{DN}}}{\Delta t_{\text{event}}} \right\},$$

where P_{1234} is defined in equation (4.41) and $t_p(s)$ is the time the particle takes to reach $\boldsymbol{s}$ from the vertex. The latter is also extracted from the simulation and stored alongside the $\left\langle \frac{dL}{dx} \right\rangle$ table. Note that it is not sufficient to approximate $v \approx c_0$, as the particle gets slower towards the end of its track. As the result of the integration depends on all seven fit parameters, it cannot be tabulated but has to be calculated on the fly. Hence, the computation time required to fit a track drastically increases compared to a fit to a point-like event.

5.4 Performance

To evaluate the performance of the track fitting, the same strategy as in section 4.5 is used: The reconstruction is applied to simulated events and the obtained results are compared to the true values of the MC.
As the dark noise (DN) was found to affect only events with true initial kinetic energies $T_s^{\text{true}} \lesssim 1\,\text{MeV}$ and the considered tracks feature energies of at least ∼100 MeV no DN was added to the simulated events. Furthermore, only contained particles are used as candidates for the reconstruction to obtain an event sample without significant edge effects. An event is tagged as contained, if the start point and the end point of the primary particle are inside the fiducial volume ($|z| < 25\,\text{m}$, $\rho < 14\,\text{m}$) or if all particles (except neutrinos) of the event are always in the fiducial volume for muon and electron type events, respectively. The particles are simulated with arbitrary directions and arbitrary start points in

a volume with $|z_s| < 25\,\mathrm{m}$ and $\rho_s < 12\,\mathrm{m}$. While the former restriction serves to suppress the influence of the lid and the bottom on the PDF (see section 4.1), the latter requirement significantly reduces the amount of computation time: Due to the restricted volume used to start the events, the fraction of contained events is significantly increased and thus the number of simulated events required to get a large enough sample of contained events is reduced. Nevertheless, the required computation time was enormous, thus Kai Loo[3] performed the simulations on the Finnish Grid Infrastructure (FGI)[4]. The evaluation of the data was done locally by the author of this thesis.

This study deals with two different types of tracks: The performance obtained for muons is presented in section 5.4.1 while the electron performance is discussed in section 5.4.2.

5.4.1 Muons

The performance of the fit is studied using two distinct sets of muon events:

- **Constant energy:** First, a set of 2450 simulated $T_s^{\mathrm{true}} = 500\,\mathrm{MeV}$ muon type events is used to derive the shape of the deviation distributions with sufficient statistics. From these events, 2367 events are contained and can thus be used for the analysis.
- **Distributed energy:** Additionally, a set of 4950 muon events (4697 contained) with $100\,\mathrm{MeV} < T_s^{\mathrm{true}} < 1\,\mathrm{GeV}$ is used to study the evolution of the performance as a function of the initial kinetic energy of the muon.

Fraction of converged events:
From the 2367 contained events of the constant energy data set, 2165 featured a converged fit. This corresponds to a fraction of converged fits of $(91.5 \pm 0.6)\,\%$. The evolution of the fraction of converged events with energy is displayed in figure 5.6. As the assumptions used to calculate the PDF for the fit (see section 5.1) deteriorate with rising energy, the fraction of converged events weakly declines with rising T_s^{true}. To eliminate the influence of events which are not properly fitted from the performance evaluation, the remainder of this section deals with converged fits only.

Start point resolution:
Figure 5.7 shows the distribution of the distance between the true and the reconstructed start point. It is fitted assuming a Gaussian distribution with equal, constant standard deviation for all three directions (confer equation (4.46)). Note that these assumptions are not fulfilled here, which is reflected in the rather bad quality of the fit. Nevertheless, the result of the fit allows for an estimation of the start point resolution with $\sigma \approx 3.7\,\mathrm{cm}$. This result is only slightly below the values obtained for point fits of 3 MeV electron events (confer section 4.5.1) indicating that the increase in photon statistics is compensated by the more complex event topology. Similar to the findings for point fits using the conservative electronics (confer section 4.5.2), there are significant outliers in the distributions: $(1.66 \pm 0.3)\,\%$ of all events feature a nearly flat distribution with $30\,\mathrm{cm} < |\boldsymbol{r}_s^{\mathrm{true}} - \boldsymbol{r}_s| \lesssim 300\,\mathrm{cm}$. These outliers were found to appear especially at higher radii: The distribution for events with $\rho_s < 6\,\mathrm{m}$ (red open dots in figure 5.7) does not

[3] University of Jyväskylä, Department of Physics, Finland
[4] This research was undertaken on Finnish Grid Infrastructure (FGI) resources.

feature these outliers even though it contains ∼28 % of all events.
To further investigate the properties of the outliers, figure 5.8 shows the distribution of the deviations between the true and the reconstructed start point projected on the true track. Note that there are an additional 28 events (corresponding to $(1.29^{+0.29}_{-0.24})$ % of all events) with deviations below −30 cm which are not shown in figure 5.8. Thus, there is a significant tail for start points shifted in track direction showing the difficulty to properly reconstruct the start point in the coordinate along the track. This difficulty arises, as the reconstruction of the particle's vertex relies on a very asymmetric light front (compare figure 5.1). It is also illustrated by the resolution obtained by a Gaussian fit: (4.53 ± 0.07) cm. It is degraded compared to the overall resolution obtained from figure 5.7. Note, that again no outliers are observed for muons with $\rho_s < 6$ m. For the events in the main peak, a small systematic shift of about 3 cm in anti-track direction is observed.
Figure 5.9 shows the dependency of the vertex resolution as a function of the true initial kinetic energy of the muon. The optimum start point resolution is achieved around ∼0.25 GeV while the resolution deteriorates for higher and lower energies. Apart from that, also the contributions of the deviations of the reconstructed vertex projected on the track and of the deviations of the reconstructed vertex perpendicular to the track to the vertex resolution are shown in figure 5.9. They show distinctly different behaviors: The parallel part of the vertex resolution monotonously deteriorates with energy due to the increasing deviations of the true track length from the mean track length. It is mainly responsible for the degradation of the overall resolution with rising energy. The perpendicular part of the resolution in contrast only slightly worsens towards higher energies but shows a significant degradation for $T_s^{\text{true}} < 0.4$ MeV which is mainly responsible for the deterioration of the total resolution towards 0.1 MeV. This degradation is mostly due to the degradation in angular resolution for lower energies (confer figure 5.12).

Start time resolution:
Closely connected to the start point resolution is the start time resolution, as a good timing information is required to triangulate the start point. Figure 5.10 shows the distribution of the deviations of the true from the reconstructed start time. While most of the data can be well described with a Gaussian of width 0.09 ns, there are again outliers on the ∼1 % level where the reconstructed start time is significantly too large. Most of the events featuring a large vertex deviation along the true track also feature a badly reconstructed start time showing the correlation of both variables. As already observed for the vertex, this deviations mostly appear at higher radii. The start time resolution degrades with rising energy (see figure 5.11) corresponding to the behavior for the parallel component of the vertex resolution (confer figure 5.9).

Angular resolution:
While all the coordinates mentioned above were already relevant for point fits, an angular resolution requires an extended object to fit. The angular deviations between true and reconstructed tracks are shown in figure 5.12. A fit with equation (5.7) reveals an angular resolution of about 2.15 deg showing a tremendous improvement compared to the primary estimates (confer figure 5.4). Again, a few muon tracks at high radii were found to produce outliers. As shown in figure 5.13, the angular resolution improves with rising initial kinetic energy due to the increased length of the track providing a larger "lever arm".

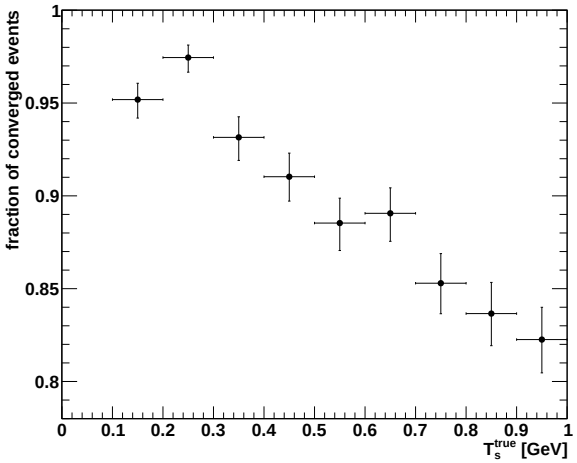

Figure 5.6: The fraction of converged events as a function of the true initial kinetic energy T_s^{true} of the particle. Note that the errors are statistical only and the horizontal error bars indicate the width of the respective bin.

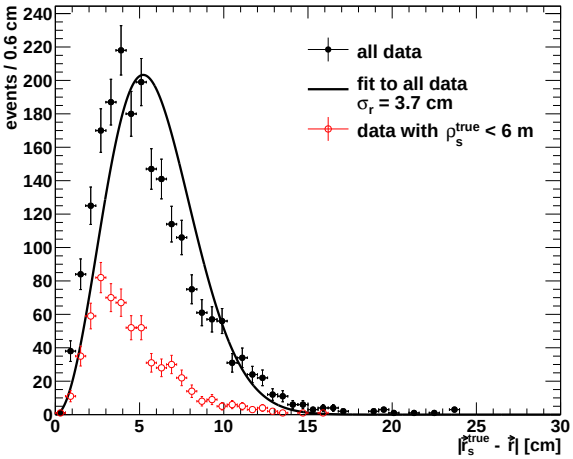

Figure 5.7: The distribution of the distance $|\boldsymbol{r}_s^{\text{true}} - \boldsymbol{r}|$ between the true and the reconstructed start point of the muon track for 2165 muon events with $T_s^{\text{true}} = 500\,\text{MeV}$ for the whole fiducial volume and for muons onto which additionally the requirement $\rho_s^{\text{true}} < 6\,\text{m}$ is imposed. The black line shows the result of a fit according to equation (4.46) to the full data set. 36 events of the full data set feature distances above 30 cm and are not shown in this plot.

Assuming that the evolution with energy can be explained using a simple model which includes resolutions for the start point and the end point and which assumes the track length to be proportional to the energy, the angular resolution should scale with $1/T_s^{\text{true}}$. Figure 5.13 shows a fit to the obtained resolutions with the function $A/(T_s^{\text{true}} + B) + C$. The resulting C is not compatible with zero showing that the simple model is insufficient to describe the obtained angular resolutions. This non-negligible constant is most probably due to the deviation of the true particle trajectory from a straight line due to multiple scattering at the scintillator nuclei.

Energy resolution:
Figure 5.14 shows the distribution of the differences between the true and the reconstructed energy. The distribution features an unexpected structure containing events where the energy was reconstructed about 50 MeV too low and which does not vanish from restricting ρ_s^{true} to 6 m. To determine the origin of this second peak, figure 5.15 plots the energy deviations as a function of $|z_s^{\text{true}}|$, showing that this additional distribution arises from events with $|z_s^{\text{true}}| \gtrsim 10\,\text{m}$. Further investigation shows that most of the events in the additional peaks feature a rather small ρ_s^{true}. The suspected reason for the additional structure is the onset of the influence of the lid or the bottom. This effect shows up much earlier for track fits than for point fits as due to the higher number of produced photons more of them reach the region close to the lid and the bottom. Close to the walls, the effect is suppressed due to the reduced field of view of the LCs. To determine the energy resolution as a function of the energy, a Gaussian function was fit-

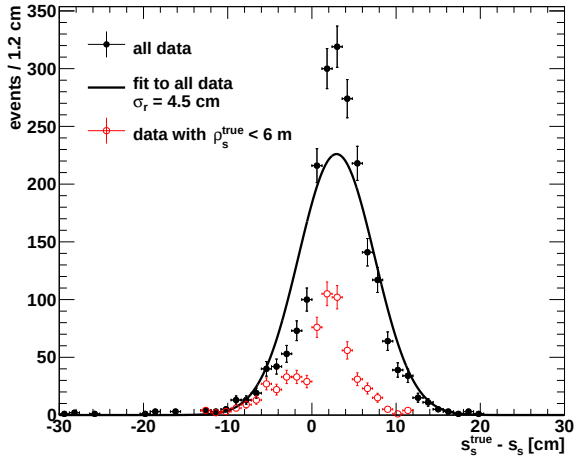

Figure 5.8: The distribution of the deviation between the true and the reconstructed start point of the muon track projected on the true muon track for 2165 muon events with $T_s^{\text{true}} = 500\,\text{MeV}$ for the whole fiducial volume and for muons on which additionally the requirement $\rho_s^{\text{true}} < 6\,\text{m}$ is imposed. The corresponding coordinate s is defined in equation (5.12). The black line shows the result of a Gaussian fit to the full data set. 28 events of the full data set feature deviations below -30 cm and are not shown in this plot.

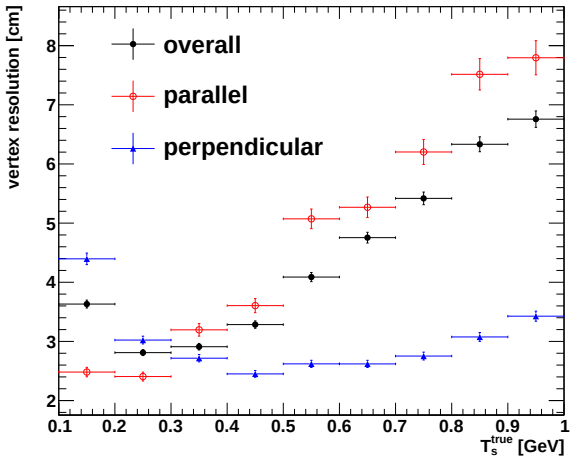

Figure 5.9: The obtained vertex resolution as a function of the true initial kinetic energy T_s^{true} of the muon. Additionally, the contributions to the vertex resolution resulting from the deviations parallel and perpendicular to the track direction are shown. Note that the errors are statistical only and the horizontal error bars indicate the width of the respective bin.

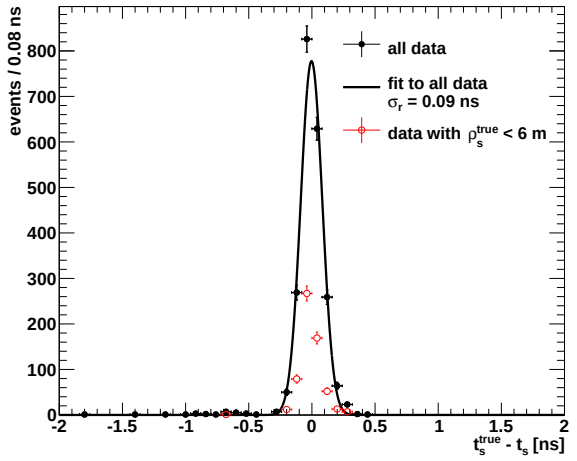

Figure 5.10: The distribution of the difference $t_s^{\text{true}} - t_s$ between the true and the reconstructed start time of the muon track for 2165 muon events with $T_s^{\text{true}} = 500\,\text{MeV}$ for the whole fiducial volume and for muons on which additionally the requirement $\rho_s^{\text{true}} < 6\,\text{m}$ is imposed. The black line shows the result of a Gaussian fit to the full data set. 9 events of the full data set feature time differences below -2 ns and are not shown in this plot.

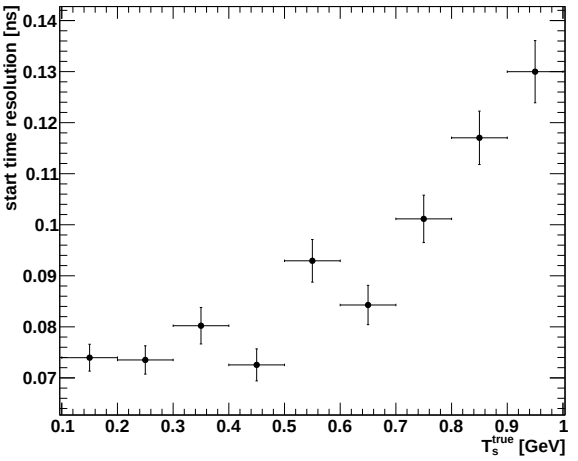

Figure 5.11: The start time resolution as a function of the true initial kinetic energy T_s^{true} of the muon. Note that the errors are statistical only and the horizontal error bars indicate the width of the respective bin.

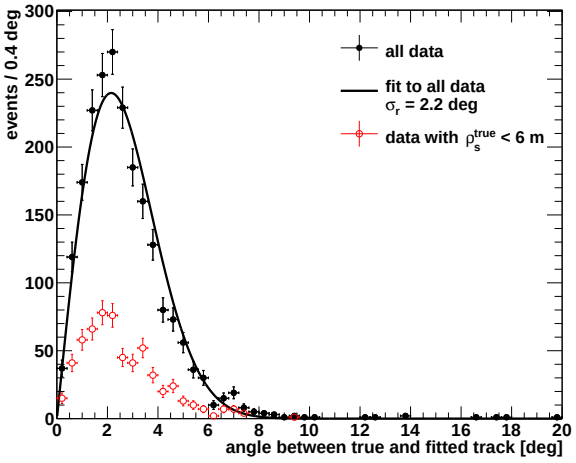

Figure 5.12: The distribution of the angle between the true and the reconstructed muon track for 2165 muon events with $T_s^{\text{true}} = 500\,\text{MeV}$ for the whole fiducial volume and for muons onto which additionally the requirement $\rho_s^{\text{true}} < 6\,\text{m}$ is imposed. The black line shows the result of a fit according to equation (5.7) to the full data set. 31 events of the full data set feature deviations above 20 deg and are not shown in this plot.

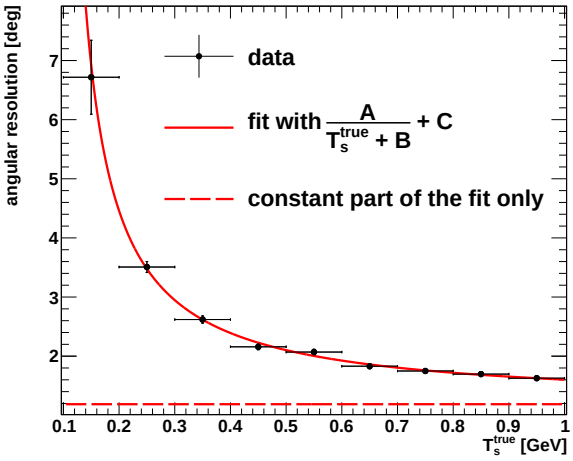

Figure 5.13: The angular resolution as a function of the true initial kinetic energy T_s^{true} of the muon. The red curve shows a fit with $A/(T_s^{\text{true}} + B) + C$. The resulting parameters are $A = (0.38 \pm 0.13)\,\text{deg/MeV}$ and $B = (-0.08 \pm 0.06)\,\text{MeV}$. The resolution corresponding to $C = (1.19 \pm 0.14)\,\text{deg}$ is indicated by the horizontal dashed red line. Note that the errors are statistical only and the horizontal error bars indicate the width of the respective bin.

ted to the obtained distribution in each energy bin in the range $|T_s^{\text{true}} - T_s| < 100\,\text{MeV}$. The result is shown in figure 5.16. Due to the non-Gaussian parts of the distribution the (statistic only) error bars are underestimating the total error of the energy resolution. Nevertheless, two safe conclusions can be drawn from figure 5.16: The relative resolution in initial kinetic energy is of order 1 % and it does not change drastically with the true initial kinetic energy.

5.4.2 Electrons

A fit to an electron track takes extremely long. Thus, in contrast to the muon case, only a sample of 2400 simulated electron events with $T_s^{\text{true}} = 500\,\text{MeV}$ is evaluated here. Of the 2400 simulated events, 2221 events are contained in the detector and can thus be used for the fit.

Fraction of contained events:
Of the 2221 simulated events which where contained, 2131 events feature a converged fit which corresponds to $(95.9^{+0.4}_{-0.5})$ %. A comparison of this result to the corresponding result obtained for muons in section 5.4.1 shows that a higher fraction of electron events feature a converged fit compared to muon events. This is due to the different shapes of the $\left\langle \frac{dL}{dx} \right\rangle$-distributions of electrons and muons (compare figure 5.5). As electrons do not feature the distinct peak at the end of their tracks, they are much more tolerant to range straggling compared to muons.

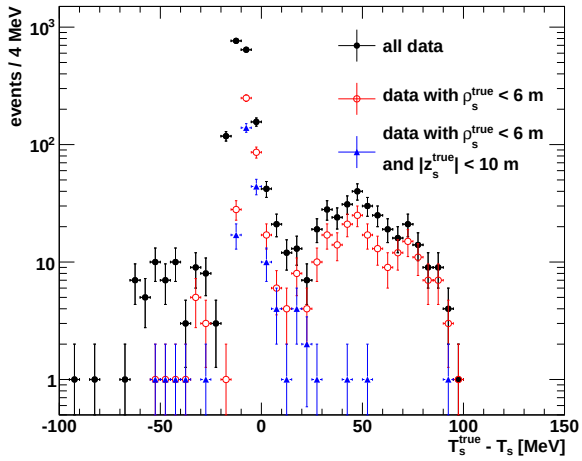

Figure 5.14: The distribution of the difference between the true and the reconstructed initial kinetic energy of the muon track for 2165 muon events with $T_s^{\text{true}} = 500\,\text{MeV}$ for the whole fiducial volume and for muons on which additionally the requirement $\rho_s^{\text{true}} < 6\,\text{m}$ is imposed. Furthermore, a data set with $|z_s^{\text{true}}| < 10\,\text{m}$ is shown. 35 events of the full data set feature absolute deviations above 150 MeV and are not shown in this plot.

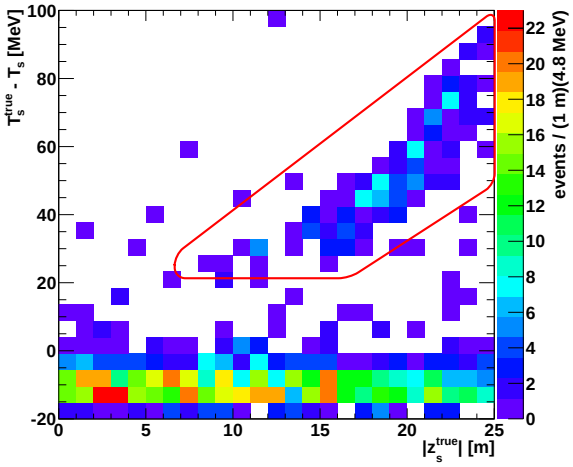

Figure 5.15: The difference between the true and the reconstructed initial kinetic energy as a function of the absolute true z coordinate of the vertex for 2165 muon events with $T_s^{\text{true}} = 500\,\text{MeV}$. The red contour shows the location of the events belonging to the right sub-structure in figure 5.14.

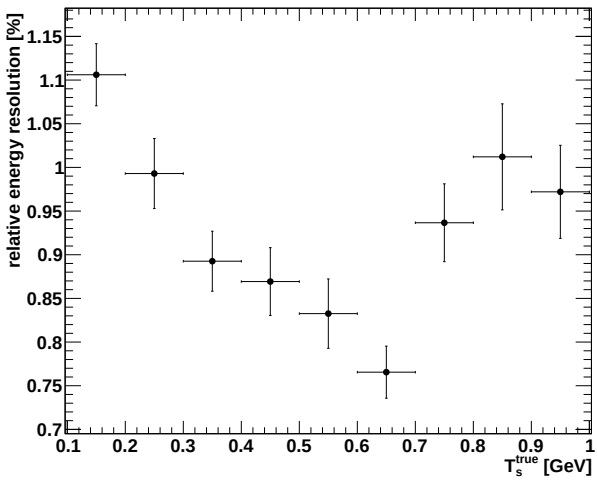

Figure 5.16: The energy resolution as a function of the true initial kinetic energy T_s^{true} of the muon. Note that the errors are statistical only and the horizontal error bars indicate the width of the respective bin.

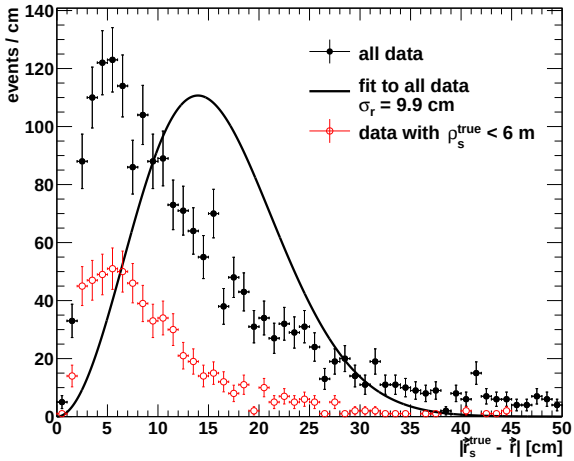

Figure 5.17: The distribution of the distance between the true and the reconstructed start point of the electron track for 2131 electron events with $T_s^{\text{true}} = 500\,\text{MeV}$ for the whole fiducial volume and for electrons on which additionally the requirement $\rho_s^{\text{true}} < 6\,\text{m}$ is imposed. The black line shows the result of a fit according to equation (4.46) to the full data set. 270 events of the full data set feature distances above 50 cm and are not shown in this plot.

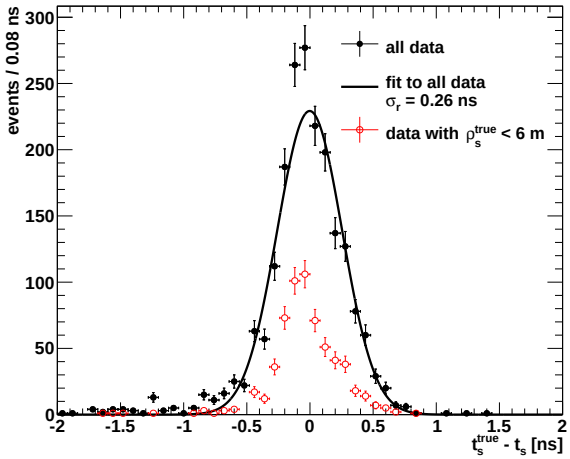

Figure 5.18: The distribution of the difference between the true and the reconstructed start time of the electron event for 2131 electron events with $T_s^{\text{true}} = 500\,\text{MeV}$ for the whole fiducial volume and for electrons on which additionally the requirement $\rho_s^{\text{true}} < 6\,\text{m}$ is imposed. The black line shows the result of a Gaussian fit to the full data set. 151 events of the full data set feature absolute deviations above 2 ns and are not shown in this plot.

Start point resolution:
Figure 5.17 shows the distribution of the distance between the true and the reconstructed start point. It is fitted assuming a Gaussian distribution with an equal, constant standard deviation for all three directions (confer equation (4.46)). Note, that these assumptions are not fulfilled here, which is reflected in the rather bad quality of the fit. The result of the fit only allows for a rough estimation of the start-point resolution with $\sigma \approx 10\,\text{cm}$ which is significantly above, both, the corresponding result for muons (see section 5.4.1) and the resolution obtained for pointlike events with $T_s^{\text{true}} \sim 3\,\text{MeV}$. This difference can be explained by the high event by event fluctuations of electron events at the given energy where showering plays an important role but no full showers with multiple generations are expected. Additionally, the data-set features a much higher number of outliers compared to the corresponding muon data-set: 270 converged events are not shown in figure 5.17 as their distance to the true vertex is too large, corresponding to $(12.7 \pm 0.7)\,\%$ of all events (compared to 1.3 % for the muon sample). By restricting the sample to events with $\rho_s^{\text{true}} < 6\,\text{m}$, the fraction of events being in the overflow of the histogram reduces to about 1.3 % (compared to no visible outliers for the muon sample). This shows two aspects: First of all, electron events produce more outliers due to the complicated and strongly varying energy-loss which was already discussed above. Secondly, the higher fraction of outliers compared to the muon events is at least partly caused by the fact, that the containment cut (see section 5.4) removes a higher fraction of muon events close to the detector boundary compared to electron events as the mean muon track length at a

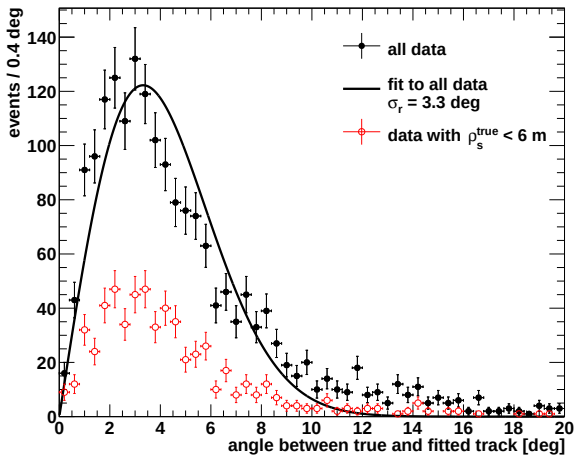

Figure 5.19: The distribution of the angle between the true and the fitted electron track for 2131 electron events with $T_s^{\text{true}} = 500\,\text{MeV}$ for the whole fiducial volume and for electrons onto which additionally the requirement $\rho_s^{\text{true}} < 6\,\text{m}$ is imposed. The black line shows the result of a fit according to equation (5.7) to the full data set. 310 events of the full data set feature deviations above 20 deg and are not shown in this plot.

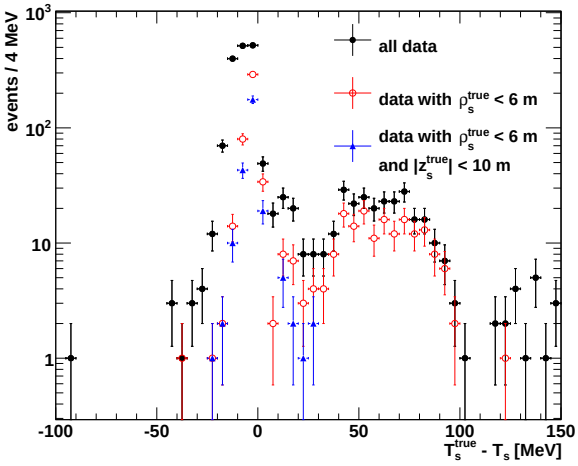

Figure 5.20: The distribution of the difference between the true and the reconstructed initial kinetic energy of the electron track for 2131 electron events with $T_s^{\text{true}} = 500\,\text{MeV}$ for the whole fiducial volume and for electrons onto which additionally the requirement $\rho_s^{\text{true}} < 6\,\text{m}$ is imposed. Furthermore, a data set with $|z_s^{\text{true}}| < 10\,\text{m}$ is shown. 212 events of the full data set feature deviations outside the plotted range and are not shown in this plot.

given energy is longer than the longitudinal extension of the event induced by the electron.

Start time resolution:
The distribution of the differences between the true and the reconstructed start time of the electron is shown in figure 5.18. The standard deviation of the fitted Gaussian is 0.26 ns. Again, a deterioration of the resolution is observed compared to the corresponding muon data-set. As the start time and the vertex of the event are highly correlated, this corresponds to the deterioration in vertex resolution. Again, 151 events feature a reconstructed start time with a deviation which is outside the histogram range, corresponding to $(7.1 \pm 0.6)\,\%$ of all converged events. For events with $\rho_s^{\text{true}} < 6\,\text{m}$, this fraction reduces about 0.3 %. Thus, for the start time, the vast majority of badly reconstructed events are events close to the detector boundaries.

Angular resolution:
Figure 5.19 shows the distribution of the deviation of the fitted from the true momentum direction of the primary electron. A fit with equation (5.7) reveals an angular resolution of about 3.3 deg. Comparing this result again with the result for the corresponding muon data-set, which features an angular resolution of 2.2 deg, shows a small deterioration of the obtained angular resolution. The degradation in resolution is much smaller compared to the vertex resolution, which shows that the direction of an event is less dependent on the energy loss of the particle compared to the position of the event. The angular deviation distribution also features some outliers: 310 events feature an angular deviation of more than 20 deg corresponding to $(14.5 \pm 0.8)\,\%$. These outliers basically feature a flat

distribution in angle and also contain events with a nearly inverted track direction even though counter measures are in place to prevent this for electron events (for an in depth discussion see [99], Section 5.3). Again, this problem is strongly reduced to about 3 % by requiring $\rho_s^{\text{true}} < 6\,\text{m}$.

Energy reconstruction
Finally, figure 5.20 shows the distributions of the obtained deviations between true and reconstructed initial kinetic energy of the electron event. It features the same additional peak which was already discovered in the muon sample (compare section 5.4.1) and which again does not vanish by the radius cut. The obtained two-dimensional distribution of the deviation in kinetic energy as a function of the true absolute z-coordinate of the vertex is very close to figure 5.15. Hence, two conclusions can be drawn: Firstly, this effect is not only a problem of the muon-track fit and secondly, the reason for this effect is likely the same as already discussed in section 5.4.1, i.e., the onset of the influence of the lid and the bottom spoils the energy resolution.

In summary, the single-electron reconstruction features a degraded performance compared to the single-muon reconstruction which is due to the high event by event variability of the energy depositions and thus of the light yield of electron events. This also leads to a significant amount of events which are only badly reconstructed.

Chapter 6

Reconstruction of high energy neutrino events

One option to determine the neutrino mass hierarchy and to look for CP-violation is a long-baseline neutrino beam, like the proposed $d_{\mathrm{CN2PY}} = 2300\,\mathrm{km}$ conventional neutrino beam from CERN to Pyhäsalmi (CN2PY) (confer section 1.4). As the most important oscillation channel for a conventional beam is the $\nu_\mu \rightarrow \nu_e$ oscillation channel, methods to discriminate the signal (ν_e-CC interactions) from all kind of NC and CC background events need to be developed (see section 3.2.7). Up to now, this is done using a MVA based on BDTs which works on parameters determined from the overall, TOF-corrected, photon pulse [100]. As muon events can be relatively well identified using their decay signature and their peculiar pulse shape caused by the long muon track and as ν_τ-CC events are relatively rare, the focus in the following discussion is on the discrimination between $\overset{(-)}{\nu}_e$-CC and NC interactions which both produce relatively well confined interactions.
Looking at chapter 5, where the reconstruction of a single track was discussed, the first approach to discriminate between NC and ν_e-CC events would be to reconstruct the post-GeV neutrino events using a likelihood fit and use the resulting minimum likelihood values for discrimination. GeV neutrino interactions are, however, much more complicated (confer section 2.1.2) than single particle tracks: While low energy QEL scattering can be well described with a single track and a point-like vertex [99], at post-GeV energies DIS interactions are dominant, leading to events with much more particles in the exit channel. Figure 6.1 shows an example for a deep inelastic CC-ν_e event featuring multiple showers with additional pions and protons. The increased complexity also requires an adaption of the simulation which is presented in section 6.1.
The complicated event structure of post-GeV neutrino interactions leads to two obstacles currently preventing the use of the method detailed in chapter 5: First, to set up a fit, a model for the event needs to be available. As there are many different possible outcomes of such an event the sheer number of possibilities prohibits using an approach where each possible model is fitted and finally the "correct" model is determined using likelihood ratios. Furthermore, even if a model would be at hand, the problem how to determine appropriate start parameters for the free parameters would persist. Thus, to fit the event, the basic properties of the event need to be established first which leads to a different approach here:
First, the overall event is split into a primary event and multiple secondary events due to decays of instable particles or neutron captures. The required clustering algorithm is

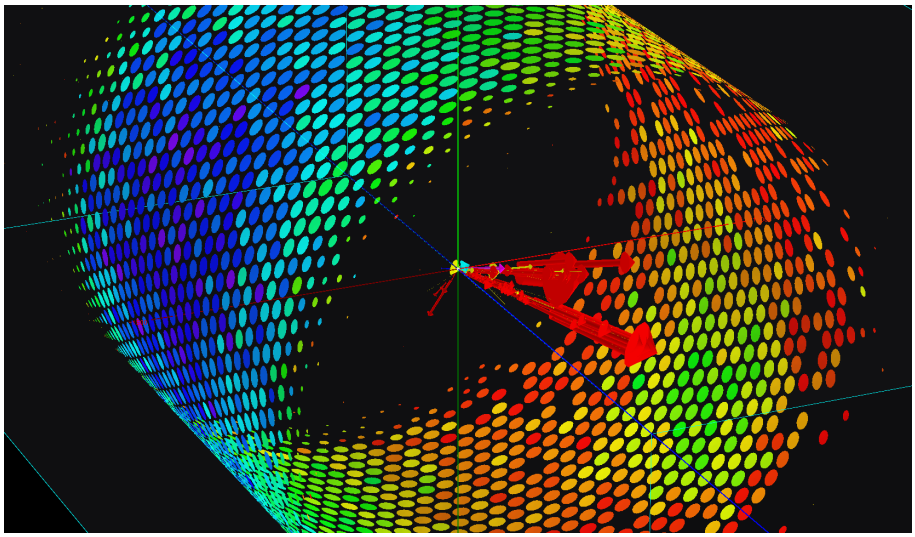

Figure 6.1: LENA event display showing a DIS ν_e-CC event. The interaction vertex is in the center of the detector. The colored circles show the detector response: The areas of the circles show the charge of the OMs $q_i \in [0, 240\,\text{photo-electrons}]$. The color of the circles shows the TOF corrected (with respect to the barycenter) first hit times t_i^0 of the respective OMs from blue corresponding to $-10\,\text{ns}$ to red corresponding to $10\,\text{ns}$. All OMs with first hit times outside this time range or without hits are not shown. The arrows display the MC-truth information: They connect the vertex and the end point of a particle's trajectory. Their thickness indicates the kinetic energy of the particle while their color indicates the particle type: Red arrows indicate $e^{\pm}$, violet arrows $\pi^{\pm}$, yellow arrows γ-rays and light blue arrows protons.

presented in section 6.2. Next, a simple energy reconstruction (see section 6.3) is done. Successively, an algorithm is used which creates an image of an event, i.e. which associates to each point in the detector volume a figure of merit (FOM) which is correlated to the probability that a photon was emitted from this point. Currently, two algorithms for this purpose are in development: One was invented by Björn Wonsak from the University of Hamburg [115]. It assumes one point on the track to be known and then superimposes "drop-like" probability contours for each registered hit. An alternative is the so-called Backtracking approach which is presented in section 6.4. A by-product of this algorithm allows to determine the vertex position of the event. Doing a TOF-correction with respect to the vertex, it is possible to derive the number and the direction of the secondary tracks by searching for clusters of OMs with minima in the TOF-corrected first hit-time distribution as discussed in section 6.5. The results of this algorithm can be used to increase the performance of LENA as a far detector for the CN2PY beam as discussed in section 6.6.

6.1 Simulation of full neutrino events

The basic geometry of the Geant4 based simulation used in this section corresponds to the simulation set-up described in section 4.1. However, to reduce the required computation time for the simulation, instead of ∼30 000 PMTs with 12" diameter, 13 472 PMTs with 20" diameter are used in the simulation. The effect of the LCs was taken into account

using the same approach as in section 4.1: The OMs were simulated as light sensitive disks corresponding to the apertures of the LCs and an angle dependent detection efficiency was applied. Using this set-up, the light-yield is slightly reduced compared to section 4.1 which is not relevant here[1], as the high energy events produce enough light anyhow.

The high-energy neutrino interactions cannot be simulated in Geant4. Hence, GENIE [42] was used to simulate the neutrino interactions in LAB. The GENIE simulations were done by Randolph Möllenberg [41]. For each event, a list of particles[2] along with their 4-momenta is produced. The particles in the Geant4 based simulation are successively generated according to this list. As the purpose of this study was to determine the capabilities of LENA when used as a far detector for the CN2PY beam, the incident neutrino direction $\hat{\boldsymbol{d}}_\nu$ is given by the connection between CERN and Pyhäsalmi:

$$\hat{\boldsymbol{d}}_\nu = \begin{pmatrix} \sin(\alpha/2) \\ 0 \\ \cos(\alpha/2) \end{pmatrix} \approx \begin{pmatrix} 0.98 \\ 0 \\ 0.18 \end{pmatrix}, \tag{6.1}$$

where $\alpha \cong d_{\mathrm{CN2PY}}/r_{\mathrm{earth}}$ is the angle spanned between the surface in CERN and the surface in Pyhäsalmi and r_{earth} is the earth radius. As the aim of the study was to determine the basic performance parameters for LENA and to develop the corresponding algorithms, all events were assumed to originate from the center of the detector. Additionally, to cover all relevant energies, the samples were generated with a specially created incident neutrino spectrum to yield a flat energy spectrum with $E_\nu^{\mathrm{true}} \in [1\,\mathrm{GeV}, 10\,\mathrm{GeV}]$, i.e. the total distribution (NC+CC) of the energies of the interacted neutrinos is flat.

To obtain sufficient statistics, Kai Loo[3] again performed the simulations on the Finnish Grid Infrastructure (FGI)[4]. Thus, a sample of nearly 100 000 ν_e-CC and ν_μ-CC interactions, 50 000 ν_τ-CC interactions and 140 000 NC interactions could be obtained. The evaluation of the data was done locally by the author of the thesis.

6.2 Clustering

Before an in depth analysis is possible, the event resulting from the simulation has to be split up into a primary event and (possibly) multiple secondary events due to the decay of unstable particles or due to the energy released by neutron captures. Thus, when analyzing the primary event, the signal considered does not feature a strong background due to decay signatures. Additionally, the number of decay events and the different types of decay events already provide a handle on the primary event. Especially decay events corresponding to muon decays are relevant, as they spotlight the presence of muons and mark the end of their tracks.
The clustering algorithm which is used to split the simulated events into its constituents is presented in section 6.2.1. Successively, the performance of the algorithm is discussed using the example of a muon decay search in section 6.2.2.

[1] The reduced light yield, however, requires a recalibration of the detector.

[2] Only particles which are long lived enough to be tracked by Geant4 were put in this list. Shorter lived particles were handled by the event generator.

[3] University of Jyväskylä, Department of Physics, Finland

[4] This research was undertaken on Finnish Grid Infrastructure (FGI) resources.

Parameter	Symbol	Value
Width of cluster candidate window	Δt_{pre}	100 ns
Seed threshold	p_{seed}	10^{-10}
Threshold to add window	p_{add}	10^{-2}
Minimum charge of cluster candidate	q_{thr}	5 p.e.
Window for cluster splitting	Δt_f	20 ns
Threshold for cluster splitting	Δf_{thr}	1000 p.e./ns
Cluster end threshold	Δf_{end}	100 p.e./ns
Inhibit after the start of the cluster candidate	t_{no}	200 ns

Table 6.1: The values of the parameters used in the clustering algorithm for the evaluation of the high-energy neutrino events. A detailed description of the parameters can be found in the text.

6.2.1 Algorithm

First of all, note that clustering is intrinsically not possible by relying only on first hits, as the primary event generally illuminates the whole detector. On the other hand, as discussed in section 5.1, at the given high occupancies on the OMs, no reconstruction of the arrival times of single photons will be possible. Thus, for the clustering algorithm, a hybrid approach is used: Assuming that FADCs will be used, their traces basically correspond to the histogrammed photon arrival times. Thus, instead of using the photon arrival times one by one as done before, only their histogram will be used. Additionally note that the clustering can be adapted by changing various parameters. The set of parameters used for the analysis of the high energy neutrino events is shown in table 6.1.

In a first step, the barycenter $\boldsymbol{r}_{bc}$ and the total deposited energy T_{tot} of the overall event are determined as already outlined in section 4.3. Successively, the TOF-corrected OM hits of all OMs are collected in a histogram. In the following, this histogram is called the "overall pulse shape".

Determination of cluster candidates:
The clustering itself starts with the determination of cluster candidates. This is done using a sliding window algorithm. A window of width Δt_{pre} is moved over the overall pulse shape starting from the smallest TOF-corrected times[5] of the overall event. The expected background due to DN in this window is

$$\mu_{\mathrm{DN}}^{\mathrm{w}} = f_{\mathrm{DN}} \cdot N_{\mathrm{PMT}} \cdot \Delta t_{\mathrm{pre}}. \tag{6.2}$$

Hence, if the observed number of hits in the window is q_{w}, the probability P_{BG} for the window to contain q_{w} or more hits can be calculated from the Poisson probability[6]. If $P_{\mathrm{BG}} < p_{\mathrm{seed}}$, where p_{seed} is the seed threshold, a cluster candidate is found. It contains all hits which are inside the window which provided the seed. The cluster is successively

[5] As the whole section deals only with TOF-corrected times, the index "TOF" is no longer explicitly mentioned in all quantities.

[6] This is not possible if $\mu_{\mathrm{DN}}^{\mathrm{w}} = f_{\mathrm{DN}} = 0$. Thus, even for events without simulated DN, $f_{DN} = 1\,\mathrm{Hz}$ was assumed.

enlarged by shifting the window by $-\Delta t_{\text{pre}}$. If P_{BG} is below the threshold for adding a window to a cluster p_{add}, the window is added to the pre-cluster and the procedure is repeated until the condition for adding the window is no longer fulfilled. Note that the condition for adding a window to a cluster is less stringent than the condition to seed a cluster, i.e. $p_{\text{add}} > p_{\text{seed}}$. Successively the procedure to enlarge the cluster is repeated, but this time the window is shifted to larger times. If the total charge q_c contained in the pre-cluster is above a given threshold q_{thr} it becomes a cluster candidate. The cluster candidate is defined by its start time t_{start} and end time t_{end}. Successively, the search for cluster candidates is restarted for $t > t_{\text{end}}$.

Splitting of cluster candidates:
By splitting the overall event into the cluster candidates, it is already decomposed into all components which are well separated in time. What is still missing is to extract secondary events which are on the tail of another event. Figure 4.14 shows that the tail of the pulse shape can locally be well described by an exponential distribution. If there is another sub-event superimposed on this tail of the pulse shape, this description no longer works. Therefore the idea is to use the deviation from an exponential shape to find the secondary events on the tail of the distribution.
To quantitatively evaluate the deviation from the exponential decay at a given (TOF-corrected) time t, an exponential function $f_e(t)$ is fitted to the time interval $[t - \Delta t_f, t]$ where Δt_f is a time window over which the exponential approximation is assumed to be correct. The deviation from the exponential prediction Δf is evaluated by calculating the total deviation from the prediction in the window $[t, t + \Delta t_f]$:

$$\Delta f(t) = \sum_{i, t_i \in [t, t+\Delta t_f]} f_e(t_i) - p_i, \tag{6.3}$$

where t_i are the bin centers of the histogram containing the overall pulse and p_i are the corresponding bin contents. A typical overall pulse shape along with the resulting $\Delta f(t)$ is shown in figure 6.2. Events on the tail of the pulse are marked by a bipolar pulse in $f(t)$. Thus, an additional event on the tail of the pulse in the cluster is identified if the deviation from the expected pulse is above a threshold Δf_{thr}. The time at which the cluster candidate is best split is successively determined by finding the closest minimum in Δf with a time smaller than the time where Δf_{thr} was crossed. To prevent multiple splittings of the cluster candidate due to one secondary event, no further splittings can occur after Δf has crossed Δf_{thr} until Δf has fallen below Δf_{end}. Additionally, as the pulse shape at the start of the primary event strongly depends on the exact event type and on the quality of the barycenter determination, no splitting is allowed for $t < t_{\text{start}} + t_{\text{no}}$ to avoid false splittings of the primary pulse. The found splitting point is also shown in figure 6.2.

6.2.2 Performance

To check the performance of the clustering, the muon tagging efficiency was studied using a data set of 3400 simulated ν_μ-CC interactions. On each of the simulated events, the clustering was applied. As most of the secondary clusters correspond to neutron captures on Hydrogen (visible energy 2.2 MeV), only secondary clusters with an estimated energy of more than $T^{\mu}_{\text{thr}} = 2.43\,\text{MeV}$ are taken into account for the estimation of the clustering

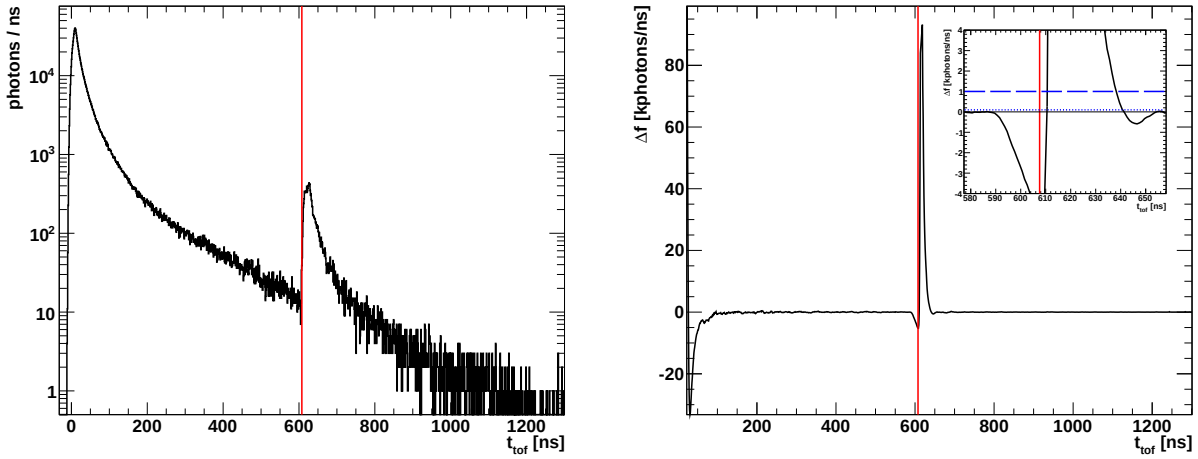

Figure 6.2: A typical, overall, TOF-corrected photon pulse of an event induced by a CC interaction of a ν_μ (left) and the corresponding deviations Δf from the exponential prediction (compare equation (6.3)) as a function of the TOF-corrected photon hit time. The vertical red line indicates the positions, where the cluster candidate was split. The inlay shows a zoom into the region around the splitting time of the clusters, showing additionally the threshold level (dashed blue line) and the cluster end threshold (dotted blue line).

performance.
Figure 6.3 shows the distribution of the time differences from a muon decay (whose time is determined from the MC-truth) to the cluster closest in time which has an energy above T^{μ}_{thr}. It shows a Gaussian distribution with flanks to the left and to the right. The right flank can be reduced by requiring a muon decay time of at least $2\,\mu$s (see red distribution in figure 6.3). For $t < 2\,\mu$s, the event is typically on the tail of the primary event thus only the upper end of the rising flank is visible which leads the cluster to be reconstructed with a slightly too high time.
Due to the tails, the muon detection efficiency is not determined using a fit but by using cuts. All events with $\Delta t \in [-20\,\text{ns},\ 50\,\text{ns}]$ are counted as signal events. The expected background in this region is investigated using a window of the same size far away from the peak ($\Delta t \in [-170\,\text{ns},\ -100\,\text{ns}]$). It is found to be below 0.7 %. The resulting efficiency as a function of the time after the primary event is displayed in figure 6.4. Additionally, the overall muon tagging efficiencies are shown in table 6.2. The efficiency for tagging μ^+ is significantly higher than the efficiency for tagging μ^- because stopped μ^- can replace an electron of an atomic shell and thus form a muonic atom. If this is the case, apart from the muon decay, there is also a second decay mode where the muon interacts with the nucleus of the capturing atom. In this direct reaction, often no electron is formed and the energy of the muon is nearly totally transferred to the produced ν_μ, which greatly reduces the deposited energy in the scintillator. Additionally, the resulting nuclear recoil is strongly quenched in LSc. Hence the associated cluster is often below the threshold imposed by the neutron capture. As the nucleus and the μ^+ are both positively charged, such a scenario is not possible for μ^+. The decay tagging efficiency declines with the clusters getting closer to the primary event, as the events have to surpass the pulse from the primary event which rises towards smaller times. For $t < 200\,\mu$s, it is practically zero due to the inhibit after the start of the cluster candidate for the primary event. To crosscheck whether the acquired clusters are actually due to muon decays, figure 6.5

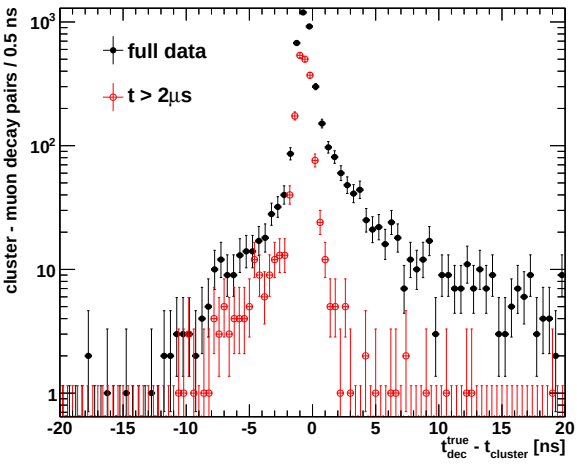

Figure 6.3: The distribution of the time differences between a muon decay and the nearest cluster with an associated energy above the threshold to suppress neutron captures. Apart from the full data set, also a data set featuring only clusters with $t_{\mu-\text{decay}} > 2\,\mu$s is shown.

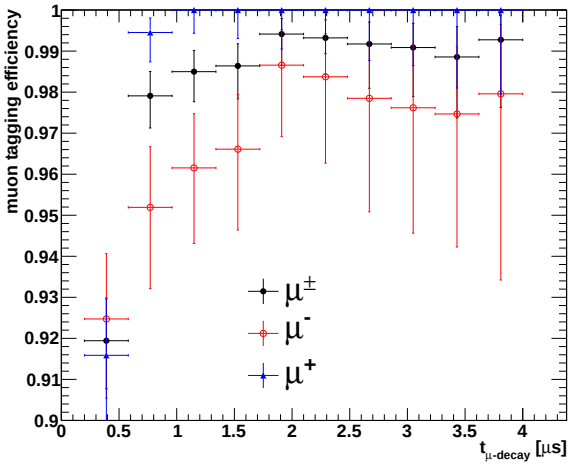

Figure 6.4: The efficiency to tag a $\mu^{\pm}$ decay as a function of the time after the primary event associated to the nearest cluster. For $t_{\mu-\text{decay}} < 0.2\,\mu$s the efficiency is effectively zero. Additionally the efficiencies to tag muons and antimuons are shown separately.

data set	muon decay tagging efficiency [%]
μ^+ and μ^-	91.0 ± 1.9
μ^-	88 ± 3
μ^+	92.4 ± 2.5

Table 6.2: The resulting overall muon-tagging efficiency for both, $\mu^{\pm}$ as well as for a data set containing only μ^- and μ^+.

shows the distribution of the time after the primary event associated to the found clusters which were tagged as muon decay candidates. A fit with an exponential to the tail of the distribution results in a muon life time of $\tau_\mu = (2.11 \pm 0.04)\,\mu$s which is well compatible[7] with the literature value $\tau_\mu = 2.196\,\mu$s [21], supporting the hypothesis that the clusters really are associated to muons.

6.3 Energy reconstruction and migration matrices

As the neutrino oscillation probability is a function of the energy, a precise reconstruction of the initial kinetic energy of the neutrino significantly increases the predictive power of oscillation experiments compared to experiments where only the number of neutrino events is counted. In contained CC-events, the total neutrino energy is deposited in the LSc. Thus, the first approach to reconstruct the neutrino energy is to use LENA as a fully scintillating calorimeter and to determine the neutrino energy from the visible energy of

[7] The deviation of the fitted value from the literature value is about 2-σ and thus might well be due to statistical fluctuations. Additionally, the small changes in efficiency with time (see figure 6.4) contribute to the deviation from the literature value.

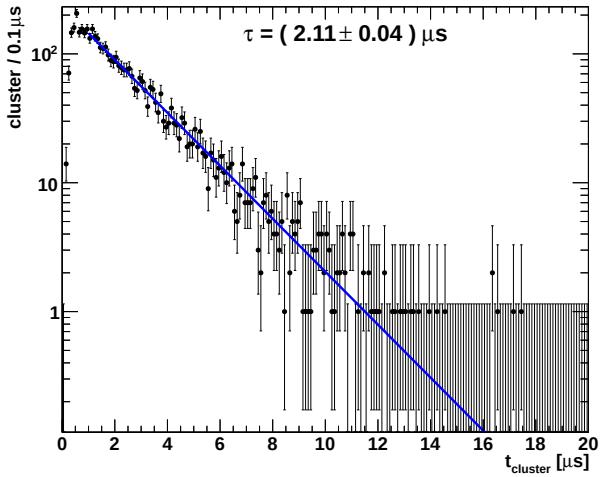

Figure 6.5: Distribution of the times associated to the found clusters which were qualified as a muon. Fitting the distribution with an exponential yields a good agreement with the muon decay time, as indicated in the plot. The rise at lower times is due to the decreased muon tagging efficiency (confer figure 6.4).

the primary event.
To reconstruct the energy of the primary event, the algorithm[8] to determine the initial kinetic energy already described in section 4.3 is used.

The energy response of a detector is generally described by the detector response, which is the PDF $P(E_\nu^{\text{rec}}|E_\nu^{\text{true}})$ to reconstruct the neutrino energy to be E_ν^{rec} given the true energy of the incident neutrino is E_ν^{true}. As the events are much too complicated to determine the detector response analytically, it has to be determined from MC simulations which requires a binning in energy. The quantity corresponding to $P(E_\nu^{\text{rec}}|E_\nu^{\text{true}})$ in the binned case is the migration matrix E_{ij} which describes the probability to reconstruct the neutrino energy E_ν^{rec} in the bin i while the true neutrino energy E_ν^{true} is in the bin j. Note, that the migration matrix is still normalized[9] in each E_ν^{true}-bin, i.e.

$$\sum_{i=1}^{N_{\text{bins}}} E_{ij} = 1 \quad \forall j, \tag{6.4}$$

where N_{bins} is the number of energy bins used. As the absolute energy resolution deteriorates with energy, a non-uniform binning was used. For energies below 5 GeV a bin size of 0.2 GeV was used while 0.5 GeV bins were used for higher energies. The resulting migration matrix for ν_e-CC events is shown in figure 6.6 along with the distribution of the relative energy deviations. A clear correlation between reconstructed and true energy is visible resulting in a relative energy resolution of about 9%. Note, however, that the

[8] As this analysis was done with an earlier version of the algorithm, instead of the data plotted in figure 4.4 a fit to this data with a polynomial of order 3 was used to determine the calibration constant k_{cal} (see section 4.3).

[9] Often the migration matrix is not normalized to one but to the efficiency for the respective bin and the respective channel, see e.g. [116]. As no energy dependent efficiencies exist for LENA, this is not done in this work.

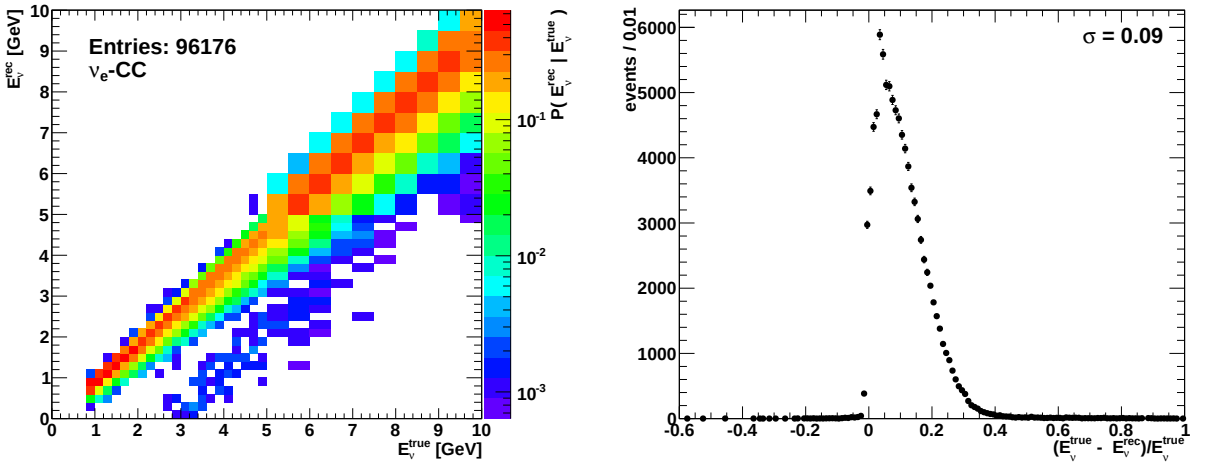

Figure 6.6: The energy response of LENA for ν_e-CC events with true neutrino energies E_ν^{true} in the range between 1 GeV and 10 GeV. The energy migration matrix, i.e. the binned PDF to reconstruct E_ν^{rec} given E_ν^{true} is shown on the left. On the right, the distribution of the relative deviation of the true from the reconstructed energy is shown along with the width of the obtained distribution.

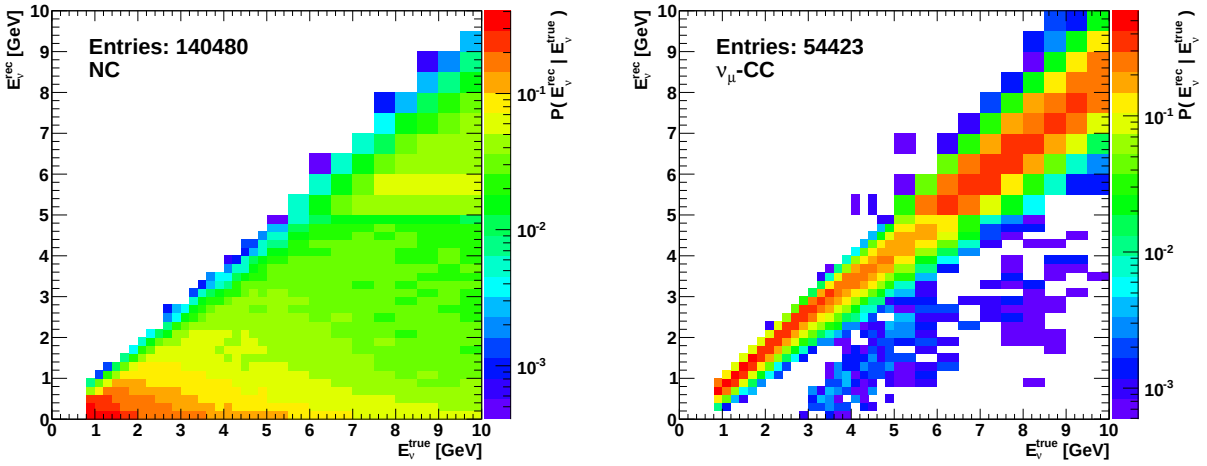

Figure 6.7: The energy migration matrix, i.e., the binned PDF to reconstruct E_ν^{rec} given E_ν^{true}, for NC events (left) and for contained ν_μ-CC interactions (right). The range of the incident neutrino energies is from 1 GeV to 10 GeV. Note, that the statistics for the ν_μ event is much lower than in figure 6.6 due to the containment cut for the muon required.

distribution of the deviations features a strongly non-Gaussian shape. Thus, a Gaussian description of the deviations of the energy resolution is not sufficient but the whole migration matrix has to be used instead. The corresponding result for NC-type events, which is shown in figure 6.7 (left), has a completely different behavior: Due to the invisible energy in the exit channel, the reconstructed energy features a broad shoulder ranging from the true neutrino energy down to zero. This shifts the mean reconstructed energy to smaller energies and thus away from the main oscillation maximum. To increase the energy resolution in the NC channel, a direction and energy reconstruction of the produced particles would be necessary.

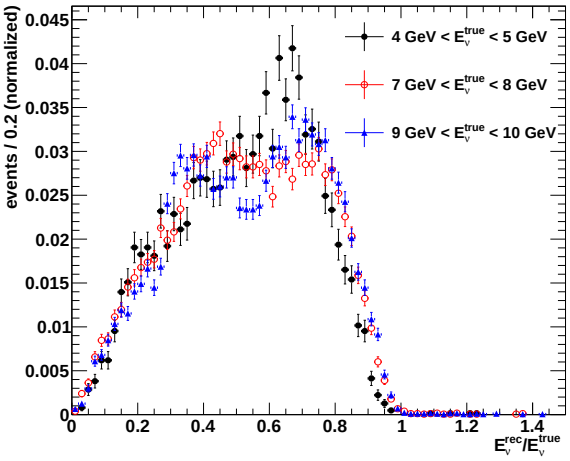

Figure 6.8: The distribution of the relative reconstructed energy of ν_τ-CC events for various slices in the true neutrino energy. The overall true neutrino energy range of the simulated ν_τ-CC interactions is from about 4 GeV to 10 GeV.

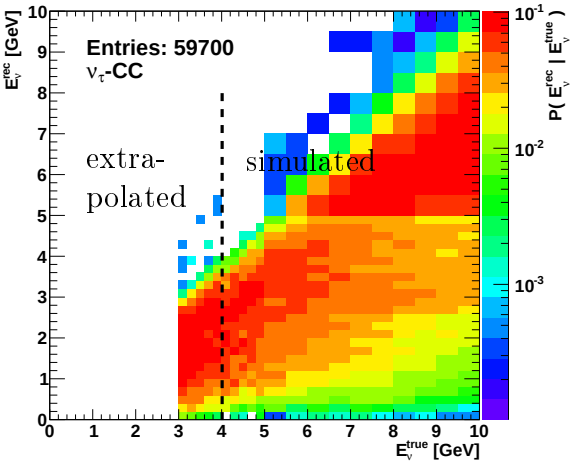

Figure 6.9: The energy migration matrix, i.e. the binned PDF to reconstruct E_ν^{rec} given E_ν^{true}, for ν_τ-CC interactions after extrapolation to lower energies. The range of the incident neutrino energies is from 1 GeV to 10 GeV. The vertical dashed line separates the simulated from the extrapolated region.

While ν_e-CC events and NC events simulated in the center of the detector are generally relatively well contained, this is not the case for ν_μ-CC events due to the high penetrating power of the muon. Thus, similar to section 5.4, only events featuring a fully contained primary muon have been taken into account. The resulting migration matrix is shown in the right plot of figure 6.7 and shows a very similar behavior to the ν_e-CC case. For the rare ν_τ-CC events, a technical problem occurred: While the cross-section used in the GENIE neutrino event generator deviates from zero for true neutrino energies starting from $\sim 3.5\,\mathrm{GeV}$, only events with $E_\nu^{\mathrm{true}} \gtrsim 4\,\mathrm{GeV}$ where produced by the event generator[10]. As this discrepancy leads to problems in the further analysis, the migration matrices obtained from the simulation were extrapolated down to 3 GeV. This extrapolation was done under the assumption that the distribution of the relative reconstructed energy is independent of the neutrino energy, which seems to be a good approximation for the simulated energy range (see figure 6.8). Using this approximation, events can be artificially sampled from the overall relative reconstructed energy distribution from the simulation and added to the migration matrix. It is shown in figure 6.9.
The relevance of the migration matrices for the estimation of the LENA physics reach is discussed in section 6.6.

Comparing the resulting resolutions with other detectors, the power of the approach to use LENA as a fully scintillating calorimeter becomes obvious: A water Cerenkov based detector often does not see any light from heavier hadronic components like nucleons as they are typically below the Cerenkov threshold. Therefore, the only viable possibility is to assume a quasielastic event and to kinematically reconstruct the neutrino energy from the lepton energy and direction. This approach obviously does not work properly for other event types and even for QEL events it is significantly flawed due to the Fermi-

[10] This problem was reproduced with different versions of GENIE.

motion of the nucleons in the nucleus. Already at sub-GeV energies, this deficit shows up in additional peaks in the distribution of reconstructed energies [116]. Even for a liquid argon based detector (see e.g. [117]), which is basically able to fully reconstruct the interaction, an energy resolution of 150 MeV is expected in the energy range from 1 GeV to 10 GeV [118]. This corresponds to a relative energy resolution between 15% and 1.5% and thus is in the same region as the relative resolution (8 %) expected for the LENA detector.

6.4 The backtracking-algorithm

As already mentioned at the start of this chapter, a likelihood-based tracking requires a relatively good knowledge of the event. Thus, additional algorithms are necessary which offer a possibility to create an image of an event without requiring any prior knowledge of the event. One of the proposed algorithms is the backtracking algorithm, which is presented in section 6.4.1. It allows to associate a figure of merit $f_{\mathrm{FOM}}(\boldsymbol{r})$ to each point $\boldsymbol{r}$ in the detector which is correlated to the number of photons emitted in the close vicinity of $\boldsymbol{r}$. While the algorithm was invented by the author of this thesis, it is currently further developed by Kai Loo[11] aiming to get the relevant physics parameters from the obtained figure of merit. In section 6.4.2, an algorithm developed by the author of this thesis is presented, which allows to determine the vertex of the interaction from the obtained f_{FOM}. To verify that the backtracking algorithm is applicable to data from a real experiment, it was shown in [119] that it can be used to reconstruct muons transversing the Borexino detector. The main result of this work are summarized in section 6.4.3.

6.4.1 Algorithm

The idea of the algorithm is based on the observation, that for larger PMT occupancies, the PDF for the first photon hit time of an OM features a nearly Gaussian shape and is nearly independent of the number of photons (see figure 4.15). To exclude OMs which are far away from the event and thus feature a low occupancy, only OMs with a charge of at least $q_t = 10$ photo-electrons are considered in the algorithm. Due to the narrow shape of the PDF for the arrival times of the first photons, the arrival time is relatively well defined by the TOF from the particle vertex to the OM on which the photon was detected. Thus, if multiple photons would be emitted from a point $\boldsymbol{r}$ in the detector, a peak would be expected in the time spectrum of the first hits after a TOF-correction with respect to $\boldsymbol{r}$. Figure 6.10 shows the TOF-corrected first hit time spectrum of a 2 GeV muon traveling from the center of the detector along the positive z-axis for two different $\boldsymbol{r}$. As expected the distribution resulting from a TOF-correction with respect to a point on the track, i.e. to a point where multiple photons were emitted, shows a clearly visible peak while the distribution originating from the TOF-correction with respect to a point far off the track, i.e. a point where no photons were emitted, only shows a flat shape. Based on this observation, the general idea to determine at which points in the detector photons were created is to look for peaks in the relevant TOF-corrected first hit time spectra.

To qualify whether a TOF-corrected first hit time spectrum features a peak, first an

[11] University of Jyväskylä, Department of Physics, Finland

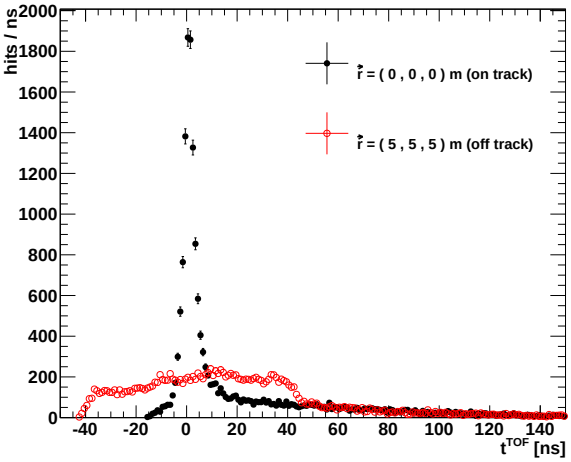

Figure 6.10: The distribution of the TOF-corrected first hits of all OMs for a 2 GeV muon traveling from the vertex along the positive z-axis. The TOF-correction was done with respect to two different points $\boldsymbol{r} = (0, 0, 0)\,\mathrm{m}$ and $\boldsymbol{r} = (5, 5, 5)\,\mathrm{m}$, the former being the track vertex and the latter being far off the track.

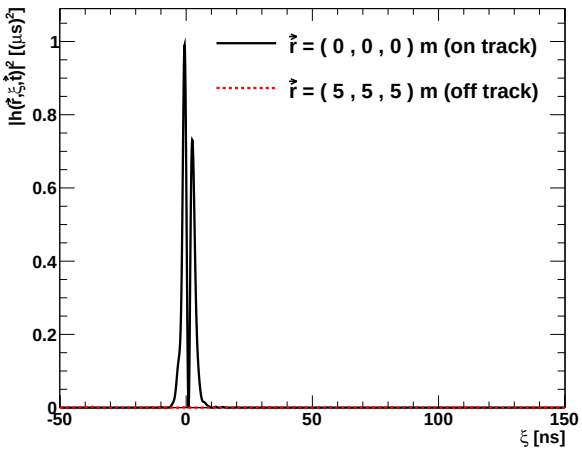

Figure 6.11: The squared modulus of the intermediate helper function $h(\boldsymbol{r}, \xi, \boldsymbol{t})$ (see equation (6.5)) as a function of ξ for two different candidate photon emission points $\boldsymbol{r}$: $\boldsymbol{r} = (0, 0, 0)\,\mathrm{m}$ and $\boldsymbol{r} = (5, 5, 5)\,\mathrm{m}$. The hit times $\boldsymbol{t}$ were taken from a simulated event of a 2 GeV muon traveling from the vertex along the positive z-axis. Thus, the first candidate photon emission point is the muon's vertex and the second is far off the track.

intermediate function $h(\boldsymbol{r}, \xi, \boldsymbol{t})$ is defined:

$$h(\boldsymbol{r}, \xi, \boldsymbol{t}) = \sum_{i=1}^{q_i > q_t} \left[t^{\mathrm{TOF}}(\boldsymbol{r}, \boldsymbol{r}_i, t_i) - \xi \right] \cdot \exp\left\{ -\frac{[t^{\mathrm{TOF}}(\boldsymbol{r}, \boldsymbol{r}_i, t_i) - \xi]^2}{2\sigma_{\mathrm{bt}}^2} \right\}, \tag{6.5}$$

where ξ is a helper variable, $\boldsymbol{t}$ are the first hit times of the OMs, $t^{\mathrm{TOF}}(\boldsymbol{r}, \boldsymbol{r}_i, t_i)$ is the TOF-corrected time corresponding to a photon emitted at $\boldsymbol{r}$ and detected at the OM at the position $\boldsymbol{r}_i$ and at the time t_i as defined in equation (4.12) and $\sigma_{\mathrm{bt}} = 1\,\mathrm{ns}$ is a parameter of the algorithm which should roughly correspond to the standard deviation of the peak in the TOF-corrected hit time spectrum. The sum is running over all OMs with a total acquired charge of at least q_t. $h(\boldsymbol{r}, \xi, \boldsymbol{t})$ constitutes a sum of derived Gaussian functions in ξ for each first hit, with the center of the Gaussian being at the TOF-corrected hit-time of the corresponding first hit. As a derived Gaussian is a bipolar function, the sum of the derived Gaussians approximately cancels out if the underlying distribution of the first TOF-corrected hit-times is flat. Contrary, if the underlying first TOF-corrected hit-times are correlated, i.e. the distribution shows a peak, a positive interference takes place leading to large absolute values of h.
To condense the information contained in $h(\boldsymbol{r}, \xi, \boldsymbol{t})$ into one single figure of merit, first the squared modulus of h is calculated. The resulting function is shown in figure 6.11 as a function of ξ for two different candidate photon emission points: The candidate point corresponding to the photon vertex leads to a much larger amplitude than the candidate

point far off the track. Finally, the figure of merit is defined by

$$f_{\mathrm{FOM}}(\boldsymbol{r}|\boldsymbol{t}) = \int_{-\infty}^{\infty} |h(\boldsymbol{r},\xi,\boldsymbol{t})|^2 d\xi \tag{6.6}$$

$$= \frac{\sqrt{\pi}\sigma_{\mathrm{bt}}}{4}\left\{2\sigma_{\mathrm{bt}}^2 N_a - \sum_{q_i>q_t}\sum_{q_j>q_t}^{j>i}\left[(t_i-t_j)^2 - 2\sigma_{\mathrm{bt}}^2\right]\exp\left[-\frac{(t_i-t_j)^2}{4\sigma_{\mathrm{bt}}^2}\right]\right\}, \tag{6.7}$$

where N_a is the number of OMs with $q_i > 10$ and $t_i = t^{\mathrm{TOF}}(\boldsymbol{r},\boldsymbol{r}_i,t_i)$. Due to the double sum in the analytical evaluation of equation (6.7), for detectors with a high number of OMs like LENA it is actually faster to evaluate equation (6.6) numerically while for smaller detectors like Borexino, the analytical calculation is preferable.

The left panel of figure 6.12 shows a slice of the backtracking estimator resulting from a 1 GeV muon starting from the center of the detector along the positive x-axis. The shown slice corresponds to the x-y plane with $z = 0$. The left plot on figure 6.12 depicts the case if only first hits are used. Comparing the color coding to the particle track shown (black arrow) the correlation between the track and $f_{\mathrm{FOM}}(\boldsymbol{r})$ is clear and the direction of the track is nicely resolved. Even the deviation from a straight line is visible. The point with the highest figure of merit is positioned on the track at about 50 cm from the start point. The end of the track is not resolved very clearly, especially no Bragg-peak is visible. This behavior can be understood by looking at figure 5.1: The spherical first-light front originating from the start of the track is seen by lots of OMs which leads to the high peak at the start of the track. As the number of photons emitted from each point on the track is finite, not only the first light front but also the light fronts arriving shortly afterwards are sampled by the backtracking algorithm which leads to the shift of the point with maximum FOM along the track. The light front from the end of the track is seen by a smaller number of OMs which leads to the suppression of the later parts of the track. Additionally, for the very final part of the track, $v \approx c_0$ no longer holds. Thus, the light can overtake the particle and therefore the light front, which is interpreted as coming from the end of the track, actually corresponds to the point of the track where $v \sim c_0/n$. On the right of figure 6.12 an event with two muons is shown, whose initial directions include a 45 deg angle: Both particle tracks are resolved, showing the capability of the backtracking to also deal with more complicated events.

6.4.2 Vertex finding

In section 6.4.1 it was found, that the maximum FOM of the backtracking algorithm tends to be close to the start of the track. This general feature of the backtracking algorithm can be used to determine the vertex position $\boldsymbol{r}_s$ of events containing full simulated neutrino interactions. First, the position $\boldsymbol{r}_{\mathrm{max}}^{\mathrm{FOM}}$ of the maximum of the FOM is determined using the `SIMPLEX` algorithm as implemented in the `MINUIT` [107] fitting package.
In a second step, the shift of the maximum of the FOM along the track, as already observed in figure 6.12, has to be corrected. For this, it is assumed that the principal direction of the event is determined by the direction of the incoming neutrino $\hat{\boldsymbol{d}}_\nu$ (see equation (6.1)). Thus, the deviation of the event position along the beam direction is

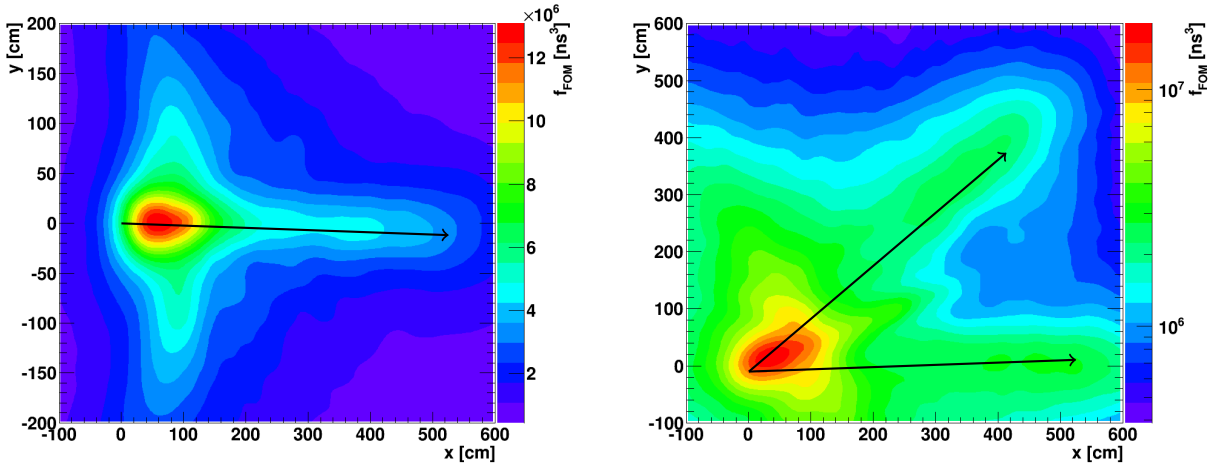

Figure 6.12: The backtracking estimator $f_{\mathrm{FOM}}(\boldsymbol{r})$ as a function of x and y for $z = 0$ for an event containing a 1 GeV muon starting from the center of the detector and starting along the positive x-axis (left) and for two 1 GeV muons starting in the center of the detector with an angle of 45 deg between the tracks. The black arrow shows the MC truth information: It connects the start and the end point of the particles. Note that these events were created in the context of the investigations for the single track reconstruction and thus feature the simulation set-up presented in section 4.1.

defined as:

$$\Delta_{\parallel} = (\boldsymbol{r}_{\mathrm{max}}^{\mathrm{FOM}} - \boldsymbol{r}_{s}^{\mathrm{true}}) \cdot \hat{\boldsymbol{d}}_{\nu}, \tag{6.8}$$

where $\boldsymbol{r}_{s}^{\mathrm{true}} = (0, 0, 0)$ is the true vertex position. Figure 6.13 shows the distribution of $\Delta_{\parallel}$ as a function of the reconstructed neutrino energy with a systematic offset being clearly visible. To correct for this offset, the means of the obtained distributions are fitted with a polynomial of order two. The polynomial resulting from the fit

$$f_{\Delta_{\parallel}}(E_{\nu}^{\mathrm{rec}}) = 16.42\,\mathrm{cm} + \frac{E_{\nu}^{\mathrm{rec}}}{\mathrm{MeV}} \left(0.0039 - \frac{E_{\nu}^{\mathrm{rec}}}{\mathrm{MeV}} \cdot 2.42 \cdot 10^{-7} \right) \mathrm{cm} \tag{6.9}$$

is also shown in Figure 6.13 as a red line. Thus, the final vertex position can be determined as:

$$\boldsymbol{r}_{s} = \boldsymbol{r}_{\mathrm{max}}^{\mathrm{FOM}} - \hat{\boldsymbol{d}}_{\nu} \cdot f_{\Delta_{\parallel}}(E_{\nu}^{\mathrm{rec}}). \tag{6.10}$$

Note, that when the interaction vertex is not fixed to the center of the detector, the correction function will most likely also depend on the position of $\boldsymbol{r}_{\mathrm{max}}^{\mathrm{FOM}}$, i.e. $f_{\Delta_{\parallel}}(E_{\nu}^{\mathrm{rec}}, \boldsymbol{r}_{\mathrm{max}}^{\mathrm{FOM}})$. Thus, the determination of the required shift in beam direction will have to be performed on a grid for the whole detector.

Figure 6.14 shows the distribution of the x-components of the reconstructed vertex for simulated events with vertices in the center of the detector. It can be nicely fitted with a Gaussian distribution with a standard deviation of about 9.5 cm and shows no significant offset. The corresponding distributions of the y- and z-components of the resulting vertex positions are shown in figure 6.15 along with their standard deviations. Even though these distributions cannot be properly described by Gaussian functions, they do not feature any long tails towards higher deviations from zero. Their standard deviations are about 7 cm which is below the width obtained in x-direction as the x-axis is nearly parallel to the

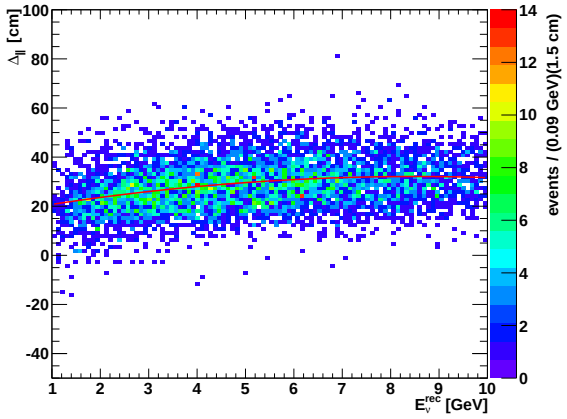

Figure 6.13: The distribution of the deviations of the maximum FOM position from the true vertex projected on the neutrino direction as a function of the reconstructed neutrino energy for 6200 simulated ν_e-CC events. The red line shows the result of a fit with a polynomial of order two.

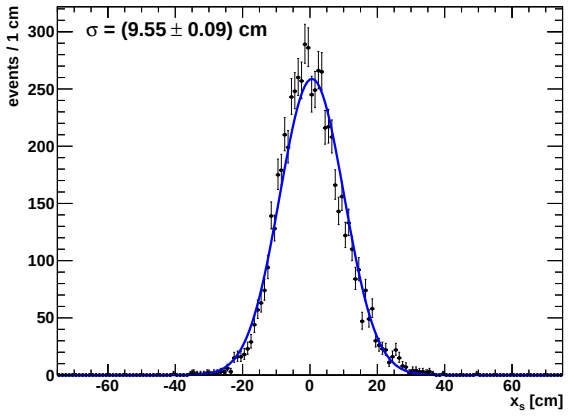

Figure 6.14: The distribution of the x-components of the reconstructed vertices of 6200 simulated ν_e-CC interactions. The true vertex is in the center of the detector, i.e., $x_s^{\text{true}} = 0$. The blue line shows the result of a Gaussian fit with standard deviation σ to the data.

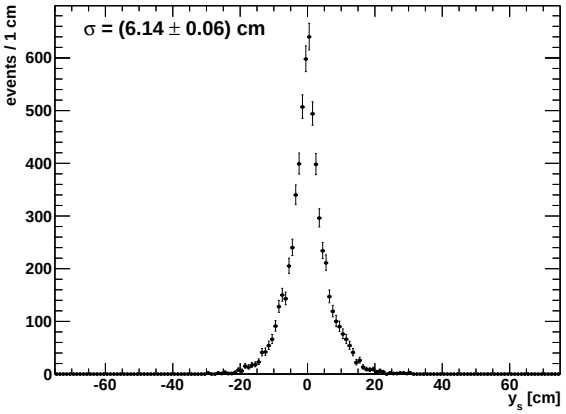

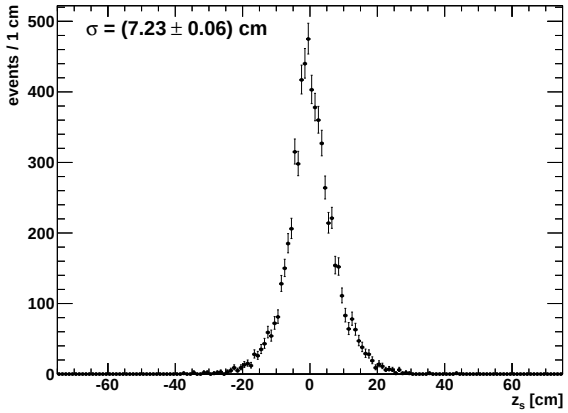

Figure 6.15: The distribution of the y-components (left) and z-components (right) of the reconstructed vertices of 6200 simulated ν_e-CC interactions. The true vertex is in the center of the detector i.e. $y_s^{\text{true}} = z_s^{\text{true}} = 0$. The standard deviations σ of the obtained distributions are additionally displayed for each plot.

beam direction: Apart from the uncertainty in the position of the maximum FOM, also the spread of the required corrections along the beam axis contributes to the obtained resolution. The z_s-distribution is slightly broader than the y_s-distribution. This is due to the geometry of the LENA detector which does not allow for a good use of the timing information to determine the z-position of an event. This has already been discussed in section 4.5.1. Additionally, the small component of $\hat{\boldsymbol{d}}_\nu$ in z-direction also has a negative influence on the resolution in z_s.
In summary, it can be stated that the vertex reconstruction works reliably with a resolution better than 10 cm in each direction.

6.4.3 Application to muons in Borexino

To show the applicability of the backtracking algorithm to data from a real detector, in [119] the algorithm as been used to reconstruct high energetic cosmic muons passing through the Borexino detector (see section 2.3.2). As these events lead to a saturation of the Borexino electronics, only the timing information of the PMTs is usable, which is sufficient for the backtracking algorithm. Note, that the coordinate system in Borexino is defined in a way, that the z-axis points upwards and the x-axis includes an angle of 6.2 deg with the **C**ERN **N**eutrinos to **G**ran **S**assos (CNGSs) beam from CERN to Gran Sasso [66].

Adaption of the algorithm to Borexino:
Due to the geometry of Borexino and due to the fact that the muon track spans the whole detector, the suppression of the later parts of the particle tracks was found to be even more pronounced than observed in figure 6.12. To improve the situation, the algorithm was adapted to consider only TOF-corrected hits in a window around the maximum position $t_{\text{max}}^{\text{TOF}}$ in the distribution of the TOF-corrected hits: Only hits with $t^{\text{TOF}} \in [t_{\text{max}}^{\text{TOF}} - 5\,\text{ns}, t_{\text{max}}^{\text{TOF}} + 10\,\text{ns}]$ are considered which significantly increases the visibility of the late parts of the track. To match the expected resolution, the FOM is determined on a regular grid with 20 cm spacing. An example of the obtained FOM-grid for a cosmic muon is shown in figure 6.16.

Determination of the track parameters:
A first estimation of the muon track can be obtained by connecting two points which are located close to the track: The first can be obtained from the position of the maximum of the FOM and the second from a weighted barycenter of the PMTs with a hit time in the first 5 ns of the event. To improve the accuracy of the reconstructed muon, a straight line was fitted to the obtained $f_{\text{FOM}}(\boldsymbol{r})$-values, using the results from the first estimation of the track as start parameters (for details see [119]). An example event containing a cosmic muon with a fitted track is shown in figure 6.17.

Verification of the fit results:
When discussing the backtracking algorithm, the basic idea is that the photons belonging to the peak in the TOF-corrected hit-time spectrum are emitted from the point used for the TOF-correction. This means that the TOF-corrected hit time of the peak corresponds to the time the first photons were emitted from this point which roughly corresponds to the time at which the muon passed this point. Based on this idea, the photon emission times are determined for grid points closer than 20 cm to the track and with a FOM of at least 1/3 of the maximum FOM. By plotting the resulting values as a function of the distance of the corresponding points to the entry point of the muon, the reconstructed track can be verified: For a well fitted muon, the distance should be a linear function of the photon emission time with the slope corresponding to the speed of light in vacuum. Thus, the obtained data is fitted with a linear function. Figure 6.18 shows two examples of such fits, one for a well fitted event (left) and one for a badly fitted event (right). Based on the results from these fits, wrongly reconstructed tracks can be rejected: For a track to be accepted, it has to satisfy the empirical conditions

$$|v - c_0| < 1 \cdot 10^8\,\text{m/s} \quad \text{and} \tag{6.11}$$

$$\chi^2/\text{NDF} < 5, \tag{6.12}$$

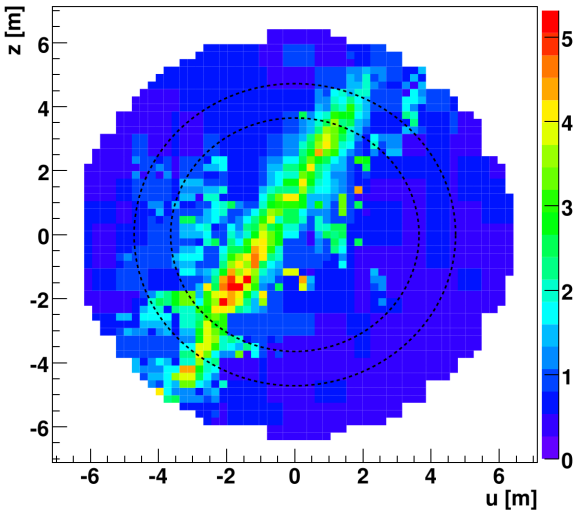

Figure 6.16: The FOM of a cosmogenic muon as a function of u and z, where u is a coordinate perpendicular to the z-axis which was chosen in a way that the muon track is in the u-z-plane [119]. The color coding indicates $f_{\mathrm{FOM}}(\boldsymbol{r})$. The dashed circles indicate the two nylon-vessels of Borexino.

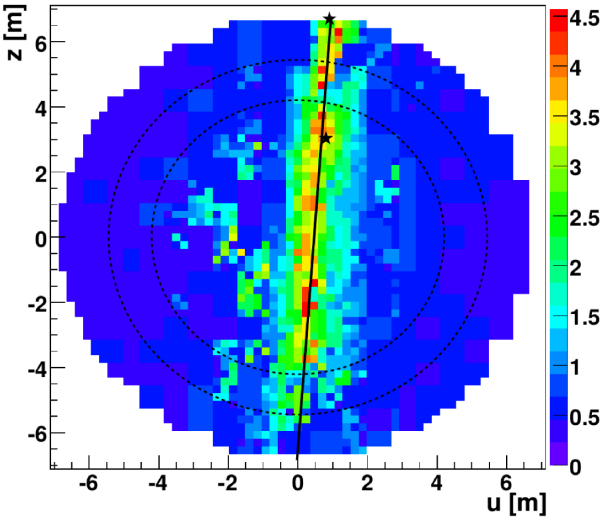

Figure 6.17: The FOM of a cosmogenic muon as a function of u and z, where u is a coordinate perpendicular to the z-axis which was chosen in a way that the muon track is in the u-z-plane [119]. The color coding indicates $f_{\mathrm{FOM}}(\boldsymbol{r})$. The black line shows the result of a line fit to the obtained $f_{\mathrm{FOM}}(\boldsymbol{r})$, the asterisks indicate the points which were used to construct a line for seeding the fit: The maximum position of the smoothed FOM and the barycenter of the early hits. The dashed circles indicate the two nylon-vessels of Borexino.

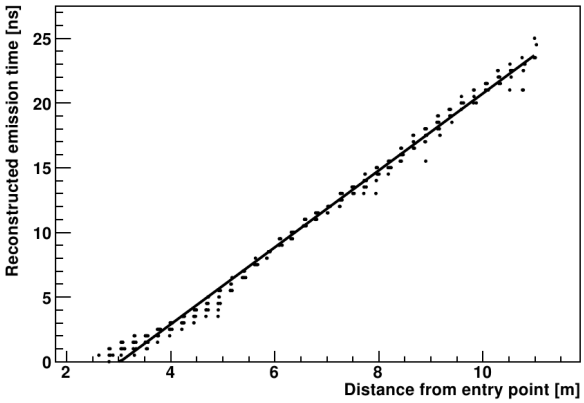

$v = 3.36 \cdot 10^8\,\mathrm{m/s}$, $\chi^2/\mathrm{NDF} = 0.3$

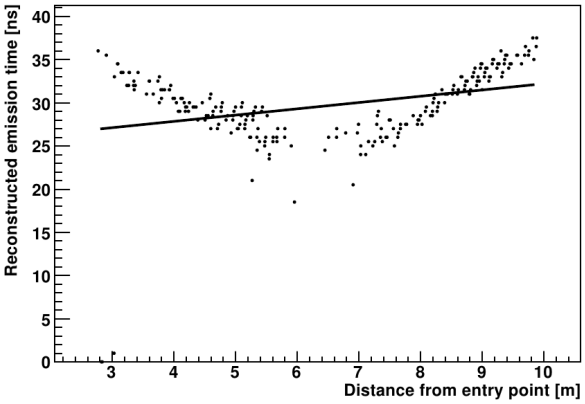

$v = 1.37 \cdot 10^8\,\mathrm{m/s}$, $\chi^2/\mathrm{NDF} = 20.5$

Figure 6.18: The reconstructed emission time of the photons as a function of the distance of the photon emission points from the vertex for a well reconstructed event (left) and a badly reconstructed event (right) [119]. Only photon emission points with a distance to the reconstructed track of less than 20 cm and with a FOM of at least 1/3 of the maximum FOM are shown. The obtained data is fitted with a straight line. The obtained velocities and reduced χ^2 values resulting from the fits are shown below the images.

	Backtracking	ID Tracking	OD Tracking
σ_α [deg]	1.63 ± 0.10	2.44 ± 0.19	3.01 ± 0.15
σ_y [cm]	35 ± 4	36 ± 5	28 ± 7
σ_z [cm]	38 ± 4	31 ± 6	45 ± 7

Table 6.3: The angular (σ_α) and spatial ($\sigma_{x,y}$) resolutions for the backtracking algorithm [119] compared to the resolutions of the existing inner detector (ID) and outer detector (OD) muon reconstruction algorithms [66, 52]. The values have been obtained from high energetic muons created by neutrino interactions of CNGS neutrinos in the rock surrounding Borexino's experimental hall, which were detected by Borexino and OPERA.

where v is the velocity resulting from the linear fit[12] and χ^2/NDF is its reduced χ^2 value. As the algorithm does not return any errors for the reconstructed emission time, they are arbitrarily assumed to be 1 ns. Therefore, the reduced χ^2 value is arbitrary, i.e. it scales inversely proportional to the squared error of the reconstructed time. Nevertheless, it still can be used to discriminate between good and bad fits as good fits will always have a better reduced χ^2 than the bad fits.

Performance:
To test the performance of the algorithm, muons have been selected which were created by neutrino interactions from the high energetic CNGS beam [120] in the rock surrounding the experimental hall and were detected in Borexino and in OPERA [120]. As the resolution of the OPERA muon tracker is an order of magnitude better than the resolution expected for the Borexino muon reconstruction [121], it provides the true directions and positions of the tracks which allows to determine the resolution of the tracking algorithm. From the 770 observed tracks, 667 passed the criteria of a good fit [119] corresponding to $(86.6 \pm 0.13)\,\%$. Table 6.3 shows the obtained performance of the backtracking algorithm. Additionally, the performance of the established Borexino muon reconstruction algorithms [66, 52] using the data of the inner detector (ID) and of the outer detector (OD) as determined from the same data set is listed. While achieving a similar performance in the lateral resolution, the angular resolution of the backtracking algorithm is significantly better than the angular resolution of the established tracking algorithms. Note that for muons created by neutrinos from the CNGS-beam which are transversing Borexino from one side to the other, the performance of the OD tracking is significantly worse compared to cosmogenic muons coming from above as the layout of the OD PMTs is designed for the latter type of muons.

Additional capabilities:
While the backtracking algorithm shows a better performance than the established tracking algorithms in Borexino, this increase in performance will not increase the capabilities of the experiment significantly as the old algorithms already provide enough information for suppressing radioactivity induced by cosmogenic muons [52]. However, there are more complicated types of muon events in Borexino, which cannot be treated with the old algorithms and thus require a veto on the total detector which reduces the efficiency. The

[12]Note that no constraint on the velocity of the particle v was applied in the fit. Thus, resulting velocities $v > c_0$ are possible.

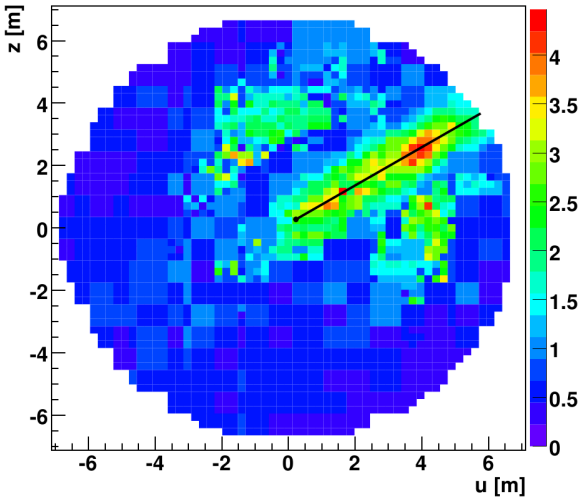

Figure 6.19: The FOM of a cosmogenic muon which was stopped in Borexino as a function of u and z, where u is a coordinate perpendicular to the z axis which was chosen in a way that the muon track is in the u-z-plane [119]. The color coding indicates $f_{\mathrm{FOM}}(\boldsymbol{r})$. The black line shows the result of a fit with the black dot marking the fitted end of the track.

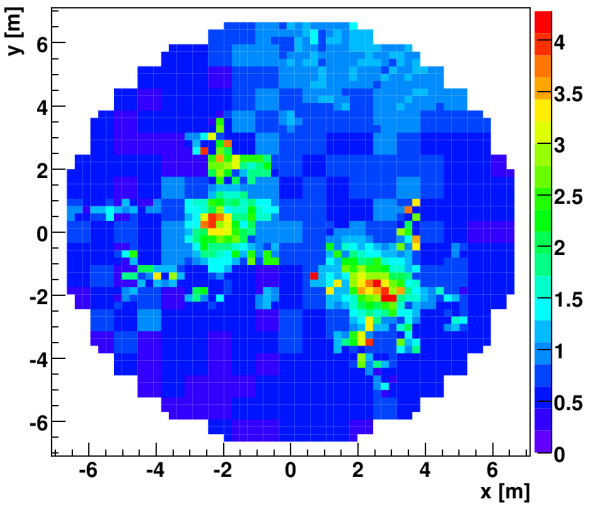

Figure 6.20: The FOM of two cosmogenic muons simultaneously passing through the Borexino detector as a function of x and y for $z = 0$ [119]. The color coding indicates $f_{\mathrm{FOM}}(x, y, z = 0)$. Two maxima are visible which correspond to the crossing points of the muons and the x-y-plane.

backtracking on the other hand is capable of dealing with these events.

Not all cosmogenic muons transverse the whole Borexino detector, some are stopped inside Borexino. As the established tracking algorithms reconstruct an entry and an exit point, they cannot handle these events. Figure 6.19 shows the FOM of such an event: The stopped muon track is clearly visible. Based on this observation, an algorithm was developed which identifies these events. Moreover, the fit was expanded to be able to fit these events and to determine the stopping point of the muon [119]. The muon track resulting from this fit along with the found end point of the track is also indicated in figure 6.19.

Another, more complicated event type is caused by the production mechanism of cosmogenic muons: Cosmogenic muons are produced in showers induced by cosmic radiation in the earth atmosphere. Often, this results in the production of more than one muon with quasi-parallel momenta due to the boost of the shower system. Thus, there are events featuring multiple simultaneous muons traveling through Borexino which cannot be dealt with the established algorithms. While no fit is available for two muon events yet, in figure 6.20, which shows the FOM in the x-y-plane, the two crossing points of the muons are clearly visible. This shows the ability of the backtracking algorithm to deal also with these more complicated events.

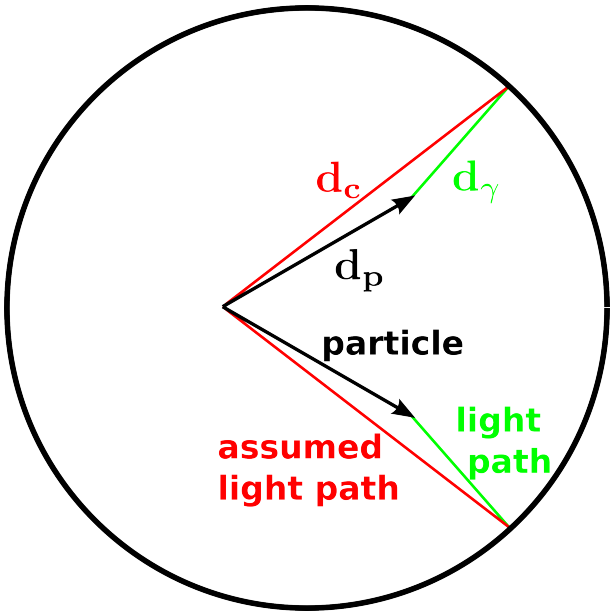

Figure 6.21: A sketch showing an event with two particles traveling on a straight line as seen in a view along the z-axis. The black arrows indicate the particle tracks, the green lines show the path the first light which is detected has to travel to the PMT and the red lines show the light path which is assumed for the TOF correction with respect to the vertex.

6.5 Estimation of the track multiplicity and the direction of significant tracks

In section 6.4.2 an algorithm was presented which determines the position of the primary vertex with ∼10 cm accuracy. This allows to gain additional information by performing a TOF-correction with respect to the primary vertex instead of performing a TOF-correction with respect to the barycenter. The basic idea is sketched in figure 6.21: As can be seen from figure 5.1, the first photons arriving on the OMs which are in track direction are emitted close to the end point of the track. Thus, their expected arrival time on the OM is

$$t^0 = t_s + t_p + t_\gamma = t_0 + t_p + \frac{n d_\gamma}{c_0} \tag{6.13}$$

where t_s is the start time of the event, t_p is the time the particle travels from its start to its end point and t_γ is the TOF of the photon. The corresponding distances are introduced in figure 6.21. Thus, the time after TOF-correction with respect to the vertex $\boldsymbol{r}_s$ is

$$t^{0,\mathrm{TOF}}_{\boldsymbol{r}_s} = t_0 + t_p + \frac{n}{c_0}\left(d_\gamma - d_c\right). \tag{6.14}$$

It is minimal if $d_\gamma - d_c$ is minimal. From figure 6.21 it can be seen, that this is the case if the OM which detected the photon is directly on the extension of the track. This means, that the direction of the tracks can be determined by looking at the position of the OM with the smallest TOF-corrected hit time. Note that for the detected first photons from the start point, which are expected on the wall in opposite track direction (see figure 5.1), the TOF-correction is done with respect to the correct point, i.e., for

these photons $t_{\boldsymbol{r}_s}^{0,\mathrm{TOF}} \approx t_0$ while for the points belonging to the minima, $t_{\boldsymbol{r}_s}^{0,\mathrm{TOF}} < 0$ as the particle travels with $v = c_0$ while the photon speed assumed for the TOF-correction is only c_0/n.

6.5.1 Algorithm

The determination of the minima on the wall is conducted in multiple, consecutive steps:

Selecting OMs with a high occupancy:
As, similar to the backtracking algorithm from section 6.4, only the first photon light front is relevant, only OMs with a high occupancy provide the required information. In this case, this is simply done by requiring

$$|z_s - z_i| < 20\,\mathrm{m}, \tag{6.15}$$

where z_i is the z-position of the PMT.

Determination of the start time of the event:
In a next step, t_0 is determined. As all neutrinos arrive from the same direction, the relativistic boost ensures that basically all tracks are pointing in forward direction. Thus, the wall facing in the direction to CERN should sample the first photon light front of the vertex, i.e. after TOF-correction, the obtained times should be approximately t_0. Therefore, t_0 is determined from the average $t_{\boldsymbol{r}_s}^{0,\mathrm{TOF}}$ of all OMs fulfilling the condition

$$\left(\frac{\varphi_i - \varphi_{\mathrm{OM}}^{\mathrm{CERN}}}{\Delta\varphi_{\mathrm{OM}}}\right)^2 + \left(\frac{z_i - z_{\mathrm{OM}}^{\mathrm{CERN}}}{\Delta z_{\mathrm{OM}}}\right)^2 < r_{\mathrm{max}}^2, \tag{6.16}$$

where $(\varphi_{\mathrm{OM}}^{\mathrm{CERN}}, z_{\mathrm{OM}}^{\mathrm{CERN}})$ are the coordinates of the OM closest to the connection between $\boldsymbol{r}_s$ and CERN, $\Delta\varphi_{\mathrm{OM}}$ and Δz_{OM} are the φ and z distances between two adjacent OMs and $r_{\mathrm{max}} = 5.2$ defines the size of the region from which t_0 is defined. Apart from the mean, also the spread σ_{t_0} of all $t_{\boldsymbol{r}_s}^{0,\mathrm{TOF}}$ is determined on this region.

Definition of a region of interest:
Before the actual region of interest (ROI) is defined, first a candidate ROI is defined. It consists of all OMs fulfilling the condition

$$t_{\boldsymbol{r}_s}^{0,\mathrm{TOF}} < t_0 - 3\sigma_{t_0}. \tag{6.17}$$

Next, isolated OMs are removed from the ROI-candidate. Subsequently, the ROI-candidate is the split into simply connected[13] sub-ROIs and all simply-connected sub-ROIs containing less than 4 OMs are discarded. Finally, the ROI is defined as the smallest rectangle containing all simply connected sub-ROIs. To avoid boundary effects, the ROI is subsequently enlarged by $\pm 2\,\mathrm{m}$ in z-direction and $\pm 0.2\,\mathrm{rad}$ in φ-direction.

Minima finding:
To determine the minima positions, first the statistical fluctuations of the arrival times

[13] A ROI is simply connected if for all possible pairs of points $\boldsymbol{x}, \boldsymbol{y}$ from the ROI, there exists a continuous connection between the points which does not leave the ROI.

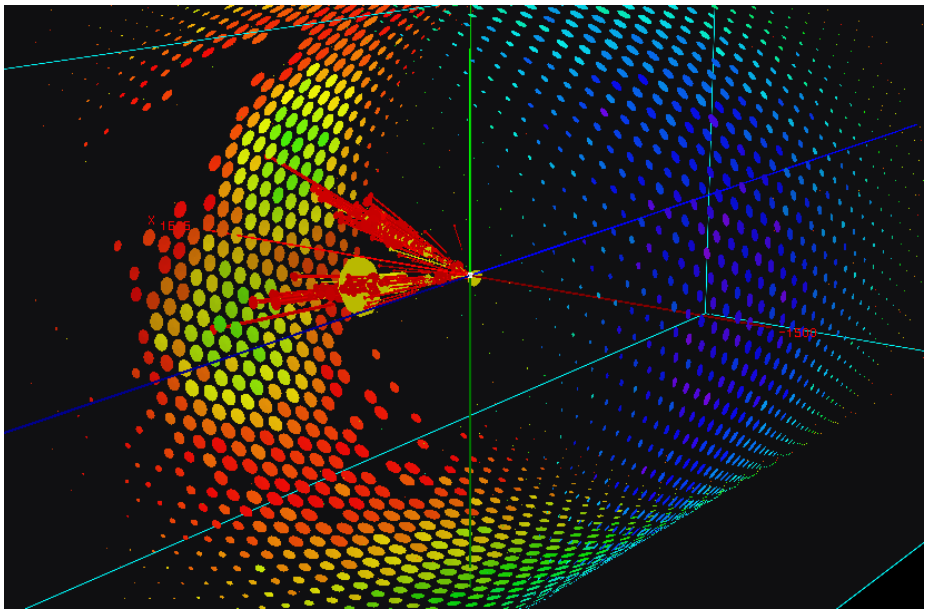

Figure 6.22: LENA event display showing a DIS ν_e-CC event containing a π^0. The interaction vertex is in the center of the detector. The colored circles show the detector response: The areas of the circles show the charge of the OMs while the color of the circles shows the TOF-corrected (with respect to the barycenter) first hit times t_i^0 of the respective OMs. The arrows display the MC-truth information: They connect the vertex and the end point of a particle's trajectory. Their thickness indicates the kinetic energy of the particle while their color indicates the particle type: Red arrows indicate $e^{\pm}$, and yellow arrows γ-rays.

of the photons on the OMs have to be dealt with. Thus, the discrete set of first, TOF-corrected arrival times $t_{\boldsymbol{r}_s,i}^{0,\mathrm{TOF}}$ is transformed into a continuous function of a weighted mean with Gaussian weights:

$$t_{\boldsymbol{r}_s}^{0,\mathrm{TOF}}(\varphi,z) = \frac{\sum_i^{\mathrm{ROI}} w_i(\varphi,z)\cdot t_{\boldsymbol{r}_s,i}^{0,\mathrm{TOF}}}{\sum_i^{\mathrm{ROI}} w_i(\varphi,z)} \tag{6.18}$$

$$\text{with } w_i(\varphi,z) = \frac{1}{2\pi\sigma_s^2}\exp\left[-\frac{(z-z_i)^2+(\varphi-\varphi_i)^2\rho_{\mathrm{OM}}^2}{2\sigma_s^2}\right], \tag{6.19}$$

with the sums running over all OMs in the ROI. Here, $\sigma_s = 1.5\,\mathrm{m}$ is the standard deviation of the Gaussian used for smoothing and ρ_{OM} is the mounting radius of the OMs in LENA. To find a minimum, $t_{\boldsymbol{r}_s}^{0,\mathrm{TOF}}(\varphi,z)$ is evaluated on a grid with size $\Delta z_G = \sigma_s$ and $\Delta\varphi_G = \sigma_s/(7\rho_{\mathrm{OM}})$. A minimum at the position $(\varphi^{\min}, z^{\min})$ is defined as a point which is smaller than all its neighbors. Note that the local minimum is preferred to the global minimum here as this allows resolving multiple tracks.
An exemplary ν_e-CC event is shown in figure 6.22. The corresponding $t_{\boldsymbol{r}_s}^{0,\mathrm{TOF}}(\varphi,z)$ is displayed in figure 6.23 for the found ROI along with the positions of the found minima.

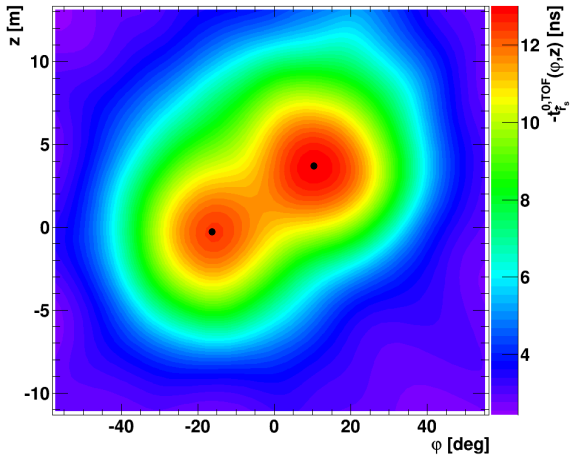

Figure 6.23: The negative, smoothed TOF-corrected hit time $-t_{\boldsymbol{r}_s}^{0,\mathrm{TOF}}(\varphi, z)$ (see equation (6.18)) as a function of φ and z for the event displayed in figure 6.22. The shown region corresponds to the ROI found for this event. The two black dots show the positions of the found minima. Note that the minima appear as maxima in the plot as the negative $t_{\boldsymbol{r}_s}^{0,\mathrm{TOF}}$ is plotted for better color display.

Extraction of the minimas' properties:
Each minimum on the wall corresponds to a possible track. Note that while the minimum can be created by a track of a single particle, this does not need to be the case. In the exemplary event shown in figures 6.22 and 6.23 the minima are caused by electromagnetic showers. For simplicity, the expression "track" will be used as a substitute for all possibilities for the remainder of this section.
The first and most relevant property of a minimum is its position on the wall. It can be converted into a prototype track direction $\hat{\boldsymbol{d}}_p$ assuming that the track which caused the minimum originates from the found vertex:

$$\hat{\boldsymbol{d}}_p = \frac{\boldsymbol{r}_m - \boldsymbol{r}_s}{|\boldsymbol{r}_m - \boldsymbol{r}_s|} \quad \text{with } \boldsymbol{r}_m = \begin{pmatrix} \rho_{\mathrm{OM}} \cos(\varphi^{\min}) \\ \rho_{\mathrm{OM}} \sin(\varphi^{\min}) \\ z^{\min} \end{pmatrix}. \tag{6.20}$$

Apart from the direction of the track, also the depth of the minimum is determined, as it is correlated to the longitudinal extension of the track. It is defined as

$$\Delta t_{\boldsymbol{r}_s}^{0,\mathrm{TOF}} = t_0 - t_{\boldsymbol{r}_s}^{0,\mathrm{TOF}}(\varphi^{\min}, z^{\min}). \tag{6.21}$$

Finally, also the width of the minimum in φ and in z direction is determined as it might be correlated to the kind of particle which created the minimum. Thus, the extension of the minimum has to be defined. This is done by associating all points $(\varphi_{i,G}, z_{i,G})$ on the grid which fulfill the condition

$$t_{\boldsymbol{r}_s}^{0,\mathrm{TOF}}(\varphi_{i,G}, z_{i,G}) < t_{\boldsymbol{r}_s}^{0,\mathrm{TOF}}(\varphi^{\min}, z^{\min}) + \frac{1}{2}\Delta t_{\boldsymbol{r}_s}^{0,\mathrm{TOF}} \tag{6.22}$$

and which can be connected to the minimum passing only points which do satisfy condition (6.22) to the minimum. This definition does not work properly in case there are

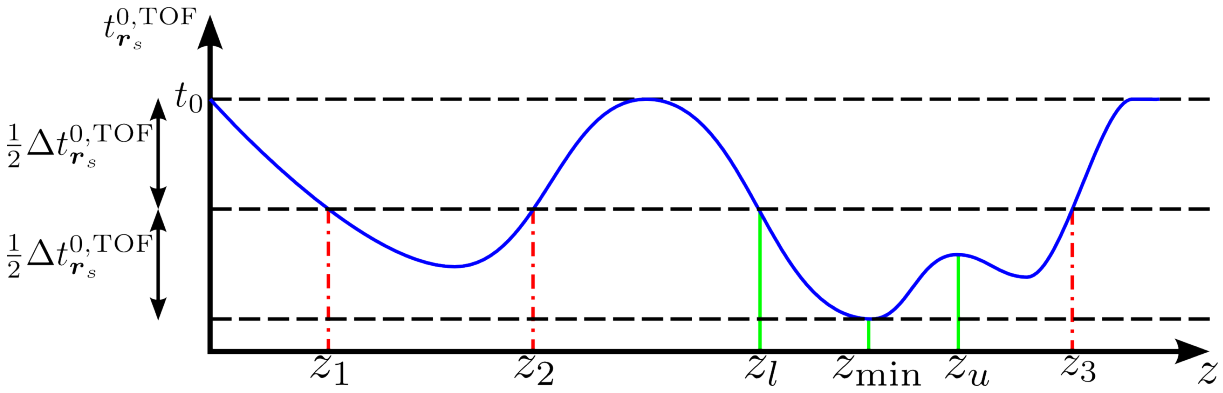

Figure 6.24: One dimensional sketch of the procedure to determine the width of the minimum, neglecting the influence of the grid. The blue curve represents the smoothed TOF-corrected hit time $t^{0,\mathrm{TOF}}_{\boldsymbol{r}_s}(z)$ (see equation (6.18)) as a function of z. It features a minimum at $z = z_{\mathrm{min}}$. According to condition 6.22, all z-values with $t^{0,\mathrm{TOF}}_{\boldsymbol{r}_s}(z)$ below the middle dashed line, i.e., all points with $z \in [z_1, z_2] \cup [z_l, z_3]$, belong to the minimum. As all points which belong to the minimum have to be connected to z_{min} passing only z values fulfilling condition 6.22, all z with $z_1 < z < z_2$ drop out as the points between z_2 and z_l do not fulfill condition 6.22. Furthermore, only points belong to the minimum from which the minimum can be reached using a steepest descent algorithm. As all the points with $z_u < z < z_3$ would end up in a local minimum, they are also removed from the minimum. Hence, the final extension of the minimum is $z_l < z < z_u$.

overlapping minima. Thus an additional condition is introduced which states that only points from which the minimum is reached using a steepest descent algorithm belong to the minimum. The definition of the extension of the minimum is illustrated in a one-dimensional sketch in figure 6.24. For each minimum, its maximum distance to the boundary of its extension in positive and negative φ and z direction are evaluated and converted to deviations in direction using equation (6.20).

6.5.2 Performance

To evaluate the performance of the algorithm presented in section 6.5.1, the found tracks have to be compared to the true tracks. This is done by applying the algorithm to the simulated ν_e-CC and ν_μ-CC events and by testing how well the algorithm is able to determine the track of the primary lepton.
The first arising question is, whether the algorithm is able to find the primary lepton track at all. The criterion used to decide whether the lepton track was successively identified is that a track-candidate was found, which encloses a smaller angle to the true lepton direction than to any other true direction of a primary particle. The resulting efficiency as a function of the true kinetic energy of the lepton T_l^{true} is displayed in figure 6.25, for both ν_e-CC and ν_μ-CC events. While being relatively small, $T_l^{\mathrm{true}} < 0.5\,\mathrm{GeV}$, it monotonously rises with the true kinetic energy of the lepton. This can be understood from the underlying principle as the depth, and therefore the distinctness of a minimum is determined by the length of the track which rises with the kinetic energy of the lepton. That the performance of the algorithm is strongly dependent on the length of the track can also be seen by comparing the results for ν_e-CC and ν_μ-CC events: As the muon track is much longer than the electron track at the same kinetic energy, the efficiency for

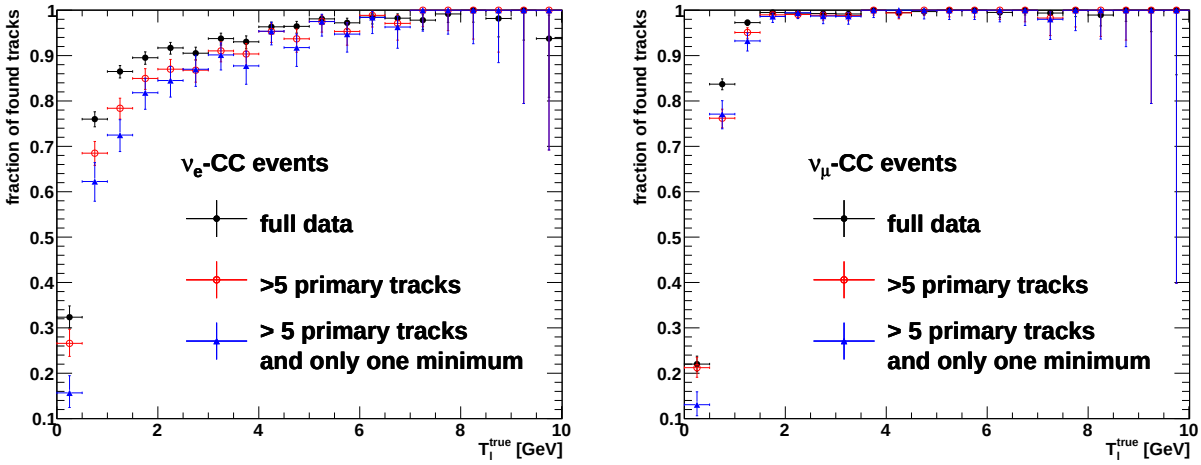

Figure 6.25: The fraction of events which feature a track candidate which is enclosed in a smaller angle to the true lepton track than to any other true primary track as a function of the true kinetic energy of the lepton T_l^{true} for ν_e-CC events (left) and ν_μ-CC events (right). Apart from the full data set, also two more data sets are shown: The first features only events with at least five true primary tracks. For the second data set, additionally the requirement that only one minimum is found is imposed.

ν_μ-CC events rises much faster than that for ν_e-CC: While the former is already basically equal to one for $T_l^{\text{true}} \gtrsim 2\,\text{GeV}$, the latter requires $T_l^{\text{true}} \gtrsim 7\,\text{GeV}$ to reach full efficiency. Additionally, the deviations from a straight line are much stronger for electron showers which also smears out the minimum.
While this already looks very promising, two additional checks were performed to make sure that the relatively good performance of the algorithm is not only due to statistical luck. First, such a result might be produced by lots of events featuring only one true track, as this would always lead to a found muon track. To make sure that this is not the case, the analysis was applied to a data set which features only events with more than five primary particles. Furthermore, a falsely positive result might be caused by lots of events featuring a huge number of found minima and therefore lots of track-candidates leading to an increased probability that one of theses tracks is very close to the lepton track even though the prototype tracks feature a totally random distribution. Thus a third data set was created and evaluated, which featured only events with at least five true primary particles and only one found prototype track. The resulting efficiencies of these two additional data sets are also shown in figure 6.25. While the resulting efficiencies are slightly worse than the efficiencies for the original data set, they are much too high to be explained by statistical luck only, thus showing that the found prototype tracks actually are correlated to the true lepton tracks.
The tracks associated to the true lepton tracks can successively be used to determine how well the direction of a particle can be resolved with this method. Figure 6.26 shows the distribution of the angular differences between the true lepton track and the closest found track candidate. With a mean deviation of only about 2.3 deg for ν_μ-CC events and 4.0 deg for ν_e-CC events the angular resolution is quite close to the resolutions obtained in single track fits (see section 5.4). Note, however, that the condition that the angle to the closest track is evaluated, statistically suppresses the possible angular differences, thus the results are not directly comparable with the results from the track fits. Finally,

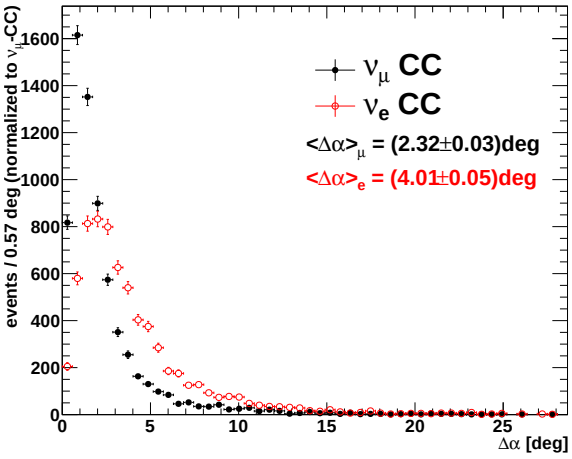

Figure 6.26: The distribution of angular differences $\Delta\alpha$ between the true lepton track and the closest found track candidate for ν_e-CC and ν_μ-CC events. The corresponding mean angular deviations are also displayed.

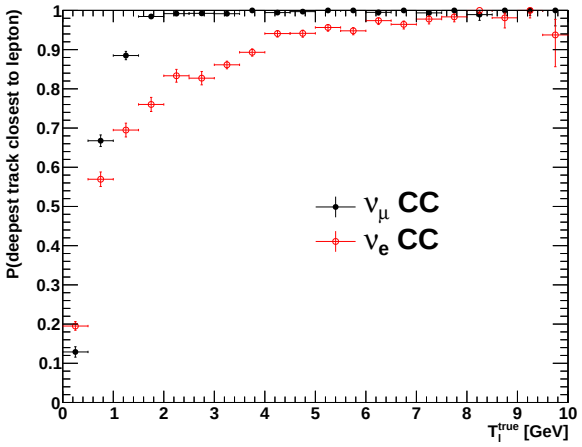

Figure 6.27: The estimated fraction of all events in which the deepest found track is also the track closest to the lepton as a function of the true kinetic lepton energy T_l^{true} for ν_e-CC and ν_μ-CC events.

the question arises whether it is possible to determine which of the found tracks belongs to the lepton track. The simplest possible approach is to assume that the candidate track corresponding to the deepest minimum belongs to the lepton track. The efficiency of this assumption in the identification of the track-candidate closest to the lepton track is shown in figure 6.27 as a function of the true kinetic energy T_l^{true} of the lepton. It shows that the assumption is valid most of the time for $T_l^{\text{true}} \gtrsim 1\,\text{GeV}$. Again, the highly penetrating muons can be tagged more easily than the electron tracks.
In summary, the presented algorithm shows promising results concerning its applicability to gain additional information on the event.

6.6 Implications for the LENA mass-hierarchy sensitivity

As already discussed in section 3.2.7 the critical background to use LENA as a far detector for the CN2PY-neutrino beam is the NC background. It is currently tackled using a MVA based on BDTs [100]. This currently leads to a reduction of the NC-background by $1 - \epsilon_{\text{NC}} = 89\,\%$ at a signal efficiency of $\epsilon_{\nu_e\text{-CC}} = 27\,\%$. Combining the efficiencies for different channels with the migration matrices from section 6.3, the physics reach of LENA as a far detector can be determined [96]: On the left of figure 6.28, the resulting statistical power[14] is shown as a function of the exposure in protons on target (POT). On the right of figure 6.28 the same plot is shown, but this time assuming a higher signal efficiency of $\epsilon_{\nu_e\text{-CC}} = 50\,\%$ at $\epsilon_{\text{NC}} = 10\,\%$. Note that the migration-matrices discussed in section 6.3 are a crucial input parameter for computation of the projected experimental sensitivities. Comparing the two results, a significant difference in the resulting statistical powers is visible. For the standard case, even at full exposure the probability to obtain

[14] The statistical power is defined as $p = 1 - \beta$, where β is the error of type II, i.e. β is the probability to reject the true hierarchy [106].

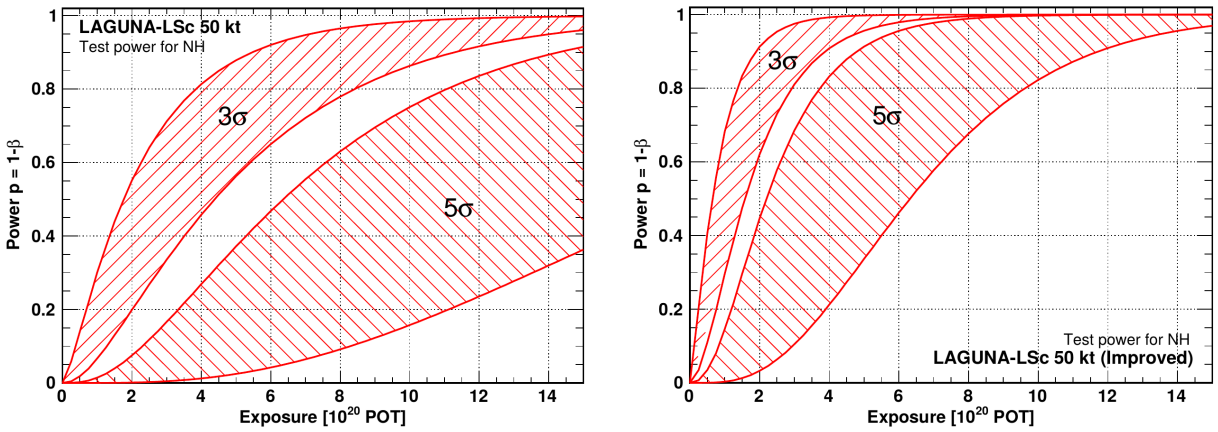

Figure 6.28: The resulting statistical power of the MH determination with LENA as a far detector for the CN2PY beam as a function of the exposure in protons on target (POT) for the standard assumptions on the efficiency for the ν_e-CC channel, $\epsilon_{\nu_e\text{-CC}} = 27\,\%$ and NC background efficiency, $\epsilon_{\text{NC}} = 11\,\%$ (left) and for an hypothetic version with $\epsilon_{\nu_e\text{-CC}} = 50\,\%$ and $\epsilon_{\text{NC}} = 10\,\%$ (right) [96]. In both cases the NH is assumed to be true. The shaded region is due to the variation of the sensitivity with the CP-phase δ. The results shown were computed using the GLoBES [31, 32] library.

a 5-σ exclusion is between 35 % and 95 % which means that there is a sizable probability that the experiment will return no conclusive result at the 5-σ level. Contrary, using the improved assumptions, the probability for a determination of the MH at the 5-σ level is above 95 % independent of δ. Equally important, a guaranteed statement at the 3-σ level can already be given at lower exposures of about $8 \cdot 10^{20}$ POT.
To go from the standard assumptions to the improved case, the discrimination of the NC-background has to be improved, i.e., additional parameters with a good discrimination power have to be added to the BDTs. Good candidates for such parameters are the results from the algorithms which have been detailed in this chapter.

The parameters presented in the following will be shown in two bins of the reconstructed energy of the primary cluster of the event: As the simulated neutrino energies start at 1 GeV (see section 6.1), the low energy bin is chosen to be $T_{\text{LE}} = [1\,\text{GeV}, 2\,\text{GeV}]$, where the discrimination is most critical due to the shift of the NC events to lower energies (see section 6.3). To also check the performance at higher energies, the second bin is chosen to be $T_{\text{HE}} = [5\,\text{GeV}, 6\,\text{GeV}]$, which is the available bin with the highest reconstructed energy still containing enough NC events.

Using the clustering algorithm presented in section 6.2, it is possible to determine the number of found secondary clusters. This can be used to discriminate between ν_e-CC and NC events: Especially NC events with a visible energy above the energy threshold of $\sim$1 GeV are very hard interactions, i.e., they feature a very high momentum transfer in the GeV range which results in a high number of hadronic particles being produced. Therefore, these events should feature many produced neutrons and pions resulting in a high number of detected secondary clusters. ν_e-CC interactions with the same visible energy on average feature smaller momentum transfer as a part of the visible energy is deposited by the primary lepton. Thus, a smaller number of secondary clusters is expected.

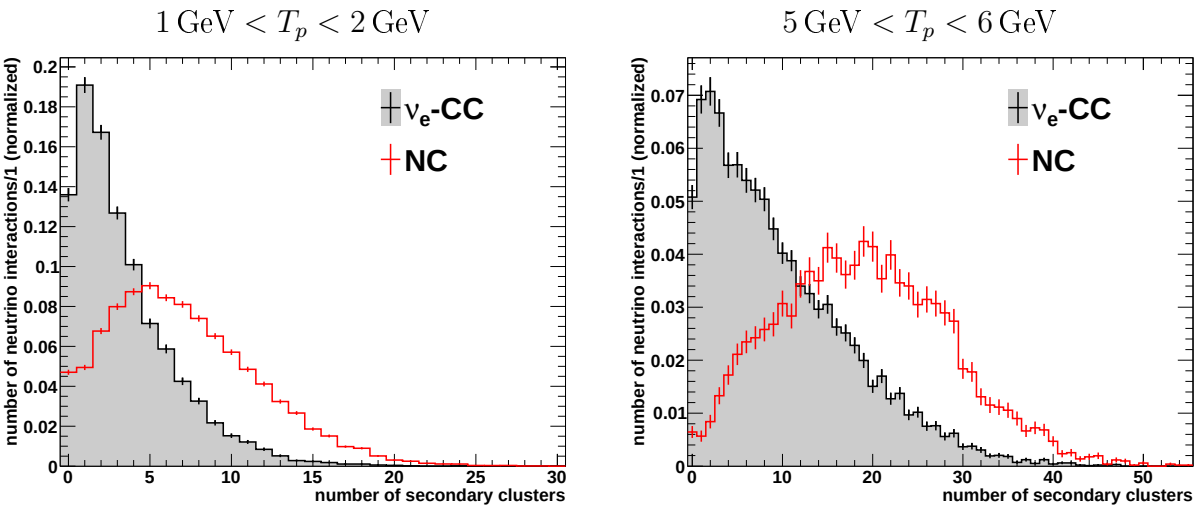

Figure 6.29: Comparison of the distributions of the number of found secondary clusters for ν_e-CC and NC events for reconstructed energies of the primary cluster T_p in the range $[1.0, 2.0]$ GeV (left) and in the range $[5.0, 6.0]$ GeV (right).

Figure 6.29 shows a comparison of the distributions of the number of found clusters between ν_e-CC and NC events for visible energies of the primary cluster T_p from 1 GeV to 2 GeV and from 5 GeV to 6 GeV. In both energy ranges, a distinct difference between the found distributions for the two event classes is visible. Thus, the number of secondary clusters provides an additional input parameter to discriminate between ν_e-CC and NC events.

Complementary input parameters for the MVA can be obtained from the algorithm to estimate candidate tracks presented in section 6.5. The simplest possible parameter is the number of candidate tracks. Its distribution for ν_e-CC and NC events is shown in figure 6.30 for T_p being in the low-energy bin T_{LE} (left) and in the high-energy bin T_{HE} (right). In the low-energy bin, there are lots of NC-events which do not feature any candidate track as the range of produced heavy hadrons is too low to create a visible minimum. This is not the case for ν_e-CC events where the electron track is typically found (see section 6.5.2) which already creates a usable difference between the distribution. Also in the high-energy bin a difference is visible, which, however, looks quite different than in the low-energy bin: At higher energies the number of found track candidates tends to be higher for NC events compared to ν_e-CC events. This shows that to reach deposited energies in this range, the NC event has to contain multiple high energetic pions which have a good range and are thus recognized as a track candidate but which are, in contrast to neutrons and protons, nearly unquenched.
Another additional parameter for the MVA can be obtained considering that the total transverse momentum of the secondaries of a neutrino event should add up to zero. As the neutrino in the exit channel of a NC event is not visible in the detector, this does not hold for the total transverse momentum of the visible secondaries. Thus, NC events are expected to be more asymmetric than CC events. An asymmetry parameter can be

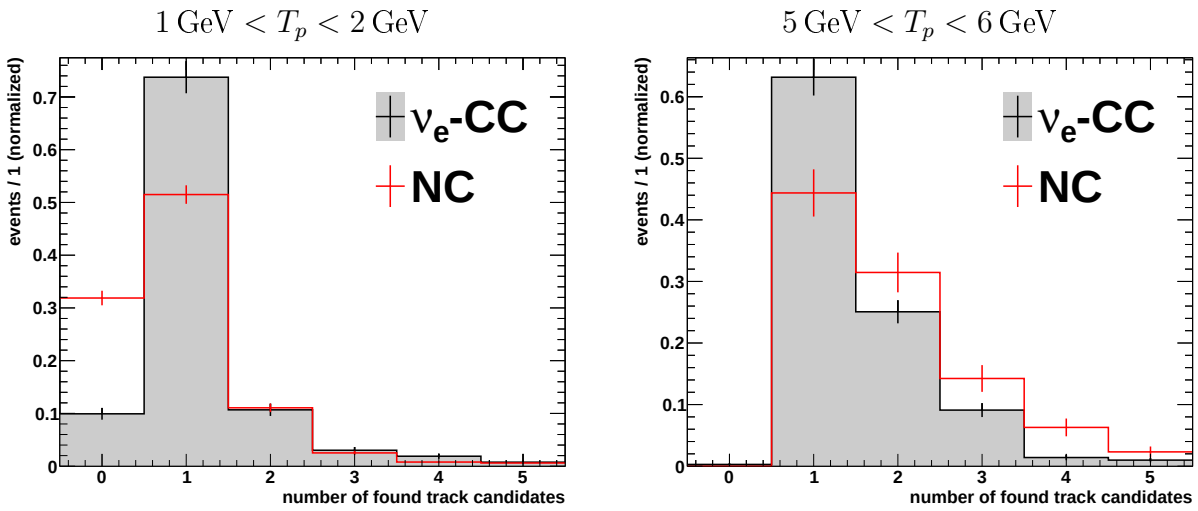

Figure 6.30: Comparison of the distributions of the number of found track candidates for ν_e-CC and NC events for reconstructed energies of the primary cluster T_p in the range $[1.0, 2.0]$ GeV (left) and in the range $[5.0, 6.0]$ GeV (right).

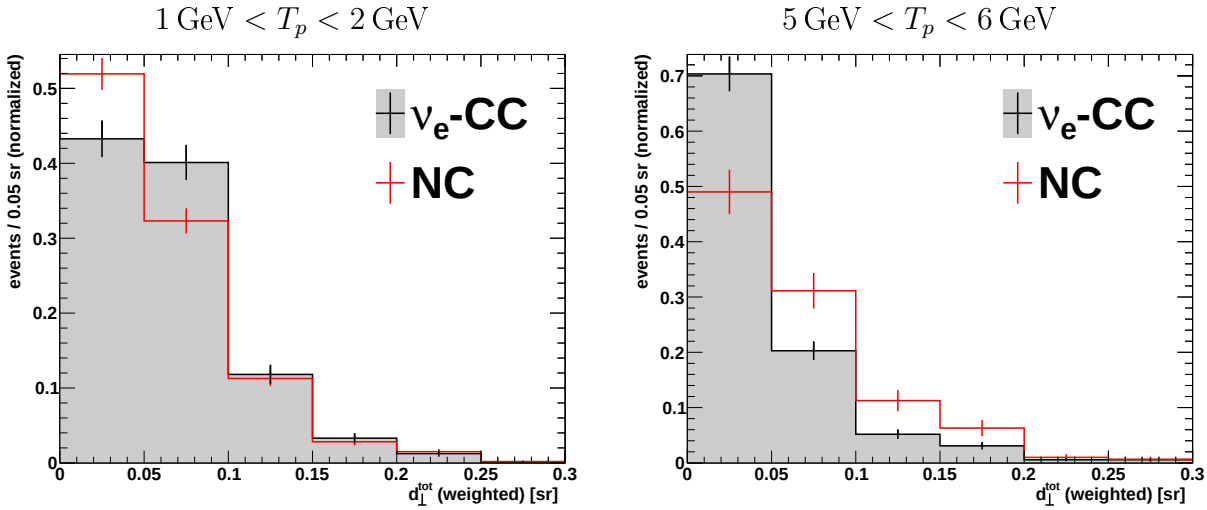

Figure 6.31: Comparison of the distributions of the area-weighted transverse direction of the event (see equation (6.23)) for ν_e-CC and NC events for reconstructed energies of the primary cluster T_p in the range $[1.0, 2.0]$ GeV (left) and in the range $[5.0, 6.0]$ GeV (right).

obtained from the directions of the track-candidates:

$$\boldsymbol{d}_\perp^{\mathrm{tot}} = \sum_{i=1}^{N_{\mathrm{candidates}}} A_i \cdot \boldsymbol{d}_i^\perp, \tag{6.23}$$

where $N_{\mathrm{candidates}}$ is the number of found track candidates, $\boldsymbol{d}_i^\perp$ is the component of the direction of the candidate track which is perpendicular to the direction of the incident neutrinos $\hat{\boldsymbol{d}}_\nu$, and A_i is the solid angle covered by the minimum. To determine A_i the minimum is assumed to be a rectangle in solid angle with the height and width given by the determined errors in the direction. The resulting distributions for ν_e-CC and NC events for the two common energy bins are shown in figure 6.31. The high-energetic bin, as expected, shows an excess of NC events at high $d_\perp^{\mathrm{tot}}$ compared to ν_e-CC events. For

the low-energy bin in contrast, the ν_e-CC sample shows a higher number of events with high $d_{\perp}^{\mathrm{tot}}$. This can be explained as at these energies, typically the hadronic component does not produce tracks which are long enough to be visible (see the discussion above about the number of found tracks). Thus, the asymmetry of the ν_e-CC sample seen here is dominated by the transverse component of the lepton track which is, of course, not existent in the NC sample which hence features smaller asymmetries.

The parameters which can be extracted from the algorithms presented in this chapter will definitely improve the situation concerning the capabilities of LENA as a far detector for the CN2PY neutrino beam and even might be sufficient to get close to the optimistic case shown in figure 6.28. However, a much stronger positive effect can be obtained once the different algorithms for visualization of the event (as, e.g., the backtracking algorithm which was discussed in section 6.4) start to produce results concerning the type, energy and direction of all primary particles which produce a track featuring a significant length. This information can successively be refined using a likelihood algorithm similar to that in chapter 5, thus opening the path for discriminating different possible event types using likelihood ratios. If it is possible to get all this machinery in place, the resulting capabilities of LENA as a far detector for a neutrino beam could significantly be improved. Note, that all the possible algorithms can, of course, be implemented not only for LENA but for any other large LSc detector like JUNO.

Chapter 7

Measurement of the attenuation length: The set-up using a LED as light source and PMTs as detectors

Due to the huge size of the next generation of liquid scintillator detectors like LENA (see chapter 3) or JUNO (see section 2.3.3), a high transparency of the LSc is required to be able to detect photons originating from the center of the detector at the PMTs. This chapter presents an experiment dedicated to measure the transparency of the LSc.

The quantity characterizing the transparency of a LSc is the attenuation length Λ_{att}. It is defined in section 7.1, where also its importance for LENA is outlined and lessons from previous experiments are discussed. The set-up resulting from these considerations is presented in section 7.2. Section 7.3 discusses the data analysis and presents the results obtained. Finally, section 7.4 describes the underlying features of the experimental set-up responsible for the systematic errors and considers possible approaches to reduce these errors.

7.1 Fundamentals

In this section, the considerations leading to the experimental set-up are presented. First, the attenuation length is defined which already yields some consequences for the measurement (see section 7.1.1). Furthermore, the relevance of the attenuation length for LENA is discussed in section 7.1.2 which sets the required range of the attenuation length the experiment has to cover. Finally, section 7.1.3 discusses lessons learned from measurements with an UV/Vis-spectrometer.

7.1.1 Light attenuation in a liquid scintillator

A photon propagating an infinitesimally short distance dl through a scintillator, has a probability dp of interacting with the scintillator. It is given by [43]

$$dp = \sum_i \sigma_i \rho \; dl = \rho \sigma_{\mathrm{tot}} \; dl, \tag{7.1}$$

where the sum runs over all possible interaction processes i of light with the scintillator, σ_i is the interaction cross section of the photon with the scintillator and ρ is the mass density of the scintillator. Note, that σ_i is constituted from the cross sections of the process on the various components on the scintillator

$$\sigma_i := \sum_k \frac{f_k}{m_k} \sigma_{i,k}, \tag{7.2}$$

where the sum runs over all constituents of the LSc, f_k denotes the mass fraction and m_k the molecular mass of the respective component. Furthermore, $\sigma_{i,k}$ is the cross section of interaction process i for the constituent k. Using this equation, the intensity $I(l)$ of a parallel monochromatic beam after transversing a distance l through the scintillator can be predicted (Lambert-Beer-Bouguer-Law) [122]

$$I(l) = I_0 \exp\left(-\frac{l}{\Lambda_{\text{att}}}\right), \quad \text{with } \Lambda_{\text{att}} := \frac{1}{\rho\sigma}. \tag{7.3}$$

Here, $I_0 = I(l = 0)$ is the initial intensity of the beam and Λ_{att} is the attenuation length. A few of the more subtle ingredients of equations (7.1) and (7.3) which are important for the experiment are listed below:

- Attenuation of light in a scintillator is a composite process consisting of absorption, absorption with successive reemission, Rayleigh-scattering and Mie-scattering. Thus, the attenuation length is composed of multiple components:

$$\frac{1}{\Lambda_{\text{att}}} = \frac{1}{\Lambda_{\text{abs}}} + \frac{1}{\Lambda_{\text{scat}}} = \frac{1}{\Lambda_{\text{abs}}} + \frac{1}{\Lambda_{\text{abs/re}}} + \frac{1}{\Lambda_{\text{Ray}}} + \frac{1}{\Lambda_{\text{Mie}}}, \tag{7.4}$$

  where Λ_{abs} denotes the absorption length, $\Lambda_{\text{abs/re}}$ the length for absorption with successive reemission, Λ_{Ray} the Rayleigh-scattering length and Λ_{Mie} the Mie-scattering length. The scattering lengths, whose effects on a parallel beam are summarized with Λ_{scat}, are determined for the LENA LSc in [123]. A more detailed description of the different interaction processes can be found in [66]. As the scattering lengths are already determined, an additional measurement of the attenuation length would allow for a complete description of the optical properties of the LSc.

- As equation (7.3) deals with the intensity of a parallel beam, all scattered components of the beam are considered to be lost. Therefore, the experiment has to be designed to remove scattered light from the measured light as effectively as possible.

- As Λ_{att} is generally dependent on the wavelength of the light, equation (7.3) only holds for a monochromatic beam. Thus, a narrow-band light beam has to be used in the experiment. In this experiment, 430 nm is chosen as the central wavelength as it is the wavelength with the highest contribution to the observed signal in a large LSc detector.

7.1.2 Effect of the attenuation length on the LENA performance

As the scattering lengths of the LSc have already been measured in [123], they state an upper boundary for the attenuation length by assuming a perfect scintillator with no absorption:

$$\Lambda_{\text{att}} \lesssim 25\,\text{m}. \tag{7.5}$$

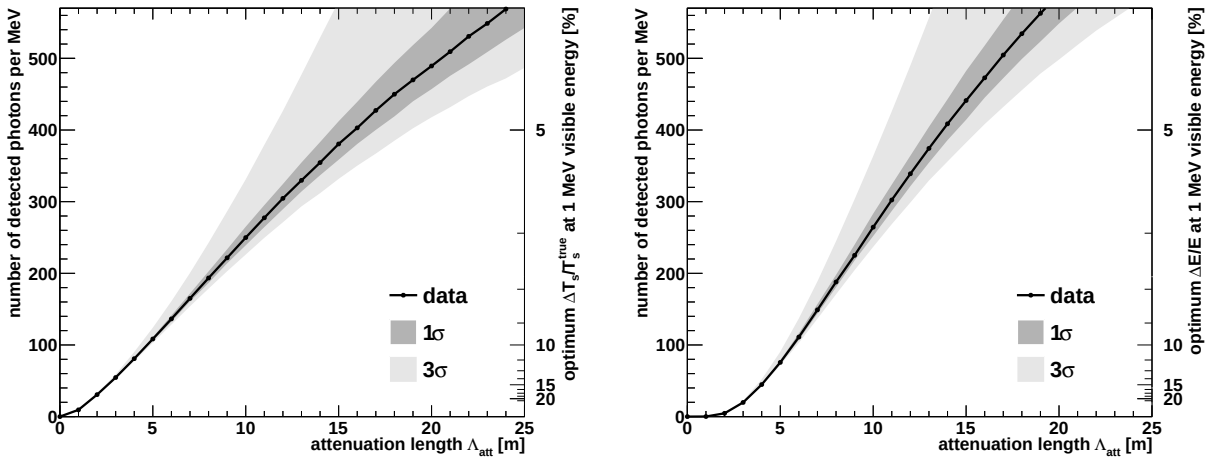

Figure 7.1: The average number of detected photoelectrons for 1 MeV electron events as a function of the attenuation length. For the left (right) panel, a 13.5 m (9 m) fiducial volume is assumed. The shaded area indicates the variations due to the uncertainties of the scattering parameters. The right axis indicates the maximal relative energy resolution $\Delta T_s/T_s^{\text{true}}$ which is achievable due to the photon statistics at 1 MeV visible energy (compare equation (4.1)).

Using the LENA simulation[1] and the results from [123], the performance of LENA was evaluated for attenuation lengths up to this boundary. Figure 7.1 shows the average number of detected photo-electrons as a function of the attenuation length. On the left, the dependency is shown for a fiducial volume with 13.5 m radius (left), corresponding to the maximally usable fiducial volume due to the reconstruction capabilities (see section 4.5.1). The effect of Λ_{att} on the detector performance is obvious. It is illustrated by the effect on the energy resolution $\Delta T_s/T_s^{\text{true}}$ obtainable on the right axis of figure 7.1. The effect of the attenuation length is even more pronounced if smaller fiducial volumes are used to suppress external γ-ray background. This is shown on the right panel of figure 7.1 for a fiducial volume of 9 m corresponding to the fiducial volume of the more background-sensitive ^{8}B analysis in [41]. Note, that the background-critical analyses, which require such a small fiducial volume, typically deal with very low visible energies where every detected photon is valuable.
From the point of view of the experiment, two conclusions can be drawn from these considerations: First, the experiment should be able to cope with attenuation lengths of up to 25 m and second, that for a precise determination of the physics potential of LENA an equally precise measurement of the attenuation length is required. Thus, a total error which is significantly below 10 % is desirable.

7.1.3 Previous measurements with a UV/Vis-spectrometer

Before the construction of the experiment, the optical transparency of LAB-based scintillators was mostly studied using UV/Vis spectrometers [62, 65, 124, 125, 126]. Typically, for these experiments, the scintillator is contained in a quartz cuvette with a length of

[1] To save computation time, the simulation was not conducted using individual OMs but using the whole detector wall as sensitive area and scaling the light yield appropriately. Note, that the angle-dependent detection efficiency due to the LCs (see figure 4.1) is nevertheless applied. For a detailed description see [41], section 1.3.1, "Simple Mode".

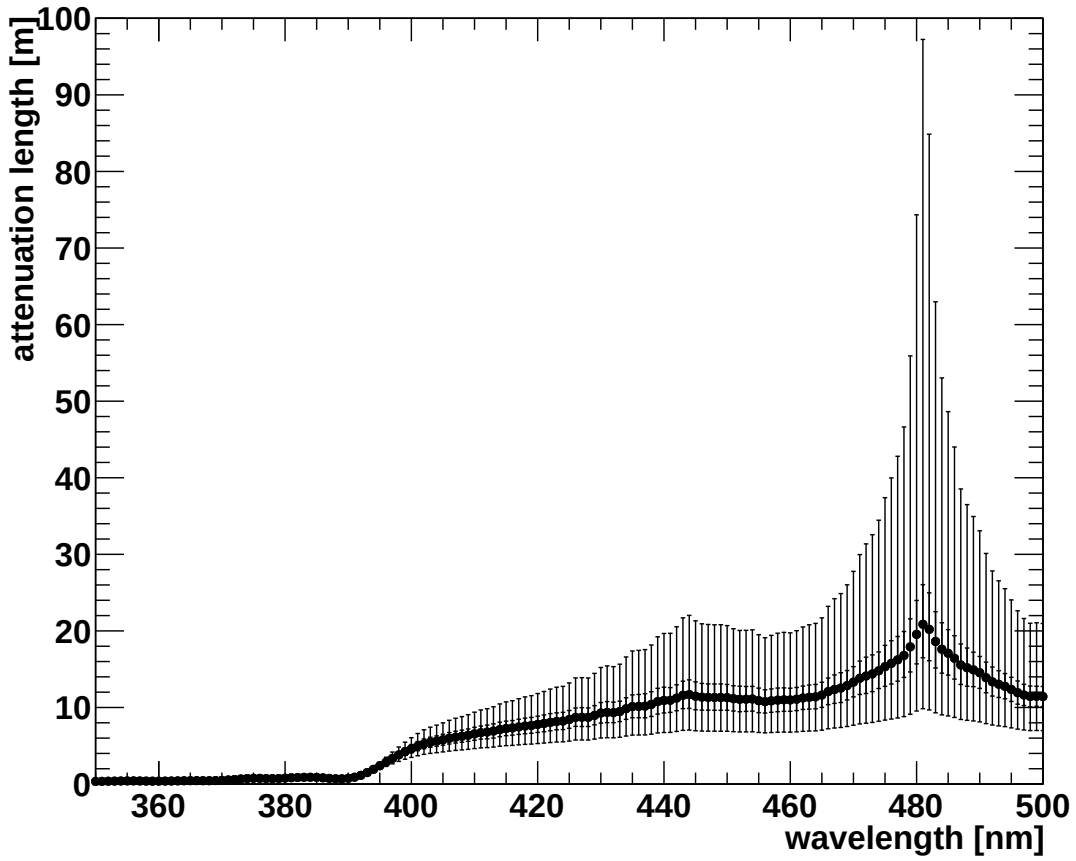

Figure 7.2: The attenuation length of LAB as a function of the wavelength as determined using a Perkin Elmer LAMBDA 850 UV/Vis-spectrometer with a 10 cm cuvette. The inner error bars show the statistical errors, the outer error bars the total errors. The raw data was taken from [62]. The LAB investigated was obtained from [58]. At the 430 nm, which is the wavelength used in this experiment, the determined attenuation length is: $\Lambda_{\mathrm{att}}(430\,\mathrm{nm}) = (9.28^{+1.4}_{-1.3}(\mathrm{stat})^{+5.7}_{-3.0}(\mathrm{syst}))\,\mathrm{m}$.

about 10 cm. Figure 7.2 shows the attenuation length of LAB as obtained from the manufacturer (including errors) determined with a Perkin Elmer LAMBDA 850 UV/Vis-spectrometer and a 10 cm cuvette. Note that the measured sample was taken from the same badge as the sample measured in this section. The figure shows one of the big advantages of the UV/Vis-spectrometer: It covers the whole wavelength range of interest. On the other hand, the obtained errors are large for attenuation lengths larger than a few meters. If $\Lambda_{\mathrm{att}} \gtrsim 10\,\mathrm{m}$, typically no stronger statement than "the attenation length is above 10 m" is possible, which of course does not comply to the requirements set in section 7.1.2.

There are two main reasons for the observed large error: Firstly, and most importantly, a $\sim$10 cm cuvette is not sufficient to measure attenuation lengths above 10 m. At an attenuation length of 10 m, the observed decline in intensity is only 1 %. Thus, even the very precise measurement provided by the UV/Vis spectrometer is not sufficient for a more accurate result. Secondly, these small deviations lead to a large dependency on systematic errors. Furthermore, the length of the scintillator-filled cuvette is fixed, which means that the effects of light reflections at the windows of the cuvette and in the quartz glass

cannot be corrected analytically. Hence, only an approximate correction of these effects is possible.
For the experiment presented here, this means that a much longer light path in the scintillator is required which should be at least a few meters and that this light path has to be variable to be able to determine the effect of the windows from the results of the measurements. Additionally, the UV-Vis-measurements show that the variability of the attenuation length in the 430 nm region is small (confer figure 7.2), thus a spectral width of the beam of ∼10 nm should be sufficient.

7.2 Experimental set-up

This section presents the experimental set-up resulting from the consideration of the experimental requirements which has been derived in section 7.1. A predecessor of this set-up is described in [99]. Section 7.2.1 provides a general overview of the experiment. Subsequently, section 7.2.2 outlines some general considerations which form the basis of the final data analysis. The following sections cover sub-systems of the experiment in more detail: The fluid system (see section 7.2.3), the used optics (see section 7.2.4) and finally the electronics and data acquisition (DAQ) (see section 7.2.5).

7.2.1 Overview of the set-up

To measure the attenuation length, the intensity of a monochromatic light beam has to be measured before and after the light transverses the liquid scintillator (see equation (7.3)). The set-up used for this purpose is sketched in figure 7.3. The light originates from a pulsed light-emitting diode (LED) which is coupled into a fiber optics. After exiting the fiber optics, the light is parallelized using an achromatic lens. A subsequent beam splitter, divides the light beam into two equal components: The intensity of the first part is monitored using a reference PMT (PMT1). The second part is deflected by a mirror and, after passing an additional aperture for further collimation, sent through the tube onto the second PMT (PMT2) which measures the intensity after the tube. A modular design was used for the 2" wide tube which allows to assemble the tube in different lengths from 1 m to 5 m in 1 m steps. In contrast to the 10 cm UV/Vis-spectrometer cell, this long tube results in a sizable effect of the light attenuation even for larger attenuation lengths. Additionally, as it offers the opportunity to measure at different lengths, the modular design allows to get rid of the effects of the front and back windows of the tube. At the connections between the different components of the tube, additional 1" apertures have been added to suppress contributions from scattered light. For a further suppression of scattered light, the tube was coated with a black Chromiumoxide layer using the electrochemical INOX-SPECTRAL [127] procedure[2].
The sample measured in the experiment consists of pure LAB obtained from the Spanish company HELM [58]. Thus, it actually does not constitute a full scintillator as the wavelength shifters are missing. It was measured at each available tube length, starting with the longest length and successively going to smaller tube lengths. The measurement was subsequently repeated in the opposite direction i.e. starting from small tube lengths and going to larger ones.

[2]The coating procedure was executed by the firm INOX-COLOR GmbH & Co.KG

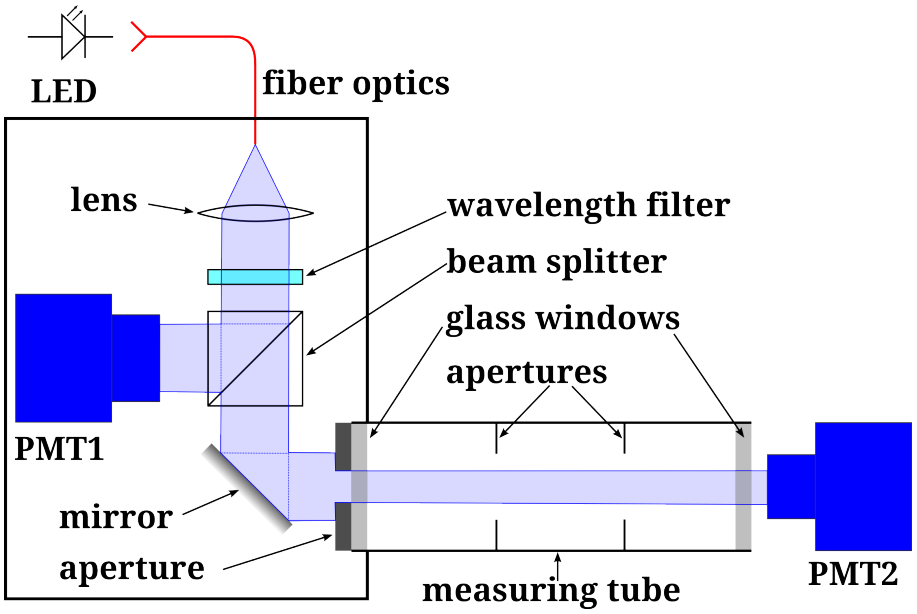

Figure 7.3: A sketch of the set-up used to measure the attenuation-length (not to scale). A pulsed LED was used as a light source. The produced light is coupled into a fiber optics which transports the light into a dark-box. The light is successively collimated using an achromatic lens. In a next step, a bandpass filter further reduces the wavelength range of the LED. The resulting nearly parallel light beam is split into two equal parts. One part is directed onto PMT1 to monitor the beam intensity, the other part is coupled into the tube by a mirror. To tighten the beam, an aperture is installed directly in front of the tube. After passing the modular measurement tube, which can be filled with LSc, the beam is detected by PMT2. Additional apertures are positioned inside the tube to suppress scattered light. Using the modular tube, light pathes in the scintillator from 1 m to 5 m can be obtained.

7.2.2 Basic considerations

To determine the attenuation length, the ratios between the intensity after the tube, as determined with the PMT2, and the intensity before the tube, as determined with PMT1, have to be measured for multiple lengths. From figure 7.3, the probability P_1 that a photon which is emitted from the fiber optics is detected by the PMT1 is given by

$$P_1 = P_{\mathrm{WL}} \cdot P_{\mathrm{BS}}^{\perp} \cdot \epsilon_{\mathrm{PMT1}}, \tag{7.6}$$

where P_{WL} is the (wavelength dependent) probability that a photon passes the wavelength filter, $P_{\mathrm{BS}}^{\perp}$ is the probability that the photon is deflected onto PMT1 by the beam splitter and $\epsilon_{\mathrm{PMT}i}$ is the quantum efficiency of PMT $i (i \in \{1,2\})$. Similarly, the probability for a photon to be detected by PMT2 after passing through the scintillator-filled tube with the length d is[3]

$$P_2^f = P_{\mathrm{WL}} P_{\mathrm{BS}}^{\parallel} \cdot R_M \cdot T_{\mathrm{A1}} \cdot \underbrace{T_{\mathrm{AG1}} \cdot T_{\mathrm{G1}} \cdot T_{\mathrm{GS1}}}_{\text{entrance window}} \cdot \exp\left(-\frac{d}{\Lambda_{\mathrm{att}}}\right) \underbrace{\cdot T_{\mathrm{GS2}} \cdot T_{\mathrm{G2}} \cdot T_{\mathrm{AG2}}}_{\text{exit window}} \cdot \epsilon_{\mathrm{PMT2}}, \tag{7.7}$$

where $P_{\mathrm{BS}}^{\parallel}$ is the probability that a photon passes through the beam splitter without being deflected, R_M is the reflectivity of the mirror, T_{A1} is the transmission of the aperture in

[3] Note that multiple reflections between parallel surfaces have been neglected.

front of the tube. Furthermore, $T_{\mathrm{AG1,2}}$ is the transmission of the air-glass surface of the entrance and exit window, respectively, $T_{\mathrm{GS1,2}}$ is the transmission of the glass-scintillator surface of the entrance and exit window and $T_{\mathrm{G1,2}}$ is the bulk transmittance of the entrance and exit window respectively. Therefore, the ratio of the intensities $I_{1,2}$ measured with PMT1 and PMT2 is

$$\begin{aligned}
\xi_f &= \frac{I_2}{I_1} = \frac{N_{\mathrm{ph}} P_2^f}{N_{\mathrm{ph}} P_1} \\
&= \frac{P_{\mathrm{WL}} P_{\mathrm{BS}}^{\parallel} R_M T_{\mathrm{A1}} T_{\mathrm{AG1}} T_{\mathrm{G1}} T_{\mathrm{GS1}} T_{\mathrm{GS2}} T_{\mathrm{G2}} T_{\mathrm{AG2}} \epsilon_{\mathrm{PMT2}}}{P_{\mathrm{WL}} P_{\mathrm{BS}}^{\perp} \epsilon_{\mathrm{PMT1}}} \exp\left(-\frac{d}{\Lambda_{\mathrm{att}}}\right), \qquad (7.8) \\
&= \mathrm{const} \cdot \exp\left(-\frac{d}{\Lambda_{\mathrm{att}}}\right) \qquad (7.9)
\end{aligned}$$

which is independent of the number of emitted photons and thus independent of variations of the light source's intensity. Equation (7.8) is a product of a constant and an exponential decay. Thus, by measuring at multiple lengths, the constant can be eliminated and Λ_{att} can be determined.

By altering the length of the tube, the set-up is modified which leads to variations in the transmissions appearing in equation (7.8) and therefore introduces systematic errors. As the different parts of the tube are connected with screws, changing the tube length always involves the risk of slightly moving the tube and therefore also the aperture at the tube entrance which is fixed to the tube thereby changing T_{A1}. But also the other components of the optical system might be involved due to vibrations during the mounting process and changing dust levels on the surfaces. This problem can be alleviated by measuring not only the transmission of the full tube but also the transmission of the empty tube. The probability to detect a photon at the PMT2 if the tube is empty is

$$P_2^e = P_{\mathrm{WL}} \cdot P_{\mathrm{BS}}^{\parallel} \cdot R_M \cdot T_{\mathrm{A1}} \cdot \underbrace{T_{\mathrm{AG1}} \cdot T_{\mathrm{G1}} \cdot T_{\mathrm{AG1}}}_{\text{entrance window}} \cdot \underbrace{T_{\mathrm{AG2}} \cdot T_{\mathrm{G2}} \cdot T_{\mathrm{AG2}}}_{\text{exit window}} \cdot \epsilon_{\mathrm{PMT2}} \qquad (7.10)$$

which leads to a ratio between the intensities measured at both PMTs of

$$\begin{aligned}
\xi_e &= \frac{N_{\mathrm{ph}} P_2^e}{N_{\mathrm{ph}} P_1} \\
&= \frac{P_{\mathrm{WL}} P_{\mathrm{BS}}^{\parallel} \cdot R_M \cdot T_{\mathrm{A1}} \cdot T_{\mathrm{AG1}} \cdot T_{\mathrm{G1}} \cdot T_{\mathrm{AG1}} \cdot T_{\mathrm{AG2}} \cdot T_{\mathrm{G2}} \cdot T_{\mathrm{AG2}} \cdot \epsilon_{\mathrm{PMT2}}}{P_{\mathrm{WL}} \cdot P_{\mathrm{BS}}^{\perp} \cdot \epsilon_{\mathrm{PMT1}}}. \qquad (7.11)
\end{aligned}$$

Taking the ratio of ξ_f and ξ_e yields the transmission of the tube

$$T(d, C, \Lambda_{\mathrm{att}}) = \frac{\xi_f}{\xi_e} = \frac{T_{\mathrm{GS1}} T_{\mathrm{GS2}}}{T_{\mathrm{GA1}} T_{\mathrm{GA2}}} \exp\left(-\frac{d}{\Lambda_{\mathrm{att}}}\right) = C \exp\left(-\frac{d}{\Lambda_{\mathrm{att}}}\right), \qquad (7.12)$$

which again allows to determine the attenuation length by measuring T for multiple lengths. Compared to equation (7.8) most of the dependencies of the constant C on the experiment's parameters are eliminated which significantly reduces systematic errors. Note, that in order for the parameters to cancel, the set-up must not be changed while the tube is filled with LSc which requires a fluid system which is able to handle this task. For the same reason the experimental procedure is to first measure the empty tube, fill the tube with LSc and finally measure the transmission of the full tube. Measuring the full tube first and the empty tube afterwards would not work, as this would require to clean the windows of the tube in between which could alter the remaining transmissions.

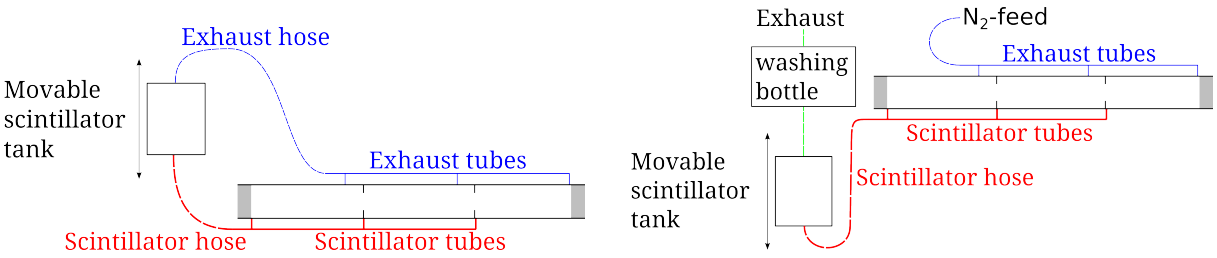

Figure 7.4: Sketch of the fluid and N_2-system in the configurations used for scintillator filling (left) and for nitrogen flushing (right). Each segment of the tube is individually connected with a tube at the bottom to transport the scintillator and at the top to allow the air in the tube to leave the tube during LSc filling. During the LSc filling, the scintillator tube and the exhaust tubes are connected to a movable scintillator container. The filling height is regulated via the height of the LSc container. For nitrogen flushing, the N_2 is pressed through the whole tubing, passes through the LSc and exits the system through a washing bottle serving as a check valve.

7.2.3 Fluid and nitrogen system

The fluid system has to fulfill two main tasks: First it has to allow filling the LSc into the tube without touching the tube to keep the systematic error under control. Of course, it also has to provide a possibility for the inverse process, i.e. to transfer the LSc from the tube to the LSc container. Second, the whole system has to be flushed with gaseous N_2 before the measurements, as oxygen contaminations in the LSc can degrade its optical properties. For both tasks, the purity of the LSc has to be preserved.

Filling and emptying the tube:
Due to the apertures between the individual tube segments, each of the tube segments has to have its own LSc access which is provided by a small tube at the bottom. To allow the air to leave the tube, an additional tube is mounted at the top of each tube segment. This is schematically shown in figure 7.4 (left). To avoid air bubbles after the filling and to allow for a complete drainage of the LSc, the tube is slightly tilted (slope about 3 cm per meter of tube). Thus, the scintillator and exhaust tubes can be mounted at the absolute lowest and highest points of the tube. The scintillator and exhaust tubes are connected via a hose with a scintillator container whose height can be adjusted with respect to the tube. Thus, by lifting the container above the tube, the scintillator is transferred to the tube; by putting the container back on the ground, which is below the level of the tube, the scintillator is drained.

N_2-flushing:
To flush the system with gaseous nitrogen, the exhaust hose is disconnected from the LSc container and connected to the nitrogen feed (see the right scheme on figure 7.4). Additionally, the top of the LSc container is connected to a washing bottle serving as a check valve. Thus, to exit the system, the nitrogen passes through the whole set-up (including all tubes) to remove the oxygen contained. Moreover, it also passes through the LSc thus bubbling the LSc which removes some of the oxygen dissolved in the LSc.

Cleanliness:
Contamination of the LSc can occur due to four different reasons:

- The sample of LSc which is used for measurements can be contaminated before it reaches the experiment, e.g., during production, filling or transport. As these steps are not under the control of the experimenter, basic tests concerning the optical properties of the LSc are performed using the a UV/Vis spectrometer. Obviously polluted samples are rejected.

- Before the LSc is filled into the system, there might be some contaminants in the system which pollute the LSc as soon as it is filled into the experimental set-up. Thus, the system was extensively cleaned before the measurements. First, each tube segment itself was cleaned using ultra pure water, an industrial detergent and isopropanol. Successively, the set-up was filled with ultra pure water (conductivity between 16 MΩ/cm and 18 MΩ/cm). The water has been drained and replaced with fresh ultra-pure water multiple times to get rid of all contaminants. To remove any residual water from the system and for additional cleaning, the whole system was filled with isopropanol which was successively drained. Finally, to remove the remnant isopropanol and any remnant non-polar impurities, the system was filled with LAB which was successively discarded.

- To prevent recontamination of the LSc by the measuring system itself, all the materials have to be compatible with the LSc. The tube and all additional components are made of stainless-steel. For additional protection, the tube including all component welded to the tube (like the access tubes and the flanges to connect two adjacent tube segments) were covered with a chromium-oxide layer, which also reduces the reflectivity of the tube (see section 7.2.1), using the INOX-SPECTRAL [127] procedure. This is especially important for the welded joints which would not be passivated otherwise. The filling system is made up from stainless steel tubes and stainless steel braided polytetrafluorethylen (PTFE) hoses. All connections in the filling system were made using metal-sealed Swagelok tube-fittings [128]; while the tube segments were connected with fluorinated ethylene propylene (FEP)-coated o-rings.

- Finally, care has to be taken that no dust or other external dirt enters the system while the tube is dismounted. Thus, while the tube is open, the fluid system is operated in the nitrogen-flushing mode. Therefore, a slight overpressure is maintained in the tube which prevents dust from entering the system. This also keeps the oxygen levels in the tube low. Additionally, due to the air-conditioning in the new Garching underground laboratory which includes filters, the external dust levels in the laboratory are very low (∼309 particles/l for particles with a diameter below 0.3 μm and ∼49 particles/l for particles with a diameter above 0.5 μm [129]). To keep dust from entering the tube sections which are currently not used, custom-designed covers were fabricated for a dust-free sealing of the segments.

7.2.4 Optics

The optics have to provide an adequately parallel light beam which is as monochromatic as possible for the experiment. Therefore the first task is to generate monochromatic light. Successively, this light has to be formed to a proper beam which finally has to be guided right through the tube to the measurement PMT.

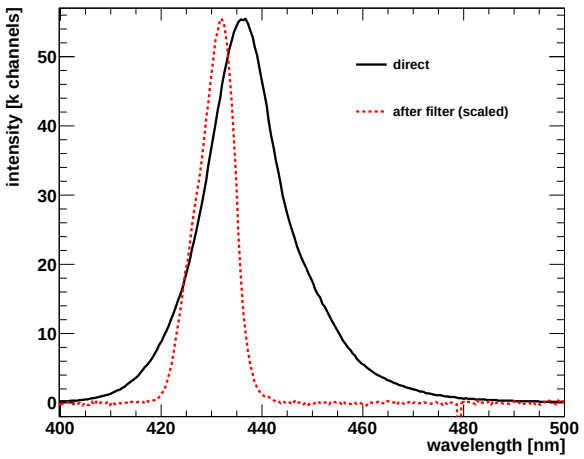

Figure 7.5: The intensity of the light beam as a function of the wavelength directly after the fiber optics and after the wavelength filter as measured with an Ocean Optics Maya2000 Pro spectrometer. The data taken after the wavelength filter was scaled to match the maximum of the data without wavelength filter. Additionally, both data sets are dark-noise corrected.

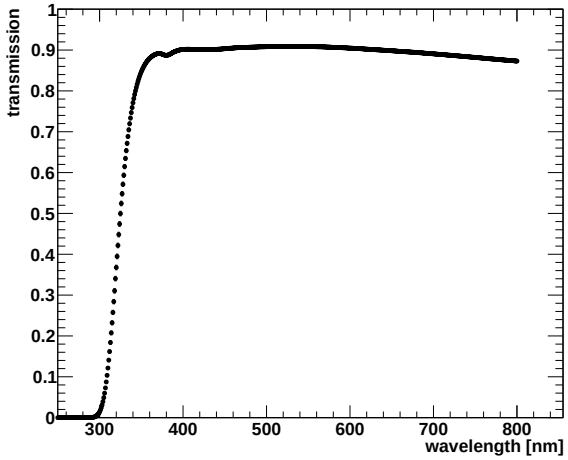

Figure 7.6: The transmission of the windows to the scintillator tube as a function of the wavelength of the light as measured with a Perkin Elmer LAMBDA 850 UV/Vis spectrometer. Note that the shown transmission corresponds to the total transmission of the window, i.e. no correction with respect to the reflection at the surfaces was applied.

Generation of monochromatic light:
The optical system starts with the LED[4] used as a light source which emits at a center wavelength of (430 ± 5) nm and a spectral range of 25 nm full width at half maximum (FWHM) [130]. It is coupled into a fiber-optics[5]. The spectrum of the light exiting the fiber was measured with an OceanOptics Maya2000 Pro spectrometer and is shown in figure 7.5. Comparing the characteristics of the LED with the data recorded by a UV/Vis-spectrometer shown in figure 7.2, such a wide-band beam clearly incorporates too many wavelengths for a meaningful result. Thus, a wavelength filter[6] with a center wavelength of 430 nm and a FWHM of 10 nm was used to further narrow the spectral width of the beam. The spectral composition of the beam after the wavelength filter is also shown in figure 7.5. The remaining spectral with is about 8.5 nm (FWHM) which is sufficiently small, that no significant variations of the attenuation length are expected in this wavelength range. Note that the central wavelength of 430 nm, which is used for the attenuation length measurements, corresponds to the wavelength with the highest contribution to the signal measured in LENA (see section 4.1). Additionally, as can be seen in figure 7.6, the used entrance and exit windows of the tube show a good transparency in the used wavelength range without any spectral features present which could distort the measurements.

[4] Roithner Laser, LED 430-33
[5] ThorLabs, M15L01 105μm, 0.22 NA SAM fiber
[6] ThorLabs FB430-10

Generation of a well correlated beam:
A parallel beam can be created by putting a point-like light source in the focal point of a lens. To generate a light source which is as close to being point-like as possible, a fiber with a small core diameter of $d_f = 105\,\mu$m was used to transport the light from the LED to the optics. Additionally, this solution prevents any stray light from the LED from entering the dark box. Albeit the small diameter of the fiber, its extension induces a non-negligible angular divergence of the light. The induced opening angle of the light beam is

$$\Delta\alpha_b \cong \frac{d_f}{2f}, \tag{7.13}$$

where f is the focal-length of the used lens. Thus, a larger focal length of the lens can reduce the divergence of the beam. On the other hand, a larger focal length means a larger distance between the end of the fiber and the lens and therefore results in a lower beam intensity[7]. Thus a compromise between angular divergence of the beam and its intensity has to be found. The lens used in this experiment[8] has a focal length of $f = 45\,$mm and a diameter of $d_l = 1''$, resulting in an angular divergence of $\Delta\alpha_b = 1.2\,$mrad. To avoid a bad quality of the beam due to lens errors like chromatic aberration, which spoiled the performance of the beam of the experiment described in [99], an achromatic lens was used which is corrected for most of the lens errors.
As the maximum diameter of the beam at PMT2 is given by the 1" aperture right in front of the PMT, the beam generated by a 1" lens is still too wide to be used. Therefore, it was restricted to a 5 mm diameter by the aperture right in front of the tube entrance window, which means the optimum diameter directly in front of measurement PMT2 is about 1.6 cm which is well within limits set by the apertures.

Alignment of the beam with the tube:
To align the beam with the LSc tube, the mirror[9] was mounted on a variable mount[10] which allows to control the beam direction with high precision. While this works well for the measurements with an empty tube, for a full tube, especially at longer tube lengths, an additional problem arises: As discussed in section 7.2.3, the system is flushed with gaseous nitrogen, which is also passing through the LSc, prior to each measurement. The nitrogen is taken from a pressurized gas cylinder. Thus, when the nitrogen is taken from the gas cylinder it adiabatically expands and therefore features a temperature below the ambient temperature. Hence, the LSc is cooled by the passing nitrogen. Consequently, when the scintillator is filled into the measurement tube, it is not in thermal equilibrium with the surrounding materials. As the scintillator's density depends on its temperature, a temperature gradient develops with the isothermal surfaces being horizontal. This translates into a gradient in refractive index which forms in the tube. Due to the small tilt of the tube required for filling and emptying the tube (see section 7.2.3), the light beam passes the surfaces of equal refractive index at a very shallow angle which leads to a refraction of the beam. This causes a displacement of the beam spot at PMT2 which

[7] Strictly speaking, this is only true if the numerical aperture of the lens $\mathrm{NA}_l = \sin[\arctan(d_l/2f)]$ [131] is smaller than the numerical aperture of the fiber $\mathrm{NA}_f = 0.22$. This condition was fulfilled for the lens used in the experiment.
[8] ThorLabs, AC254-045-A, 1" diameter
[9] ThorLabs, BB1-E02, broadband dielectric mirror
[10] ThorLabs, KM100

is strong enough to cause clipping and therefore distorts the measurement. This has two important consequences for the measurement: First of all, it takes time for the situation to stabilize. Especially at a tube length of 5 m, directly after filling the tube the beam was found to move quite rapidly which forbids any measurements. Thus, after filling the tube, the system was allowed to thermalise for two days prior to the measurement. After this time, the beam position was found to be stable but still has to be readjusted for the longest tube lengths.

7.2.5 Light detection and data acquisition

The intensity of the light after the beam splitter and after the measurement tube is determined using two PMTs[11]. The diameter of PMT2 is 1.13" which is significantly larger than the diameter of the final aperture used to suppress edge effects. To avoid problems with the linearity of the PMTs, they were operated in photon counting mode. Therefore, the height of the rectangular pulses of $\Delta t_p \approx 2\,\mu$s width provided by the pulser[12] to drive the LED was adjusted to result in 3 to 4 photons detected (on average) by each of the PMTs during each light pulse. As the FWHM of a single electron pulse is only 3.1 ns [132] and 5 ns [133], respectively, the probability for two single photon signals to overlap is very tiny.
As shown in figure 7.7, the signal obtained by the PMTs is amplified[13] and successively digitized using a fast Analog-to-Digital-Converter (ADC)[14] with a sampling frequency of $f_s = 500$ MHz at a resolution of 8 bit. The read out of the ADC is triggered by a logical signal emitted by the pulser synchronously to each emitted pulse. For each pulse, 2048 samples are acquired corresponding to an acquisition window $\Delta t_a = 4096$ ns, which is about twice Δt_p. By setting a proper trigger position, this allows for a well defined determination of the baseline before the pulse starts as well as for enough time for the afterglow of the LED to decay away. The data recorded by the ADC is read out using the Versa Module Eurocard-bus (VMEbus) backplane[15]. Finally, the obtained data is transferred from the crate controller[16] to the DAQ-PC[17] via an optical fiber. Typically 150 000 pulses are acquired and saved on disk for each measurement to collect the required statistics.
The required software to control the DAQ via the VMEbus has been developed in the course of this thesis. Profiting from the experiences gained in [134], it was designed and written from scratch using C++ by the author of this thesis. For fast control of the experiments' parameters, a graphical user interface has been developed using the Qt-libraries [135] enhanced with the Qwt-libraries [136] for scientific plotting. This also gives rise to the possibility to perform some very preliminary live analysis during data-taking which allows to fix many errors before doing the actual data-analysis. Finally, the data was written to disk using the data-format provided by the ROOT-framework [108]. The sustained event rate obtained during the measurements was about 1.1 kHz, which means

[11] PMT1: Electron tubes 911B with RB1107 Voltage Divider, PMT2: Electron tubes 9124B
[12] Philips PM 5770
[13] Kuhne Electronics Broadband Super Low Noise Amplifier KU LNA BB 0515 A-SMA-445
[14] CAEN V1721 8Ch 8 Bit 500 MS/s
[15] Used VME crate: Wiener 6U VME64x 6021
[16] CAEN V2718 VME-PCI Optical Link Bridge
[17] Used PCI-Card: CAEN A2818

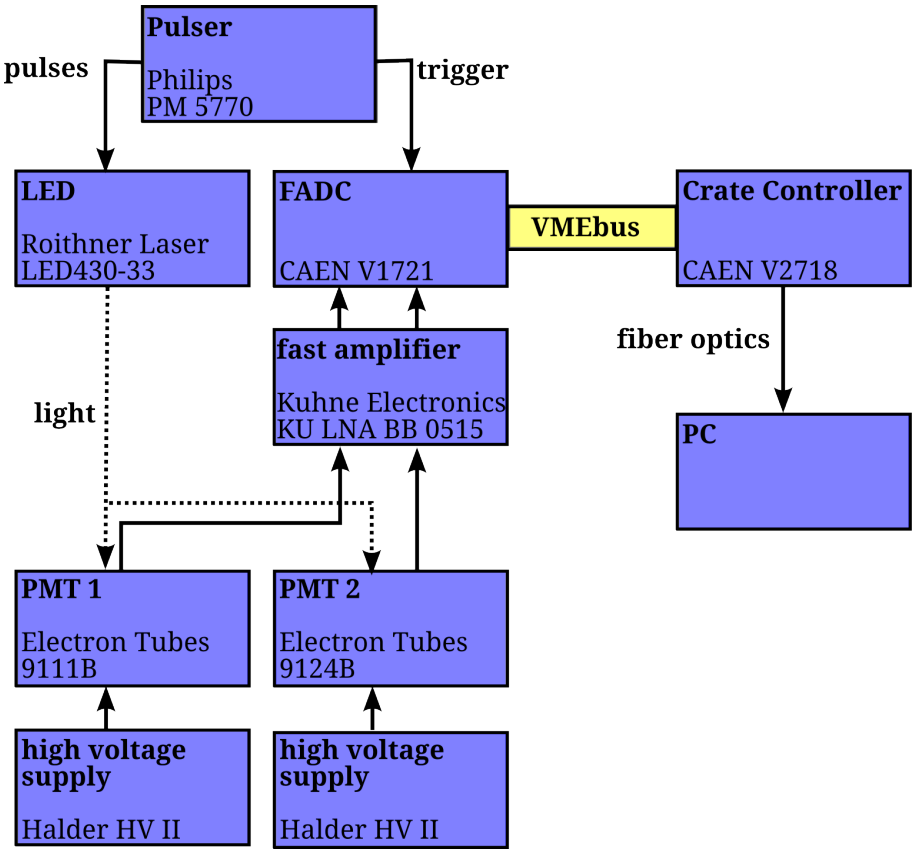

Figure 7.7: Block diagram of the electronics set-up used for the measurement of the attenuation length. The LED providing the light for the experiment is driven by a pulser which also triggers the readout of the PMTs which detect the light. The signals from the PMTs are amplified and digitized by a fast ADC (FADC), which is read out via the VMEbus. Finally the data is transferred from the crate controller to the DAQ-PC via a fiber-optics.

that a measurement took a bit more than two minutes. The readout software developed in this thesis is currently also used by an experiment for liquid argon spectroscopy [137] and the core modules from this library serve as the innermost building blocks of other programs for VMEbus based DAQ [62, 138, 139, 140].

7.3 Data analysis

To determine the attenuation length of the measured LAB, the transmission as defined in equation (7.12) has to be determined from the acquired data for all measured tube lengths. Starting from the raw traces as recorded by the ADC, the first step is to determine the number of detected photons within each photon pulse (see section 7.3.1). Successively, the data obtained in the series of measurements for each length is combined to determine the transmission, as detailed in section 7.3.2. As already discussed in section 7.1.1, scattered light which is detected by PMT2 might produce a false result. The possible influence of scattered light on the experimental result is discussed in section 7.3.3. Apart from scattered light, there are also additional systematic errors due to instabilities of the set-up and the necessary changes of the set-up while changing the tube length. Their effect

on the accuracy of the measurement is outlined in section 7.3.4. In section 7.3.5, the previous results are combined resulting in a final value for the attenuation length of the scintillator. As the LED provides a pulsed light beam, additionally the effective index of refraction of the LSc can be determined, as outlined in section 7.3.6.

7.3.1 Preprocessing

The first step in the data analysis chain is to extract the number of photons detected at each PMT for each pulse. This starts with the determination of the baseline $b_{1,2}$ of the pulses of PMT1 and PMT2, respectively. It is calculated from the mean of the first 200 samples of the acquired traces, which corresponds to a time window of 400 ns. Due to the used pretrigger settings, no photons are expected in this part of the pulse. Successively, the pulses are corrected with respect to the obtained baseline value , i.e.,

$$u_{ij}^{b} = u_{ij} - b_j, \tag{7.14}$$

where u_{ij} is the i$^{\text{th}}$ raw sample obtained in the channel corresponding to PMT $j \in \{0, 1\}$ and the superscript b indicates the value after baseline correction. Figure 7.8 shows a sample raw pulse[18] after baseline correction. To determine the number of single photons recorded during each pulse, a simple threshold algorithm is used: Every time the baseline-corrected pulse rises above the threshold $u_{ij}^{b} > u_{\text{thr}}$ the number of detected photons is increased by one. To make sure that every photon is counted only once, no additional photons are accepted in a window of $t_i = 20\,\text{ns}$ width each time the baseline-corrected pulse crosses the threshold. Additionally, the time and the height of the photon pulse are determined by searching for the first global maximum in the 20 ns window after crossing the threshold[19]. Note that the photon search is not applied in the region of the trace which was used to determine the baseline.

To determine a suitable threshold for the analysis, one measurement was analyzed with the lowest possible threshold corresponding to one ADC channel and the pulse height spectrum was determined. It is depicted in figure 7.9. Successively, the threshold was set to $u_{\text{thr}} = 35.1\,\text{mV}$ which removes the non-Gaussian part at low pulse heights. Note that the exact threshold used for the analysis is not relevant for the analysis as long as the contribution of the noise is negligible and that a significant amount of single-photon pulses still triggers the algorithm. It is, however, relevant that the threshold is kept constant for all analyzed samples as changing the threshold would change the efficiencies of the PMTs and thus invalidate equation (7.12). The positions of the pulses found with the determined u_{thr} for the sample pulse, shown in figure 7.8, are also indicated in the figure.

7.3.2 Determination of the transmission

With the photons in the events being identified, the next step is to calculate the transmission as given in equation (7.12). Thus, the found photon pulses of a complete measurement at a fixed tube length are histogrammed according to their distance in time from the start

[18] The pulses obtained from the PMTs feature a negative polarity. They are, however, inverted during the amplification process.

[19] No proper constant fraction discriminator could be used to determine the time of the pulses as the time resolution of the ADC is not sufficient to properly sample the pulse shape.

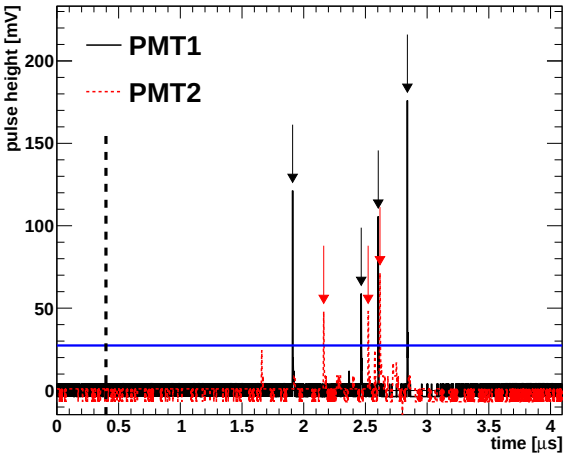

Figure 7.8: A sample raw trace of both PMTs as obtained from the ADC after baseline correction. The blue, horizontal line indicates the threshold used to detect the pulses. The position of the found pulses is indicated by arrows. The trace left of the vertical dashed line is used to determine the baseline of the pulse.

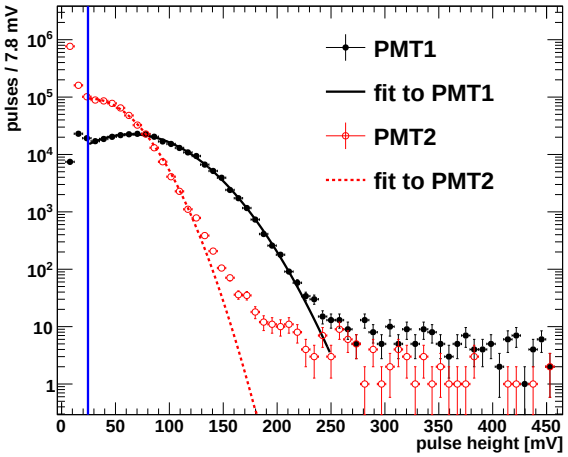

Figure 7.9: The single photo-electron pulse height spectrum as obtained by both PMTs. The solid curves indicate the results of Gaussian fits to the obtained distributions. The threshold used in the analysis to detect pulses is shown by the vertical blue line.

of the pulse as shown in figure 7.10. In a next step, the dead time introduced by the inhibit window after each pulse is taken into account. As on average only 3 to 4 photons per 2 μs pulse are detected, the probability that a photon is shadowed due to the dead time is in the percent region, which is significant in this experiment. Thus, a dead time correction which is adapted from [43] is done. The true possibility p_i^{true} to have a photon pulse in a given bin i is given by the measured probability p_i^{meas} and the probability that a pulse has been shadowed by a previous pulse

$$p_i^{\text{true}} = p_i^{\text{meas}} + p_i^{\text{true}} \sum_{j=i-N_i}^{i-1} p_j^{\text{meas}}, \tag{7.15}$$

where $N_i = 10$ is the number of bins the inhibit window corresponds to. Note, that only measured pulses can trigger the dead time, thus in the shadowing term p_j^{meas} appears. Solving this equation for p_i^{true} and replacing the probabilities by their best fit values from the obtained number of photon pulses in the event $p_i = n_i/N_{\text{pulses}}$, where N_{pulses} is the number of acquired pulses and n_i the number of photon pulses in the i$^{\text{th}}$ bin, yields

$$n_i^c = \frac{n_i}{1 - \frac{1}{N_{\text{pulses}}} \sum_{j=i-N_i}^{i-1} n_j}, \tag{7.16}$$

where n_i^c is the dead time corrected count rate. The statistical error of the single bins are propagated by Gaussian error propagation [106]. Note that the sum in equation (7.16) leads to a small correlation between the bins which is neglected in the following.

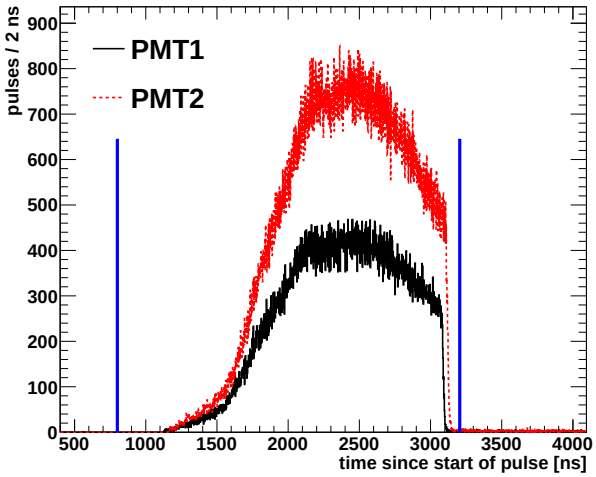

Figure 7.10: The time distributions of the detected single photons for both PMTs. Note that the first 400 ns of the pulse are not shown as they are used for baseline determination and not for pulse finding. The time window between the two vertical blue lines is the region where the photons from the LED pulse are expected. It is used to determine the number of photons detected on each PMT (see equation (7.17)). Note that PMT2 features a higher number of detected photons in comparison to PMT1 due to its higher quantum efficiency.

The DN of the PMTs at the used threshold was generally below 100 Hz directly after closing the box and continuously decreases thereafter. Thus, the probability to obtain a dark count in the window of the LED pulse is below $100\,\mathrm{Hz} \cdot 2\,\mu\mathrm{s} = 2 \cdot 10^{-4}$. Due to this small DN rate, it was also not possible to determine the DN from the window between the baseline and the start of the LED pulse (see figure 7.10) as the number of obtained dark counts in this region generally was zero. Thus, due to the very low DN rate, the DN was neglected in the analysis.

Note that there is a small number of photons behind the main LED pulse, which are most properly due to very slowly decaying states in the LED. They can be removed by a time cut. Due the difference in TOF of photons, the position of the LED-pulse in the histogram is dependent on the tube length. This induces a small difference in the effect of this cut with changing tube length, which is, however, not relevant for the analysis.

Finally, the number of photons N_γ detected by a PMT is given by

$$N_\gamma = \sum_{i}^{800\,\mathrm{ns}<\tau_i<3200\,\mathrm{ns}} n_i^c, \tag{7.17}$$

where τ_i is the time corresponding to the center of the i$^{\mathrm{th}}$ bin. Thus, the measured transmission T^m, as defined in equation (7.12), can, for a given tube length, be calculated using

$$T^m = \frac{\xi_f}{\xi_e} = \frac{N_{\gamma,2}^{\mathrm{full}}/N_{\gamma,1}^{\mathrm{full}}}{N_{\gamma,2}^{\mathrm{empty}}/N_{\gamma,1}^{\mathrm{empty}}}, \tag{7.18}$$

where the indices full and empty denote the results of the full and empty measurement, respectively, and the number index denotes the PMT.

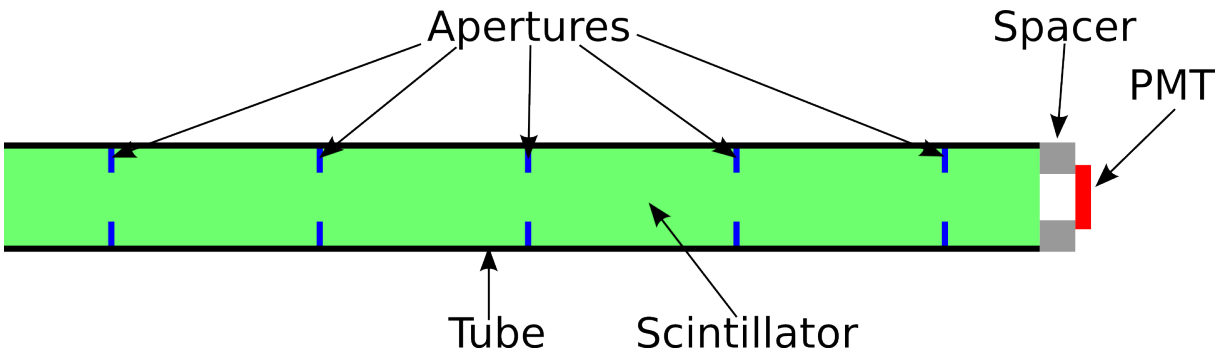

Figure 7.11: Sketch of the set-up of the simulation used to determine the effect of the scattering on the result of the attenuation length experiment (not to scale). Light is injected into the set-up from the left. It propagates through a cylindrical tube which is filled with LAB and which features apertures at the distances corresponding to the real experiment. Analogously to the experiment, the PMT is attached to the tube by a small spacer. The PMT is simulated using a single, photosensitive disk.

7.3.3 Influence of scattering in the scintillator on the measured transmission

As already discussed in section 7.1.1, equation (7.3), which describes the light intensity as a function of the length the light traveled through the LSc, is only valid as long as all scattered light is taken to be lost. This is experimentally not totally possible due to the finite extension of the light detector. Additionally, even though the tube was blackened on the inside and even though apertures are used to suppress stray light (see section 7.2.1) a small amount of reflected light might also be detected on PMT2. To study the effect of the scattering on the determined attenuation length, the set-up was simulated with a Geant4[20] [102, 103] based simulation which was written in the course of this thesis. The simulated set-up, which is a simplified version of the real set-up, is depicted in figure 7.11. It consists of a 2" tube, which is filled with LAB. Inside the tube, 1" apertures are added at the same positions as in the real experiment. The length of the simulated tube can be varied to take the different tube lengths which can be assembled in the real experiment into account. At the end of the tube, there is a 2.5 cm long spacer with a diameter of 1". Behind the spacer, a photosensitive disk is mounted which registers the positions of arriving photons. If a scattered photon arrives at the photosensitive disk, it is tagged as scattered and the position of its first scattering is written to disk.
The optical properties of the components used in the simulation are critical for the result of the simulation. To obtain a realistic optical behavior for the scintillator, the enhanced optical description developed for the LENA-simulation has been used (see section 4.1). Also the values for the different optical properties of the scintillator are taken from section 4.1. As the reflectivities of neither the tube nor the aperture nor the spacer are known, the values have been conservatively estimated. These values form the "standard assumptions" and are listed in table 7.1. Additionally, a set of unrealistically high reflectivities, the so called "high reflectivity assumptions" which are also listed in table 7.1, is used to check for the most extreme case. Note that all surfaces were assumed to have a perfect surface

[20] Version 4.10.1

Property	Standard assumptions	High reflectivity assumptions
Tube reflectivity	50%	90%
Spacer reflectivity	20%	90%
Aperture reflectivity	90%	98%

Table 7.1: Assumed optical properties of the mechanical components of the experiment. All components were assumed to have perfect surfaces and to be polished.

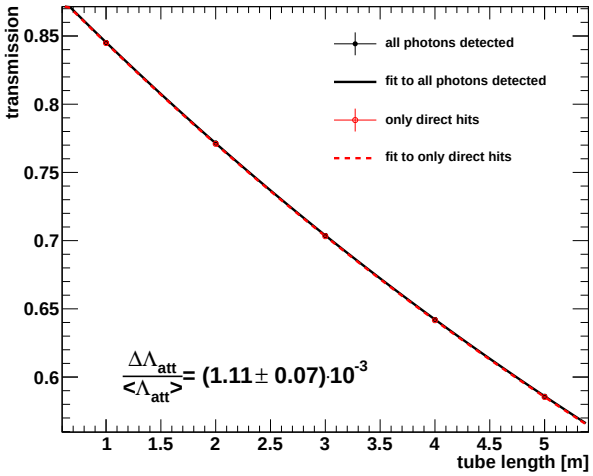

Figure 7.12: The simulated transmission as a function of the tube length using the unrealistically conservative high-reflectivity assumptions. Additionally, the data obtained taking only non-scattered photons into account is shown. Both data sets have been fitted according to equation (7.12). The resulting relative difference in the attenuation length is $\frac{\Delta\Lambda_{att}}{\langle\Lambda_{att}\rangle} = \frac{\Lambda_{att}^{all}-\Lambda_{att}^{direct}}{(\Lambda_{att}^{all}+\Lambda_{att}^{direct})/2} = (1.11 \pm 0.07) \cdot 10^{-3}$, where $\Lambda_{att}^{all,direct}$ denotes the attenuation length resulting from the fit to the total data sets ("all") and to the dataset containing only direct light ("direct") respectively. For the standard reflectivity assumptions, $\frac{\Delta\Lambda_{att}}{\langle\Lambda_{att}\rangle} = (9.0 \pm 2.0) \cdot 10^{-5}$.

finish which should be a very good approximation, especially for the tube with its surface treatment. For each simulation, 10^7 photons are started from the side of the tube opposing the light-sensitive disk using a circular beam profile with linearly expanding radius.

The simulation shows that the detection of scattered photons is very rare. Using standard reflectivity assumptions, a fraction between $1.3 \cdot 10^{-4}$ and $1.7 \cdot 10^{-4}$ (dependent on the tube length) of all detected photons have been scattered before they were detected. For high reflectivity assumptions this value rises to about $6 \cdot 10^{-4}$.
Figure 7.12 shows the transmissions obtained as a function of the tube length using the very conservative high-reflectivity assumptions. Additionally, the transmissions obtained taking only direct, i.e. non-scattered, photons into account are shown. The data sets are fitted according to equation (7.12) to extract the attenuation lengths Λ_{att}^{all} and Λ_{att}^{direct} obtained using all detected photons and only the direct photons, respectively. The relative

deviation between both attenuation lengths is

$$\frac{\Delta\Lambda_{\mathrm{att}}}{\langle\Lambda_{\mathrm{att}}\rangle} = \frac{\Lambda_{\mathrm{att}}^{\mathrm{all}} - \Lambda_{\mathrm{att}}^{\mathrm{direct}}}{(\Lambda_{\mathrm{att}}^{\mathrm{all}} + \Lambda_{\mathrm{att}}^{\mathrm{direct}})/2} = (1.11 \pm 0.07) \cdot 10^{-3}. \tag{7.19}$$

which is negligible compared to the effect of the other systematic errors of the measurement. Note, that this relative deviation was determined using the unrealistically pessimistic high-reflectivity assumptions. Using the still conservative standard assumptions results in

$$\frac{\Delta\Lambda_{\mathrm{att}}}{\langle\Lambda_{\mathrm{att}}\rangle} = (9.0 \pm 2.0) \cdot 10^{-5} \tag{7.20}$$

being one order of magnitude smaller than in the high reflectivity case due to the lower amount of scattered photons which arrive at the detector. Thus, it can be concluded that the influence of the scattered light on attenuation length determined from the experiment is negligible.

7.3.4 Systematic errors

While the investigation of the effect of scattering on the attenuation length in the last section showed that this contribution is negligible, some other systematic errors connected to the used set-up and to the used measurement procedure are relevant. They will be discussed in the following.

Time instabilities

Due to changing environmental conditions, some of the parameters which seem to be eliminated during the calculation of the transmission (see equation (7.12)) actually do not fully cancel as they vary with time. In this set-up, the efficiencies of the PMTs (due to fluctuations in the high voltage) and the transmission of the aperture directly in front of the tube[21] are most susceptible for changes with time. To investigate the time stability of the set-up, a 24-hour measurement was performed with a reduced data taking rate. This measurement was successively subdivided into 100 measurements of equal size each containing roughly the statistics of a normal measurement. As all measurements feature a slightly different statistical error, it is not sufficient to determine the total error from the spread of the distribution and then solve for the systematic error. Thus, a different approach is used: First, the weighted average of all calculated intensity ratios ξ_e (see equation (7.18)) is calculated:

$$\langle\xi_e\rangle(\sigma_t) = \sum_i \frac{w_i \cdot \xi_{e,i}}{w_i}, \quad \text{with } w_i = \frac{1}{\sigma_i} = \frac{1}{\sqrt{\Delta\xi_{e,i,\mathrm{stat}}^2 + \sigma_t^2}}, \tag{7.21}$$

where $\Delta\xi_{e,\mathrm{stat}}$ is the statistical error of $\xi_{e,i}$ and σ_t is the systematic error due to time instabilities. Successively, the distribution of the relative deviations

$$\frac{\xi_{e,i} - \langle\xi_e\rangle}{\sqrt{\Delta\xi_{e,i,\mathrm{stat}}^2 + \sigma_t^2}} \tag{7.22}$$

[21] The aperture directly in front of the tube is critical as the beam before the aperture is inhomogeneous. Thus, a small change in the optical set-up, e.g., due to thermal effects, leads to a noticeable change of the aperture's transmission. Moreover, the aperture is mounted directly at the tube to assure a central beam. Hence, the aperture can change its position with respect to the incident light beam due to movements of the tube which might occur, e.g., due to the added weight during filling.

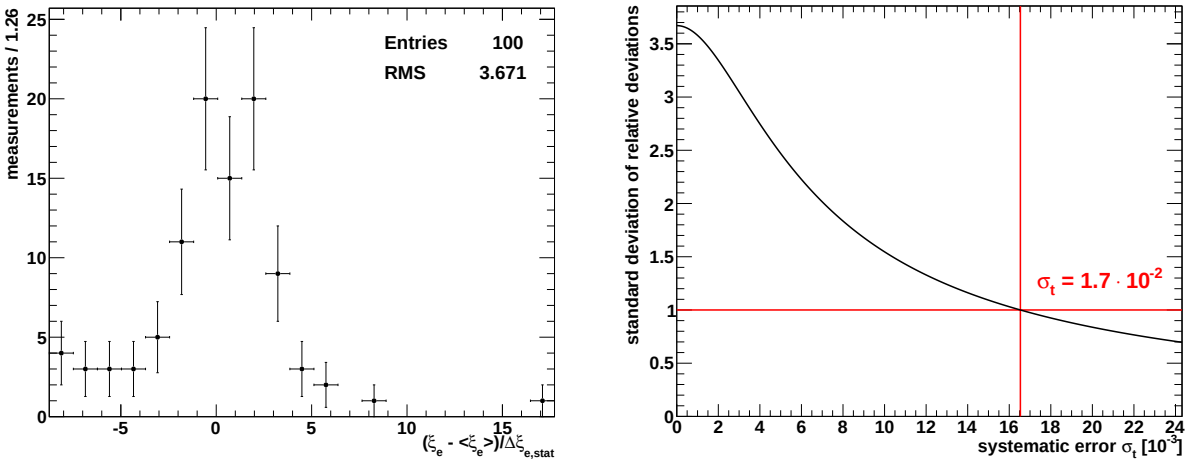

Figure 7.13: Results from a 24 h stability measurement. The collected data was subdivided into 100 equal parts, each with roughly the statistics of a normal measurement. On the left, the obtained distribution of the relative deviations of the measurements from the mean value is shown, taking only statistical errors into account. The used bin width in $\xi_e - \langle\xi_e\rangle/\Delta\xi_{e,\mathrm{stat}}$ is 1.26. On the right, the standard deviation of the relative deviations of the measurements from the mean value is shown as a function of the added systematic error. The most probable systematic error is given by the point where the standard deviation of the relative deviation of the measurement is equal to one. It is marked in the right graph.

is determined. Figure 7.13 (left) shows the obtained distribution of the relative deviations from the mean, when only statistical errors are taken into account ($\sigma_t = 0$). If no systematics would be present, the standard deviation of the distribution should be compatible with 1, which is not the case. Thus, to determine the systematic error, the systematic error is increased until the spread of the distribution equals 1. The resulting spread of the distribution of the relative deviations from the mean as a function of the systematic error σ_t is shown on the right of figure 7.13. This leads to a systematic error due to timing uncertainties of $\sigma_t = 1.7\,\%$. Note that this value has not been determined on the transmission but on the ratio of the count rate of the PMTs for an empty tube. It thus has to be propagated to determine the full systematic error due to timing. Here, a quadratic propagation is adequate as the time variations do not follow a given direction, i.e., the correlation between the deviations due to time instabilities can be considered to be small.
Finally, note that the stability of the light source is not sufficient for this experiment, thus a reference measurement of the beam intensity before it enters the tube is necessary. Without this measurement, the error due to the timing uncertainty would be about an order of magnitude higher.

Window cleaning:
Between a measurement with a scintillator-filled tube and a measurement with the empty tube, the remaining scintillator has to be removed from the entrance and the exit window of the experiment. The cleaning of the windows is done with isopropanol which is washed off using ultra pure water. Finally, the window is dried using lint-free wipes. Note, that this cleaning procedure requires to unmount the windows from the tube. While utmost care was taken to remove any remaining dirt from the cleaned windows, especially to

Nominal length [m]	Measured length [m]
1	1.030
2	2.045
3	3.060
4	4.075
5	5.090

Table 7.2: The measured and the nominal lengths for the different tubes. The uncertainty of the measurement is estimated to 0.5 cm.

prevent contamination of the scintillator, it is more difficult to ensure that the window has exactly the same optical properties each time it is mounted. This error could be significantly reduced by mounting the circular windows always with the same direction as the optical properties of the window are not totally homogeneous.
To determine the effect of dismounting, cleaning and remounting the windows on the measurement, 10 measurement each have been conducted with an empty tube with a length of 5 m and 1 m. Between two successive measurements, the windows were dismounted, cleaned and mounted again. To maximize the effect of the cleaning procedure of the entrance window on the measurement, the measurements with the 5 m long tube are evaluated to determine the corresponding systematic error. To separate the error due to the timing and the statistical error from the error due to the window cleaning, the same approach that was already used to determine the systematic errors due to time variations of the set-up was used. As a result, the systematic error introduced by the cleaning procedure of the entrance window is $\sigma_w = 1.7\,\%$. To keep the influence of other systematics on the effects of the exit window as low as possible, it was evaluated using the measurements with a 1 m tube. No significant effect of the back window cleaning procedure could be found, therefore it is neglected in the following. Thus, the effect of the cleaning of the entrance window being much stronger than the effect of the cleaning of the exit window. This shows that this error is mainly caused by variations in the optical path of the beam due to the front window mounting. Thus, this error could be significantly reduced by using a detector with a response, which is more homogeneous over its active surface than a PMT, the latter can exhibit quite significant changes of the quantum efficiencies over its active surface, see e.g. [141].

Tube length:
While the original parts of the tube were exactly 1 m long, they were machined in the workshop to attach the required access tubes and the flanges required for connecting the tubes. Thus the tube lengths had to be remeasured. The values found are listed in table 7.2. The measurement used incorporates an error which was estimated to be 0.5 cm which enters the calculations as a systematic error. While this value can be surely improved if necessary, it turned out that its contribution to the error is nearly negligible. Thus there is no benefit of a more exact measurement of the tube length.

7.3.5 Final fit

The final step to determine the attenuation length from the obtained data is to fit the data with equation (7.12).

Fresnel factor:
The constant C in equation (7.12) is generally called the Fresnel-factor. It can be calculated, if the refractive indices of the glass (n_G) the scintillator (n_S) and the air (n_A) are known [131] using the following equation

$$C = \frac{T_{\mathrm{GS1}} T_{\mathrm{GS2}}}{T_{\mathrm{AG1}} T_{\mathrm{AG2}}} = \frac{(1 - R_{GS})^2}{(1 - R_{AG})^2} = \left[\frac{1 - \left(\frac{n_G - n_S}{n_G + n_S} \right)^2}{1 - \left(\frac{n_G - n_A}{n_G + n_A} \right)^2} \right]^2 . \tag{7.23}$$

As n_S and n_G are not known precisely enough, C has to be determined from the fit. Nevertheless, an approximate calculation is possible using $n_S = 1.484$ from the LENA simulation, $n_G \approx 1.52$ [142] and $n_a \cong 1$ which yields $C \approx 1.09$. The most critical problem for evaluating C is that the exact optical properties of the glass windows are not known. Judging from the spread of the available n_G in [142], the obtained value for C is accurate only to 1 % - 2 %.

χ^2-fit:
To determine the attenuation length from the acquired data $D = \{(d_i, T_i^m)\}$, a χ^2-fit, which is a special case of a negative logarithmic likelihood fit where all errors are of Gaussian shape [106], can be used. Taking only statistical errors into account, the χ^2-function reads

$$\chi^2(C, \Lambda_{\mathrm{att}} | D) = \sum_{i=1}^{N_m} \left[\frac{T_i^m - T(d_i, C, \Lambda_{\mathrm{att}})}{\Delta T_i^{\mathrm{stat}}} \right]^2 , \tag{7.24}$$

with N_m being the number of measurements and $\Delta T_i^{\mathrm{stat}}$ being the statistical uncertainty of the i$^{\mathrm{th}}$ measurement at a distance d_i. To determine the attenuation length and the Fresnel factor, $\chi^2(C, \Lambda_{\mathrm{att}} | D)$ has to be minimized with respect to C and Λ_{att}.
To take the systematic errors into account, the nuisance parameters $\tilde{d}_j$ and $\tilde{T}_i$ are introduced, which shall describe the possible variation of the parameters [143]. Note, that the nuisance parameter for the tube length features a different index to indicate that the errors of the tube length for multiple measurements at the same length are 100 % correlated. The nuisance parameters are coupled to the corresponding measured value using pull terms thus incorporating the information of the measurement in the fit [143]. Consequently, the final χ^2-function reads:

$$\begin{aligned} \chi^2(C, \Lambda_{\mathrm{att}} | D) \rightarrow \; & \chi^2(C, \Lambda_{\mathrm{att}}, \{\tilde{T}_i\}, \{\tilde{l}_j\} | D) = \\ = & \sum_{i=1}^{N_m} \left\{ \left[\frac{\tilde{T}_i - T(\tilde{d}_i, C, \Lambda_{\mathrm{att}})}{\Delta T_i^{\mathrm{stat}}} \right]^2 + \left(\frac{T_i^m - \tilde{T}_i}{\Delta T^{\mathrm{syst}}} \right)^2 \right\} + \sum_{j=1}^{5} \left(\frac{d_j - \tilde{d}_j}{\Delta l^{\mathrm{syst}}} \right)^2 , \end{aligned} \tag{7.25}$$

where ΔT^{syst} is the systematic error as discussed in section 7.3.4, with the different sub-errors linearly added, and Δl^{syst} is the error of the tube length. Using this approach, the full correlation of all systematic errors is taken into account. To determine Λ_{att} in

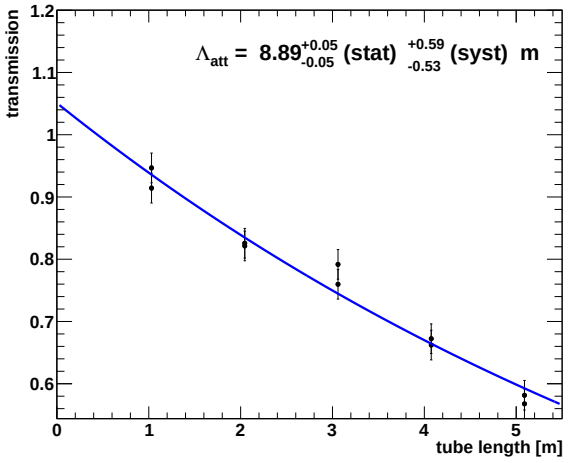

Figure 7.14: The measured transmission as a function of the tube length. The blue line shows $T(d_i, C, \Lambda_{\mathrm{att}})$ using the parameters obtained from the final fit as input parameters. The attenuation length resulting from the fit is indicated in the plot. The error bars show the total error of each measurement as determined from the quadratic addition of statistical and systematic error. The axis intercept of the fit function corresponds to the Fresnel factor C (compare equation (7.23)).

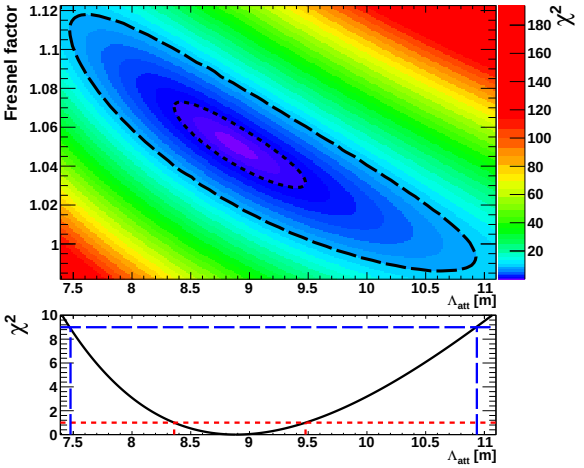

Figure 7.15: The obtained χ^2 as a function of the Fresnel factor and the attenuation length Λ_{att} (top) with the nuisance parameters being profiled out. The short and the long dashed lines show the 1-σ and 3-σ region (one parameter boundaries), respectively. One color is 0.3-σ wide. The one-dimensional graph below below shows χ^2 as a function of Λ_{att} with all other parameters being profiled out. The red and blue dashed lines indicate the 1-σ and 3-σ region of Λ_{att}, respectively.

this case, the minimization has to be done with respect to the full set of parameters $C, \Lambda_{\mathrm{att}}, \{\tilde{T}_i\}$ and $\{\tilde{l}_j\}$. Figure 7.14 shows the data along with the fit result.

Determination of the error:
To determine the error of Λ_{att}, first the other degrees of freedom of the χ^2 function have to be dealt with. This is done by calculating the profile χ^2-function

$$\chi^2_{\mathrm{prof}}(\Lambda_{\mathrm{att}}) = \min_{C,\{\tilde{T}_i\},\{\tilde{l}_j\}} \left[\chi^2(C, \Lambda_{\mathrm{att}}, \{\tilde{T}_i\}, \{\tilde{l}_j\}|D)\right]. \tag{7.26}$$

The confidence interval CI of Λ_{att} at the n-σ confidence level can finally be calculated as [106]

$$CI = \left\{\Lambda_{\mathrm{att}} : \chi^2_{\mathrm{prof}}(\Lambda_{\mathrm{att}}) - \chi^2_{\mathrm{min}} < n^2\right\}, \tag{7.27}$$

where χ^2_{min} is the global minimum of the χ^2-function. This procedure to determine the errors for Λ_{att} is illustrated in figure 7.15. To split the total error σ_{tot} obtained with this method into a statistical error σ_{stat} and a systematic error σ_{syst}, the whole procedure is repeated using the χ^2 function from equation (7.24) to determine the statistical error. Finally, the systematic error is determined using

$$\sigma^2_{\mathrm{tot}} = \sigma^2_{\mathrm{stat}} + \sigma^2_{\mathrm{syst}} \tag{7.28}$$

for the lower and the upper error separately.

Final result:
The final result of the measurement is

$$\Lambda_{\text{att}} = (8.89 \pm 0.05(\text{stat})^{+0.59}_{-0.53}(\text{syst}))\,\text{m} \tag{7.29}$$

which is compatible with the result obtained using UV/Vis-spectroscopy (see section 7.1.3). The resulting value of the Fresnel factor is $C = 1.051 \pm 0.003(\text{stat})\ ^{+0.022}_{-0.021}(\text{syst})$, showing a 1.8 sigma deviation from the estimated value of $C = 1.09$. Even though this might hint to a possible problem of the experiment, considering also the uncertainty of the estimation of C the significance of this deviation is further reduced and thus no hint for a potential problem of the experiment can be found.
Figure 7.14 shows that the fitted curve passes through all error bars, which already indicates that the errors have been estimated rather conservatively. An additional cross-check of the given error estimates can be obtained by looking at the relative deviation of the nuisance parameters from the measured values. With a standard deviation of $0.8 < 1$, no hints for a strong deviation of the data from the model and therefore an underestimation of the errors can be found.

As the found errors are still relatively large, a new version of the experiment was designed and built which is described in chapter 8. For an in-depth comparison of the results obtained with the UV/Vis-spectrometer, the result from this experiment, and the result from the new experiment see section 8.3.

7.3.6 Determination of the effective index of refraction

As the LED is used as a pulsed light source, the difference in the photon arrival times induced by the dependence of the TOFs on the different tube lengths can principally be traced by looking at the time shift between the photon distributions obtained for PMT1 and PMT2. As both, the pulse time and the rise time of the pulse are much longer than the expected time shift Δt, the latter cannot be determined by a constant fraction trigger but has to be obtained by matching the two distributions to each other as, for example, done in [144]. By fitting the obtained Δt values as a function of the tube length with a linear function, the velocity c of light in the scintillator can be determined and thus the effective[22] index of refraction $n_{\text{eff}} = c_0/c$ can be obtained, where c_0 is the velocity of light in vacuum.

However, during the data analysis, it turned out that the obtained photon distributions (see figure 7.10) are modulated with half the sampling frequency of the ADC, i.e. 250 MHz. This can be seen by looking at the Fast-Fourier transformation (FFT) [145] of the photon distribution after dead time correction as shown in figure 7.16 for a typical measurement. The peak at 250 MHz is clearly visible. This modulation is most probably due to a cross-talk between the ADC-clock and the analogue input signal. The problem is that it also spoils the χ^2-comparison between the histograms: For time shifts corresponding to an even number of 2 ns bins, the resulting χ^2-values are reduced compared to the χ^2-values

[22] n_{eff} is called effective index of refraction to emphasize that it is connected to the group velocity of photons in the scintillator in contrast to the normal index of refraction n which describes the phase velocity of the light. They can be connected using $n_{\text{eff}} = n + \omega\frac{\partial n}{\partial \omega}$ [131], where ω is the angular frequency of the light.

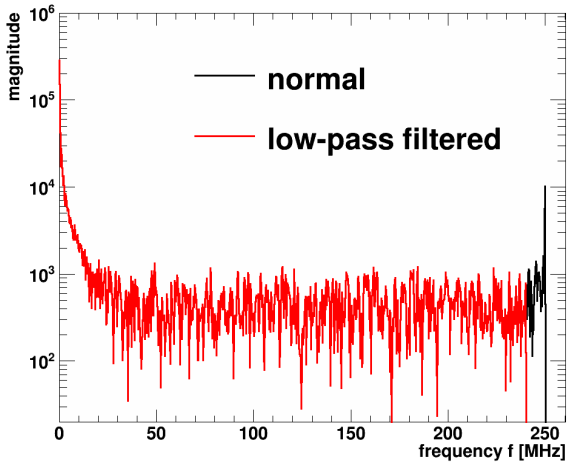

Figure 7.16: The magnitude of the FFT of the dead time corrected single photon timing spectrum before (black) and after (red) low pass filtering with maximum frequency of $f_{\text{cut}} = 240\,\text{MHz}$ as a function of the frequency. Note the peak at 250 MHz in the original spectrum which is due to correlated noise on the ADC. The differences between the spectra for $f < f_{\text{cut}}$ are due to the numerical inaccuracies of the FFT.

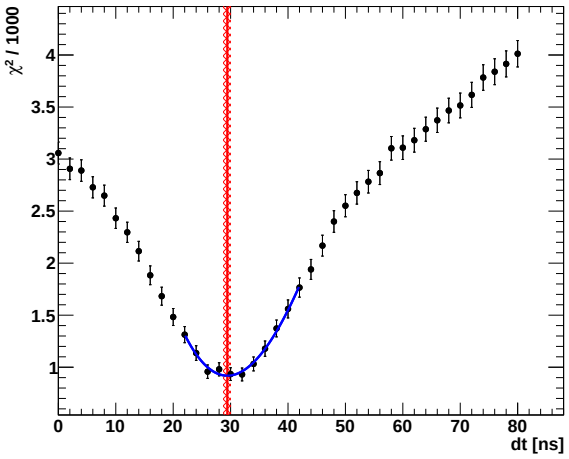

Figure 7.17: The obtained minimum χ^2-values as a function of the time shift dt between the photon distributions of the two PMTs for a measurement with an empty 5 m tube. The obtained values have been fitted by a polynomial of order 3 (blue line). The vertical red line shows the fitted time shift Δt, the small red-crossed area indicates the error of Δt.

resulting from time shifts corresponding to an odd number of time bins which makes a precise determination of the minimum impossible. To overcome this problem, all photon distributions are low pass filtered before matching the distributions: They are first transformed into the frequency domain using a FFT, then all components corresponding to frequencies above $f_{\text{cut}} = 240\,\text{MHz}$ are discarded and the inverse FFT is applied to obtain the filtered spectrum in the time domain. The frequency spectrum of the measurement after the cut is also shown in figure 7.16. Due to this low pass filtering, the statistic of the histogram is changed: The error of a bin is no longer given by the square root of its contents and the bins are no longer independent. However, due to the cut removing selectively only a very small part of the frequency range, this effect should be very small. Hence, they are neglected in the following.

After removing the crosstalk of the ADC-clock, another effect has to be taken into account: The time resolution[23] of PMT1 $\sigma_1 = 0.5\,\text{ns}$ [132] does not match the time resolution of the PMT2 $\sigma_2 = 1.7\,\text{ns}$ [133]. This difference in resolution leads to a mismatch of the photon time spectrum obtained on the PMTs. This causes a systematic offset of Δt which is correlated to the transmission of the measurement. This effect can be reduced by smearing the obtained photon time spectrum of PMT1 with a Gaussian PDF with a standard deviation of $\Delta\sigma = \sqrt{\sigma_2^2 - \sigma_1^2}$ in order to obtain approximately the same resolution for the photon distributions from both PMTs. Thus, the number of entries $n_i^{c(1)}$ in the i^{th} bin of

[23] As the exact shape of the transit-time spread of the PMTs is not known, it is approximated by its main Gaussian component (see section 4.2).

the dead time corrected photon time distribution of PMT1 becomes:

$$\begin{aligned} n_i^{c(1)} \to \tilde{n}_i^{c(1)} &= \sum_{j=1}^{N_{\text{bins}}} \int_{t_{i<}}^{t_{i>}} dt' n_j^{c(1)} \left\{ \frac{1}{\sqrt{2\pi}\Delta\sigma} \exp\left[-\frac{t^2}{2(\Delta\sigma)^2} \right] \otimes \frac{1}{\delta t_b} \Theta\left(|t - t_j| - \frac{\delta t_b}{2} \right) \right\} (t') \\ &= \sum_{j=1}^{N_{\text{bins}}} \int_{t_{i<}}^{t_{i>}} dt' \frac{n_j^{c(1)}}{2\delta t_b} \left[\text{erf}\left(\frac{t' + \delta t_b/2}{\sqrt{2}\Delta\sigma} \right) - \text{erf}\left(\frac{t' - \delta t_b/2}{\sqrt{2}\Delta\sigma} \right) \right], \end{aligned} \tag{7.30}$$

where N_{bins} is the number of bins in the histogram, $t_{i<}$ and $t_{i>}$ are the upper and lower boundaries of the i$^{\text{th}}$ bin, δt_b is the width of a bin and $\Theta(x)$ denotes the step function which is 1 for $x \geq 0$ and 0 otherwise. The summand in the first line of equation (7.30) corresponds to a convolution of the Gaussian time resolution with a rectangular bin at position t_j.

Finally, the obtained dead time corrected photon distributions can be matched using a χ^2-comparison. As the histograms can also differ in number of detected photons, the χ^2-function depends on two parameters: The (integer) time difference dt in units of bin widths and the transmission[24] τ:

$$\chi^2(dt, \tau) = \sum_i \frac{\left[\tilde{n}_i^{c(1)} - (\frac{1}{\tau}) n_{i+dt}^{c(2)} \right]^2}{\tilde{n}_i^{c(1)} + \left(\frac{1}{\tau}\right)^2 n_{i+dt}^{c(2)}}, \tag{7.31}$$

where the sum runs over all signal bins between $t_{\text{min}}^f = 800\,\text{ns}$ to $t_{\text{max}}^f = 3600\,\text{ns}$ which have at least $n_{\text{min}}^{\chi^2} = 20$ entries. Here, $n_i^{c(2)}$ is the number of photons in the i$^{\text{th}}$ bin for the distribution belonging to PMT2. The quadratic error in the denominator is calculated from the sum of the quadratic errors of $n_i^{c(1)}$ and $(1/\tau) n_{i+dt}^{c(2)}$. Obviously, for such a conversion, only integer values of dt are possible. Therefore, $\chi^2(dt, \tau)$ is minimized separately with respect to τ for each possible dt value between[25] $\Delta t_{\text{min}} = 0$ and $\Delta t_{\text{max}} = 80\,\text{ns}$. The resulting minimum χ^2-values are subsequently plotted as a function of dt as shown in figure 7.17 for a tube length of 5 m. In the region of the point with the minimum χ^2-value $(dt_{\text{min}}, \chi^2_{\text{min}})$, the χ^2-function is fitted by a polynomial of order 3, where the fit region is defined as $[dt_{\text{min}} - 10\,\text{ns}, dt_{\text{min}} + 10\,\text{ns}]$. The minimum obtained is subsequently considered to be the time shift Δt between the two distributions. Note, that Δt does not directly correspond to the difference in time of flight of the photons between PMT1 and PMT2, as it features a constant offset due to differences in the transit time of the PMTs[26] Figure 7.18 shows a comparison of the photon-time distributions of both PMTs after shifting the distribution of PMT2 by[27] dt_{min}. The two obtained distributions match

[24] The transmission here does not correspond to the transmission as defined in equation (7.12) as it does not take both, the full and the empty measurement into account. Thus, also a different symbol is used.

[25] Typically, the minimum is in the range between 10 ns and 45 ns. Using such a large interval in dt to look for the minimum ensures the absence of boundary effects.

[26] There should be only a negligible constant offset due to differing cable lengths as both PMTs were connected to the ADC with a 10 m cable.

[27] As the photon time distributions can only be shifted by integer bin widths, it is impossible to shift the distribution by Δt. Thus, dt_{min} is used instead.

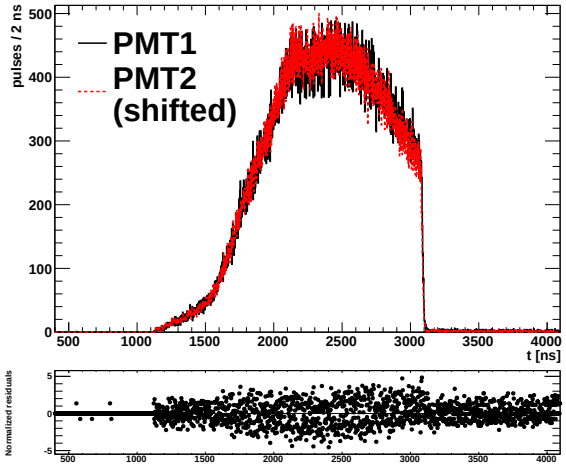

Figure 7.18: The upper panel shows the dead time corrected photon time distributions for both channels after shifting the distribution of PMT2 by $dt_{\min}$ (see text) and scaling it to the corresponding distribution of PMT1. The lower panel shows the normalized residuals of the comparison between the two histograms.

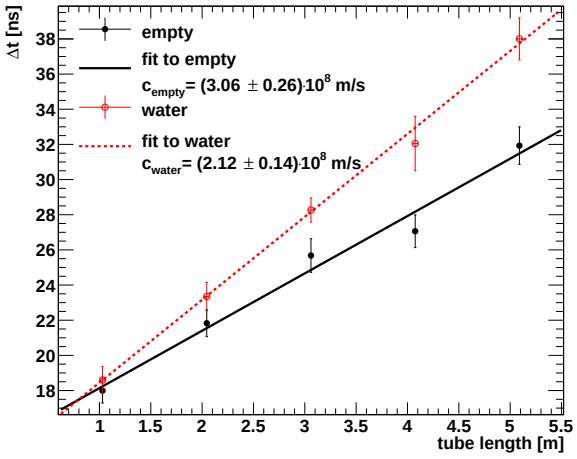

Figure 7.19: The obtained time shifts between the photon distributions on the first and second PMT as a function of the tube length for a calibration measurement with ultra pure water and for the corresponding measurements with the empty tube. The lines indicate the best fit with a linear function. The corresponding speeds of light for both measurements are indicated in the legend together with their statistical errors.

well even at the steep slope.

To be able to assign a proper statistical error to the position of the minimum, an error for the $\chi^2(dt)$-values is required. The error of this value is due to the statistical fluctuations of the bin contents [146]. It is determined by applying Gaussian error propagation to equation (7.31). Successively, the error of the minimum can be calculated from the fit errors by Gaussian error propagation. Here, it is relevant to take the correlations between the parameters into account [106]. Note, that in this case the error cannot be determined directly from the fitted χ^2-function using equation (7.27) as the error obtained this way is much smaller than the error due to the statistical fluctuations of the different points[28]. Figure 7.19 shows the resulting Δt as a function of the tube length including errors for a measurement with ultra pure water and for the corresponding measurements with an empty tube. By fitting the data with a linear function, the speed of the photons in the empty tube can be determined. The obtained values are compatible with the speed of light in vacuum $c_0 = 2.998 \cdot 10^8\,\mathrm{m/s}$ [21] and the speed of light in water [147, 131]

$$c_{\mathrm{water}} = \frac{c_0}{n_{\mathrm{eff,water}}} = \frac{2.998 \cdot 10^8\,\mathrm{m/s}}{1.3733} = 2.183 \cdot 10^8\,\frac{\mathrm{m}}{\mathrm{s}}. \tag{7.32}$$

To also obtain a systematic error for the determination of the velocity of the photons in the scintillator, all available measurements, where the effective index of refraction was known, were collected compared to their literature values. Figure 7.20 shows the absolute

[28] The relevant difference between section 7.3.5 and this section is that in the former case a function is fitted to experimental values while in this section two experimental distributions are tried to match.

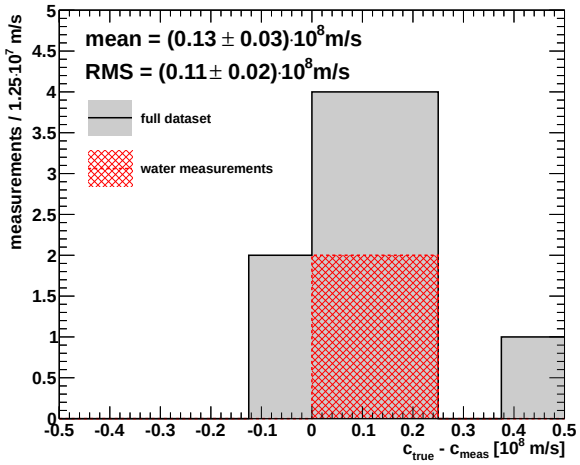

Figure 7.20: The distribution of the deviation of the reconstructed value from the true value of the speed of light in air and ultra pure water. The distribution of the ultra pure water measurements is shown separately. Additionally, the obtained mean and the obtained root mean square (RMS) of the full data-set is indicated.

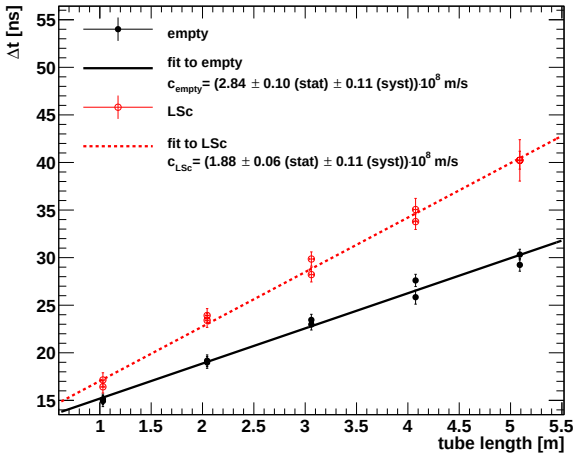

Figure 7.21: The obtained time difference Δt between the photon distributions obtained with PMT1 and PMT2 as a function of the tube length for the final measurement done with LAB (compare section 7.3.5). The different graphs show the results obtained with the empty tube and with the full tube, respectively. The lines indicate the best fit with a linear function. The corresponding speeds of light for both measurements are indicated in the legend together with their statistical errors.

deviations between true and reconstructed speed of light. The distribution shows a systematic offset of $\Delta c_{\text{offset}} = (0.13 \pm 0.03) \cdot 10^8\,\text{m/s}$. It is caused by the remaining effect of the differences between the two time resolutions of the PMTs. This effect cannot be fully taken into account as the real shape of the TTSs of the PMTs is not known and as the effect of the PMTs' TTS would have to be added before the crosstalk of the ADC-clock affects the distribution which is, of course, not possible. To correct for this effect, all obtained photon velocities are increased by Δc_{offset}. As this correction is also afflicted with an error, a systematic error corresponding to the spread of the distribution shown in figure 7.20 is added[29]: $\Delta c_{\text{syst}} = 0.11 \cdot 10^8\,\text{m/s}$.

Finally, figure 7.21 shows the result obtained from the LAB measurement shown in section 7.3.5. The resulting speed of light in the empty tube is compatible with c_0 and the speed of light in the LAB is found to be

$$c_{\text{LAB}} = (1.88 \pm 0.06(\text{stat}) \pm 0.11(\text{syst})) \cdot 10^8\,\frac{\text{m}}{\text{s}}. \tag{7.33}$$

This translates to an effective index of refraction of

$$n_{\text{eff}} = 1.59 \pm 0.05(\text{stat}) \pm 0.10(\text{syst}). \tag{7.34}$$

[29] The error of the correction is by default of course given by the error of the mean. However, as it cannot be excluded that this effect varies from measurement to measurement, here the sample error is used instead.

Note, that the result is compatible to the index of refraction used in section 4.1. A higher accuracy could, of course, be reached by using a beam with shorter pulses. This, however, would have required a dedicated measurement which was not performed, as the main goal is to determine the attenuation length in a liquid scintillator.

7.4 Drawbacks of the used set-up

The error of the attenuation length obtained in section 7.3.5 is dominated by systematical errors. The most relevant contributions are the timing instability of the set-up and the large effect of the window dismounting-cleaning-remounting procedure on the transmission of the optical system. These large errors can be traced back to a few properties of the set-up used for the measurement (see section 7.2):

- PMTs were used to detect the intensities of the reference beam and of the beam after the tube. The PMT gain G is strongly coupled to the supply voltage V [43]

$$\frac{dG}{G} = n_D \frac{dV}{V}. \tag{7.35}$$

  Here, $n_D = 10$ [132] and $n_D = 11$ [133] are the number of dynodes of the PMT1 and PMT2, respectively. Hence, even small fluctuations in the voltage lead to significant differences in the gain of the PMTs and thus in their photon detection efficiencies. Additionally, even μ-metal shielded PMTs are susceptible to magnetic fields which can be produced by other experiments in the same laboratory.

- At the full tube length of 5 m, the width of the beam is in the same order as the diameter of the apertures. Additionally, due to the coupling of the LED into the fiber, the beam intensity was very small even if the LED was continuously driven at full power. This made the alignment of the beam very difficult. It therefore cannot be fully excluded that a part of the observed systematic errors is due to an unobserved clipping of the beam.

- The quantum efficiency of a PMT generally varies by $\sim$10 % over the surface of the PMT (see e.g. [141]). Thus, even small changes of the intensity distribution in the beam and/or of the position of the beam lead to significant changes in the overall quantum efficiency.

- As already discussed in section 7.2.4, the beam position varies due to refractive-index layering in the LSc in the tube. As the used PMTs do not feature any position resolution for the detected photons, it is difficult to ascertain that the set-up really has entered a stable state before the measurement starts.

- The used combination of a LED and a pulser does not constitute a very stable light source which is, of course, not optimal even though most of the effect of the light source's variability is suppressed by the reference PMT.

- The aperture used to collimate the light before entering the tube was fixed at the tube and thus very prone to changes of its position inducing a possible systematic error.

- Changing the tube length requires lots of mechanical work and significant changes in the set-up which is the root of many systematic errors.

The listed problems of the experiment motivate the construction of an improved experiment for measuring the attenuation length as presented in chapter 8. In the improved experiment, all listed points could be addressed except the last one. It would require a redesign of the tube which will be done in the planned upgrade of the experiment presented in chapter 8 (see section 8.5).
However, the improvement in the attenuation-length accuracy comes at the price, that the upgraded experiment will no longer be able to measure the effective index of refraction n_{eff} of the scintillator as a continuous light beam is used for the measurement. Hence, instead of using one measurement to measure n_{eff} and Λ_{att}, the idea is to use two specialized measurements which feature an improved performance in measuring one parameter each. As the present thesis is about the measurement of the attenuation length, no further experiment was designed to measure n_{eff}.

Chapter 8

Measurement of the attenuation length: The set-up using a halogen light bulb as light source and a CCD as detector

Even though the precision in attenuation length obtained using the experiment described in chapter 7 is a major progress compared to the measurements with the UV/Vis-spectrometer, the obtained accuracy is not sufficient to determine large attenuation lengths of order 24 m, as required for JUNO (see section 2.3.3), with a precision significantly below 10 %. Based on the considerations in section 7.4, a new set-up was constructed which is presented in section 8.1. After adapting the data-analysis to the new set-up (see section 8.2), an improved result is derived which is presented in section 8.3. The consequences of the obtained attenuation-length results for LENA and JUNO are briefly outlined in section 8.4. In section 8.5, a further step in the evolution of the experiment, which is currently being installed, is presented. Finally, section 8.6 outlines why the accuracy obtained with the set-up presented in this chapter makes this experiment an important factor for the success of the next generation of LSc detectors.

8.1 Experimental set-up

As discussed in section 7.4, a significant part of the systematic error of the experiment presented in section 7.2 is due to a combination of an unstable light source, using PMTs as light detectors and an insufficient performance of the optical system. Thus, a new set-up was developed in which these critical parts have been completely redesigned.

Section 8.1.1 provides a general overview of the new set-up while the following sections provide an in-depth description of the relevant changes of the set-up compared to the set-up presented in section 7.2, i.e., the new optical system (section 8.1.2) and the new light detector (section 8.1.3).

8.1.1 Overview of the set-up

The overall set-up of the experiment is shown in figure 8.1. It uses the same sample container as the experiment described in section 7.2, i.e., the modular tube which can be

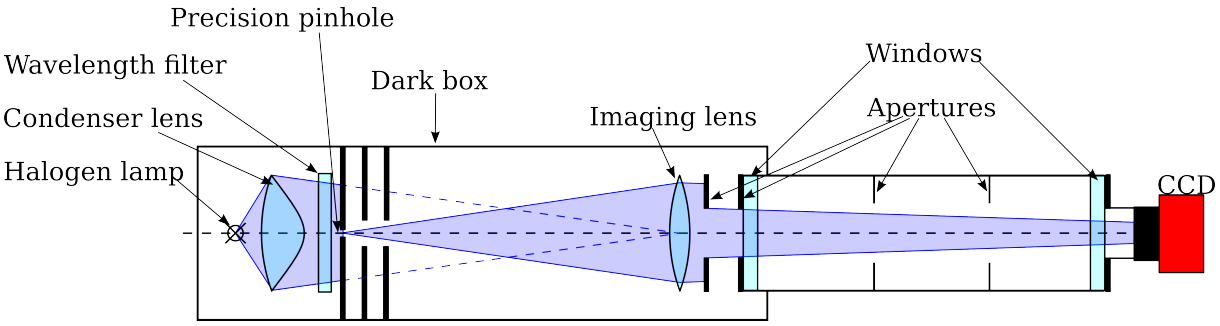

Figure 8.1: Sketch of the second generation of the experiment to determine the attenuation length in liquid scintillators. The measured fluid is contained in a modular tube which can be assembled to feature a length between 1 m and 5 m in 1 m steps. Its inside is blackened and it features additional apertures to suppress scattered light. A continuous halogen light bulb with a band-pass wavelength filter is used as light source. The produced light is collected using a condenser lens. From the collimated light, a small light source is created using a pinhole. This pinhole is imaged onto the detector, a CCD-camera, using a lens. Before entering the tube, the light beam is collimated by an aperture.

assembled to have a length between 1 m and 5 m in 1 m steps. Also the apertures mounted in the flanges of the tube, which suppress the scattered light, are still present. As the same tube is used, also the fluid system, which is described in detail in section 7.2.3, has not been changed. Note, that this also means that the orientation of the tube is still the same, i.e. that the time required for the experiment to enter a thermally stable condition is still 2 days. For a better comparison of the performances of the two set-ups, the fluid measured in both experiments is the same LAB. The light is generated by a continuous halogen light bulb and successively collected by a condenser lens. Using a pinhole, a small object is created which is imaged onto the detector, which is a 8.4 MPixel-CCD camera. The whole optical system is contained in a dark box to prevent ambient light from entering the system.

The intensity I_f measured by the detector for a full tube[1] is

$$I_f = I_0 \cdot T_{\mathrm{A1}} \cdot T_{\mathrm{AG1}} \cdot T_{\mathrm{G1}} \cdot T_{\mathrm{GS1}} \cdot \exp\left(-\frac{d}{\Lambda_{\mathrm{att}}}\right) \cdot T_{\mathrm{GS2}} \cdot T_{\mathrm{G2}} \cdot T_{\mathrm{AG2}} \cdot \epsilon_{\mathrm{CCD}}, \tag{8.1}$$

where I_0 is the intensity of the beam after the imaging lens and ϵ_{CCD} is the quantum efficiency of the charge-coupled device (CCD). The remaining parameters have already been introduced in section 7.2.2. Analogously, the intensity measured for an empty tube is

$$I_e = I_0 \cdot T_{\mathrm{A1}} \cdot T_{\mathrm{AG1}} \cdot T_{\mathrm{G1}} \cdot T_{\mathrm{AG1}} \cdot T_{\mathrm{AG2}} \cdot T_{\mathrm{G2}} \cdot T_{\mathrm{AG2}} \cdot \epsilon_{\mathrm{CCD}}. \tag{8.2}$$

Taking again the ratio of these two quantities yields the transmission

$$T(d, C, \Lambda_{\mathrm{att}}) = \frac{I_f}{I_e} = \frac{T_{\mathrm{GS1}} T_{\mathrm{GS2}}}{T_{\mathrm{GA1}} T_{\mathrm{GA2}}} \exp\left(-\frac{d}{\Lambda_{\mathrm{att}}}\right) = C \exp\left(-\frac{d}{\Lambda_{\mathrm{att}}}\right) \tag{8.3}$$

corresponding to equation (7.12).

[1] Again, the effect of multiple reflections on parallel surfaces is neglected.

8.1.2 Optics

As the inadequate performance of the optics was one of the major problems of the experiment presented in section 7.2, a new optical system was designed following a discussion with A. Ulrich [148]. In contrast to the optics presented in section 7.2.4, here no nearly parallel beam is produced but a small object emitting light is imaged onto the detector. This incorporates two tasks: Generation of a well defined object emitting nearly monochromatic light, and imaging the object onto the detector. Additionally, the set-up has to suppress parasitic light from the light bulb. The whole optical system was mounted in a rigid frame[2] to ensure a good stability of the set-up.

Generation of the light:
The light is generated using a 100 W halogen light bulb[3]. As in this configuration of the experiment no monitoring of the initial beam intensity was implemented, the time stability of the light source is of utmost concern. Thus, a very stable current source[4] was used to drive the halogen lamp. To obtain maximum stability, the lamp was driven in a current-controlled mode with the a current of 4.8 A. This was significantly below the specifications for the lamp but already provided enough intensity for the experiment. Even though the lamp was not driven at its specified working point, a very high stablity in time is accomplished (see section 8.2.3).
The light emitted from the lamp was collimated by a 2" aspheric condenser lens[5]. To prevent accidental imaging of the filament of the lamp[6], the condenser lens was adjusted to produce an image of the filament in the imaging lens. Strictly speaking this is, of course, only true for the case that the imaging lens was adjusted for the 5 m tube. For all other tube lengths, the image of the filament was either ∼5 cm in front of the imaging lens (4 m tube) or after the imaging lens which also prevents a real image of the filament at the detector position.
The light obtained from the condenser lens is successively monochromated using a band pass wavelength filter[7]. Its transmission is depicted in figure 8.2. Finally, the required object for imaging is defined by a precision pinhole[8]. A photo of the set-up is shown in figure 8.3.

Imaging optics:
As the size of the detector is only 17.6 mm times 13.52 mm [149], the produced image at the end of the tube has to be very small. The magnification M of the image compared to the object is [131]

$$M = -\frac{b}{a} = 1 - \frac{b}{f}, \tag{8.4}$$

[2]Spindler & Heuer (now Linos), Macrobench
[3]LOT-QuantumDesign, LSB117/5
[4]Heinzinger TH 30-300
[5]Thorlabs, ACL50832U-A
[6]The filament features a complicated three-dimensional structure. Thus, it cannot be fully imaged on a flat detector. If this is attempted, small changes of the optical set-up lead to imaging of different parts of the filament and thus compromise the stability of the experiment.
[7]As the wavelength filter in the old experiment could not stand the high light intensity produced by the halogen light bulb, a new filter had to be used: LOT-QantumDesign, 430FS10-25
[8]Edmund Optics, E39-730

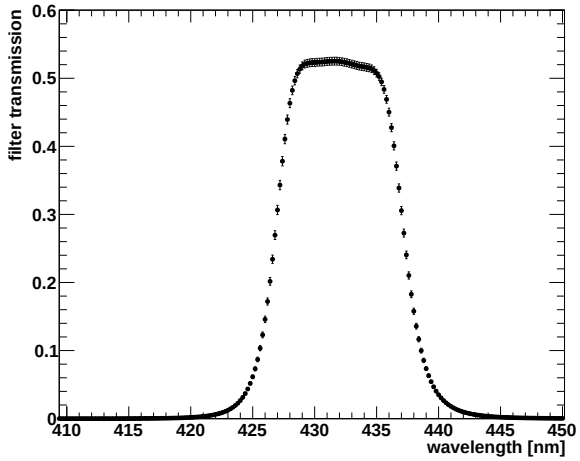

Figure 8.2: The transmission of the used wavelength filter as a function of the wavelength as measured with a Perkin Elmer LAMBDA 850 UV/Vis-spectrometer. The blocking outside the transmission region is better than 10^{10}.

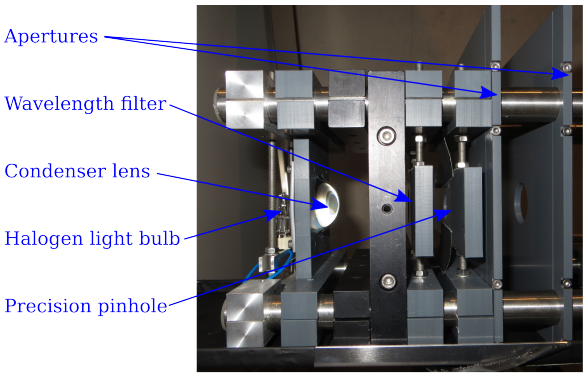

Figure 8.3: A photo of the set-up for generating a well defined object to be imaged. From the left to the right, the halogen light bulb, the condenser lens, the wavelength filter, the precision pinhole and the additional apertures to catch stray light from the halogen light bulb are visible. All elements are mounted on custom-designed holders in a rigid frame.

where f is the focal length of the imaging lens, b is the image distance and a is the object distance, i.e., the distance between the pinhole and the imaging lens. Thus, as in the experiment $b > f$ holds, the modulus of M increases with rising b and declines with rising focal length of the lens. In contrast to section 7.2.4, a lens with a much longer focal length can be used, as much more light is available and thus more losses are acceptable. Here, the focal length is basically limited by the available space in the frame holding the optics as a longer focal length requires a larger distance between the precision pinhole and the imaging lens. Finally, two lenses were used: One lens[9] with 50 cm focal length for tube lengths of 3 m and below ($|M| \lesssim 6$) and one lens[10] with focal length of 1 m for tube lengths of at least 4 m ($|M| \lesssim 4.5$). Both lenses were achromatic doublets to avoid aberrations. With their 2" diameter, the lenses are larger than required[11] to obtain the 1" beam to fit through the apertures mounted in the tube. This allows to utilize the good imaging properties in the center of the lenses. To obtain a beam which fits the tube, the size of the beam was reduced by an aperture mounted right behind the imaging lens. In contrast to the optics described in section 7.2.4, in this case the aperture was deliberately not attached to the tube. Note that the requirement to refocus the optics as soon as the tube length is changed, leads to a few important points which are mentioned in the following:

- Due to the refocusing of the optics, the intensity I_0 after the imaging lens (see equations (8.1) and (8.2)) differs for every tube length. Therefore, in this set-up

[9] Thorlabs, AC508-500-A-ML - f=500 mm, Ø2" Achromatic Doublet
[10] Thorlabs, C508-1000-A-ML - f=1000 mm, Ø2" Achromatic Doublet
[11] Typically, the best imaging properties of a lens are obtained close to its optical axis where the paraxial-approximation works best. Thus, by using only the central Part of a lens, the imaging properties can be improved.

the comparison between the measurements with an empty tube and a full tube does not only reduce the systematic error but is mandatory to determine the attenuation length.

- The differences in intensity I_0 also pose a problem for the dynamic range of the detector. As the lamp current was kept constant to keep the wavelength spectrum of the emitted light constant, the intensity at the detector is regulated by the diameter of the aperture directly behind the imaging lens. While for the 5 m measurement an aperture radius of 12 mm is used, the aperture radius is reduced down to 3.5 mm for smaller tube lengths. As the aperture is positioned directly behind the imaging lens, it does not reduce the imaging quality.

- As the scintillator has a refractive index of $n \approx 1.48 > 1$, it is not possible to obtain an image directly on the detector for both, the empty and the full tube measurements. Experience has shown, that the best overall performance can be achieved by adjusting the position of the imaging lens to result in a sharp image $\sim$10 % of the tube length behind the detector.

To be able to position the image directly on the detector, the optical setup can be precisely aligned using two precision x- and y-actuators which are installed at the front and at the back of the frame holding the optical assembly.

Suppression of parasitic light:
As the intensity of the halogen light bulb is strongly reduced by the monochromator and the pinhole, direct light from the lamp must not enter the measuring tube. Thus, directly behind the precision pinhole, two 1" apertures are mounted which block all direct light paths from the lamp to the entrance of the tube. The apertures expand all the way out to the dark box. Using two apertures also effectively suppresses light which might pass through the point where the dark box touches the aperture. Additionally, the inside of the dark box and the apertures are covered with a low reflectivity foil[12]. This also eliminates ambient light entering through the openings in the dark box required for the ventilation of the light-bulb.

8.1.3 Light detection

The light is detected using a 8.4 MPixel-CCD detector[13]. Figure 8.4 (left) shows an example of a beam detected after transversing an empty 5 m tube. The beam is nicely circular with a radius between 2 mm and 3 mm showing the good performance of the optical system. On the right of figure 8.4, the same beam is shown but this time after transversing a 5 m tube freshly filled with LAB. Compared to the beam spot measured with an empty beam, the shape of the detected beam changed drastically: It is now significantly flattened in the horizontal direction. The breaking of the beam's symmetry is due to the thermal layers which correspond to layers in refractive index which develop in the non-thermalised scintillator (confer section 7.2.4). The passing of these layers at a very high angle with respect to the axis of incidence leads to a focusing effect in the vertical direction. As already mentioned above, before each measurement the system was allowed to thermally

[12] Thorlabs, BKF12 Matte Black Aluminum Foil
[13] ATIK 383L+ (monochrome version)

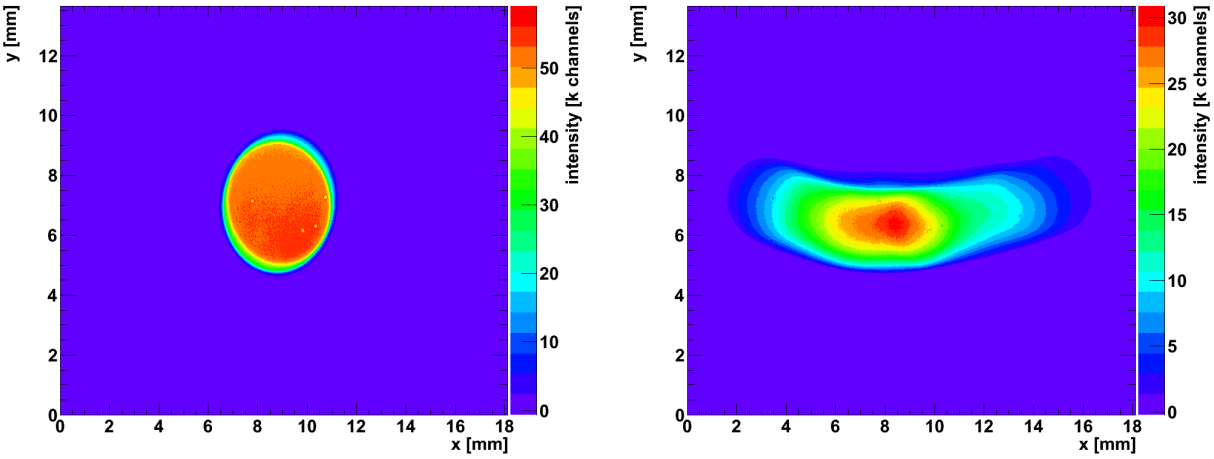

Figure 8.4: The image of the beam as recorded by the CCD for a measurement with an empty tube (left) and with a full tube (right). Both images were taken using a 5 m tube. The right image was taken directly after filling the tube. The deformation of the beam is due to the refractive index layers which are created in the tube due to the non-thermalised scintillator (compare section 7.2.4). The small visible dots (see, e.g., left figure) featuring a different intensity are due to dust on the entrance window of the CCD camera.

stabilize for at least two days. After this stabilization period, the deformation of the beam is reduced but it is still visible, showing that even after two days of stabilization, a small layering effect remains. However, after two days the impact of this effect is reduced to a shift of the beam position of less than 0.5 mm per hour thus providing acceptable measurement conditions. The small points which are visible in the images shown in figure 8.4 correspond to small dust particles on the entrance window of the CCD camera. To avoid bigger effects due to dust, the CCD camera was always covered immediately after being removed from the tube. Additionally, the reduced dust conditions in the laboratory (confer section 7.2.3) are advantageous for keeping the camera clean.
Compared to a PMT, a CCD camera shows a much higher homogeneity of the quantum efficiency over its surface. This significantly reduces the impact of the window cleaning procedure from 1.7 % (see section 7.3.4), which was caused by a small tilt of the beam due to the different mounting of the windows, down to about 0.3 % (see section section 8.2.3). As, on the other hand, the stability of the light source was not controlled, the sequence of the measurements was conducted the other way around compared to the procedure presented in section 7.2.2: First, the measurement using the full tube is performed. Successively, the tube is emptied, the windows are cleaned and the empty tube is measured. Thus, the measurements of the empty and the full tube are separated by typically around two hours instead of two days which is required for a thermally stable scintillator.
The camera's CCD chip can be cooled down to a preset temperature which is at maximum 40 °C below ambient temperature using a Peltier element. This has two advantages: First of all, cooling the CCD chip significantly reduces the chip's noise and especially strongly reduces the number of pixels which show an excess noise. Additionally, as the temperature is controlled by the shipped software [150] to about 0.1 °C [149], this results in a very stable detector. In all the measurements, the ambient temperature was at (22 ± 1) °C. Consequently, the chip's temperature was set to -15 °C, not to drive the cooler to its limits and thus obtain a stable measurement under all circumstances.

8.2 Data analysis

To determine the attenuation length, again the transmission has to be obtained from the acquired data for each tube length. In a first step, the CCD camera is calibrated (see section 8.2.1). Using this information allows to determine the transmission for each length as discussed in section 8.2.2. Successively, as elaborated in section 8.2.3, the systematic errors of the experiment are investigated. Finally, the attenuation length can be determined according to the procedure already described in section 7.3.5. The result is presented in section 8.3.

8.2.1 Calibration of the CCD

The calibration of the CCD camera consists of three steps: First, some of the pixels show an excess noise and have to be removed from the analysis. Successively, the linearity of the device is tested using flat field measurements. Finally, a pixel-by-pixel gain calibration is performed to reduce the error of the measured intensity.

Removal of hot pixels:
To identify pixels with an excess dark noise, so called hot pixels, measurements in a dark environment were conducted. This environment was provided by a walk-in dark box. Additionally, using a dedicated function in the software, the shutter of the camera was disabled. Thus, it was kept closed during the exposure. Figure 8.5 shows the distribution of the pixels' intensities recorded in such a dark measurement. While the obtained distribution can generally be well described by a Gaussian (see blue curve in figure 8.5), there is a small shoulder as well as a flat tail to higher intensities. These deviations from the Gaussian behavior are due to pixels with an excess dark noise. Note, that the shoulder of the distribution can be removed by not taking the first line of the CCD into account, already indicating that the performance of the first line is not optimal (see figure 8.5). The flat tail however is nearly unchanged by this cut, indicating that there are additional hot pixels in the remainder of the detector. To identify the hot pixels, 100 dark measurements, each with a 2 s exposure, were acquired. The intensity distribution obtained from each of these measurements was fitted with a Gaussian distribution using a χ^2-fit[14] resulting in a mean μ_I and a standard deviation σ_I for each distribution. All pixels with an intensity $I_{ij} > \mu_I + 5\sigma_I$ were tagged as hot pixels of this measurement. Figure 8.6 shows the distribution of the number of measurements where a specific pixel was tagged as hot. Obviously, most of the pixels which were tagged as hot multiple times are from the first line, even though the pixels which are tagged hot in all the measurements are not from the first line.
All pixels which were tagged hot in at least three of the 100 measurements were declared as global hot pixels and thus removed from any further analysis. Additionally, all pixels from the first line were removed from the analysis as the first line features too many hot pixels to be used anymore. This results in a loss of $3{\cdot}10^{-4}$ of all pixels. Considering the first line to be lost anyhow, the remaining globally hot pixels make up only a very small fraction ($\sim 5{\cdot}10^{-6}$) of all pixels. Figure 8.7 shows the positions of all global hot pixels. Apart from the first line, no further clusters of hot pixels can be found. Finally, figure 8.8

[14] In this case the χ^2 fit was preferred compared to the binned negative logarithmic likelihood fit as it is less sensitive to small tails of the distribution.

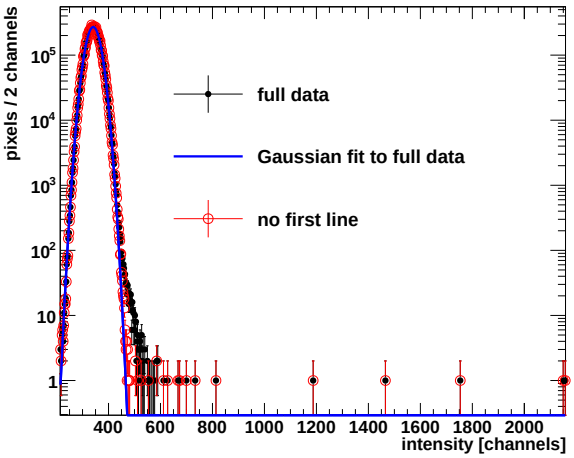

Figure 8.5: Distribution of the intensities of the pixels of the CCD obtained from a dark measurement. The blue curve shows the result of a Gaussian fit to the distribution. Additionally, the same distribution is shown after removing the first line from the data set. Note that for intensities above ∼600 channels the full dataset and the dataset without first line feature the same bin contents.

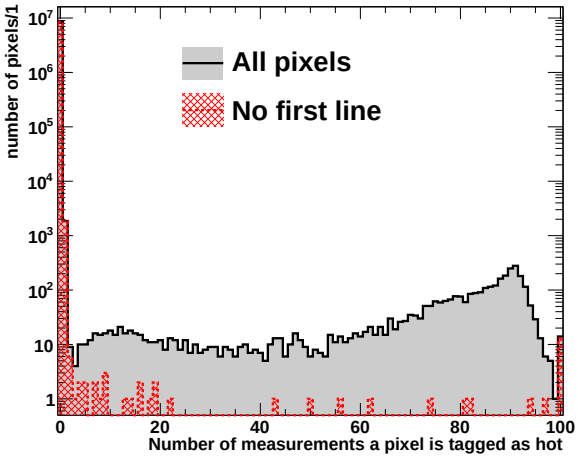

Figure 8.6: The distribution of the number of measurements (out of 100 conducted) where a pixel intensity is more than 5σ above the mean of the intensity distribution. Additionally, the same distribution is shown after removal of the pixels from the first line.

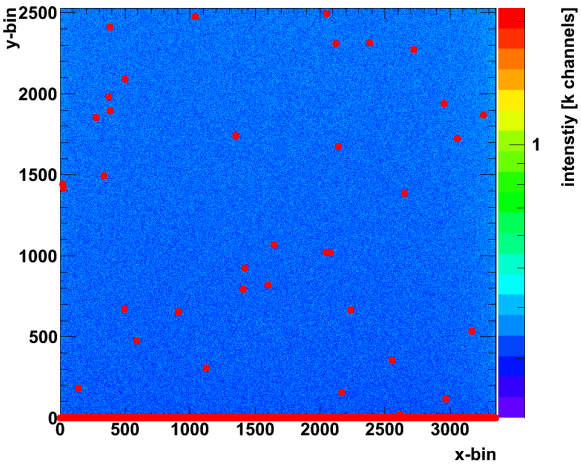

Figure 8.7: The 2D intensity distribution obtained from a dark measurement. Superimposed, the red dots show the positions of the hot pixels which are excluded from the further analysis.

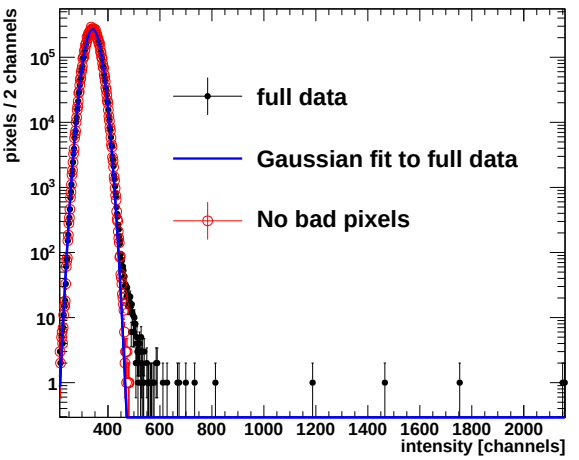

Figure 8.8: Distribution of the intensities of the pixels of the CCD for a dark measurement. The blue curve shows the result of a Gaussian fit to the obtained distribution. Additionally, the same distribution is shown after removal of the hot pixels.

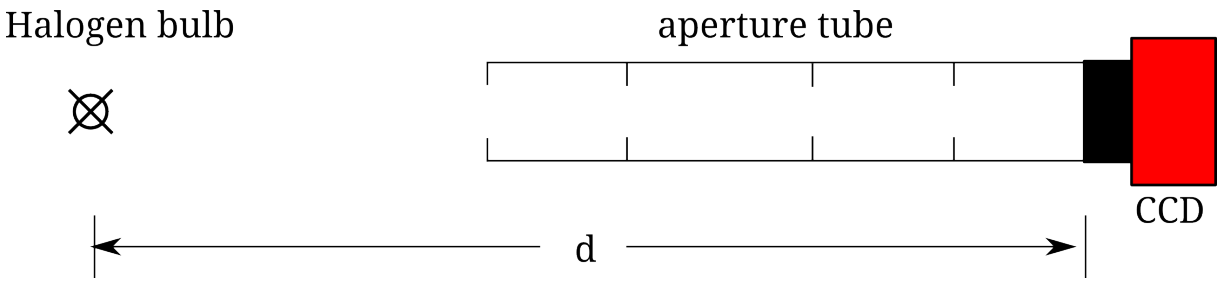

Figure 8.9: The set-up (not to scale) used to test the linearity of the CCD camera. The camera was put into a walk-in dark box and illuminated by a halogen light bulb which was positioned at a variable distance d to the CCD camera. To reduce the influence of light reflected from the walls of the dark box, a cardboard tube with apertures was fixed in front of the camera.

shows a comparison of the intensity distributions obtained before and after removing the hot pixels from the data-set. The resulting intensity distribution after removal of the hot pixels shows no deviations from a Gaussian shape.

Linearity test:
To test the linearity of the CCD, the set-up shown in figure 8.9 is used. The CCD is mounted on an optical rail facing a halogen light bulb which is mounted on the same optical rail. By varying the position of the halogen light bulb on the optical rail, the distance d between the camera and the light bulb can be changed. To avoid influences from ambient light, the set-up is mounted in the same walk-in dark box already used to determine the hot pixels. As the walls of this dark box feature a reflecting color, a $\sim 1\,\mathrm{m}$ cardboard tube with apertures was mounted in front of the CCD camera to ensure that only direct light can hit the CCD. As the lamp cannot be positioned inside the cardboard tube, this imposes $d > 1\,\mathrm{m}$. Thus, for all the measurements $d \gg d_{\mathrm{CCD}}$ holds, where $d_{\mathrm{CCD}} = 22\,\mathrm{mm}$ is the maximum extension of the CCD chip. This has two important consequences: First of all, the light intensity should be nearly constant over the whole active area of the CCD. At a $d = 1\,\mathrm{m}$, the maximum deviation from the constant intensity is about $2 \cdot 10^{-4}$. Furthermore, the solid angle covered by the CCD is well described by $\Omega \propto 1/d^2$. Thus, the mean intensity after dark noise correction (for details see section 8.2.2) should follow

$$\langle I \rangle = \frac{I_0}{d^2} = \frac{I_0}{(x - x_0)^2}, \tag{8.5}$$

where x is the position of the light bulb on the optical rail, x_0 is the position of the CCD and I_0 is a normalization parameter. Due to the used holder for the CCD camera on the optical rail, a precise determination of the position of the camera on the optical rail is difficult. As the uncertainty of x_0 is about a few cm, this parameter is treated as a free parameter. Figure 8.10 shows the obtained data together with a fit according to equation (8.5). The resulting value for $x_0 = (28 \pm 8)\,\mathrm{mm}$ is well within expectations. As the fitted curve matches the data quite well ($\chi^2/NDF = 19.5/15 = 1.3$) and the residuals (not shown) do not show any preferred direction, it can be concluded that within this calibration measurement no hints for a deviation from a linear behavior of the CCD can be found. As the linearity of the CCD is very important for this measurement, two additional calibration measurements have been conducted which are not shown here in detail: The transmission of a precision quartz-glass plate was measured as a function of the

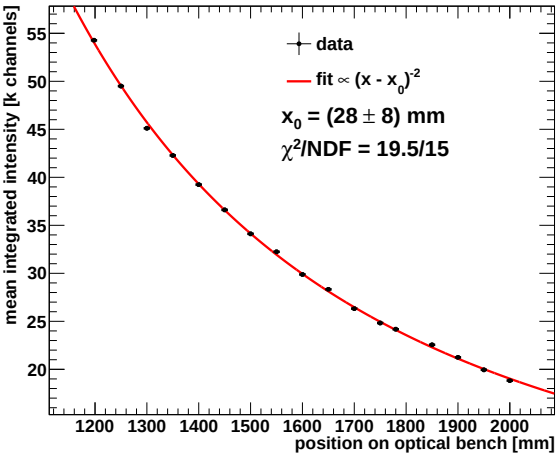

Figure 8.10: The mean intensity (after dark noise correction) detected at the CCD camera as a function of the position of the light bulb on the optical rail. The red line shows a fit with a function $I \propto 1/(x-x_0)^2$ where x is the position of the light bulb on the optical rail and x_0 (free parameter) is the position of the CCD on the optical rail. The resulting values for x_0 as well as for χ^2/NDF are also shown. Note, that the vertical error bars are generally smaller than the extension of the marker and thus not visible.

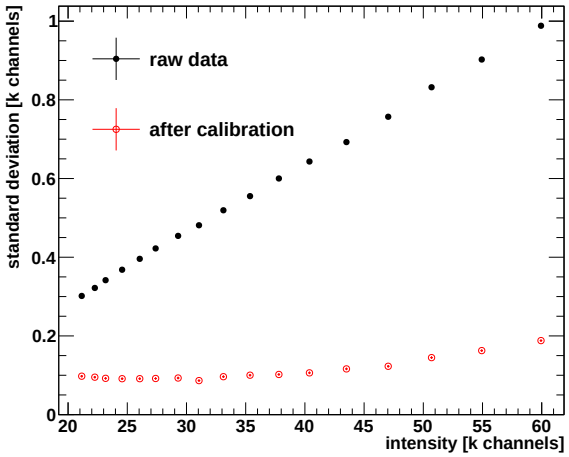

Figure 8.11: The standard deviation of the intensity distributions of all non-hot pixels of the CCD as a function of the overall mean intensity for the raw data and after calibration using the data shown in figure 8.10.

angle of incidence of the light and compared to the predictions by the Fresnel-formulas. Additionally the transmission of two successive polarizers was measured as a function of the angle between the polarization directions and again the results were compared to the predictions. In both cases, no significant deviation from the predictions and thus no deviation from linearity of the CCD could be found.

Pixel-by-pixel gain calibration:
Figure 8.11 shows the standard deviation of the intensities of all CCD pixels (except the hot pixels) as a function of the recorded intensity using the data already shown in figure 8.10. The variation of the intensities is a linear function of the overall mean intensity. Note that this deviation is much higher than expected due to the inhomogeneities of the incident intensity. One explanation for this behavior are small differences between the gains of the different pixels. Thus, to increase the resolution of the CCD, a pixel by pixel gain correction factor c_{ij} is introduced. Hence, the calibrated intensity I^c_{ij} reads

$$I^c_{ij} = c_{ij} I_{ij}, \tag{8.6}$$

where the indices i and j denote the line and the column number of each pixel. To determine c_{ij}, equation (8.5) was applied to every pixel:

$$I_{ij}(x, I_{0,ij}) = \frac{I_{0,ij}}{d^2} = \frac{I_{0,ij}}{(x-x_0)^2}. \tag{8.7}$$

For x_0, the value form the global fit was used. By fitting equation (8.7) to the data of every pixel, $I_{0,ij}$ can be determined. Finally, the correction factor can be calculated to be

$$c_{ij} = \frac{\langle I_{0,ij} \rangle}{I_{0,ij}}, \tag{8.8}$$

where $\langle I_{0,ij} \rangle$ is the mean over all $I_{0,ij}$ from pixels which are not tagged as hot. The resulting spread of the recorded pixel intensities as a function of the mean overall intensity after the calibration is also shown in figure 8.11. A significant improvement in comparison to the same data without calibration is found. Therefore, for the remainder of this thesis, the calibrated intensity is used to evaluate the measurements. Note, that the calibration coefficients were determined after dark noise correction (see section 8.2.2)) and thus shall also be applied after dark noise correction.
To make sure that this improvement is not due to the fact that the same data was used for calibration and testing of the calibration, a test was performed where the calibration was done by simply taking the measurement with the highest intensity and defining $c_{ij} = \langle I_{ij} \rangle / I_{ij}$. Even this simple calibration resulted in a significant improvement compared to the raw data for all measurements. However, as the obtained standard deviations are approximately 30 % worse than the standard deviations resulting from the more sophisticated calibration method detailed above, the results presented above are used for the remainder of this chapter.

8.2.2 Determination of the transmission

After the calibration of the CCD, the transmission of the scintillator can be determined from the data obtained with the set-up shown in figure 8.1. To reduce the statistical variations of the intensity measurement, $N_{\text{images}} = 10$ images were taken for each measurement[15]. They are combined by calculating the mean intensity for each pixel:

$$\langle I \rangle_{ij} = \frac{1}{N_{\text{images}}} \sum_{k=1}^{N_{\text{images}}} I_{ij}^{(k)}, \tag{8.9}$$

where $I_{ij}^{(k)}$ is the intensity on the pixel ij recorded in the k^{th} measurement. In a next step, the dark noise is removed. Therefore, directly after measuring the beam intensity, N_{images} additional measurements are performed with the light beam being blocked directly after the precision pin hole. Thus, the final intensity for each pixel after dark noise correction and calibration is given by

$$I_{ij}^{c} = c_{ij} \left[\langle I \rangle_{ij}^{\text{light}} - \langle I \rangle_{ij}^{\text{dark}} \right], \tag{8.10}$$

where the superscripts "light" and "dark" denote the measurements with normal and with blocked beam, respectively. Finally, the intensity I attributed to a measurement is the mean of the dark noise corrected and calibrated intensity of all pixels, which are not tagged as hot:

$$I = \frac{1}{N_{\text{active pixels}}} \sum_{ij}^{N_{\text{active pixels}}} I_{ij}^{c}, \tag{8.11}$$

[15] The procedure shown here to reduce the statistical variations of the measurement as well as the removal of the dark noise by means of a measurement without light, were also applied to the CCD calibration measurements.

where a pixel is called "active" if it is not tagged as hot and $N_{\text{active pixels}}$ is the number of active pixels.

Finally, the measured transmission T^m is given by

$$T^m = \frac{I_{\text{full}}}{I_{\text{empty}}}, \tag{8.12}$$

where the indices "full" and "empty" denote the measurement performed with the full and the empty tube, respectively.
The statistical error of the measurement is determined by calculating the error of the mean intensity $I_{\text{full,empty}}$ from the spread of the intensities of the individual pixels. As $I_{\text{empty}} \gtrsim I_{\text{full}}$, the statistical error of T^m can be calculated by Gaussian error propagation[16].

8.2.3 Systematic errors

For the measurements with the improved set-up, the same types of systematic errors have to be taken into account which have already been discussed in section 7.3.4.
As the same tube system is used, the error of the length is still the same as in section 7.3.4: $\Delta l^{\text{syst}} = 0.5\,\text{cm}$. For the same reason, also the statement made in section 7.3.3 that scattering has a negligible influence on the resulting attenuation length still holds.

To determine the systematic error of the transmission ΔT^{syst}, a different approach is chosen compared to section 7.3.4: The transmission of a LAB-filled 5 m tube is measured four times following the full measurement protocol for each measurement. Thus, every measurement includes the filling of the tube, the two days of thermalization time, the measurement with the full tube, the removal of the scintillator from the tube, the cleaning of the tube windows and finally the measurement with the emptied tube. The spread of these measurements

$$\Delta T_{\text{syst}} = (0.39 \pm 0.20)\,\% \tag{8.13}$$

is used as a measure for the systematic error, conservatively neglecting the influence of the statistical errors. As the influence of the systematic errors should be maximal for a 5 m tube, this value was conservatively adopted as the systematic errors for all lengths. Comparing this systematic error to the systematic errors obtained in section 7.3.4 for the PMT based experiment, an improvement of nearly one order of magnitude is found. To ensure that this very good result is not due to the low number of measurements, the bottom-up approach from section 7.3.4 was repeated to cross check the result obtained above:

First the **time instabilities** were investigated by measuring the intensity[17] at the end of an empty 5 m tube regularly over a period of 18 h. The resulting relative deviations

[16] As the glass-air transmission is lower than the glass-scintillator transmission, $I_{\text{empty}} > I_{\text{full}}$ can be violated in a very clean scintillator where situations up to $I_{\text{full}} \approx 1.09 I_{\text{empty}}$ can be possible (see section 7.3.5). Even for this extreme scenario, Gaussian error propagation is well applicable.

[17] As the measurement system is conducting the measurements automatically, no dark measurements could be obtained for every measurement. Thus, all measurements were corrected with respect to a dark measurement taken prior to the long-term measurement.

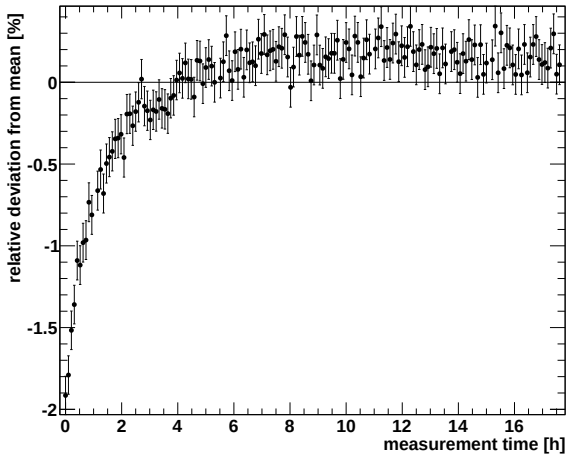

Figure 8.12: The relative deviation from the mean intensity of all measurements as a function of the time of the measurement since the first measurement. The data shown was obtained during an 18 h long-term measurement with an empty 5 m tube.

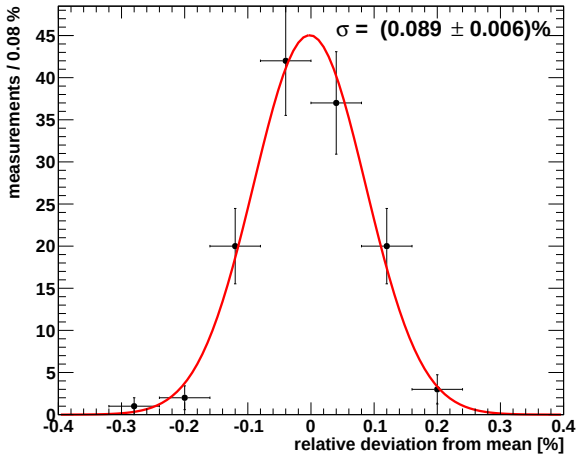

Figure 8.13: The distribution of the relative deviations of the long-term measurement shown in figure 8.12 for measurement times above 4 h. The red curve shows the result of a Gaussian fit to the data. The resulting standard deviation of the fitted Gaussian is also shown.

from the mean intensity are shown in figure 8.12 as a function of the time since the long-term measurement was started. After a warm-up period of about 4 h a very stable measurement condition was reached. As it is important to reach this high stability in each measurement, the halogen light bulb was switched on at least 4 h prior to each measurement. Figure 8.13 shows the distribution of the obtained intensities for measurement times above 4 h. Fitting the obtained distribution with a Gaussian function shows that the obtained distribution can be assumed to follow a Gaussian with a width of

$$\left(\frac{\Delta I}{I}\right) = (0.089 \pm 0.006)\,\%. \tag{8.14}$$

Comparing this result to the result obtained in section 7.3.4 shows that the time stability of the system has increased by more than an order of magnitude even though the initial intensity of the beam is not monitored in the new set-up.

To assess the effect of the **window cleaning**, five measurements were conducted with an empty 5 m tube. Between each of the five measurements, both windows were dismounted, cleaned the same way as in the measurements with the scintillator and remounted again. Again conservatively neglecting the statistical errors, the mean relative deviation of the intensity after the tube due to the window cleaning procedure was found to be $(0.26 \pm 0.08)\,\%$. Comparing this value to the value obtained for the old set-up in section 7.3.4, again a strong reduction of the error is found, showing that the majority of the effect of the window cleaning is not due to a changed transmission of the window itself but due to the change in the optical parameters which leads to a deflection of the beam that in turn results in an error if the detector response is not homogeneous enough over its surface.

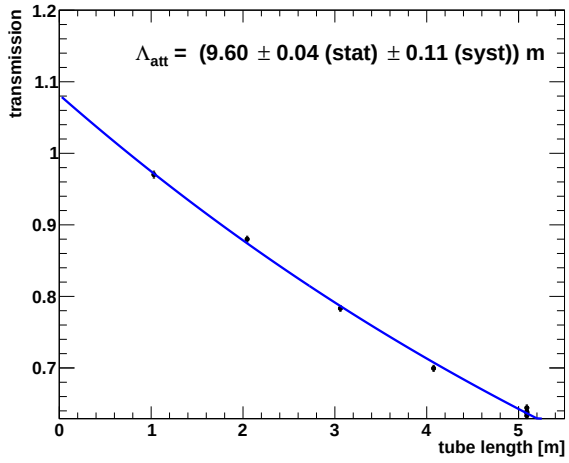

Figure 8.14: The measured transmission as a function of the tube length. The blue line shows $T(d_i, C, \Lambda_{\text{att}})$ (see equation (8.3)) using the parameters resulting from the final fit as input parameters. The attenuation length Λ_{att} resulting from the fit is indicated in the plot. The error bars show the total error of each measurement as determined from the quadratic addition of statistical and systematic error.

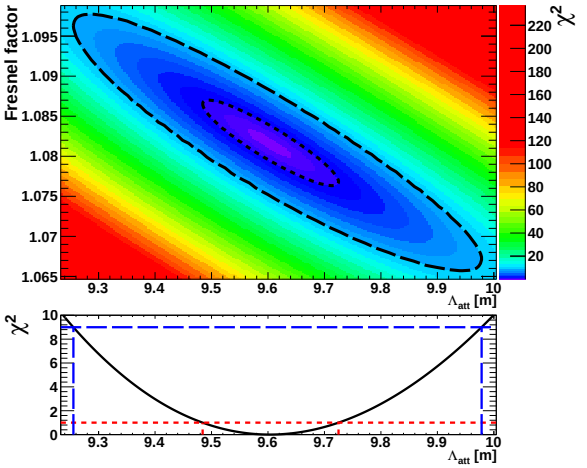

Figure 8.15: The obtained χ^2 as a function of the Fresnel factor and the attenuation length Λ_{att} (top) with the nuisance parameters being profiled out. The short and the long dashed lines show the 1 σ and 3 σ regions (one parameter boundaries), respectively. One color is 0.3 σ wide. The panel below shows χ^2 as a function of Λ_{att} with all other parameters being profiled out. The red and blue dashed lines indicate the 1 σ and 3 σ regions of Λ_{att}, respectively.

Combining the errors of the window cleaning and of the time instability, the relative error of the transmission is expected to be $(0.35 \pm 0.08)\,\%$. As the transmissions are of order 1, this is well compatible with the value determined above, showing that the improvement in the systematic error is due to both, to an improvement of the stability of the measurement in time and due to a reduced susceptibility of the system to the changes in the optical system caused by the window cleaning procedure.

8.3 Result

Using the systematic errors discussed in section 8.2.3 and the fitting procedure presented in section 7.3.5, the attenuation length for the used LAB sample can be determined from the data. Figure 8.14 shows the obtained data together with the prediction for the transmission resulting from the best-fit values. Figure 8.15 shows the corresponding χ^2-function as a function of the Fresnel factor C and the attenuation length Λ_{att}. All other parameters have been profiled out. The final result of the experiment is

$$\Lambda_{\text{att}} = (9.60 \pm 0.04(\text{stat}) \pm 0.11(\text{syst}))\,\text{m} \quad (8.15)$$

$$C = 1.082 \pm 0.002(\text{stat}) \pm 0.005(\text{syst}). \quad (8.16)$$

In section 7.3.5 the Fresnel factor was estimated to be $C \sim 1.9$. While there was a slight tension between and the estimated value for C and the value measured in the first version

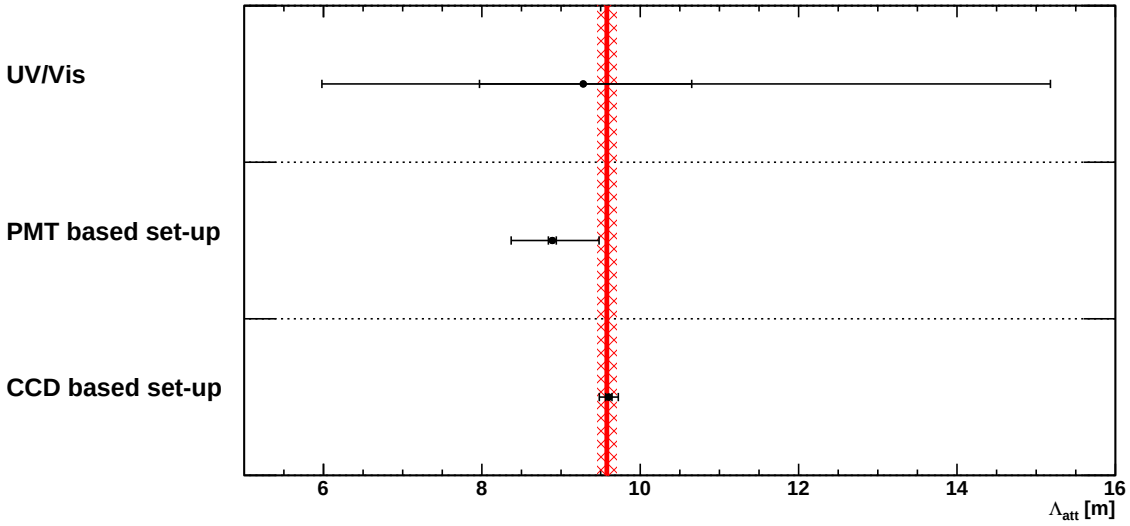

Figure 8.16: A compilation of all available results for the attenuation length Λ_{att} of the measured LAB sample at a wavelength of 430 nm with the inner error bars showing the statistical errors and the outer error bars showing the total errors. The red line indicates the global best fit value and the red-crossed area the corresponding error of the global best fit. Note, that no correlations were taken into account when combining the experiments. The UV/Vis result corresponds to the measurement shown in section 7.1.3, the PMT based set-up is the result presented in section 7.3.5 while the CCD based set-up corresponds to the result presented in this section.

of the experiment (see section 7.3.5), this tension is resolved by the results presented in this section: The obtained Fresnel factor is well compatible to the estimation of C. Figure 8.16 shows an overview of all measurements performed in the present thesis on the same LAB sample along with the global mean of all measurements. While the UV/Vis measurement presented in section 7.1.3 is compatible with both measurements due to its huge errors, the two measurements using the long tube show a slight disagreement at the $1.2\,\sigma$ level. Due to the low significance of the disagreement, the most probable reason for the deviation is that it is just caused by a statistical fluctuation.

With the attenuation length given in equation (8.15) and the scattering lengths already being measured in [123] ($\Lambda_{\text{scat}} = (25 \pm 1.9(\text{stat}) \pm 1.6(\text{syst}))$ m), the absorption length can be calculated using equation (7.4) resulting in

$$\Lambda_{\text{abs}} = (15.6 \pm 0.8(\text{stat}) \pm 0.9(\text{syst}))\,\text{m}. \tag{8.17}$$

8.4 Applicability of the measured LAB for the next generation of liquid-scintillator detectors

The next step is to determine the applicability of the LAB measured in the present thesis for the planned next generation of experiments, i.e., the LENA detector (see section 8.4.1) and the JUNO experiment (see section 8.4.2). The discussion will be based on the assumption that the addition of fluors to the LAB will not affect the attenuation length at 430 nm which is a good assumption for the obtained attenuation length [65] of $\Lambda_{\text{att}} = 9.6$ m. For

attenuation lengths of order 20 m, however, a much cleaner solvent (i.e., a much cleaner LAB) is required. Thus, even though the optical scattering and absorption effects induced by the fluors are suppressed by the small concentration of the fluors, they may significantly contribute to the total attenuation of the light. Thus, the influence of the fluors on attenuation lengths of order 20 m will have to be examined in the future.

8.4.1 LENA

The LENA detector, which is presented in detail in chapter 3, has only relatively modest requirements on the attenuation length: The baseline design foresees an attenuation length between 10 m and 20 m [57] and the simulation used to determine LENA's physics potential - by default - assumes $\Lambda_{\mathrm{att}}^{\mathrm{sim}} = 10.9\,\mathrm{m}$.
Therefore, the measured $\Lambda_{\mathrm{att}} = 9.6\,\mathrm{m}$ is already quite close to the requirements of the detector. Using the LENA MC-simulation, the number of observed photo-electrons for events featuring electrons with a kinetic energy of $T = 1\,\mathrm{MeV}$ can be determined as a function of the attenuation length (see figure 7.1). Thus, the difference between the default performance of the LENA simulation and the performance expected from the measured scintillator can be estimated:
Considering a full fiducial volume[18] of 13.5 m radius, the number of obtained photo-electrons is reduced by about 16 % (about 17 % for the 9 m radius fiducial volume). This means that using the measured scintillator in LENA would degrade the attainable energy resolution by about 10 %. On the other hand, using a better scintillator with an attenuation length of about 20 m would allow to increase the attainable energy resolution by about 30 %. Applied to the end point of the electron-recoil spectrum caused by interactions of ^{7}B-neutrinos at 665 keV [110], the measured scintillator would result in a relative energy resolution[19] of 7.8 %, the default scintillator ($\Lambda_{\mathrm{att}}^{\mathrm{sim}} = 10.9\,\mathrm{m}$) from the simulation would yield 7.1 % and a scintillator with 20 m attenuation length results in 5 % relative energy resolution. Thus, while the measured scintillator and the scintillator used per default in the simulation produce relatively similar results, a significant increase in performance could be expected from an even cleaner scintillator.

8.4.2 JUNO

For the JUNO experiment (see section 2.3.3), the requirements for the transparency of the scintillator are much more stringent compared to the LENA experiment due to the different geometry and the required excellent energy resolution. In [6] it is stated that the attenuation length of the scintillator has to be more than 24 m. Obviously, this requirement is not fulfilled by the measured scintillator. While there exist measurements [151] which state that some scintillators feature attenuation lengths of about 15 m as delivered from the company, this is still not good enough for JUNO. Thus, the scintillator has to be optically purified. Currently, the most promising possibility to enhance the transparency of the scintillator is by column purification using Al_2O_3 as packing material. In this method, the scintillator passes through a column which is filled with Al_2O_3 that absorbs

[18] Using the full 14 m-radius cylinder of the detector as fiducial volume does not work as no reliable energy and position reconstruction can be performed for events with a distance to the wall smaller than 0.5 m, see section 4.5.1 and [41].

[19] Here the values from the 9 m fiducial volume are used.

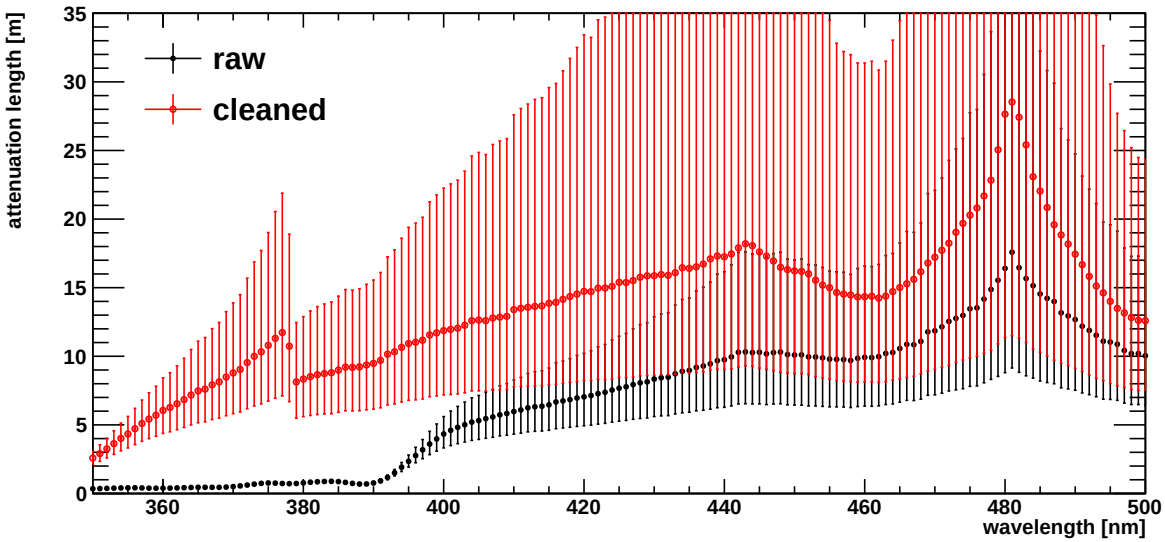

Figure 8.17: Comparison of the attenuation lengths as a function of the wavelength obtained in the LAB sample measured in this experiment and in the same sample after passing the scintillator through 50 g of acid Al_2O_3 with 90 Å pore size. The measurement was done by S. Prummer [152] using a Perkin Elmer LAMBDA 850 UV/Vis-spectrometer with a 10 cm cuvette. The step in the attenuation length of the cleaned measurement around 377 nm is due to an experimental artifact of the used spectrometer which switches between two lamps used as light sources at this wavelength.

some of the scintillators' impurities thus increasing its transparency. Figure 8.17 shows a comparison of the attenuation lengths of the investigated sample in its raw state and after Al_2O_3-column purification. A significant improvement of the attenuation length can be observed over the whole wavelength region. The plan for the JUNO scintillator is to apply Al_2O_3-column purification to the scintillator which already features a good attenuation length in its raw state to obtain the required attenuation lengths. Additionally, the purification effect of Al_2O_3 can be increased by passing the scintillator successively through different kinds of Al_2O_3 [152].

8.5 Planned upgrades

The set-up presented in chapter 8 is a major improvement compared to the set-up described in chapter 7 as the obtained resolution is now adequate for the needs of the next generation of LSc experiments. However, the practical usability of the set-up to develop new scintillators as well as to study methods for scintillator purification is limited due to multiple factors:

- It takes three days to measure one transmission for a given length: Two days of thermal stabilization and another day for the measurement and the required construction works to change to the next length of the modular-tube. Thus, the whole experiment takes up to one month. The long measurement times make a fast prototyping of scintillator purification methods difficult.

- The fact that the scintillator tube has to be opened includes the danger of polluting the LSc sample. A set-up where this is not the case would be preferable.

- One measurement requires 24 l of LSc: 12 l for the initial flushing of the experiment to remove residual impurities from the previously measured LSc and the same amount for the actual measurement run. In comparison, the typical amount of scintillator which can be purified with the current purification set-up in one go is ∼200 ml [152]. Hence, a production of a sample with a sufficient size to be characterized with the experiment is very time consuming. Additionally, the amount of packaging material which can be used in the current purification set-up is $\lesssim$100 g which is not enough to ensure constant purification properties during the production of a 32 l sample [152]. Thus, an experiment with a significantly reduced sample size would be beneficial.

- Currently, the attenuation length is measured at a wavelength of ∼430 nm. While the wavelength filter can of course be changed, the measurement at the next wavelength would take an additional month. Additionally, due to the used optics, only wavelengths above ∼390 nm can be measured due to the lacking UV-transmission of the optical components. A measurement in the UV would be highly desirable as it would allow to compare the results with those of the UV/Vis-spectrometer in the UV wavelength region where it still provides accurate results due to the lower attenuation lengths in this wavelength region. Thus, a set-up with a higher wavelength flexibility would be preferable.

To solve this issues, a new set-up, which is depicted in figure 8.18, was designed together with A. Ulrich [148] and S. Prummer [152]. It is currently being set-up by S. Prummer. Instead of a nearly horizontal tube, the new set-up features a vertical tube as inspired by [151, 153]. Thus, the distance the light beam travels through the scintillator can be changed by altering the liquid scintillator level in the tube without mechanical modifications of the set-up. This is technically realized by a fluid tank which can be moved vertically and which is connected to the tube. The current liquid level is determined by two pressure sensors measuring the liquid pressure P_{F} at the bottom of the tube and the gas pressure P_{G} at the top of the tube. To reduce the required amount of fluid, a thinner tube without apertures is used. To suppress the scattered light, an additional tube is mounted above the scintillator tube which features apertures. Additionally, the tube is of course blackened and passivated using the INOX-SPECTRAL [127] method. Using the Geant4-based simulation already presented in section 7.3.3, this new method is found to feature an increased suppression of scattered light by a factor of two for the high reflectivity assumptions and by more than one order of magnitude for the standard assumptions (see table 7.1). Additionally, the layers of equal refractive index are now perpendicular to the beam direction which significantly reduces their influence on the beam direction. Therefore, the long measurement times due to the required thermalization of the LSc can be significantly reduced. Moreover, as the tube can be kept closed throughout the measurement, no additional nitrogen flushing is required. Thus it should suffice to let the scintillator thermalize once.
Concerning the optics used, the first idea was to use the same optics as in section 8.1.2 with the wavelength filter being removed. Additionally, the CCD detector would have been replaced by the entrance fiber of a spectrometer. Note that as the spectrometer fiber does

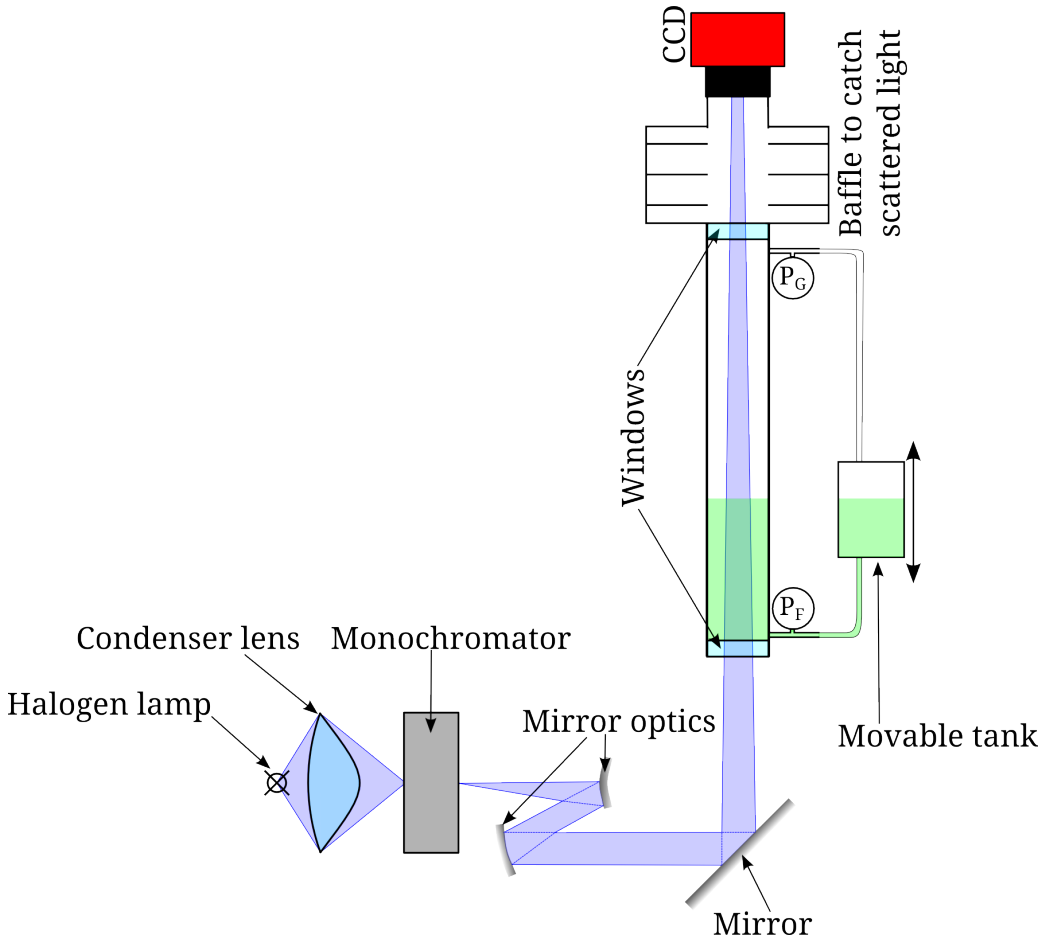

Figure 8.18: Sketch of a possible next generation of the experiment presented in this chapter (not to scale). Here, the 5 m tube is oriented vertically and the distance the light beam travels through the scintillator can be adjusted by varying the fluid level which is determined by the position of the scintillator tank. To reduce the amount of fluid required, a thinner tube without apertures is used. Thus, an additional tube with apertures is added after the tube to provide the required suppression of scattered light. The optics are oriented horizontally and the light beam is coupled into the tube by a mirror. To obtain monochromatic light at an adjustable wavelength, a monochromator is used. The imaging is done using mirror optics to provide achromatic imaging down to the UV. The same CCD camera as presented in section 8.1.3 is used as a light detector.

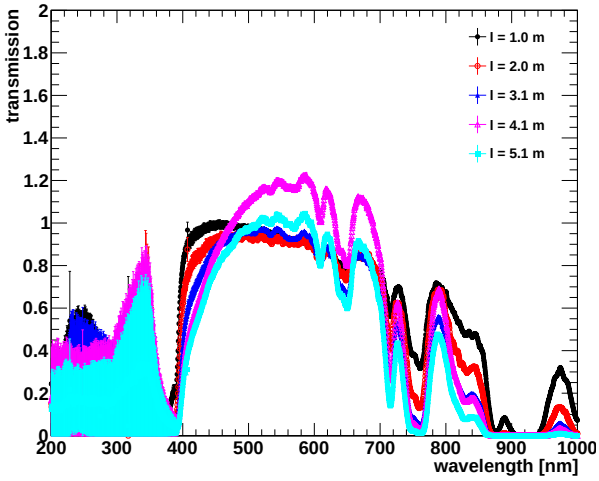

Figure 8.19: The transmission as a function of the wavelength for various tube lengths as determined using an OceanOptics Maya2000 Pro spectrometer as detector instead of the CCD camera. The transmission was normalized to the result presented in section 8.3. Note that the maximum transmission for the 4 m tube is significantly too high and that the ordering of the transmissions changes with wavelength. Possible reasons for this behavior are discussed in the text.

not cover the full beam, a measurement with the CCD and the wavelength filter in place would still be required for an absolute normalization of the intensity. Figure 8.19 shows the result of a measurement conducted using the set-up presented in section 8.1 and a spectrometer[20] as light detector. The resulting transmissions are unphysical in two ways: First, between 500 nm and 600 nm, the transmission resulting from the measurement with a 4 m tube features a transmission which is significantly above the maximum possible transmission $C \approx 1.09$. This odd feature was reproduced in multiple measurements which also featured other measurements in between, i.e., between two of the conducted measurements the tube was assembled for another tube length. Furthermore, the transmissions change their order with changing wavelength. From equation (8.3) the ordering

$$T(1\,\mathrm{m}) \gtrsim T(2\,\mathrm{m}) \gtrsim \ldots \gtrsim T(5\,\mathrm{m}) \tag{8.18}$$

would be expected which is obviously not the case in the 500 to 600 nm region. After extensive investigations which included the linearity of the used spectrometer and the variability of the spectrometer's noise with time, the most probable reason for this defect was concluded to be the the strong dependency of the acceptance of the spectrometer fiber on the angle of the incident light. As the index of refraction of the LSc is greater than one and dependent on the wavelength of the light, this leads to a wavelength-dependent distribution of the angles of incidence of the light and thus to a wavelength-dependent acceptance of the light which leads to the problems mentioned above. Thus, in the vertical set-up, instead of a spectrometer behind the tube, a monochromator is used instead of the wavelength filter to obtain monochromatic light with an adjustable wavelength. To ensure an achromatic behavior of the imaging optics down to the UV a mirror-based imaging system is used. Additionally, the windows of the tube are exchanged for windows

[20] OceanOptics, Maya2000Pro

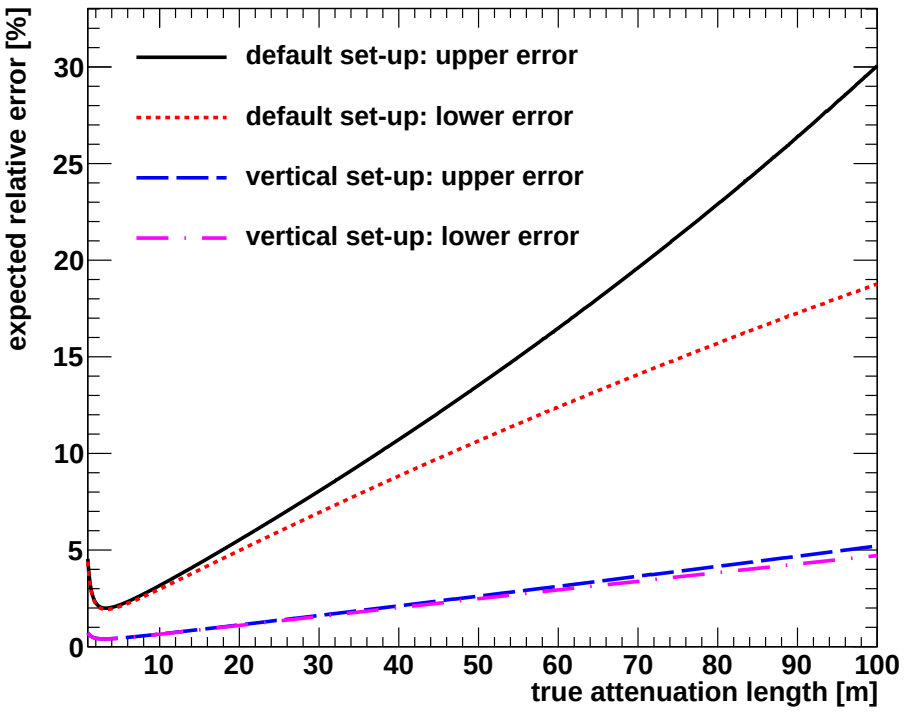

Figure 8.20: The expected relative upper and lower errors as a function of the true attenuation length for the experiment presented in section 8.1 ("default set-up") and for the next generation update presented in this section ("vertical set-up"). Note that the expected relative error is larger than the error on the result shown in equation (8.15) as the simulation assumes only one measurement per available tube length while two measurements for each length were preformed in the measurement presented in chapter 8.

made from quartz glass to ensure sufficient transmission for wavelengths below 330 nm which is difficult with normal glass (see figure 7.6). The light detection is still done with the CCD camera presented in section 8.1.3.

While the design of the new set-up is mainly driven by practical concerns, the new design also reduces the systematic errors as no more window cleaning will be required during the measurements. Thus, in the best case, the systematic errors can be reduced to the uncertainty in time (see section 8.2.3). For this optimistic case, the expected relative errors as a function of the true attenuation length are shown in figure 8.20 assuming a measurement at 10 different light paths in the scintillator. They were computed using the Asimov data-set [154] for each true attenuation length after validating the results at one attenuation length using a full MC to generate the data. For comparison, the errors expected using the set-up presented in section 8.1 are additionally shown. The superior performance of the new set-up is clearly visible.
Thus, the next generation of the set-up will provide faster measurements at multiple wavelengths and a continuously adjustable light path length in the scintillator with a smaller error at a reduced sample-volume. It therefore will constitute a good tool to study the effects of scintillator cleaning and to develop new high-performance scintillators.

8.6 Importance of the obtained accuracy for the next generation of liquid-scintillator based neutrino detectors

The attenuation length of $\Lambda_{\mathrm{att}} = (9.60 \pm 0.04(\mathrm{stat}) \pm 0.11(\mathrm{syst}))\,\mathrm{m}$, which was determined with the current system, is insufficient for the next generation of neutrino detectors (see section 8.4). On the other hand, it was shown that the set-up allows to measure this attenuation length with an accuracy of 1.2 %.
This high accuracy is required by the next generation of liquid-scintillator based neutrino experiments especially for two tasks:

- As already discussed in section 8.4, the best scintillators provided by the manufacturers feature an attenuation length of ∼15 m. Thus, purification procedures, like Al_2O_3 column purification, need to be developed to improve the optical properties of the LSc for wavelengths around 430 nm, which are most relevant for the photon transport in LScs. Typically, this is done using an UV/Vis-spectrometer to characterize the optical properties of the scintillator before and after purification. However, the resolution of an UV/Vis-spectrometer is not sufficient to resolve the effect of the purification in the relevant wavelength region. Thus, often the performance of purification methods is assessed by looking at the purification effect at lower wavelengths which feature a lower attenuation length that can be precisely measured by the UV/Vis. However, recent measurements have shown that the purification effect strongly depends on the photon wavelength [152]. Thus, a method to precisely measure the attenuation length of purified scintillators around 430 nm is mandatory for the successful development of purification methods.

- When a detector is built, it has to be filled with LSc prior to data-taking. As removing the scintillator from the detector is difficult, expensive and time consuming it should be avoided. Thus, a quality control of the scintillator is necessary before it enters the detector to exclude contamination of the scintillator. Checking the optical properties of the scintillator, including the attenuation length, is a major part of this quality control. Thus, a high precision measurement of the attenuation length is required for quality control of the scintillator prior to filling.

For the experiment presented in chapter 8, the expected relative resolution in attenuation length is plotted as a function of the true attenuation length in figure 8.20. It would allow to measure a scintillator with an attenuation length of 24 m, which is the projected goal for the JUNO-LSc, at a precision of 6.5% (corresponding to about 1.6 m) which is sufficient for scintillator development and quality assurance. If the upgrade of the experiment (see section 8.5) works as expected, the resolution at an attenuation length of 24 m will even be reduced to 1.2 %, corresponding to about 0.3 m.

Chapter 9

Conclusions

This work is focused on preparative work that is required to ensure the success of the next generation of liquid scintillator (LSc) based neutrino detectors like the planned 20 kt JUNO detector and the proposed 50 kt LENA detector. The first part covers the development of algorithms used to reconstruct the event properties in LENA from the observed light signal at the photomultiplier tubes (PMTs). As the photons produced in the LSc have to reach the PMTs, the second part of this thesis deals with measuring the transparency of LScs.

9.1 Event reconstruction

The work to reconstruct events is split up into three parts. In a first step, events with deposited energies in the MeV regime (e.g., caused by interactions from geo-neutrinos or astrophysical neutrinos), which is the energy region the detectors are designed for, are reconstructed. In the next step, the algorithms are extended to cover single lepton tracks. In a final step, the events resulting from neutrino interactions at the GeV scale, as e.g., caused by atmospheric neutrinos or neutrinos from a neutrino beam, are dealt with. As LENA does not exist yet, the performance of these algorithms is evaluated using events obtained from a Monte Carlo (MC) simulation [41] based on the Geant4 libraries [102, 103].

Reconstruction of MeV events:
Interaction of (anti-)neutrinos with energies in the MeV range typically produce electrons or positrons in the same energy range. The range of these particles is generally below $\sim$1 cm which can be considered to be point-like with respect to the position resolution of the detector ($\sim$10 cm). Thus, no directional information can be obtained from these particles. Therefore, an algorithm was developed which allows to determine the position, the kinetic energy and the time of single particle events. It is based on a full likelihood fit to the obtained photon multiplicities and arrival times of the PMTs. The calculation of the required probability density function (PDF) takes into account the light concentrators' acceptance function, scattered light, the dark noise (DN) of the PMTs, the finite size of the light detectors and the transit-time spread (TTS) of the PMTs. The fitting procedure was extended to deal with the multiple minima appearing for events close to the detector boundary.
The performance of the algorithms was tested on single electrons with kinetic energies between 0.2 MeV and 3 MeV, distributed over the fiducial volume of the detector which is

at least 25 m away from the detector end-caps (see section 4.1). The fraction of converged events was found to be nearly 99 % for low-energy events and declines slightly to 97 % for events with a kinetic energy of 3 MeV due to the rising probability for bremsstrahlung emission. For events with a distance to the principal symmetry axis of the detector of less than 10 m, the one-dimensional resolution in the x-y-plane can be well described by $\Delta x = \Delta y = (6.25 \pm 0.12)\,\mathrm{cm}/\sqrt{T_s^{\mathrm{true}}/\mathrm{MeV} - (0.07 \pm 0.06)}$, with T_s^{true} being the true kinetic energy of the event. For events closer to the detector wall, the resolution improves by up to 50 %. In z-direction, the resolution in the detector center increases with rising energy from about 24 cm for 0.2 MeV events to about 6.5 cm for 3 MeV events, but cannot be described by a simple function like the resolution in the x-y-plane. Furthermore, the z-resolution can improve by more than a factor of two when going to higher radii. The start-time resolution is below 0.6 ns for the whole detector over all energies which is sufficient for all applications. It can even go down below 0.14 ns for central 3 MeV events. The relative energy resolution was found to be well described by $\Delta T_s/T_s^{\mathrm{true}} = (6.0 \pm 0.1)\,\%/\sqrt{T_s^{\mathrm{true}}/\mathrm{MeV} - (0.01 \pm 0.06)}$. This is compatible with the relative resolution expected from photon statistics only, demonstrating that the performance of the algorithm has reached its statistical maximum. A significant degradation of all resolutions was found for events with a distance of less than ∼30 cm from the outer cylinder walls, showing that this region of the detector is too inhomogeneous to be properly handled by a reconstruction and thus cannot be used for physics analysis.
Subsequently, the influence of the DN rate f_{DN} on the performance was determined for f_{DN} up to 50 kHz. It was found that the DN only affects events with a kinetic energy below ∼1 MeV. For very low energetic events with T_s ∼0.2 MeV, in contrast, a deterioration of the resolutions of up to a factor of 5 was found. Additionally, to ensure a high robustness of the fit, an advanced detector electronics is required which allows to resolve multiple photon hits on a single PMT.
Moreover, the influence of the TTS on the obtained resolutions was investigated. It was found that using the full TTS from the Borexino PMTs [105] instead of the Gaussian assumption which is generally used in this thesis, decreases the spatial resolutions only by about 2 cm and the time resolution only by about 0.06 ns over the whole energy range. The energy reconstruction is not influenced by the TTS.

Reconstruction of single lepton tracks:
The likelihood fit was subsequently expanded to be able to additionally deal with extended events, which requires to take into account the light-yield of a particle as a function of its distance to the start point. Testing the algorithm with simulated muon events with energies between 0.2 GeV and 1 GeV revealed an one-dimensional vertex resolution of below 10 cm and a start-time resolution below 0.15 ns over the whole energy range. The angular resolution improves with energy from 7 deg down to 1.8 deg with a reconstruction efficiency between 80 % and 98 %. The relative energy resolution was found to be about 1 % for the covered energy range. Some badly reconstructed tracks occur for events being very close to the detector boundary. Additionally, the performance was determined for a set of 0.5 GeV electron events, which are more challenging to reconstruct than muon events due to the higher event by event variations in the energy loss. While the fraction of converged events improved by about 4 % compared to the muon events, it was found that the vertex resolution as well as the time resolution are about 4 to 5 times worse than in the muon case. In contrast, the angular resolution deteriorates by only 50 % compared

to the muon value and basically no difference is visible for the energy reconstruction. For both, the electron and the muon data-set, a significant number of outliers was observed. In case of the muon data-set, they were connected to events which passed close to the wall of the detector. For the electron dataset, a small fraction of events additionally suffered from a very high deviation of the realized from the mean shower profile at a given energy.

Analysis of full neutrino interactions:
The likelihood analysis cannot be applied to full neutrino interactions, due to the high diversity of possible outcomes of such an interaction and due to the missing start parameters, which are required by the used numerical minimization methods. Nevertheless, algorithms were designed to extract basic information from these events which in the future might pave the way to gather enough information to finally be able to do a full fit to the events.
First, a clustering algorithm was developed which splits the high energy neutrino interactions into the primary interaction and the secondary interactions. It was tested on 3400 simulated ν_μ-CC interactions. The resulting total detection efficiency for a muon decay is $(88 \pm 3)\,\%$ for μ^- and $(92.4 \pm 2.5)\,\%$ events for μ^+.
In a next step, the energy response of LENA for high energy neutrino events was determined which is a required input to evaluate the capabilities of LENA as a far detector for a neutrino beam [96].
Furthermore, an algorithm was developed, which allows to visualize the muon event. It was applied to muons passing through Borexino [119] resulting in an angular resolution of $(1.62 \pm 0.10)\,\mathrm{deg}$, which is a significant improvement compared to the established muon reconstruction methods in Borexino ($(2.44 \pm 0.19)\,\mathrm{deg}$ on the same data set). Applying this algorithm to simulated neutrino interactions in LENA, it was possible to determine the vertex of the resulting events with a one-dimensional accuracy of below 10 cm.
By performing a time-of-flight correction with respect to the reconstructed vertex of the interaction, the number and the direction of tracks in the exit channel with a significant length could be determined. This method was tested on simulated high-energy CC neutrino interactions resulting in a good performance of the method for reconstructing primary lepton tracks: For primary lepton energies above 1 GeV this technique allows to identify more than 60 % of all primary electrons and above 95 % of all primary muons.
As ν_e-CC events are the most important signal channel when using LENA as a far detector for a conventional neutrino beam, an attempt was made to obtain new parameters to discriminate between ν_e-CC and ν_x-NC interactions from the results of the developed algorithms. Here, especially the number of secondary clusters and the number of track candidates were found to be promising. By including these parameters in the event discrimination used for LENA [96, 100], there is a good chance to increase the capabilities to determine the mass hierarchy using LENA as a far detector for a neutrino beam (see section 6.6).

9.2 Attenuation-length measurements

The huge sizes of the next generation of neutrino detectors requires very transparent liquids with attenuation lengths of at least 10 m (LENA) and 24 m (JUNO), respectively. To determine the attenuation length of liquid scintillators, an experiment was devised which

allows to measure the drop in intensity of a light beam after transversing a modular tube filled with LSc which has a length between 1 m and 5 m. The wavelength of the light beam is 430 nm which is the most important wavelength for the transport of scintillation light in LSc over distances of order ∼10 m. As scattered light is a background for the attenuation-length measurement, a strong suppression of scattered light is required. Thus, the tube was blackened on the inside and additional apertures were added to the inside of the tube to deflect scattered light. Using a MC simulation, the effect of the scattered light on the determined attenuation length was estimated to be $\lesssim 0.9 \cdot 10^{-3}$ at an attenuation length of 11 m.

PMT based set-up:
In the first version of the experiment, PMTs were used to monitor the intensity of the beam before and after transversing the LSc. The light beam was provided by a pulsed LED which was coupled into a fiber optics. After exiting the fiber optics, the light was subsequently parallelized. To obtain a narrow wavelength spectrum, the light additionally passes a wavelength filter. As a main obstacle of measuring the attenuation length, thermal layers in the nearly horizontal tube were identified. They cause a gradient in refractive index which deflects the beam and thus disturbs the measurement. Hence, a thermalisation time of two days was required prior to each measurement. Using this set-up, the attenuation length of the measured LAB sample was determined to be $\Lambda_{\text{att}} = (8.89 \pm 0.05(\text{stat})^{+0.59}_{-0.53}(\text{syst}))\,\text{m}$.
By evaluating the time shift of the detected light as a function of the distance the light travels through the scintillator, the speed of light in LAB could be evaluated to be

$$c_{\text{LAB}} = (1.88 \pm 0.06(\text{stat}) \pm 0.11(\text{syst})) \cdot 10^8 \,\frac{\text{m}}{\text{s}}, \tag{9.1}$$

resulting in an effective index of refraction of

$$n_{\text{eff}} = 1.59 \pm 0.05(\text{stat}) \pm 0.10(\text{syst}). \tag{9.2}$$

CCD based set-up:
The large systematic error of the attenuation length as determined with the PMT-based set-up rooted in a lacking time stability and a high variability of the observed transmission after cleaning the window which is positioned at the entrance of the tube containing the LSc. As these problems are believed to be mainly due to the high variability of the PMT's quantum efficiency over its surface, the unstable light source and the bad beam-quality, a new set-up was devised. In this set-up, the light was detected by a 8.4 MPixel temperature-stabilized CCD-camera mounted at the end of the tube. Intensive investigations confirmed the high uniformity and the high linearity of this device. Due to the small active size of the CCD, a new optical system was set up which imaged a precision pinhole, illuminated by a halogen light bulb, directly on the CCD. To achieve monochromatic light, a bandpass wavelength filter was used. With a variation of the transmission of the empty 5 m tube of less than 10^{-3} over 14 h of measurement time, the set-up was found to be more than one order of magnitude more stable than the PMT-based set-up. Additionally, the influence of the window cleaning was reduced by a factor of ∼5. With the improved set-up, the attenuation length of the same LAB sample was determined to be

$$\Lambda_{\text{att}} = (9.60 \pm 0.04(\text{stat}) \pm 0.11(\text{syst}))\,\text{m}. \tag{9.3}$$

Using the scattering lengths determined in [123], this corresponds to an absorption length of

$$\Lambda_{\mathrm{abs}} = (15.6 \pm 0.8(\mathrm{stat}) \pm 0.9(\mathrm{syst}))\,\mathrm{m}. \tag{9.4}$$

The measured attenuation length makes the measured, uncleaned LAB definitely not suitable for the JUNO detector and only marginally usable for LENA, even without taking a possible degradation of the attenuation length in a full scintillator due to added fluors into account (see section 8.4). Thus, a purification of the scintillator to improve its optical properties is necessary. A promising possibility is column-purification using Al_2O_3 as packing material, which was found to greatly improve the attenuation length of LAB [152].
Using the obtained result, the expected accuracy of the experiment for larger attenuation lengths was determined: At an attenuation length of $\Lambda_{\mathrm{att}} = 24\,\mathrm{m}$, which is required for JUNO, the experiment described in this thesis will still feature an accuracy in attenuation length of about 6.5 %. Thus, the accuracy achieved with the experiment is sufficient for the requirements of both next-generation detectors.
However, one measurement takes about one month which makes it very cumbersome to be used in scintillator development. Thus, based on the experiences with the current set-up, the next generation of the set-up is currently under construction (see section 8.5). Its main improvement is a vertical tube which will allow the experimenter to continuously change the distance the light travels through the LSc. Additionally, this will make modifications of the tube during the measurement unnecessary and thus further reduce the systematic errors: With the next-generation experiment, the expected accuracy at an attenuation length of 24 m will be improved to 1.2 %. Moreover, a monochromator will be used instead of the wavelength filter to be able to easily change the wavelength.
Hence, this new set-up will provide faster measurements at multiple wavelengths and a continuously adjustable light path in the scintillator with a smaller error. It therefore will constitute an important tool to study the effects of scintillator cleaning and to develop new high-performance scintillators.

Appendix A

Calculation of atmospheric neutrino rates

The doubly differential interaction rate $R_\nu^\alpha(E_\nu, \cos(\vartheta_\nu))$ of atmospheric neutrinos of flavor α with energy E_ν and angle ϑ_v with respect to the z-axis in LENA is given by

$$R_\nu^\alpha(E_\nu, \cos(\vartheta_\nu) = \sum_{\beta \in e,\mu,\tau} \sigma_\nu^\alpha(E_\nu) \cdot \Phi_0^\beta(E_\nu) \cdot P_{\nu_\beta \to \nu_\alpha}(E_\nu, \cos(\vartheta_\nu)) \frac{m_T}{m_n} \tag{A.1}$$

where $\sigma_\nu^\alpha(E_\nu)$ is the total CC cross section per target nucleon for ν_α which was extracted from GENIE [42], $\Phi_0^\beta(E_\nu)$ is the unoscillated atmospheric ν_β flux [1] taken from [155], $m_T = 50\,\mathrm{kt}$ is the target mass and m_n is the mass of a nucleon. Finally, the oscillation probability $P_{\nu_\beta \to \nu_\alpha}(E_\nu, \cos(\vartheta_\nu))$ was calculated with the GLoBES library [31, 32] using the PREM model of the earth to model the density in the earth [33, 34]. As it is impossible to discriminate ν from $\bar{\nu}$ on an event by event basis, given the detector is not magnetized, the relevant quantity in the detector is

$$R^\alpha = R_\nu^\alpha + R_{\bar{\nu}}^\alpha. \tag{A.2}$$

The result for muon neutrinos can be seen in figure 3.5.
The doubly differential rate including detector effects $R_d^\alpha(E_d, \cos(\vartheta_d))$ is given by:

$$\begin{aligned} R_d^\alpha(E_d, \cos(\vartheta_d)) &= \int_0^\infty dE_\nu \int_{-1}^{1} d\cos(\vartheta_\nu)\ R_\nu^\alpha(E_\nu, \cos(\vartheta_\nu)) \cdot \\ &\cdot \quad \epsilon^\alpha(E_\nu, \cos(\vartheta_\nu)) \cdot P(E_d, \cos(\vartheta_d) | E_\nu, \cos(\vartheta_\nu)) \end{aligned} \tag{A.3}$$

where $\epsilon^\alpha(E_\nu, \cos(\vartheta_\nu)) \in [0, 1]$ is the efficiency to detect a neutrino with energy E_ν and angle ϑ_ν and $P(E_d, \cos(\vartheta_d) | E_\nu, \cos(\vartheta_\nu))$ is the detector response function, i.e. the probability density function to reconstruct a neutrino with properties $E_d, \cos(\vartheta_d)$ given the incident neutrino featured the parameters $(E_\nu, \cos(\vartheta_\nu))$. Note, that any kinds of misidentification of events is not accounted for in this calculation.

[1] The flux given in [155] is for the Super Kamiokande location. In principle, it has to be adjusted to the different latitude of Pyhäsalmi. As this just represents an initial rough study and as full calculations for Pyhäsalmi are done [156] but not yet available, this was not done here. Thus, the atmospheric neutrino flux might be about a factor of two too low.

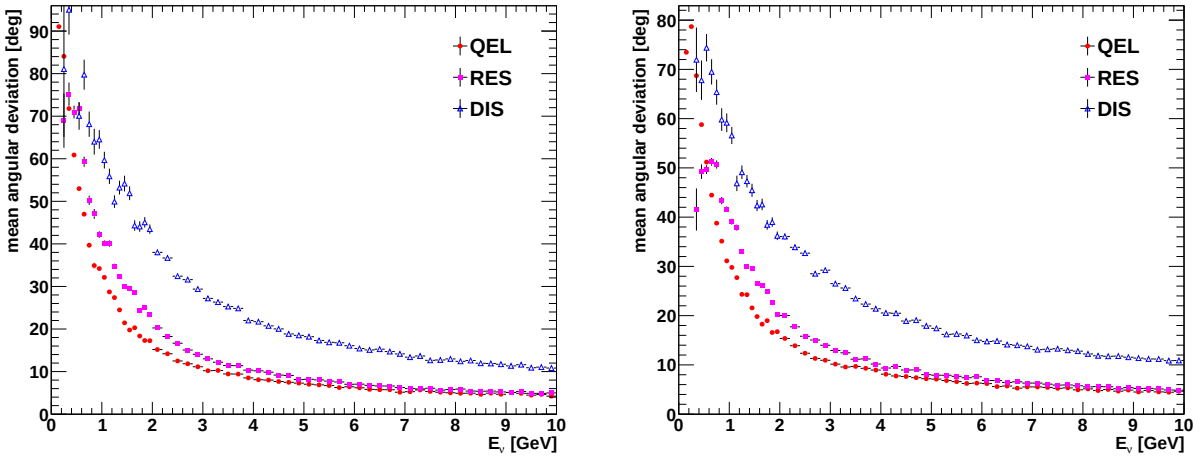

Figure A.1: Mean angle between the neutrino momentum and the momentum of the primary lepton as a function of the energy split up in the different interaction types for ν_e (left) and ν_μ (right).

As the detector response to atmospheric neutrinos is not known, a few assumptions were made to come up with a detector response function. First of all, for an initial glimpse, all efficiencies were treated to be one: $\epsilon^\alpha(E_\nu, \cos(\vartheta_\nu)) = 1$. Given that the real efficiencies for beam events are typically about 30% this will overestimate the detected rate. The energy resolution was assumed to be Gaussian, taking the RMS of the beam events as resolution: $\Delta E/E = 8\%$ (confer section 6.3). Note that the energy resolution does not depend on the angle of the incident neutrino. To estimate the angular resolution of the detector, the assumption was made that it is dominated by the deviation of the lepton direction and the neutrino direction. Thus, the angular resolution of the detector has been neglected. Therefore, the probability to detect a given angle is independent of the reconstructed neutrino energy. Hence, the detector response function separates:

$$P(E_d, \cos(\vartheta_d)|E_\nu, \cos(\vartheta_\nu)) = P(E_d|E_\nu) \cdot P(\cos(\vartheta_d)|E_\nu, \cos(\vartheta_\nu)). \tag{A.4}$$

To determine the corresponding angular PDF $P(\cos(\vartheta_d)|E_\nu, \cos(\vartheta_\nu))$, neutrino interactions were simulated using the GENIE [42] event generator. The resulting mean deviations as a function of the true neutrino energy is shown in figure A.1. Slices through the final PDF are shown in figure A.2. Note that these distributions significantly deviate from a Gaussian distribution i.e. using a Gaussian distribution is not enough.
The final distributions including detector effects are shown in figure 3.6.

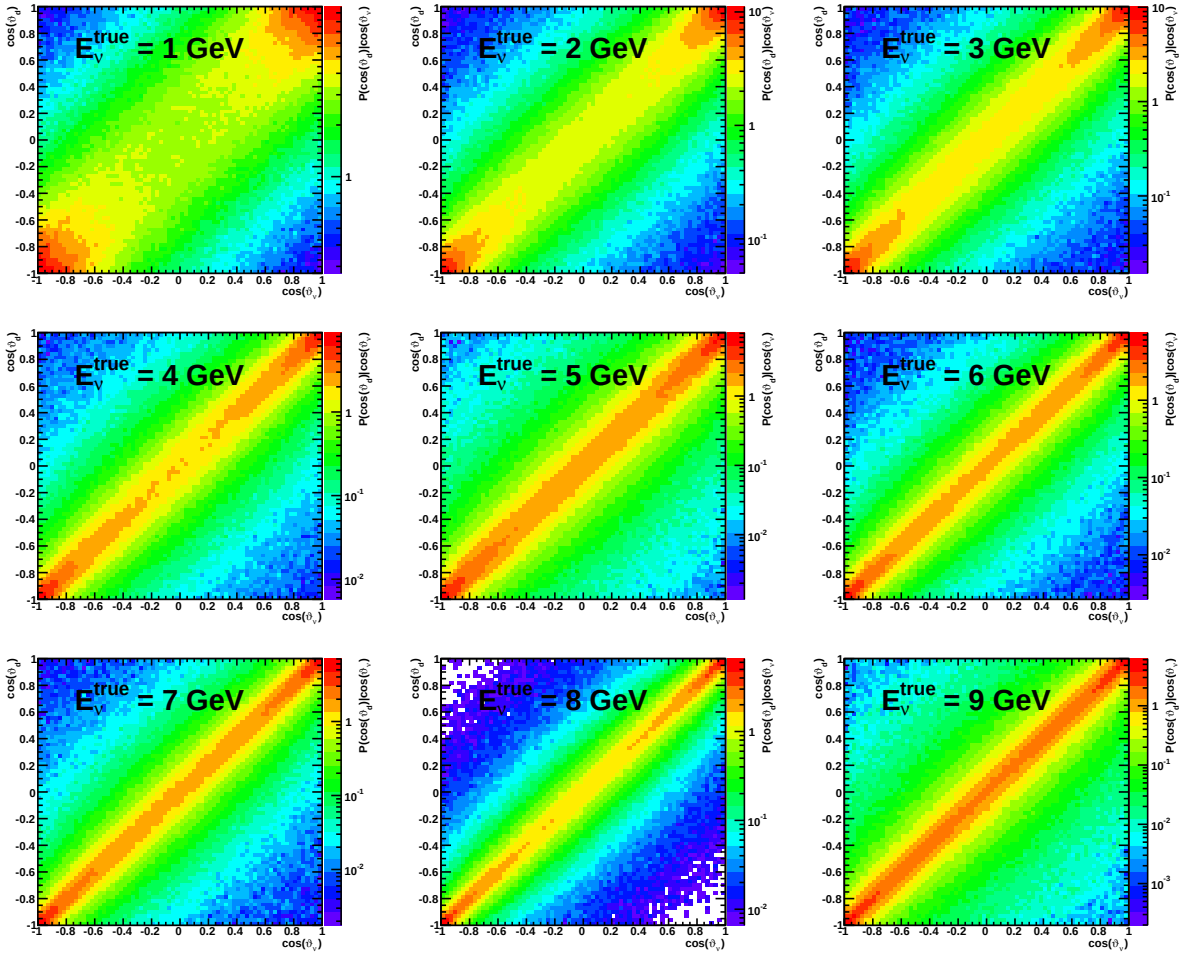

Figure A.2: The PDF $P(\cos(\vartheta_d)|E_\nu, \cos(\vartheta_\nu))$ for various fixed true neutrino energies as indicated in the different plots.

Appendix B

Dimensionality reduction using the full detector geometry

In chapter 4 the dimensionality of the required tables is reduced by exploiting the symmetries of the detector. To reduce the final dimensionality, the only events with $|z| < 25\,\mathrm{m}$ are dealt with to be able to neglect the influence of the end caps. In this chapter, the same reduction is done without this simplification.
Given a function $f(\boldsymbol{r}_s|\boldsymbol{r})$, where r_s is a position inside LENA and r is the position of a PMT, which describes some physics in the detector. An example for such a function is $R(\boldsymbol{r}_s|\boldsymbol{r})$ (see equation (4.31)). As the PMT is confined to the wall of the detector, its position is dependent only on two variables (φ, ξ) where φ is the same angle as used in cylindric coordinates and ξ defines the position of the PMT on the wall:

$$\xi = \begin{cases} z & \text{for PMTs on the sidewall of LENA} \\ \frac{1}{2}h_{\mathrm{LENA}} + \rho_{PMT,wall} - \rho & \text{for PMTs on the top of LENA} \\ -\frac{1}{2}h_{\mathrm{LENA}} - \rho_{PMT,wall} - \rho & \text{for PMTs on the bottom of LENA,} \end{cases} \tag{B.1}$$

where h_{LENA} is the height of the fiducial volume and $\rho_{PMT,wall}$ is the mounting radius of the PMTs on the sidewall of LENA.
Due to the rotational symmetry of LENA around the z axis a, transformation in a coordinate system $s^{(1)}$ with $\varphi^{(1)} = 0$ does not change the physics: $f^{(1)}(\boldsymbol{r}_s^{(1)}, \varphi^{(1)} = 0, \xi^{(1)}) = f(\boldsymbol{r}_s^{(1)}, \varphi^{(1)} = 0, \xi^{(1)})$ which already reduces the dimensionality to from six to four. Note, that in this case $\xi^{(1)} = \xi$.
While it is not possible to reduce the dimensionality of the function any more, the size of the parameter space can be further reduced. Using LENA's symmetry with respect to the x-y-plane, a coordinate system $s^{(2)}$ can be found, with the PMT being in the upper half of LENA: $\xi^{(2)} > 0$. Again, due to the symmetry of LENA, the f is invariant with respect to this transformation. Note, that the second transformation does not change φ: Thus, $\varphi^{(2)} = 0$. Finally, using the mirror symmetry with respect to the x-z plane, the final dependency of f is given by:

$$f(\boldsymbol{r}_s|\boldsymbol{r}) = f(x_s^{(2)}, |y_s^{(2)}|, z_s^{(2)}, \xi^{(2)}). \tag{B.2}$$

Thus, in comparison to chapter 4, one additional dimension is required for the tabulations.

Acronyms

ADC Analog-to-Digital-Converter 132
BDT boosted decision tree 37
Bis-MSB 1,4-Bis(2-methylstyryl)benzen 23
CCD charge-coupled device 152
CNGS **C**ERN **N**eutrinos to **G**ran **S**asso 106
COH Coherent pion production 12
DAQ data acquisition 125
DIS Deep inelastic scattering 12
DN dark noise 42
FEP fluorinated ethylene propylene 129
FFT Fast-Fourier transformation 144
FOM figure of merit 92
FWHM full width at half maximum 130
IH inverted hierarchy 5
JUNO **J**iangmen **U**nderground **N**eutrino **O**bservatory 1
LAB Linear Alkylbenzene 23
LC light concentrator 17
LED light-emitting diode 125
LENA **L**ow **E**nergy **N**eutrino **A**stronomy 1
LNGS Laboratori Nazionali del Gran Sasso 17
LSc liquid scintillator 1
MC Monte Carlo 39
MH mass hierarchy 5
MVA multi variate analysis 37
NH normal hierarchy 5
NLL negative logarithmic likelihood 48
OM optical module 23
PDF probability density function 42

PMT	photomultiplier tube	1
POT	protons on target	116
PPO	2,5-Diphenyloxazole	23
PTFE	polytetrafluorethylen	129
QEL	Quasielastic scattering	11
RES	Resonant pion production	11
ROI	region of interest	111
SM	Standard Model	2
TOF	time of flight	45
TTS	transit-time spread	42
VMEbus	Versa Module Eurocard-bus	132

Bibliography

[1] F. Reines and C. L. Cowan, *Detection of the Free Neutrino*, Phys. Rev. **92**, 830 (1953).

[2] C. L. Cowan, F. Reines, F. B. Harrison, H. W. Kruse and A. D. McGuire, *Detection of the Free Neutrino: a Confirmation*, Science **124**, 103 (1956), [http://www.sciencemag.org/content/124/3212/103.full.pdf].

[3] BOREXINO Collaboration *et al.*, *The Borexino detector at the Laboratori Nazionali del Gran Sasso*, Nuclear Instruments and Methods in Physics Research A **600**, 568 (2009), [0806.2400].

[4] KamLAND Collaboration, K. Eguchi *et al.*, *First results from KamLAND: Evidence for reactor anti-neutrino disappearance*, Phys.Rev.Lett. **90**, 021802 (2003), [hep-ex/0212021].

[5] Super-Kamiokande Collaboration, K. Abe *et al.*, *Solar neutrino results in Super-Kamiokande-III*, Phys.Rev. **D83**, 052010 (2011), [1010.0118].

[6] JUNO Collaboration, JUNO Conceptual Design Report, To be published in 2015.

[7] LENA Collaboration, M. Wurm *et al.*, *The next-generation liquid-scintillator neutrino observatory LENA*, Astropart.Phys. **35**, 685 (2012), [1104.5620].

[8] S. Bilenky, *Neutrino. History of a unique particle*, Eur.Phys.J. **H38**, 345 (2013), [1210.3065].

[9] K. Nakamura and P. D. Group, *Review of Particle Physics*, Journal of Physics G: Nuclear and Particle Physics **37**, 075021 (2010).

[10] Super-Kamiokande Collaboration, Y. Fukuda *et al.*, *Evidence for oscillation of atmospheric neutrinos*, Phys.Rev.Lett. **81**, 1562 (1998), [hep-ex/9807003].

[11] DAYA-BAY Collaboration, F. An *et al.*, *Observation of electron-antineutrino disappearance at Daya Bay*, Phys.Rev.Lett. **108**, 171803 (2012), [1203.1669].

[12] SNO Collaboration, B. Aharmim *et al.*, *Combined Analysis of all Three Phases of Solar Neutrino Data from the Sudbury Neutrino Observatory*, Phys.Rev. **C88**, 025501 (2013), [1109.0763].

[13] T2K Collaboration, K. Abe *et al.*, *Observation of Electron Neutrino Appearance in a Muon Neutrino Beam*, Phys.Rev.Lett. **112**, 061802 (2014), [1311.4750].

[14] J. Kopp, P. A. N. Machado, M. Maltoni and T. Schwetz, *Sterile Neutrino Oscillations: The Global Picture*, JHEP **1305**, 050 (2013), [1303.3011].

[15] M. Gonzalez-Garcia, M. Maltoni, J. Salvado and T. Schwetz, *Global fit to three neutrino mixing: critical look at present precision*, JHEP **1212**, 123 (2012), [1209.3023].

[16] S. Bilenky, *On the phenomenology of neutrino oscillations in vacuum*, 1208.2497.

[17] Particle Data Group, C. Amsler *et al.*, *The Review of Particle Physics*, Phys. Lett. **B667**, 1 (2008).

[18] D. Perkins, *Particle Astrophysics*, 2 ed. (Oxford University Press, 2009).

[19] M. Zralek, *From kaons to neutrinos: Quantum mechanics of particle oscillations*, Acta Phys.Polon. **B29**, 3925 (1998), [hep-ph/9810543].

[20] B. Kayser, Neutrino oscillation phenomenology, in *Neutrinos in particle physics, astrophysics and cosmology*, edited by F. Soler, C. D. Froggatt and M. Franz, , Scottish graduate series No. 61, pp. 51–64, CRC Press, 2009.

[21] Particle Data Group, J. Beringer *et al.*, *Review of Particle Physics (RPP) and 2013 partial update for the 2014 edition*, Phys.Rev. **D86**, 010001 (2012).

[22] S. Pascoli and T. Schwetz, *Prospects for Neutrino Oscillation Physics*, Advances in High Energy Physics **2013**, 29 (2013).

[23] Borexino Collaboration, G. Bellini *et al.*, *First evidence of pep solar neutrinos by direct detection in Borexino*, Phys.Rev.Lett. **108**, 051302 (2012), [1110.3230].

[24] W. Winter, *Neutrino mass hierarchy determination with IceCube-PINGU*, Phys.Rev. **D88**, 013013 (2013), [1305.5539].

[25] K. Abe *et al.*, *Letter of Intent: The Hyper-Kamiokande Experiment — Detector Design and Physics Potential —*, ArXiv e-prints (2011), [1109.3262].

[26] L. Zhan, Y. Wang, J. Cao and L. Wen, *Experimental Requirements to Determine the Neutrino Mass Hierarchy Using Reactor Neutrinos*, Phys.Rev. **D79**, 073007 (2009), [0901.2976].

[27] LAGUNA-LBNO Collaboration *et al.*, *The mass-hierarchy and CP-violation discovery reach of the LBNO long-baseline neutrino experiment*, ArXiv e-prints (2013), [1312.6520].

[28] E. K. Akhmedov, R. Johansson, M. Lindner, T. Ohlsson and T. Schwetz, *Series expansions for three flavor neutrino oscillation probabilities in matter*, JHEP **0404**, 078 (2004), [hep-ph/0402175].

[29] P. Zucchelli, *A novel concept for a $\bar{\nu}_e/\nu_e$ neutrino factory: the beta-beam*, Physics Letters B **532**, 166 (2002).

[30] S. Geer, *Neutrino beams from muon storage rings: Characteristics and physics potential*, Phys. Rev. D **57**, 6989 (1998).

[31] P. Huber, M. Lindner and W. Winter, *Simulation of long-baseline neutrino oscillation experiments with GLoBES (General Long Baseline Experiment Simulator)*, Computer Physics Communications **167**, 195 (2005), [hep-ph/0407333].

[32] P. Huber, J. Kopp, M. Lindner, M. Rolinec and W. Winter, *New features in the simulation of neutrino oscillation experiments with GLoBES 3.0: General Long Baseline Experiment Simulator*, Computer Physics Communications **177**, 432 (2007), [hep-ph/0701187].

[33] A. M. Dziewonski and D. L. Anderson, *Preliminary reference Earth model*, Physics of The Earth and Planetary Interiors **25**, 297 (1981).

[34] F. D. Stacey, *Physics of the Earth*, 2 ed. (John Wiley & Sons Inc, Hoboken, 1977).

[35] M. Fukugita and T. Yanagida, *Physics of Neutrinos*, 1 ed. (Springer-Verlag, Berlin, 2003).

[36] A. Strumia and F. Vissani, *Precise quasielastic neutrino/nucleon cross-section*, Physics Letters B **564**, 42 (2003).

[37] Double Chooz Collaboration, Y. Abe *et al.*, *First Measurement of θ_{13} from Delayed Neutron Capture on Hydrogen in the Double Chooz Experiment*, Phys.Lett. **B723**, 66 (2013), [1301.2948].

[38] M.J. Berger, J.S. Coursey, M.A. Zucker and J. Chang, ESTAR, PSTAR, and ASTAR: Computer Programs for Calculating Stopping-Power and Range Tables for Electrons, Protons, and Helium Ions (version 1.2.3), Online database, 2010.

[39] J. Formaggio and G. Zeller, *From eV to EeV: Neutrino Cross Sections Across Energy Scales*, Rev.Mod.Phys. **84**, 1307 (2012), [1305.7513].

[40] H. M. Gallagher, *Neutrino oscillation searches with the Soudan 2 detector*, PhD thesis, University of Minnesota, 1996.

[41] R. Möllenberg, *Monte Carlo Study of Solar ^8B Neutrinos and the Diffuse Supernova Neutrino Background in LENA*, PhD thesis, Technische Universität München, 2013.

[42] C. Andreopoulos *et al.*, *The GENIE Neutrino Monte Carlo Generator*, Nucl. Instrum. Meth. **A614**, 87 (2010), [0905.2517].

[43] W. R. Leo, *Techniques for nuclear and particle physics experiments: a how-to approach*, 2 ed. (Springer-Verlag, 1994).

[44] M. Daimon and A. Masumura, *Measurement of the refractive index of distilled water from the near-infrared region to the ultraviolet region*, Appl. Opt. **46**, 3811 (2007).

[45] D. H. Perkins, *Introduction to High Energy Physics*, 4 ed. (Cambridge University Press, 2000).

[46] Y. Fukuda *et al.*, *The Super-Kamiokande detector*, Nucl. Instrum. Meth. **A501**, 418 (2003).

[47] D. L. Horrocks, *Applications of Liquid Scintillation Counting* (Academic Press Inc., 1974).

[48] A. Noujaim, C. Ediss and L. Wiebe, editors, *Proceedings of the International Conference on Liquid Scintillation Science and Technology*, 1976.

[49] G. Laustriat, *The luminescence decay of organic scintillators*, Molecular Crystals **4**, 127 (1968).

[50] J. B. Birks, *The Scintillation Process in Organic Systems*, IRE Transactions on Nuclear Science **7**, 2 (1960).

[51] G. Bellini *et al.*, *Cosmogenic Backgrounds in Borexino at 3800 m water-equivalent depth*, Journal of Cosmology and Astroparticle Physics **2013**, 049 (2013).

[52] J. Q. Meindl, *Reconstruction and Measurement of Cosmogenic Signals in the Neutrino Experiment Borexino*, PhD thesis, Technische Universität München, 2013.

[53] G. Bellini *et al.*, *Precision measurement of the 7Be solar neutrino interaction rate in Borexino*, Phys.Rev.Lett. **107**, 141302 (2011), [1104.1816].

[54] Borexino Collaboration, G. Bellini *et al.*, *Measurement of the solar 8B neutrino rate with a liquid scintillator target and 3 MeV energy threshold in the Borexino detector*, Phys.Rev. **D82**, 033006 (2010), [0808.2868].

[55] Borexino Collaboration, *Neutrinos from the primary proton-proton fusion process in the Sun*, Nature **512**, 383 (2014).

[56] J. Sawatzki, *Sensitivity Study of the Neutrino Mass Hierarchy Determination in JUNO Using Reactor Antineutrinos*, Master's thesis, Technische Universität München, 2014.

[57] L. Oberauer, P. Pfahler and M. Wurm, Liquid scintillator specification document, LAGUNA internal report, 2012.

[58] HELM AG, *Linear Alkylbenzene, EC safety data sheet*, 2011.

[59] SIGMA-ALDRICH, *2,5-Diphenyloxazole, Sicherheitsdatenblatt*, 2012.

[60] SIGMA-ALDRICH, *1,4-Bis(2-methylstyryl)benzene, Sicherheitsdatenblatt*, 2012.

[61] J. Winter, *Detection of Supernova Neutrinos in the Liquid-Scintillator Experiment LENA*, PhD thesis, Technische Universität München, 2013.

[62] P. Hackspacher, *Studies of Light Quenching effects in Liquid Scintillators and Parameter Determination of the Buffer and Veto Fluids of the Double Chooz Near Detector*, Master's thesis, Technische Universität München, 2014.

[63] J. Winter, *Phenomenology of Supernova Neutrinos, Spatial Event Reconstruction and Scintillation Light Yield Measurements for the Liquid-Scintillator Detector LENA*, Diploma thesis, Technische Universität München, 2007.

[64] G. Alimonti *et al.*, *Light propagation in a large volume liquid scintillator*, Nuclear Instruments and Methods in Physics Research Section A: Accelerators, Spectrometers, Detectors and Associated Equipment **440**, 360 (2000).

[65] C. Oppenheimer, *Determination of the light yield and transparency of LAB-scintillators as a function of the Bis-MSB concentration*, Bachelor's thesis, Technische Universität München, 2013.

[66] M. Wurm, *Cosmic Background Discrimination for the Rare Neutrino Event Search in BOREXINO and LENA*, PhD thesis, Technische Universität München, 2009.

[67] F. Ajzenberg-Selove, *Energy levels of light nuclei A = 13–15*, Nuclear Physics A **523**, 1 (1991).

[68] G. Beischler, *Engineering of an Optical Module for the LENA Detector with a Focus on the Development of a Light Concentrator*, Master's thesis, Technische Universität München, 2013.

[69] S. C. di Lorenzo, *Dèveloppement et caractérisation d'un ASIC de lecture de macro-cellule de photo-détecteurs de grande dimension*, PhD thesis, Université Paris 11, 2010.

[70] KamLAND Collaboration, A. Gando *et al.*, *Reactor On-Off Antineutrino Measurement with KamLAND*, Phys.Rev. **D88**, 033001 (2013), [1303.4667].

[71] Borexino Collaboration, G. Bellini *et al.*, *Measurement of geo-neutrinos from 1353 days of Borexino*, Phys.Lett. **B722**, 295 (2013), [1303.2571].

[72] K. A. Hochmuth *et al.*, *Probing the Earth's interior with a large-volume liquid scintillator detector*, Astropart.Phys. **27**, 21 (2007), [hep-ph/0509136].

[73] N.-H. Haag, *Experimental Determination of the Antineutrino Spectrum of the Fission Products of ^{238}U*, PhD thesis, Technische Universität München, 2013.

[74] H. Kleingrothaus, *Teilchenastrophysik* (Teubner, Stuttgart, 1997).

[75] J. N. Bahcall, A. M. Serenelli and S. Basu, *New solar opacities, abundances, helioseismology, and neutrino fluxes*, Astrophys. J. **621**, L85 (2005), [astro-ph/0412440].

[76] M. Wurm *et al.*, *Search for modulations of the solar Be7 flux in the next-generation neutrino observatory LENA*, Phys. Rev. D **83**, 032010 (2011), [1012.3021].

[77] A. Y. Smirnov, *The MSW effect and solar neutrinos*, hep-ph/0305106.

[78] M. Rampp, *Radiation Hydrodynamics with Neutrinos: Stellar Core Collapse and the Explosion Mechanism of Type II Supernovae*, PhD thesis, Technische Universität München, Max Plank Institute for Plasma Physics, 2000.

[79] K. Scholberg, *Supernova Neutrino Detection*, Annual Review of Nuclear and Particle Science **62**, 81 (2012), [1205.6003].

[80] M. Koshiba, *Observational neutrino astrophysics*, Physics Reports **220**, 229 (1992).

[81] M. Kaiser, *Supernova Neutrinos in LENA, Towards a Time- and Flavor-Resolved Analysis*, Master's thesis, Universität Hamburg.

[82] J. Gava, J. Kneller, C. Volpe and G. McLaughlin, *Dynamical Collective Calculation of Supernova Neutrino Signals*, Physical Review Letters **103**, 7 (2009), [0902.0317].

[83] M. Wurm, S. Lorenz, M. Kaiser and R. Möllenberg, Detection of astrophysical neutrinos in lena, LAGUNA deliverable, 2014.

[84] Super-Kamiokande Collaboration, K. Bays *et al.*, *Supernova relic neutrino search at super-Kamiokande*, Phys. Rev. D **85**, 052007 (2012).

[85] G. Senjanović, Proton decay and grand unification, in *American Institute of Physics Conference Series*, edited by G. Alverson, P. Nath and B. Nelson, , American Institute of Physics Conference Series Vol. 1200, pp. 131–141, 2010, [0912.5375].

[86] Super-Kamiokande, H. Nishino *et al.*, *Search for Proton Decay via $p \to e^+\pi^0$ and $p \to \mu^+\pi^0$ in a Large Water Cherenkov Detector*, Physical Review Letters **102**, 141801 (2009), [0903.0676].

[87] Super-Kamiokande, K. Kobayashi *et al.*, *Search for nucleon decay via modes favored by supersymmetric grand unification models in Super- Kamiokande-I*, Physical Review **D72**, 052007 (2005), [hep-ex/0502026].

[88] T. M. Undagoitia, *Measurement of light emission in organic liquid scintillators and studies towards the search for proton decay in the future large-scale detector LENA*, PhD thesis, Technische Universität München, 2008.

[89] G. D. Barr, T. K. Gaisser, P. Lipari, S. Robbins and T. Stanev, *Three-dimensional calculation of atmospheric neutrinos*, Phys. Rev. D **70**, 023006 (2004), [astro-ph/0403630].

[90] R. Abbasi *et al.*, *Measurement of the atmospheric neutrino energy spectrum from 100 GeV to 400 TeV with IceCube*, Phys. Rev. D **83**, 012001 (2011), [1010.3980].

[91] M. G. Aartsen *et al.*, *Measurement of Atmospheric Neutrino Oscillations with IceCube*, Physical Review Letters **111**, 081801 (2013), [1305.3909].

[92] The IceCube-PINGU Collaboration, *Letter of Intent: The Precision IceCube Next Generation Upgrade (PINGU)*, ArXiv e-prints (2014), [1401.2046].

[93] U. F. Katz, *The ORCA Option for KM3NeT*, ArXiv e-prints (2014), [1402.1022].

[94] M. S. Athar *et al.*, INDIA-BASED NEUTRINO OBSERVATORY, INO, Project Report Volume 1, 2006.

[95] J. Wenninger, CERN Accelerators and Beams Department Operations group, Private communication, XLIV. Arbeitstreffen Kernphysik in Schleching.

[96] Lorenz, Sebastian and Michael, Wurm, Report on comparison of detector-site options for lbl, liquid scintillator section, LAGUNA-LBNO Deliverables, 2014.

[97] J. J. Gomez-Cadenas *et al.*, *Physics Potential of Very Intense Conventional Neutrino Beams*, ArXiv e-prints (2001), [hep-ph/0105297].

[98] G. Vyacheslav, Optimized numu flux cern, Provided on the LAGUNA-LBNO Plone, `http://laguna.ethz.ch:8080/Plone/work/cern_beam_fluxes/optimized-numu-flux-cern/all-optimization-merged/at_download/file`.

[99] D. Hellgartner, *Lepton track reconstruction in LENA and attenuation length measurements in liquid scintillators*, Diploma thesis, Technische Universität München, 2011.

[100] S. Lorenz, *Discrimination of Neutral Current Background in a Future Long-Baseline Experiment with LENA*, Diploma thesis, Universität Hamburg, 2012.

[101] S. Lorenz, M. Wurm, D. Hellgartner and R. Möllenberg, Report on unified detector performance evaluation, lsc section, LAGUNA-LBNO Deliverables, 2014.

[102] The Geant4 Collaboration, *G4—a simulation toolkit*, Nuclear Instruments and Methods in Physics Research Section **506**, A250 (2003).

[103] The Geant4 Collaboration, *Geant4 developments and applications*, IEEE Transactions on Nuclear Science **53**, 270 (2006).

[104] L. Oberauer, C. Grieb, F. von Feilitzsch and I. Manno, *Light concentrators for Borexino and CTF*, Nuclear Instruments and Methods in Physics Research A **530**, 453 (2004), [physics/0310076].

[105] O. Y. Smirnov, P. Lombardi and G. Ranucci, *Precision measurements of timing characteristics of the 8' ETL9351 series photomultiplier*, Instrum.Exp.Tech. **47**, 69 (2004), [physics/0403029].

[106] G. Cowan, *Statistical data analysis* (Clarendon Press Oxford University Press, Oxford New York, 1998).

[107] F. James, *MINUIT-Function minimization and error analysis*, CERN Program Library Long Writeup D506.

[108] I. Antcheva *et al.*, *ROOT – A C++ framework for petabyte data storage, statistical analysis and visualization*, Computer Physics Communications **180**, 2499 (2009), 40 YEARS OF CPC: A celebratory issue focused on quality software for high performance, grid and novel computing architectures.

[109] I. Bronstein and K. Semendjajew, *Taschenbuch der Mathematik* (BG Teubner Verlagsgesellschaft, Stuttgart Leipzig und Verlag Nauka, Moskau, 1991).

[110] Borexino Collaboration, C. Arpesella *et al.*, *First real time detection of ^{7}Be solar neutrinos by Borexino*, 0708.2251.

[111] S. c. Wu, *Nuclear Data Sheet*, Nuclear Data Sheets **110**, 681 (2009).

[112] J. Peltoniemi, *Liquid scintillator as tracking detector for high-energy events*, ArXiv e-prints (2009), [0909.4974].

[113] J. G. Learned, *High Energy Neutrino Physics with Liquid Scintillation Detectors*, ArXiv e-prints (2009), [0902.4009].

[114] D. E. Groom, N. V. Mokohv and S. I. Striganov, *MUON STOPPING POWER AND RANGE TABLES*, Atomic Data and Nuclear Data Tables **76** (2001).

[115] B. Wonsak, K. Loo, D. Hellgartner, S. Lorenz and M. Wurm, Advanced particle tracking in liquid scintillator detectors, In preparation.

[116] MEMPHYS Collaboration, L. Agostino *et al.*, *Study of the performance of a large scale water-Cherenkov detector (MEMPHYS)*, JCAP **1301**, 024 (2013), [1206.6665].

[117] LAGUNA-LBNO collaboration, S. K. Agarwalla *et al.*, *Optimised sensitivity to leptonic CP violation from spectral information: the LBNO case at 2300 km baseline*, ArXiv e-prints (2014), [1412.0593].

[118] P. Coloma, T. Li and S. Pascoli, *A comparative study of long-baseline superbeams within LAGUNA for large θ_{13}*, ArXiv e-prints (2012), [1206.4038].

[119] T. Stempfle, *Reconstruction of Spatially Extended Events in Borexino*, Master's thesis, Technische Universität München, 2013.

[120] OPERA Collaboration, N. Agafonova *et al.*, *Observation of a first ν_τ candidate in the OPERA experiment in the CNGS beam*, Phys.Lett. **B691**, 138 (2010), [1006.1623].

[121] R. Acquafredda *et al.*, *The OPERA experiment in the CERN to Gran Sasso neutrino beam*, Journal of Instrumentation **4**, P04018 (2009).

[122] D. Meschede, *Gerthsen Physik*, 23 ed. (Springer, Berlin, 2005).

[123] M. Wurm *et al.*, *Optical scattering lengths in large liquid-scintillator neutrino detectors*, Review of Scientific Instruments **81**, 053301 (2010), [1004.0811].

[124] S. E. Quirk, *Purification of Liquid Scintillator and Monte Carlo Simulations of Relevant Internal Backgrounds in SNO+*, PhD thesis, Queen's University, Kingston, Canada, 2008.

[125] J. Meyer, *Realization and Characterization of the Muon Veto Scintillator and the Buffer Liquid of the Double Chooz Experiment*, Diploma thesis, Technische Universität München, 2010.

[126] S. Prummer, *Bestimmung optischer Parameter und der Stabilität des Flssigszintillators für den LENA Detektor*, Bachelor's thesis, Technische Universität München, 2012.

[127] INOX-COLOR GmbH & Co.K, 74725 Walldürn, Deutschland, Webpage, 2011.

[128] F. Callahan, *Swagelok Tube Fitter's Manual* (Swagelok, Solon, Ohio, 1993).

[129] J. Janicsko, private communication, 2015, Technische Universität München.

[130] Roithner Laser, *LED 430-33, Datasheet.*

[131] W. Demtröder, *Experimentalphysik 2, Elektrizität und Optik*, 5 ed. (Springer-Verlag, Berlin, 2009).

[132] ET Enterprises, *9111B series data sheet.*

[133] ET Enterprises, *9124B series data sheet.*

[134] C. Ciemniak, *Setup of a Neutron Scattering Facility for the Measurement of Scintillation Light Quenching Factors of Low-Temperature Detectors Used in the Direct Dark Matter Search Experiments CRESST and EURECA*, PhD thesis, Technische Universität München, München, 2011.

[135] Qt Project, Webpage, 2015, `http://qt-project.org/`.

[136] Qwt Project, Webpage, 2015, `http://qwt.sf.net`.

[137] A. Himpsl, *In preparation*, PhD thesis, Technische Universität München, 2018.

[138] V. Zimmer, *In preparation*, PhD thesis, Technische Universität München, 2015.

[139] M. Willers *et al.*, *Neganov-Luke amplified cryogenic light detectors for the background discrimination in neutrinoless double beta decay search with TeO_2 bolometers*, JINST **10**, P03003 (2015), [1407.6516].

[140] C. Bruhn, *Production and characterization of scintillating $CaWO_4$ single crystals for rare event searches*, Master's thesis, KTH Royal Institute of Technology, Stockholm, Sweden and Technische Universität München, 2015.

[141] R. Abbasi *et al.*, *Calibration and characterization of the IceCube photomultiplier tube*, Nuclear Instruments and Methods in Physics Research Section A: Accelerators, Spectrometers, Detectors and Associated Equipment **618**, 139 (2010).

[142] SCHOTT, *Optical Glass Data Sheets.*

[143] F. James, L. Lyons and Y. Perrin, editors, *Comment on Methods for setting Confidence Limits*, Workshop on confidence limits, CERN, CERN-Library, 2000.

[144] OPERA collaboration, T. Adam *et al.*, *Measurement of the neutrino velocity with the OPERA detector in the CNGS beam*, JHEP **1210**, 093 (2012), [1109.4897].

[145] M. Frigo and S. G. Johnson, *The Design and Implementation of FFTW3*, Proceedings of the IEEE **93**, 216 (2005), Special issue on "Program Generation, Optimization, and Platform Adaptation".

[146] S. Klupp, *A calibration experiment for the AGATA pulse shape analysis*, Diploma thesis, Technische Universität München, 2011.

[147] M. Daimon and A. Masumura, *Measurement of the refractive index of distilled water from the near-infrared region to the ultraviolet region*, Appl. Opt. **46**, 3811 (2007).

[148] A. Ulrich, private communication, 2014, Technische Universität Müncen.

[149] ATIK Cameras, *Atik 383L+ user manual, Version 1.2.*

[150] ATIK Cameras, *Artemis Capture user's manual, Version 2.1.*

[151] G. Long *et al.*, *Attenuation length measurements of a liquid scintillator with LabVIEW and reliability evaluation of the device*, Chinese Physics C **37**, 076001 (2013).

[152] S. Prummer, Master's thesis, Technische Universität München, 2015, in preparation.

[153] J. Goett *et al.*, *Optical attenuation measurements in metal-loaded liquid scintillators with a long-pathlength photometer*, Nuclear Instruments and Methods in Physics Research Section A: Accelerators, Spectrometers, Detectors and Associated Equipment **637**, 47 (2011).

[154] G. Cowan, K. Cranmer, E. Gross and O. Vitells, *Asymptotic formulae for likelihood-based tests of new physics*, European Physical Journal C **71**, 1554 (2011), [1007.1727].

[155] M. Honda, T. Kajita, K. Kasahara and S. Midorikawa, *Improvement of low energy atmospheric neutrino flux calculation using the JAM nuclear interaction model*, Phys. Rev. D **83**, 123001 (2011), [1102.2688].

[156] M. Sajjad Athar, M. Honda, T. Kajita, K. Kasahara and S. Midorikawa, *Atmospheric neutrino flux at INO, South Pole and Pyhäsalmi*, Physics Letters B **718**, 1375 (2013), [1210.5154].

Danksagung

Diese Arbeit wäre nicht möglich gewesen, ohne die Unterstützung durch meine Kollegen und Freunde. Euch allen gebührt an dieser Stelle ein großes Dankeschön.

Zuerst möchte ich mich bei Prof. Stefan Schönert für die Aufnahme an seinem Lehrstuhl, für die Möglichkeit diese Arbeit anzufertigen sowie für sein fortwährendes Interesse an dieser Arbeit bedanken.
Meinem Doktorvater Prof. Lothar Oberauer gebührt ein großes Dankeschön für die hervorragende Betreuung dieser Arbeit. Seine offene Art und die vielen Diskussionen, nicht nur über physikalische Themen, waren eine echte Bereicherung.
Auch bei Priv.-Doz. Dr. Andreas Ulrich möchte ich mich ganz herzlich bedanken: Ohne seinen Rat und seine Unterstützung wäre die zweite Iteration des Abschwächlängenexperiments nicht möglich gewesen.
Abgesehen davon, dass er durch das Bereitstellen der LENA-Simulation und seine GENIE-Simulationen meine Arbeit überhaupt erst ermöglicht hat, war Dr. Randolph Möllenberg für mich ein hervorragender Kollege. Vielen vielen Dank. Außerdem möchte ich mich bei ihm auch noch für das Korrekturlesens des ersten Teils meiner Arbeit sowie für seine offene, direkte Art und für die vielen Diskussionen die weit über die Physik hinausgingen bedanken. Seine Fähigkeit die für eine Arbeit benötigte Zeit einzuschätzen grenzt an Hellseherei.
Ein gorßer Dank gebührt auch Dr. Walter Potzel für das kritische, kompetente und zeitnahe Korrekturlesen dieser Arbeit.
Vincenz Zimmer und Andreas Zöller danke ich für die gute Zusamenarbeit in meiner ganzen Zeit am Lehrstuhl, für ihre Hilfsbereitschaft und für die vielen Diskussionen, die häufig weit über die Physik hinausgingen. Auch eure tollen Kuchen werde ich so schnell nicht vergessen.
Ein großes Dankeschön geht auch an die ganze LENA-Gruppe: Prof. Michael Wurm, der diese Doktorarbeit wesentlich mit angestossen und vorangetrieben hat, Dr. Björn Wonsak für sein umfangreiches Fachwissen in der Rekonstruktion von Hochenergieevents in LENA und für das Korrekturlesen von Kapitel 4, Sebastian Lorenz für seine tolle Arbeit mit GLoBES, Kai Loo für das kompetente Weiterführens meines Backtrackingalgorithmus sowie für das Bereitstellen der nötigen Rechenleistung, Dr. Wladyslaw Trzaska für seinen Optimismus im Bezug auf LENA und für seine Bereitschaft sich in LAGUNA immer für LENA einzusetzen sowie Tobias Stempfle für die grandiose Implementierung des Backtrackingalgorytmusses in Borexino. Auch Abseits der Arbeit konnte man mit euch immer seien Spaß haben, was so manches LAGUNA-Meeting überhaupt erst erträglich gemacht hat.

Meine experimentellen Arbeiten wären nicht möglich gewesen ohne die Hilfe von Dr. Honghanh Trinhthi ohne die ich weder LAB noch sauberer Rohre gehabt hätte. Auch Sabrina Prummer gilt ein großer Dank für ihre "Helfenden Hände", die super Zusammenarbeit, sowie für ihre Bereitschaft das Abschwächlängenexperiment weiter zu führen. Alexander Neumeier gilt ein großer Dank für die Einführung in die Handhabung der ATIK sowie für die Bereitstellung seiner Befestigungsmaterialien. Bei Dr. Sabine Roth möchte ich mich für den Rat und die vielen Diskussionen über meine Versuchsergebnisse bedanken.
Ohne die tadellose Arbeit unseres Werkstattteams Harald Hess, Raffael Jahrstorfer, Lukas Hein und Thomas Richter, wäre diese Arbeit nicht möglich gewesen. Vielen Dank für die Beratung beim mechanischen Design meiner Experimente und für die Herstellung von gefühlt 100 000 Bauteilen.
Was nutzt einem die schönste Elektronik wenn man im Rauschen untergeht? Vielen Dank an Herrn Hermann Hagn, der das durch seine Wissen und seine Erfahrung noch immer zu verhindern wusste. Michael Franke möchte ich für die Anfertigung der Platinen für die Auslese der Drucksensoren danken.
Dr. Jozsef Janicsko und Christoph Wiesinger möchte ich für die gute Zusammenarbeit im UGL danken und dafür, dass sie es mir nie übel nahmen, wenn ich mal wieder das Labor abgedunkelt habe.
Ein Dank gebührt auch Dr. Michael Willers, der dafür dass er halb im UGL wohnt ein bemerkenswertes Talent hat sein Experiment fernzusteuern, für die gemeinsame Zeit im UGL, dafür dass ich mir immer seinen Lötkolben leihen durfte und für seinen Einsatz als Admin. Norbert Gärtner danke ich dafür, dass er die meisten Strahlenschutzsachen stets von mir ferngehalten hat.
Bedanken möchte ich mich auch bei Dr. Jean-Côme Lanfranchi, für die gute Zusammenarbeit bei der Astroteilchenvorlesung und dafür das er aus seinem schlechten Gewissen einen sorgenfreien Doktoranden gemacht hat.
Bei meinen Bürokollegen Julia Sawatzki, Simon Appel, Dominik Jeschke, Raimund Strauß, Marc Wüstrich und Christian Ciemniak möchte ich mich für die gute Atmosphäre und das gute Arbeitsklima bedanken. Letzterem gebührt noch ein besonderes Dankeschön für seine Einführung in die VME-Programmierung.
Unseren Sekretärinnen Maria Bremberger, Elke Krüger, Petra Zweckinger, Sigrid Weichs und Sabine Kaps gebührt ein besonderer Dank dafür, dass sie in der "Uni die Verrückte macht" immer den Überblick behalten haben und mir mit Rat und Tat bei allen Verwaltunsfragen zur Seite gestanden sind.

Bedanken möchte ich mich auch bei Robert Lang für die langjährige gute Freundschaft und für die vielen Abende, an denen die wir über Gott und die Welt diskutiert haben.
Ein Dank geührt auch meinen alten Freunden Martin und Monika Riedl, Martin Maierhofer und Matthias Fuchs dafühir das ihr noch immer Zeit gefunden habt irgendetwas mit mir zu unternehmen.
Auch bei all den Leuten die regelmäßig mit mir tanzen gehen, möchte ich mich ganz herzlich bedanken: Ihr habt immer dafür gesorgt dass es zumindest ein paar Stunden in jeder Woche gab in denen ich nicht an diese Arbeit gedacht habe.
Ein besonderer Dank gebührt meiner Familie, die mich in all den Jahren des Studiums und der Doktorarbeit immer unterstützt haben. Wenn ich jetzt hier alles aufschreiben müsste, für was ich meiner Frau Stefanie Hellgartner alles dankbar bin, dann wird das eine sehr lange Arbeit. Deshalb hier nur kurz: Vielen vielen Dank für alles!